DEVELOPMENT OF
HIGH RESOLUTION GAS FILLED DETECTOR
FOR HIGH ENERGY PHYSICS EXPERIMENTS

Thesis submitted for the degree of
Doctor of Philosophy (Science)
of the
University of Calcutta

By
Saikat Biswas

Department of Physics
University of Calcutta

2010

Dedicated to

Prof. Satyajit Saha
Prof. Sudeb Bhattacharya
Dr. Yogendra Pathak Viyogi
and
Dr. Subhasis Chattopadhyay

ACKNOWLEDGMENTS

<div align="right">
Saikat Biswas
Kolkata, India
</div>

Abstract of The Thesis

In this thesis the detailed study of the development of bakelite Resistive Plate Chambers (RPCs) for the Iron Calorimeter (ICAL) prototype for India-based Neutrino Observatory (INO) has been described.

The Resistive Plate Chambers (RPCs), first developed by Santonico et al. are being used extensively in high energy physics and neutrino physics experiments. RPC is a gas filled detector utilizing a constant and uniform electric field produced by two parallel electrode plates made of a material of high bulk resistivity ($\sim 10^9$-10^{12} Ω cm, e.g. Glass, Bakelite) separated by spacers, made of polycarbonate. The use of large area RPCs in experiments like BELLE, BaBar, BESIII, and several LHC experiments (ALICE, ATLAS, CMS etc.) are mainly for a) relatively low cost of materials used in making RPCs, b) robust fabrication procedure and handling and c) good time and position resolutions. RPCs are used in neutrino experiments like OPERA where its excellent time resolution and tracking capabilities are exploited.

In the proposed India-based Neutrino Observatory (INO) the phenomenon of neutrino oscillation will be studied through the detection of muons (produced through the interaction of neutrinos) in an Iron Calorimeter (ICAL). In ICAL, the RPCs have been chosen as the active detector for muon detection. As proposed presently, ICAL is a sampling calorimeter consisting of 140 layers of magnetized iron each of 60 mm thickness. RPCs of 2 m $\times$ 2 m area act as the active media sandwiched between the iron plates. When fully installed, a 50 kton ICAL is expected to consist of about 27000 RPC modules.

Detailed R&D program is being pursued elsewhere on glass RPCs for INO. In this thesis I have presented a parallel effort on building and testing of the RPC modules using different grades of bakelite paper laminates, produced and commercially available in India. The bakelite RPC prototypes, operated in the streamer mode using argon, tetrafluroethane (R-134a) and isobutene in 55:37.5:7.5 volume mixing ratio, are tested for the efficiency and stability with cosmic rays. A particular grade of bakelite (P-120, NEMA LI-1989 Grade XXX), used usually for high voltage insulation under humid conditions, when used as RPC electrodes, was found to give satisfactory performance with stable efficiency of >90%, counting rate of ~ 0.1 Hz/cm^2 and time resolution (FWHM) ~ 2 ns continuously for a long period in streamer mode. A thin coating of silicone fluid on the inner surfaces of the bakelite plates was found to be necessary for the operation of the detector with high efficiency.

In this thesis: Motivation of this development in the context of INO, a review of RPC development elsewhere, the fabrication details of bakelite-based RPC, their testing with cosmic muons and R&D for attaining required performance have been presented. Installation and commissioning of the ICAL prototype have also been presented.

Contents

List of Figures

List of Tables

Chapter 1

Introduction

1.1 Introduction

Over the last few decades a coherent picture of the existence and creation of elementary particles has slowly emerged. Since the development of the atomic model, improvements in the experimental techniques and precision have allowed physicists to investigate finer structures of the matter. Atom is made of a nucleus and electrons. Even the atomic nucleus, which contains practically the total mass of an atom, is a composite object. Protons and neutrons which are the building blocks of the nucleus, consist of more elementary particles as become obvious in electron-nucleon scattering experiments. The nucleons consist of three quarks. So, the onion-type structure consisting of smaller constituents of particles emerged slowly that were initially considered to be fundamental and elementary.

The "Standard Model" of particle physics is a model describing the existence and the way the elementary particles of matter interact. In the Standard Model there are twelve building blocks of matter; six different kinds of quarks: up (u), down (d), charm (c), strange (s), top (t) and bottom (b); three different types of charged leptons: electron (e^-), muon (μ^-), tau (τ^-), and three neutrinos ν_e, ν_μ, ν_τ associated with each charged lepton and their antiparticles. Three quark generations have one-to-one correspondence with three lepton generations:

$$\text{Quarks}: \begin{pmatrix} u \\ d \end{pmatrix}, \begin{pmatrix} c \\ s \end{pmatrix}, \begin{pmatrix} t \\ b \end{pmatrix}$$
$$\text{Leptons}: \begin{pmatrix} \nu_e \\ e^- \end{pmatrix}, \begin{pmatrix} \nu_\mu \\ \mu^- \end{pmatrix}, \begin{pmatrix} \nu_\tau \\ \tau^- \end{pmatrix}$$

Table 1.1: The table of the elementary particles: matter particles [1]

LEPTONS ℓ, spin $\frac{1}{2}\hbar$ (antileptons $\bar{\ell}$)						
electric charge [e]	1. generation		2. generation		3. generation	
	flavour	mass [GeV/c^2]	flavour	mass [GeV/c^2]	flavour	mass [GeV/c^2]
0	ν_e electron neutrino	$< 2.5 \times 10^{-9}$ at 95% CL	ν_μ muon neutrino	$< 1.9 \times 10^{-4}$ at 90% CL	ν_τ tau neutrino	< 0.018 at 95% CL
-1	e electron	5.11×10^{-4}	μ muon	0.106	τ tau	1.777
QUARKS q, spin $\frac{1}{2}\hbar$ (antiquarks $\bar{q}$)						
electric charge [e]	flavour	$\simeq$ mass [GeV/c^2]	flavour	$\simeq$ mass [GeV/c^2]	flavour	$\simeq$ mass [GeV/c^2]
+2/3	u up	1.5×10^{-3} to 4×10^{-3}	c charm	1.15 to 1.35	t top	174.3
-1/3	d down	4×10^{-3} to 8×10^{-3}	s strange	0.08 to 0.13	b bottom	4.1 to 4.4

The properties of these fundamental matter particles are listed in Table 1.1. Quarks are con-
stituents of strongly interacting hadronic matter. Quarks have fractional electric charges (in the
units of the elementary charge e). Different kinds of quarks (u, d; c, s; t, b) in three respective
generations or families are characterized by different flavours. Though the quarks interact pri-
marily through the strong force, they also experience all other three basic interactions of nature
i.e. electromagnetic, weak and gravity. Their binding through the colour (strong) interaction
gives rise to the proton, the neutron, nuclei and all other hadrons. The charged leptons do not
interact via the colour force, but experience other three forces.

The interaction between the elementary particles are governed by four different forces as men-
tioned in the last paragraph. They are strong, electromagnetic, weak and gravitational in-
teractions. In 1960 it was possible to unify the electromagnetic and weak interactions into
the electroweak theory. The carriers of all the four interactions are particles with integer spin
(bosons), in contrast to the matter particles which all have half-integer spin (fermions). While

Table 1.2: The properties of interaction [1]

interaction →	gravitation	electroweak		strong
property ↓		weak	electro-magnetic	
acts on	mass-energy	flavour	electric charge	colour charge
affected particles	all	quarks, leptons	all charged particles	quarks, gluons
exchange particles	graviton G	W^+, W^-, Z	γ	gluons g
range	∞	$\approx 10^{-3}$ fm	∞	≈ 1 fm
relative strength	10^{-40}	10^{-5}	10^{-2}	1
example	system Earth-Moon	β decay	atomic binding	nuclear binding

the existence of the gauge bosons of electroweak interactions (W^+, W^-, Z and γ), and the gluons g of strong interactions are well established, the carrier of the gravitational force, the *graviton*, has not yet been discovered. The properties of all the interactions are summarized in Table 1.2. It is apparent from the comparison that the gravitational force can be completely neglected in the microscopic domain, because its strength is very small compared to the others.

Neutrinos are leptons without electric charge. There are three known types of neutrino, which are all very light. These leptons are electron-type, muon-type and tau-type neutrino for the electron, muon and tau family. At the LEP experiments it could be shown that apart from the three already known neutrino generations there is no further generation with light neutrinos (m<45 GeV/c^2) [1].

The birth of the neutrino due to W. Pauli in 1930 was a rather desperate attempt to explain the continuous Beta-spectrum:

"...I have considered ... a way out for saving the law of conservation of energy. Namely, the possibility that there could exist in the nuclei electrically neutral particles, that I will call neutrons (which are today called neutrinos) which have spin $\frac{1}{2}$ and follow the exclusion

principle. The continuous beta-spectrum would then be understandable assuming that in beta-decay together with the electron, in all cases, also a neutron is emitted in such a way that the sum of energy of neutron and of electron remains constant... I admit that my solution appears to you not very probable ... But only who dares wins, and the gravity of the situation in regard to continuous beta-spectrum..."

Their name is due to Enrico Fermi who, in 1934, made them the basis for a theory of weak interactions. This particle is very difficult to observe because of their very small interaction cross sections with matter. But in a series of experiments Reines and Cowan conclusively proved their existence through the inverse beta-decay weak interaction process where an electron-type antineutrino is captured by a proton p giving rise to a positron e^+ and a neutron n.

Neutrinos can pass from one end of the earth to another without any interaction since they hardly interact with matter. So they are very difficult to detect. Neutrinos can interact only via weak interactions. There is no effect of strong or electromagnetic interaction on neutrinos. The weak interaction (ν_e + e $\rightarrow \nu_e$ + e) cross-section (σ) of neutrino is $\sim 10^{-43}$ cm^2. The σ for a typical electromagnetic interaction is $\sim 10^{-27}$ cm^2 whereas that for strong interaction is $\sim 10^{-23}$ cm^2. So one can get an idea how weakly neutrinos interact.

The sources of Neutrinos available to us are:

1) Solar neutrino,
2) Atmospheric neutrino,
3) Neutrinos from Reactor,
4) Neutrinos from Accelerator.

Within the Standard Model, neutrinos of three types or flavours and their antiparticles are massless and interact with matter only through the weak interaction and hence are difficult to detect. It is precisely this lack of interaction strength that makes the neutrinos elusive. Since in the Standard Model the lepton flavour or family number is conserved, there is no scope for the neutrino flavours to "oscillate" into each other, i.e. to change from one type/flavour to another. If, however, neutrinos have mass, and, furthermore, the neutrino flavour-states which participate in the weak interactions are mixtures of mass eigenstates with different masses, then quantum mechanical evolution of these flavour states leads to the phenomenon of neutrino

oscillations. The admixture of mass eigenstates in a given flavour state are parametrised by a set of mixing angles. A large mixing angle implies a large mixing between the eigenstates.

Over the last few years, data from several neutrino detectors around the world, in particular, those from the Super-Kamiokande (Super-K) [2, 3, 4, 5, 6, 7] and KamLAND [8] detectors in Japan, and the Sudbury Neutrino Observatory (SNO) [9, 10, 11] in Canada have shown that the neutrinos have mass and they oscillate. Results of these experiments constrain the extent of mixing angles as well as the squared differences of the three masses so called mass-squared difference . Since the absolute masses themselves are not constrained by such observations , at least two of the neutrinos must be massive and have different masses. This provides the first unambiguous evidence for physics beyond the Standard Model of particle physics.

1.2 The Solar Neutrino Problem

Eddington suggested that the nuclear fusion process is the source of the solar energy. He noticed that four hydrogen atoms ($_1\text{H}^1$) weight slightly more than one atom of helium-4 ($_2\text{He}^4$). This implied in view of Einstein's $E = mc^2$ relation that the fusion of four hydrogens would be energetically possible, and would release a substantial amount of energy. The *mechanism* for binding the hydrogens together was unknown until Chadwick's discovery of the neutron and Pauli's invention of the neutrino.

In 1938, Hans Bethe worked out the details of this nuclear fusion mechanism. In heavy stars the dominant mechanism is the CNO (Carbon-Nitrogen-Oxygen) cycle, in which the fusion process is 'catalyzed' by small amounts of those three elements, but in the sun and other relatively light stars the dominant process is the so-called *pp* chain shown in Table 1.3. To begin with, two protons (hydrogen nuclei) combine to make a deuteron, a positron, and an electron-type neutrino. The deuteron is a nucleus made with a proton and a neutron, so what really happened here is that a proton converted into a neutron, a positron and a neutrino - the reverse of neutron decay. Alternatively, the outgoing positron could be replaced by an incoming electron *i.e.* a pair of protons and an electron combine to make a deuteron and a neutrino. Either way, protons produced deuterons along with some neutrinos. The deuteron soon picks up another proton to form a helium-3 nucleus (composed of two protons a neutron), releasing energy in the form

of photon. Helium-3 can undergo three possible reactions: it can combine with another loose proton to make an alpha particle - the helium-4 nucleus (a system composed of two protons and two neutrons). In this reaction, once again, a proton converted into a neutron with emission of a positron and a neutrino. Or a pair of helium-3s can get together to make an alpha particle and two protons. Or the helium-3 nucleus can combine with an alpha particle, produced in one of the previous two reactions, to make beryllium-7, with the emission of photon. Finally, the beryllium-7 can either absorb an electron, producing a lithium-7, which picks up a proton, yielding two alpha particles, or else the beryllium-7 absorbs a a proton, making a boron-8, which goes to an excited state of beryllium-8, and from there to two alpha particles.

The pp Chain

Step 1: Two protons make a deuteron.

$$p + p \rightarrow d + e^+ + \nu_e$$

$$p + p + e^- \rightarrow d + \nu_e$$
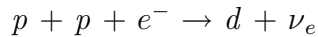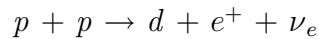
Step 2: Deuteron plus proton makes ^{3}He.

$$d + p \rightarrow {}^3\text{He} + \gamma$$

Step 3: Helium-3 makes α particle or ^{7}Be.

$$^3\text{He} + p \rightarrow \alpha + e^+ + \nu_e$$

$$^3\text{He} + {}^3\text{He} \rightarrow \alpha + p + p$$
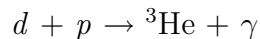
$$^3\text{He} + \alpha \rightarrow {}^7\text{Be} + \gamma$$

Step 4: Beryllium makes α particles.

$$^7\text{Be} + e^- \rightarrow {}^7\text{Li} + \nu_e$$

$$^7\text{Li} + p \rightarrow \alpha + \alpha$$

$$^7\text{Be} + p \rightarrow {}^8\text{B} + \gamma$$

$$^8\text{B} \rightarrow {}^8\text{Be}^* + e^+ + \nu_e$$

$$^8\text{Be}^* \rightarrow \alpha + \alpha$$
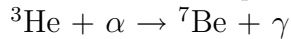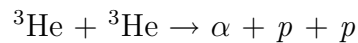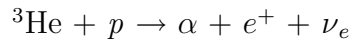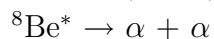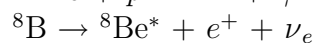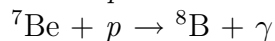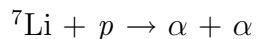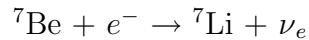
Table 1.3: The *pp* chain: how protons produce alpha particles in the sun [12]

The main feature of this *pp* chain is that it all starts out as protons (hydrogen nuclei), and it all ends up as alpha particles (helium-4 nuclei) in association with some electrons, positrons, photons and neutrinos (electron type). Among all the particles since neutrinos only interact weakly with matter, they emerge virtually unscathed by passage from the centre to the surface of the sun. They practically carry all the information of solar energy. Neutrinos are, therefore, the perfect probes for studying the interior of the sun.
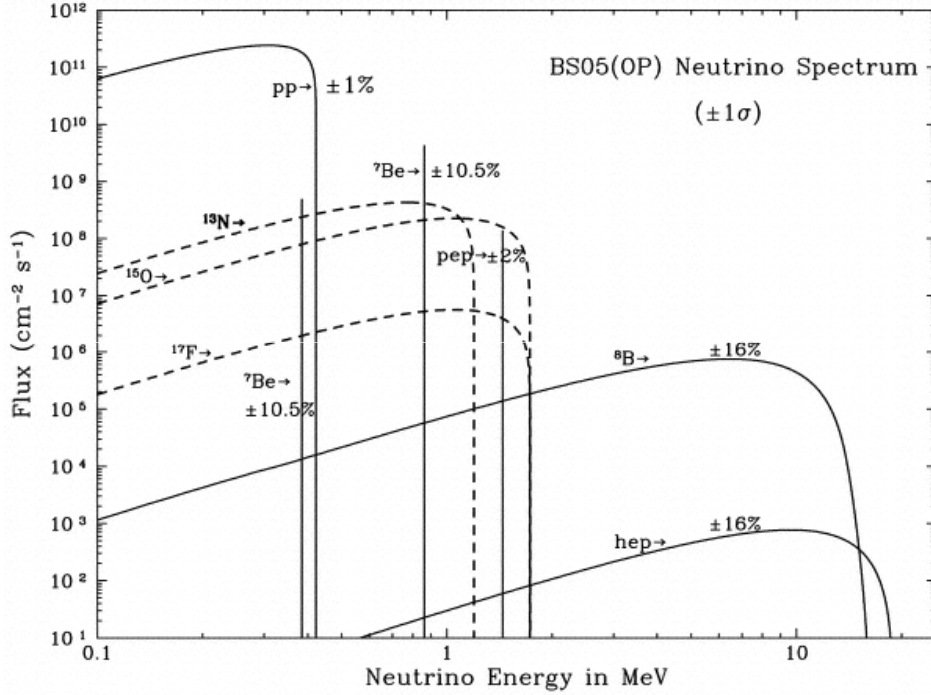
Figure 1.1: The calculated energy spectra of the solar neutrinos. (The Figure is adopted from Ref. [13]).

The sun is a pure electron-neutrino source. It does not produce electron antineutrinos and in particular, no other neutrino flavours (ν_μ, ν_τ). In the *pp* chain there are five reactions that yield neutrinos, and for each reactions the neutrinos come out with a characteristic energy spectrum, as shown in Figure 1.1. The major contribution comes from the initial reaction $p + p \rightarrow d + e^+ + \nu_e$. 86% of solar neutrinos are produced in this proton-proton reaction [1]. Unfortunately, these neutrinos carry relatively low energy, and most detectors are insensitive in this energy regime. For that reason, even though the boron-8 decay contributes only at the level of 0.02%, most experiments actually work with them. In total, the solar neutrino flux at earth amounts to about 7×10^{10} particles per cm^2 per second.

There are certainly plenty of neutrinos coming from the sun. John Bahcall was responsible for most of the calculations of solar neutrino abundances. The historically first experiment for the search of solar neutrinos, was reported by Ray Davis *et.al.*, in 1968, using a huge tank of tetrachloroethylene (C$_2$Cl$_4$) in the Homestake mine in South Dakota [14]. Because of the low capture rate of less than one neutrino per day the experiment must be shielded against atmospheric cosmic rays. Therefore, it was operated in a gold mine at 1500 meter depth under

the earth's surface. Chlorine can absorb a neutrino and convert to argon by the reaction $\nu_e + {}^{37}\mathrm{Cl} \rightarrow {}^{37}\mathrm{Ar} + e^-$ where the actual mechanism was $\nu_e + n \rightarrow p + e$. This experiment collected the argon atom for several months at a rate of about one atom every two days. The total accumulation was only about one third of the value, predicted by John Bahcall [15]. This anomaly between theory and experiment gives rise the famous *solar neutrino problem*.

1.3 Atmospheric neutrino

The sun is not the only supplier of neutrinos. For real neutrino astronomy neutrinos from atmospheric sources are an annoying background. Primary cosmic rays (high-energy protons from the outer space) interact in the atmosphere with the atomic nuclei of nitrogen and oxygen. In these interactions nuclear fragments and predominantly charged and neutral pions (π^+, π^-, π^0) are produced. The charged pions, having an average lifetime of 26 ns decay into muon and muon neutrinos according to:

$$\pi^+ \rightarrow \mu^+ + \nu_\mu, \qquad \pi^- \rightarrow \mu^- + \overline{\nu}_\mu. \tag{1.1}$$

Muons themselves are also unstable and decay with an average lifetime of 2.2 μs according to:

$$\mu^+ \rightarrow e^+ + \nu_e + \overline{\nu}_\mu, \qquad \mu^- \rightarrow e^- + \overline{\nu}_e + \nu_\mu. \tag{1.2}$$

Therefore, according to equations (1.1) and (1.2)the atmospheric neutrino should contain muon-type and electron-type neutrinos in the ratio

$$\frac{N(\nu_\mu, \overline{\nu}_\mu)}{N(\nu_e, \overline{\nu}_e)} \equiv \frac{N_\mu}{N_e} \approx 2. \tag{1.3}$$

One of the largest experiment measuring the atmospheric neutrino is Super-Kamiokande in the Kamioka mine in Japan.In this experiment the neutrino interaction are recorded in a huge tank of approximately 50 kilotons of ultrapure water. The electron-type neutrinos transfer a part of their energy to the electrons in the detector medium via the interaction,

$$\nu_e + e^- \rightarrow \nu_e + e^-, \tag{1.4}$$

or produce electrons in the interaction with nucleons:

$$\nu_e + N \rightarrow e^- + N'. \tag{1.5}$$

Muon neutrinos produce the corresponding charged-lepton muons in the neutrino-nucleon interaction according to:

$$\nu_\mu + N \rightarrow \mu^- + N'. \tag{1.6}$$

Similarly, $\overline{\nu}_e$ and $\overline{\nu}_\mu$ produce the corresponding charged leptons e^+ and μ^+ in the interaction with the nucleons. The charged leptons (e^-, e^+, μ^-, μ^+) are detected via the Cherenkov radiation in the water. The produced Cherenkov light is detected by 11200 photomultiplier tube of 50 cm cathode diameter. The electrons in the GeV-range produced characteristic electromagnetic cascades of short range while muons gives long straight tracks in this energy range. This is the basis for distinguishing electron-type neutrino from muon-type neutrino.

The result of the Super-Kamiokande experiment shows that the number of electron-neutrino events matches well with the theoretical prediction but there is a clear deficit of events initiated by muon type neutrinos. There is different acceptance for electrons and muons in the water Cherenkov detector. So the ratio of numbers of the muon and electron events obtained in the experiment is compared with that ratio obtained from Monte Carlo simulation. For the double ratio

$$R = \frac{(N_\mu/N_e)_{data}}{(N_\mu/N_e)_{MonteCarlo}} \tag{1.7}$$

one would expect the value $R = 1$ to match the simulation with experiment. However, the Super-Kamiokande experiment obtains

$$R = 0.69 \pm 0.06 \tag{1.8}$$

which shows a clear deviation from the expectation.

After careful analysis of the experimental results and investigations of possible systematic effects the general opinion prevails that the deficit of muon neutrino from the expected value can only be explained by *neutrino oscillation*.

1.4   Neutrino Oscillation

In 1908, Bruno Pontecorvo suggested a simple and beautiful explanation for the solar neutrino problem. He suggested that the electron-type neutrinos produced at sun are transformed into a different flavours (muon-type neutrinos, say) in flight, and Davis' experiment was insensitive to

this new flavour [16]. This is the mechanism of the so called *neutrino oscillation*. The neutrino oscillation is a quantum mechanical phenomena depending on the superposition principle.

The eigenstates of weak interactions $\mid \nu_e \rangle$, $\mid \nu_\mu \rangle$ and $\mid \nu_\tau \rangle$ are superpositions of mass eigenstates $\mid \nu_1 \rangle$, $\mid \nu_2 \rangle$ and $\mid \nu_3 \rangle$. An electron-type neutrino ν_e born in sun could be transformed during the propagation from the source to the detector into a different neutrino flavour. If the electron neutrino in reality was a mixture of two different mass eigenstates $\mid \nu_1 \rangle$ and $\mid \nu_2 \rangle$, these two states would propagate with different velocities if their masses were not identical and so the mass components get out of phase with each other. This could possibly result in a different neutrino flavour at the detector. If, however, all neutrinos were massless, they would all propagate precisely with the velocity of light, and the mass eigenstates can never get out of phase with each other.

For simplicity consider the case of two neutrino flavours - say, ν_e and ν_μ. If one flavour spontaneously convert into the other, it means that neither is an eigenstate of the Hamiltonian. In this case the weak eigenstates $\mid \nu_e \rangle$ and $\mid \nu_\mu \rangle$ could be expressed as the orthogonal linear superposition of the mass eigenstates $\mid \nu_1 \rangle$ and $\mid \nu_2 \rangle$.

$$\mid \nu_e \rangle = \mid \nu_1 \rangle cos\theta + \mid \nu_2 \rangle sin\theta; \qquad \mid \nu_\mu \rangle = - \mid \nu_1 \rangle sin\theta + \mid \nu_2 \rangle cos\theta \qquad (1.9)$$

The *mixing angle* θ determines the degree of mixing. This assumption requires that the neutrinos are massive and, in addition, $m_1 \neq m_2$ must hold.

According to the Schrödinger equation, the eigenstates $\mid \nu_1 \rangle$ and $\mid \nu_2 \rangle$ have the simple time dependence $e^{-iE_1 t}$. (Here and below the natural system of units is used in which the velocity of light $c = 1$ and reduced Planck constant $\hbar = 1$.)

$$\mid \nu_1(t) \rangle = \mid \nu_1(0) \rangle e^{-iE_1 t}; \qquad \mid \nu_2(t) \rangle = \mid \nu_2(0) \rangle e^{-iE_2 t} \qquad (1.10)$$

Suppose, that the particle starts out as an electron-type neutrino at t=0. The time evolution of electron neutrino is

$$\mid \nu_e(t) \rangle = cos\theta\, e^{-iE_1 t} \mid \nu_1 \rangle + sin\theta\, e^{-iE_2 t} \mid \nu_2 \rangle \qquad (1.11)$$

This leads to

$$\langle \nu_\mu \mid \nu_e(t) \rangle = sin\theta\, cos\theta \left(e^{-iE_2 t} - e^{-iE_1 t} \right) \qquad (1.12)$$

because

$$\begin{aligned}
\langle \nu_\mu \mid \nu_e(t)\rangle &= \left(-sin\theta\langle \nu_1 \mid + cos\theta\langle \nu_2 \mid\right)\left(cos\theta e^{-iE_1 t} \mid \nu_1\rangle + sin\theta e^{-iE_2 t} \mid \nu_2\rangle\right) \\
&= -sin\theta \, cos\theta \, e^{-iE_1 t} \ + \ sin\theta \, cos\theta \, e^{-iE_2 t}
\end{aligned}$$

since $\mid \nu_1\rangle$ and $\mid \nu_2\rangle$ are orthogonal states. The probability that the electron neutrino has converted into a muon neutrino, after a time t, is evidently

$$\begin{aligned}
\mid \langle \nu_\mu \mid \nu_e(t)\rangle \mid^2 &= (sin\theta \, cos\theta)^2 \ \left(e^{-iE_2 t} - e^{-iE_1 t}\right) \ \left(e^{iE_2 t} - e^{iE_1 t}\right) \\
&= \frac{sin^2(2\theta)}{4} \ \left(1 - e^{i(E_2 - E_1)t} - e^{-i(E_2 - E_1)t} + 1\right) \\
&= \frac{sin^2(2\theta)}{4} \ [2 - 2 \ cos\{(E_2 - E_1)\,t\}] \\
&= \frac{sin^2(2\theta)}{4} \ 4 \ sin^2\left(\frac{E_2 - E_1}{2}t\right)
\end{aligned}$$

or

$$P_{\nu_e \to \nu_\mu}(t) \ = \ \left[sin\,(2\theta) \ sin\left(\frac{E_2 - E_1}{2}t\right)\right]^2 \tag{1.13}$$

So, ν_e will convert to ν_μ, and then back again, sinusoidally. In this theory the electron-type and muon-type neutrinos themselves do not have well-defined energies - or masses; the 'mass eigenstates' are ν_1 and ν_2, with masses m_1 and m_2. For a particle of mass m and momentum $\overrightarrow{p}$ the mass-energy relation is $E^2 - \mid \overrightarrow{p} \mid^2 = m^2$, so

$$E^2 \ = \ \mid \overrightarrow{p} \mid^2 \ + \ m^2 \ = \ \mid \overrightarrow{p} \mid^2 \left(1 + \frac{m^2}{\mid \overrightarrow{p} \mid^2}\right)$$

In the relativistic regime

$$E \ \approx \ \mid \overrightarrow{p} \mid \left(1 + \frac{1}{2}\frac{m^2}{\mid \overrightarrow{p} \mid^2}\right) \ = \ \mid \overrightarrow{p} \mid \ + \ \frac{m^2}{2 \mid \overrightarrow{p} \mid}$$

Evidently, then,

$$E_2 - E_1 \ \approx \ \frac{m_2^2 - m_1^2}{2 \mid \overrightarrow{p} \mid} \ \approx \ \frac{m_2^2 - m_1^2}{2E} \tag{1.14}$$

and hence

$$P_{\nu_e \to \nu_\mu}(t) \ = \ \left[sin\,(2\theta) \ sin\left(\frac{m_2^2 - m_1^2}{4E}t\right)\right]^2 \tag{1.15}$$

In time t the neutrinos have traveled a distance $x \approx t$ (in natural system of units), hence we can write,

$$
\begin{aligned}
P_{\nu_e \to \nu_\mu}(x) &= \left[sin(2\theta) \; sin\left(\frac{m_2^2 - m_1^2}{4E}x \right) \right]^2 \\
&= \left[sin(2\theta) \; sin\left(\frac{\delta m^2}{4E}x \right) \right]^2 \\
&= \left[sin(2\theta) \; sin\left(\frac{\pi x}{\lambda} \right) \right]^2
\end{aligned}
\tag{1.16}
$$

where $\delta m^2 = m_2^2 - m_1^2$ is the mass-squared difference and

$$
\lambda = \frac{2.54 \; E[MeV]}{\delta m^2 [eV^2]} m
\tag{1.17}
$$

is the so-called oscillation length expressed here in terms of the neutrino energy E. On the right hand side of Eq. 1.16 the first factor is a consequence of the 'mixing' while the second factor leads to the 'oscillatory' behaviour. In particular, after a distance $\frac{\lambda}{2}$ the probability of conversion hits a maximum, $sin^2(2\theta)$, and at λ they are all back to electron neutrinos.

Since the state $| \nu_e \rangle$ and $| \nu_\mu \rangle$ are orthogonal to each other, one has

$$
\begin{aligned}
P_{\nu_e \to \nu_e}(x) &= 1 - P_{\nu_e \to \nu_\mu}(x) \\
&= 1 - \left[sin(2\theta) \; sin\left(\frac{\pi x}{\lambda} \right) \right]^2
\end{aligned}
\tag{1.18}
$$

It is seen from Eq. 1.18 that $P_{\nu_e \to \nu_e}(x)$ can be less than or equal to unity. The essential ingredients for the neutrino oscillation are twofold:

1. The neutrinos must be massive and non-degenerate.

2. The mass eigenstates of the neutrinos - ν_1, ν_2 - must be different from the flavour eigenstates - ν_e, ν_μ.

If, finally, also the correct powers of $\hbar$ and c are introduced, one obtains

$$
\begin{aligned}
P_{\nu_e \to \nu_e}(x) &= 1 - \left[sin(2\theta) \; sin\left(\frac{1}{4\hbar c}\delta m^2 \frac{x}{E} \right) \right]^2 \\
&= 1 - \left[sin(2\theta) \; sin\left(1.27 \; \delta m^2 \frac{x}{E} \right) \right]^2
\end{aligned}
\tag{1.19}
$$

where δm^2 is measured in eV^2, x in km, and E in GeV [1].

For the general case of mixing of all three neutrino flavours the essential point is again that: neutrinos *interact as flavour eigenstates* - ν_e, ν_μ, ν_τ, but they *propagate* as eigenstates of the

free-particle Hamiltonian - the *mass eigenstates* - ν_1, ν_2, ν_3. The flavour eigenstates evolve in time in a complicated, oscillatory manner, because they really carry three different masses that are playing off against each other.

In case of mixing of three neutrino flavours one obtain as generalisation of Eq. 1.9

$$
\begin{pmatrix} \nu_e \\ \nu_\mu \\ \nu_\tau \end{pmatrix} = \begin{pmatrix} U_{e1} & U_{e2} & U_{e3} \\ U_{\mu1} & U_{\mu2} & U_{\mu3} \\ U_{\tau1} & U_{\tau2} & U_{\tau3} \end{pmatrix} \begin{pmatrix} \nu_1 \\ \nu_2 \\ \nu_3 \end{pmatrix} = U \begin{pmatrix} \nu_1 \\ \nu_2 \\ \nu_3 \end{pmatrix}
\tag{1.20}
$$

where U is a (3×3) unitary matrix known as the neutrino mixing matrix expressed in terms of three mixing angles $(\theta_{12}, \theta_{23}, \theta_{13})$ and one phase factor (δ):

$$
U = \begin{pmatrix} c_{12}c_{13} & s_{12}c_{13} & s_{13}e^{-i\delta} \\ -c_{23}s_{12} - s_{23}s_{13}c_{12}e^{i\delta} & c_{23}c_{12} - s_{23}s_{13}s_{12}e^{i\delta} & s_{23}c_{13} \\ s_{23}s_{12} - c_{23}s_{13}c_{12}e^{i\delta} & -s_{23}c_{12} - c_{23}s_{13}s_{12}e^{i\delta} & c_{23}c_{13} \end{pmatrix}
\tag{1.21}
$$

where $c_{ij} = cos\theta_{ij}$ and $s_{ij} = sin\theta_{ij}$.

The 3×3 neutrino mass matrix M_ν^2 in the basis of the charged leptons e, μ and τ is diagonalised by U as:

$$
U^\dagger M_\nu^2 U = diag\left(m_1^2, m_2^2, m_3^2\right)
\tag{1.22}
$$

The probability of an initial neutrino ν_α of flavour α and energy E being detected as a neutrino ν_β of the same energy but with flavour β after traveling a distance x in vacuum is

$$
P_{\alpha\beta} = \delta_{\alpha\beta} - 4\sum_{i>j} Re\left[U_{\alpha i}U_{\beta i}^* U_{\alpha j}^* U_{\beta j}\right] sin^2\left(\frac{\pi x}{\lambda_{ij}}\right) + 2\sum_{i>j} Im\left[U_{\alpha i}U_{\beta i}^* U_{\alpha j}^* U_{\beta j}\right] sin\left(2\frac{\pi x}{\lambda_{ij}}\right),
$$

where $\lambda_{ij} = 2.47$ km$(E/GeV)(eV^2/\delta_{ij})$ when x is also expressed in km, and $\delta_{ij} = m_i^2 - m_j^2$. The above expression is given for vacuum. In matter, the probabilities are drastically modified. Neutrinos passing through matter, unlike their propagation in vacuum, interact with electrons in matter. While both charge and neutral current weak interactions contribute to the interactions of electron type neutrinos, only the neutral current contributes in the case of other flavours [17].

Since U is a unitary matrix $(U^{-1} = U^\dagger)$, it is easy to express the mass eigenstates in terms of the flavour eigenstates as:

$$
\begin{pmatrix} \nu_1 \\ \nu_2 \\ \nu_3 \end{pmatrix} = \begin{pmatrix} U_{e1}^* & U_{e2}^* & U_{e3}^* \\ U_{\mu1}^* & U_{\mu2}^* & U_{\mu3}^* \\ U_{\tau1}^* & U_{\tau2}^* & U_{\tau3}^* \end{pmatrix} \begin{pmatrix} \nu_e \\ \nu_\mu \\ \nu_\tau \end{pmatrix}
\tag{1.23}
$$

So, a mass eigenstate can be expressed as the admixture of three flavour eigenstates.

13

1.5   Signature of Neutrino oscillation

In case of atmospheric neutrinos, the deficit of muon neutrinos can now be explained by the assumption that during propagation from the point of production to the detector some of the muon neutrinos transform themselves into a different neutrino flavour, *e.g.*, into tau neutrinos. If, however, muon-type neutrinos have oscillated into tau-type neutrinos, a deficit of muon neutrinos will be observed in the detector because tau neutrinos would only produce the corresponding charged lepton taus in the water Cherenkov detector, but not muons. Since, however, the mass of the tau is rather high (1.77 GeV/c^2), tau-type neutrinos normally would not meet the requirement to provide the necessary centre-of-mass energy for tau production. Consequently, they would escape from the detector without any interaction. If the deficit of muon neutrinos would be interpreted by ($\nu_\mu \rightarrow \nu_\tau$) oscillations, the mixing angle and the mass square difference δm^2 can be determined from the experimental data. The measured value of the double ratio R = 0.69 (Eq. 1.8) leads to

$$\delta m^2 \approx 2 \times 10^{-3} \ eV^2 \qquad (1.24)$$

at maximal mixing ($sin^2 2\theta = 1$, corresponding to $\theta = 45°$)[1]. If one assumes that in the neutrino sector a similar mass hierarchy exists as in the sector of charged leptons ($m_e \ll m_\mu \ll m_\tau$), then the mass of the heaviest neutrino can be estimated from Eq. 1.24 as,

$$m_{\nu_\tau} \approx \sqrt{\delta m^2} \approx 0.045 \ eV. \qquad (1.25)$$

The validity of this conclusion relies on the correctly measured absolute fluxes of electron neutrinos and muon neutrinos. Because of the different Cherenkov pattern of electrons and muons in the water Cherenkov detector the efficiencies for electron-type and muon-type neutrino detections might be different. To sustain the neutrino oscillation hypothesis one would therefore prefer to have an additional independent experimental result. This is provided in an impressive manner by the ratio of up-coming to down-going muon neutrinos. Upward-coming atmospheric neutrinos have traveled the whole earth ($\approx$ 12800 km). They would have a much larger probability to oscillate into tau-type neutrinos compared to the downward-going neutrinos which

---

[1]The value of δm^2 given by the Super-Kamiokande experiment is 1.3×10^{-3} eV$^2 \leq \delta m^2 \leq 3 \times 10^{-3}$ eV^2 at 90% confidence level. The accelerator experiment K2K sending muon neutrinos to the Kamioka mine gets $\delta m^2 = 2.8 \times 10^{-3}$ eV^2 [18]. K2K - from KEK to Kamioka, Long-baseline Neutrino Oscillation Experiment.

have traversed a distance typically ~ 20 km. Actually, according to the result of the Super-Kamiokande experiment the up-coming muon neutrinos which have traveled through the whole earth are suppressed by a factor of two compared to the down-going muon neutrinos. This is taken as a strong indication for the existence of neutrino oscillations. For the ratio of up-coming to down-going muon neutrinos one obtains

$$S \;=\; \frac{N(\nu_\mu, up)}{N(\nu_\mu, down)} \;=\; 0.54 \pm 0.06, \tag{1.26}$$

which presents a clear effect in favour of neutrino oscillation.

Details of the observed zenith-angle dependence of atmospheric ν_e and ν_μ fluxes also represent a particularly strong support for the oscillation model.
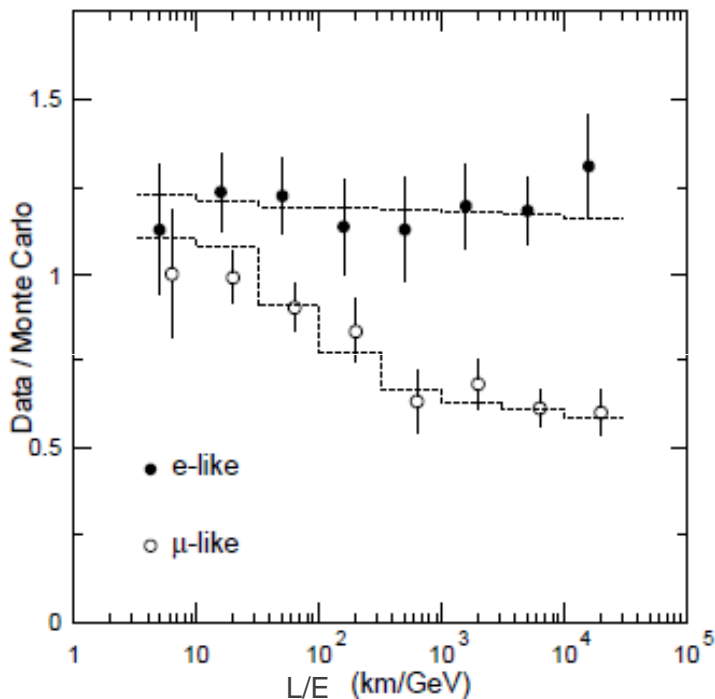
Figure 1.2: Ratio of fully contained events measured in the Super-Kamiokande experiment as a function of the reconstructed value of distance over energy (L/E). The lower histogram for μ-like events corresponds to the expectation for $\nu_\mu \leftrightarrow \nu_\tau$ oscillations with $\delta m^2 = 2.2 \times 10^{-3}$ eV^2 and $sin2\theta = 1$. (The Figure is adopted from Ref. [2]).

Since the production altitude L and energy E of atmospheric neutrinos are known (≈ 20 km for vertically down-going neutrinos), the observed zenith-angle dependence of electron neutrinos and muon neutrinos can also be converted into dependence of the data versus the reconstructed

ratio of L/E. The ratio data/Monte Carlo for fully contained events as measured in the Super-Kamiokande experiment is shown in Figure 1.2. The data of the Super-Kamiokande experiment exhibit a zenith-angle-(i.e. distance-) dependent deficit of muon neutrinos, while the electron neutrinos follow the expectation for no oscillations. The observed behaviour is consistent with $(\nu_\mu \leftrightarrow \nu_\tau)$ oscillations, where a best fit is obtained for $\delta m^2 = 2.2 \times 10^{-3}$ eV^2 for maximal mixing $(sin2\theta = 1)$.

In the Standard Model of elementary particles neutrinos have zero mass. Therefore, neutrino oscillations represent an important extension of the physics beyond the Standard Model. in this example of neutrino oscillations the synthesis between astrophysics and particle physics becomes particularly evident.

1.6 Neutrino oscillation parameters from previous experiments

The reactor neutrino experiment data shows that there is very little admixture of the mass eigenstate ν_3 in the flavour eigenstate ν_e. So, in the chosen parametrisation of the neutrino mixing matrix, U, this means that θ_{13} is small and the solar neutrino problem can be well-approximated as a 2-flavour problem involving only ν_1 and ν_2. Hence only two parameters δ_{21} and θ_{12} appear in the analysis of these solar and the KamLAND reactor experiments. For the same reason, there is only one dominant mass-square difference δ_{32} and one mixing angle θ_{23} appearing in the atmospheric neutrino experiment.

Results from Solar and KamLAND reactor experiment: Assuming CPT invariance, the 3σ allowed range of parameters and the spread of δ_{21} and $sin^2\theta_{12}$ from solar and 766.3 day KamLAND data [19] are given by

$$7.2 \times 10^{-5} \ eV^2 < \delta_{21} \equiv \delta_{sol} < 9.5 \times 10^{-5} \ eV^2;$$
$$0.21 < sin^2\theta_{12} \equiv sin^2\theta_{sol} < 0.37.$$

The best-fit points are $\delta_{21} = 7.9 \times 10^{-5}$ eV^2 and $sin^2\theta_{12} = 0.31$ [20]. δ_{21} has to be positive for MSW [21] mechanism to work for solar neutrinos.

Results from Atmospheric and accelerator experiment: From atmospheric and K2K data [22], the 3σ allowed range of parameters is

$$1.4 \times 10^{-3} < |\delta_{32}|/eV^2 \equiv \delta_{atm} < 3.3 \times 10^{-3} \ eV^2;$$

$$0.34 \leq sin^2\theta_{23} \equiv sin^2\theta_{atm} \leq 0.68$$

The best-fit values are $|\delta_{32}| = 2.2 \times 10^{-3} \ eV^2$ and $sin^2\theta_{23} = 0.5$. Whereas the δ_{21} is positive, the sign of δ_{32} is not known.

Results from Solar, CHOOZ reactor and KamLAND experiment: From the combination of solar data, and the KamLAND and CHOOZ reactor data the upper bound [19] of the parameter θ_{13} at 3σ allowed range is given by,

$$sin^2\theta_{13} \leq 0.046$$
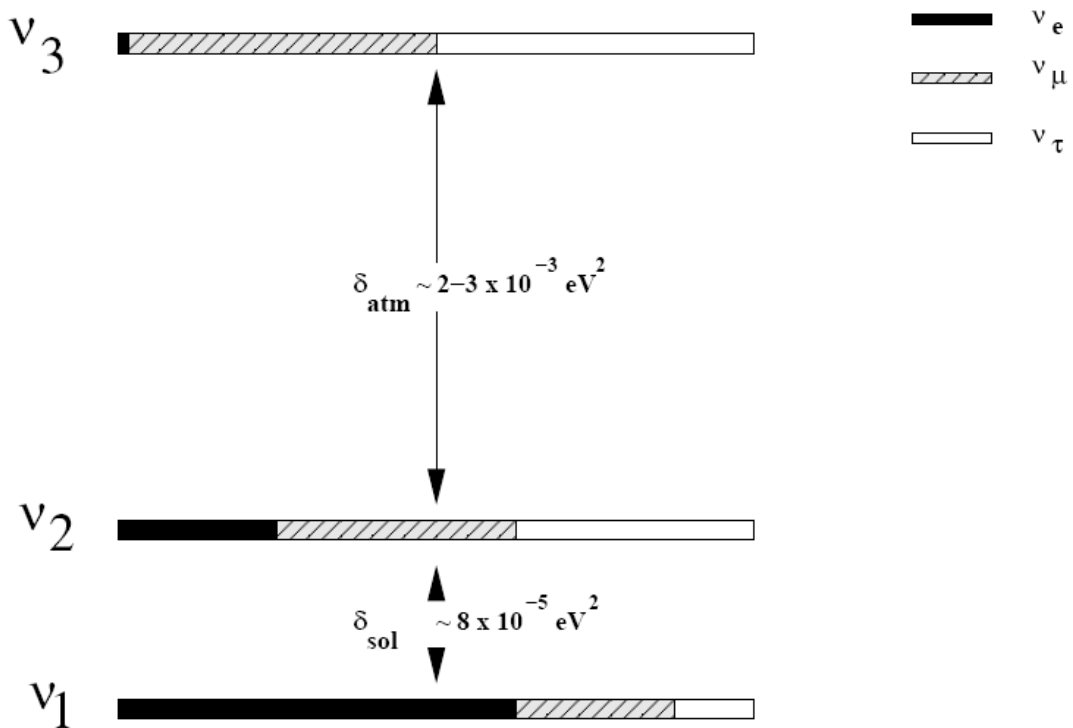
Figure 1.3: Schematic illustration of the status of masses and mixing of neutrino eigenstates. The flavour content is indicated by different shading; the ν_e contribution shown in the third mass eigenstate is an upper bound. The direct or normal mass hierarchy is assumed here; in the case of the inverted hierarchy, the ν_3 state would be the lightest. The mass squared differences as obtained from the data are also shown. (The Figure is adopted from Ref. [17]).

17

The bound, which requires a three-flavour analysis, is sensitive to the value of $\mid \delta_{32} \mid$ [23]. the result of the CHOOZ experiment, which requires the U_{e3} element to be small, plays a key role here. Due to the small value of θ_{13}, the 2-flavour bounds are stable.

A schematic of the present status of masses and mixing is shown in Figure 1.3 as obtained from a combined analysis of the data from solar, atmospheric, reactor and accelerator neutrino experiments. Note that we have chosen $m_3^2 - m_1^2 > 0$ in this figure. The present data does not distinguish between the two possible mass orderings: $m_3^2 > m_2^2 > m_1^2$ (direct), $m_2^2 > m_1^2 > m_3^2$ (inverted). Also, this figure does not include the unusual results obtained by the LSND Collaboration in Los Alamos laboratory [24], which are yet to be confirmed by an independent experiment.

1.7   Physics goals of India-based Neutrino Observatory

The India-based Neutrino Observatory (INO) is a proposed underground facility in Southern India, which is being planned to determine the neutrino oscillation parameters precisely using atmospheric neutrinos [17]. A single 22 m wide, 120 m long and 30 m in height experimental hall will be constructed at the end of a 1.5 km long tunnel. At least 1 km of rock will be overburden in all directions. INO will have a 50 kiloton magnetised Iron CALorimeter (ICAL) capable of detecting atmospheric ν_μ and $\overline{\nu}_\mu$ interactions. It may also host some other experiments (e.g neutrino-less double beta decay searches) which require low cosmic ray background environment.

The major physics goals of the INO experiment are:

- To reconfirm the occurrence of oscillation in atmospheric muon neutrinos through the explicit observation of first oscillation swing in ν_μ disappearance as a function of L/E,

- A significantly improved measurement of the oscillation parameters with respect to the earlier measurements,

- To obtain unambiguous evidence for matter effects in neutrino oscillation,

- Determination of the sign of the mass-squared difference between 2nd and 3rd mass eigenstate (δ_{23}) using the matter effect,

- To determine whether the mixing angle θ_{23} is maximal, if not explore how well its octant can be determined.

- To improve the existing upper limit on the mixing angle θ_{13} and to ascertain if its value is different from zero or not.

- To determine whether the leptonic CP phase δ is non-zero, and if so, obtain some measure of its magnitude, provided $\theta_{13} \neq 0$.

- To determine whether sterile neutrinos exist.

- Discrimination between the $\nu_\mu \to \nu_\tau$ and the $\nu_\mu \to \nu_s$ oscillation (where ν_s is sterile neutrino),

- Probing CPT violation in neutrino sector using atmospheric neutrinos and

- Constraining long range leptonic forces.

The atmospheric neutrino physics program possible with a magnetised iron tracking calorimeter is substantial. It is possible to observe a clear signal of oscillation by observing one full oscillation period so that the precision of the parameters, δ_{32} and θ_{23}, can be improved to 10%. Apart from their charge discrimination capability, magnetised iron calorimeters have a large range in sensitivity to both path length L (see Figure 1.4) and neutrino energy, E, and indeed in their ratio, L/E variations (possible with atmospheric neutrinos) compared to water Cerenkov detectors and can substantiate the evidence of neutrino mass and oscillation already observed by Super-K, via the observation of dips and peaks in the event rate versus L/E. This also offers the opportunity to probe a large range of δ_{32}.

The path-length traversed, L, is related to the zenith angle θ as

$$L = \sqrt{(R_0 + L_0)^2 - (R_0 sin\theta)^2} - R_0 cos\theta . \tag{1.27}$$

where $\theta = 0$ corresponds to neutrinos reaching the detector vertically downwards after traversing a distance L_0 which is the average height above the surface of the earth at which the atmospheric
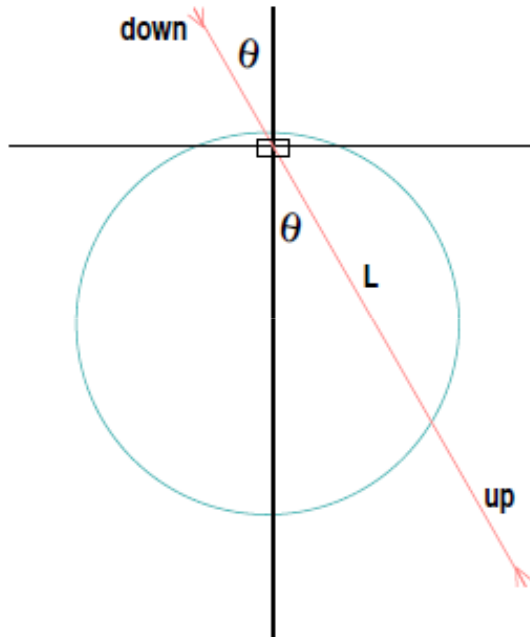
Figure 1.4: Schematic showing the up-coming and down-going neutrino directions and the path length L associated with the zenith angle θ. (The Figure is adopted from Ref. [17]).

neutrinos are produced. We take this to be about 15 km, as is the convention. Here R_0 is the radius of the earth.

The replacement of the zenith angle, $\theta \leftrightarrow (\pi - \theta)$, effectively changes the sign of the second term in Eq. 1.27, thus taking, for instance, a down-going neutrino to an up-coming one. We define the reference path length L for down-going neutrinos to be that of the associated up-going neutrino with zenith angle $(180 - \theta)$ so that the range of L/E remains the same for up-going and down-going neutrinos [25].

A useful measure of oscillations is the ratio of upward-coming to downward-going neutrinos with nadir/zenith angles interchanged. The fluxes of atmospheric neutrinos from directions θ and $(\pi - \theta)$ are expected to be similar in the absence of oscillations, especially for larger energies, E > a few GeV. This deviates from unity in the presence of oscillations, when the up-going neutrino rates are expected to be modified.

The ratio of events in the up-down directions for a given $x = $ L/E, therefore, reflects the asymmetry of the up-down fluxes, due to oscillations, and hence is a direct measure of the

oscillation probability. We define

$$\mathcal{R}(x) \; = \; \frac{U}{D}(x) \; = \; \frac{No.\ of\ events\ from\ up-coming\ muon\ neutrinos\ (x)}{No.\ of\ events\ from\ down-going\ muon\ neutrinos\ (\widetilde{x})} \; .$$

Note that the event rates are a function of L/E alone only in the case of vacuum oscillations. In the presence of matter the rates become separately a function of E,L. For the sake of simplicity, we consider here the case $\theta_{13} = 0$, which corresponds to taking the 2-flavour limit.
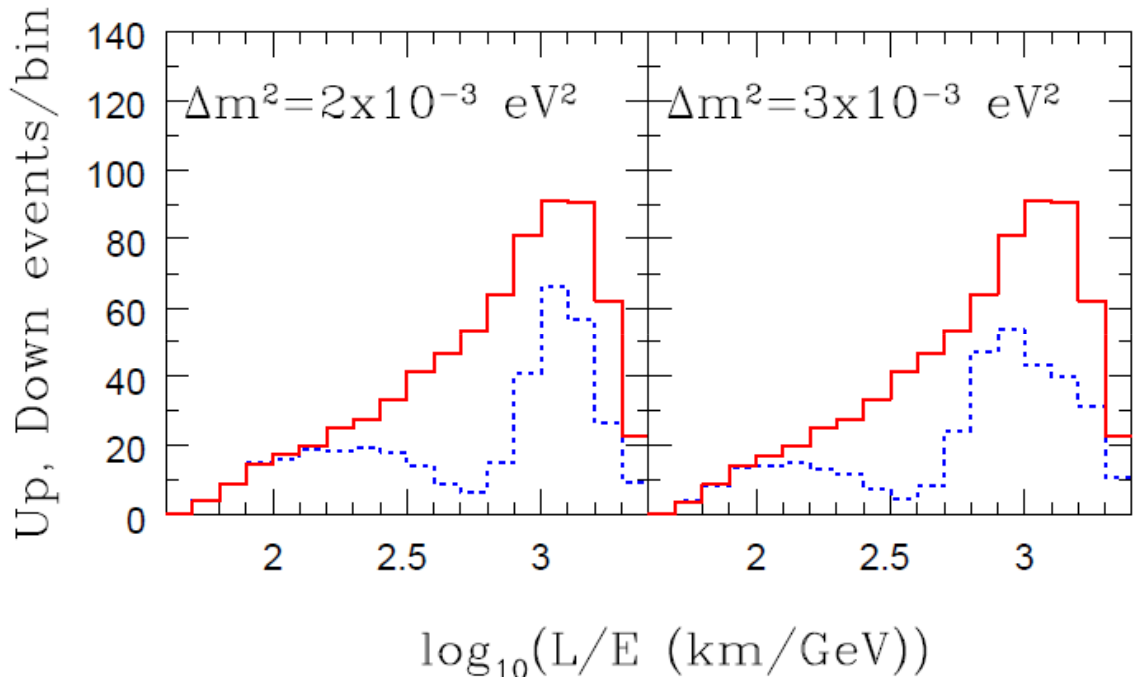
Figure 1.5: The number of up- (broken histogram) and down-going (solid histogram) muons (of either sign) in L/E bins are presented for two values of $|\ \delta_{32}\ | = 0.002,\ 0.003\ eV^2$ and $sin^2\theta_{23} = 0.5$ for an exposure of 250 kton-years at ICAL. (The Figure is adopted from Ref. [17]).

In Figure 1.5, the number of up-coming and down-going muons (of either sign) in $x = $ L/E bins ($\widetilde{x}$ for down-going neutrinos) are presented as solid and broken histograms respectively for two values of δ_{32}, for an exposure of 250 kton-years.

The two histograms are similar in the absence of oscillations. When oscillations are included, the rate for the down-going neutrinos is virtually the same while that for up-coming neutrinos is greatly modified. The dips in L/E bins visible in Figure 1.5 for the up-going case are the effect of oscillations; the first dip is especially clear.

Figure 1.6, shows, for the same values of δ_{32}, the ratio $\mathcal{R}$ of up to down going muons in the detector. Note that such a ratio eliminates [25] the large systematic errors in the normalisation of the atmospheric neutrino flux, which may be as large as 30%. Since the down-going neutrino event rate is hardly affected by oscillations, we expect $\mathcal{R}$ to be a measure of the ν_μ survival probability, $P_{\mu\mu}$, smeared, however, by the finite detector resolution.
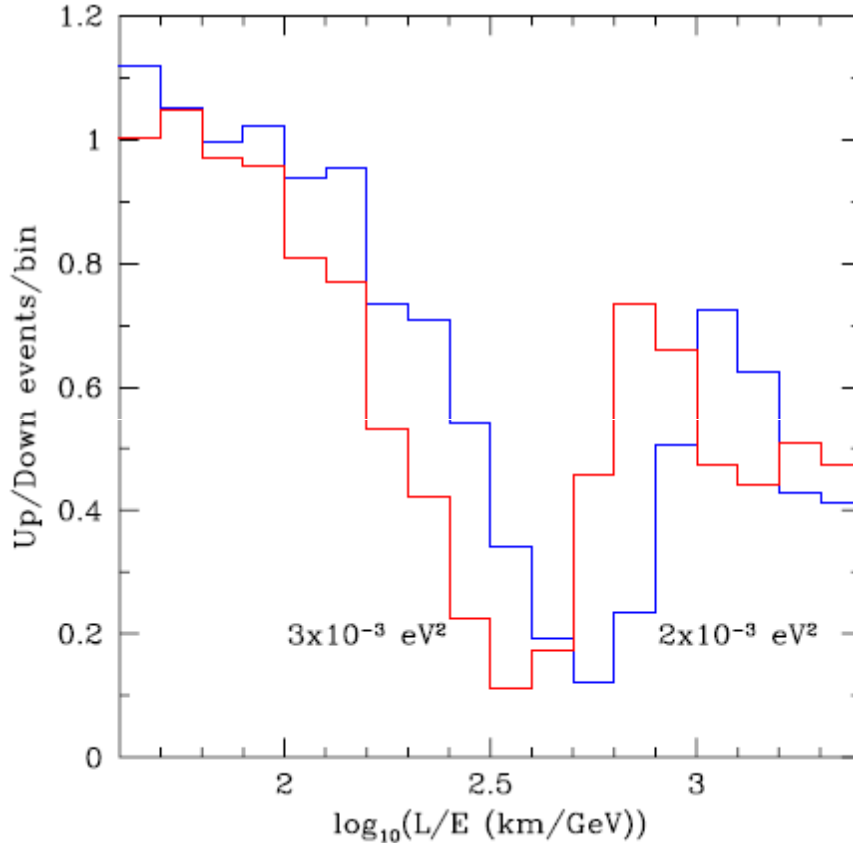
Figure 1.6: The ratio of up to down muon events shown in Figure 1.5. It is seen that the position of the dip is sensitive to the magnitude of δ_{32} while the value of the ratio at the dip is sensitive to $sin^2 2\theta_{23}$. (The Figure is adopted from Ref. [17]).

1.8   Detector for INO

The basic criteria for selecting the detector for INO experiment can be outlined as follows :

- A large target mass to achieve a statistically significant number of neutrino interactions in a reasonable time-frame (say 5 years) for the confirmation of atmospheric neutrino oscillation,

- Good energy and angular resolution so that L/E can be measured with an accuracy better than half of the modulation period,

- Identification of the electric charge of muons so as to distinguish between neutrino and anti-neutrino interactions. Charge determination is necessary to achieve most of the physics goals of INO.

The Iron CALorimeter (ICAL) detector satisfies all of the design criteria listed above. The ICAL is a large modular detector consisting of magnetized iron plates interleaved with layers of position sensitive detectors (Resistive Plate Chambers) having a time resolution ~ 2 ns and spatial resolution ~ 1 cm.

As proposed, ICAL is a sampling calorimeter consisting of a stack of 140 horizontal layers of magnetised iron plates $\sim$ of 6 cm thickness separated by 2.5 cm gaps to place the active detector RPC. The 50 kton ICAL detector will be subdivided into three modules each of dimension 16 m $\times$ 16 m $\times$ 12 m. This modular structure will allow early operation with the completed modules while constructing others.

Resistive Plate Chambers (RPC) have been chosen as the active detector for this Iron CALorimeter to satisfy the spatial resolution (~ 1 cm) and time resolution (~ 2 ns) criteria mentioned earlier. The overall layout of the ICAL detector is shown in Figure 1.7 and the sketch of a typical RPC unit for INO is shown in Figure 1.8.

The ICAL detector will be built using the 6 cm thick iron plates in such a way that the layer above resting on the layer immediately below using iron spacers located every 2 m along the X-direction. This will create 2 m wide roads along the Y-direction for the insertion of RPC trays. The details are shown in Figure 1.9. There will be a total of 8 such roads per module in a particular layer. In each road there will be 8 RPC modules each of dimension 2 m $\times$ 2 m. The iron plates will be magnetised with a field of about ~ 1.3 Tesla.

The basic RPC detector element for ICAL will be 2 m in length and 2 m wide. Eight such elements will cover a road of 16 m $\times$ 2 m. A total of $\sim$27000 such elements will be needed to complete the detector.
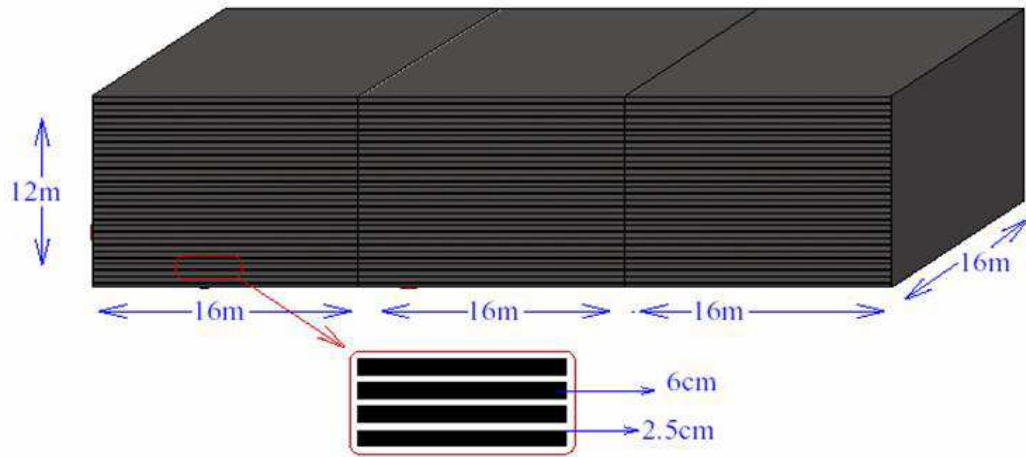
Figure 1.7: Schematic view of the 50 kton iron calorimeter detector consisting of 3 modules each having 140 layers of iron plates. (The Figure is adopted from Ref. [17]).
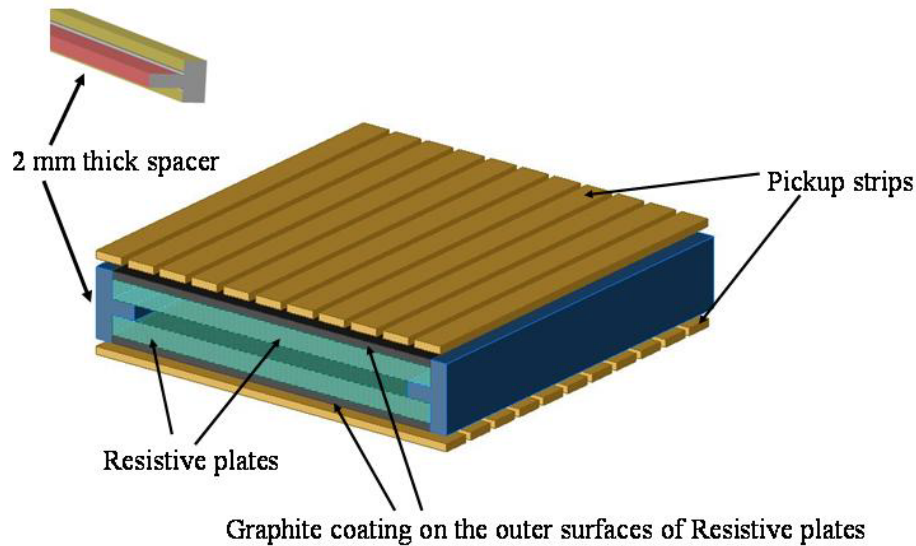
Figure 1.8: Sketch of a typical RPC unit for INO-ICAL. (The Figure is adopted from Ref. [17]).

The readout of the RPCs will be performed by external orthogonal pickup strips (X and Y strips). A localised streamer discharge due to the passage of charged particles will induce pulses on the appropriate strips. These will go to front end ASICs located near the strip ends which will have fast discriminators that will provide a fast timing signal. Presently we are proposing 3 cm wide strips. However this can be optimised through simulation studies which are currently ongoing. Thus in the current plan each road of RPCs will be read out by 64 strips
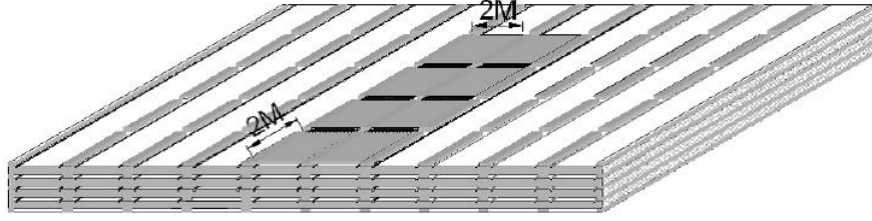
Figure 1.9: Structural detail of mounting RPC in ICAL. (The Figure is adopted from Ref. [17]).

Table 1.4: Specifications of the ICAL detector and the RPC modules [17]

ICAL	
No. of modules	3
Module dimension	16 m × 16 m × 12 m
Detector dimension	48 m × 16 m × 12 m
No. of layers	140
Iron plate thickness	∼ 6 cm
Gap for RPC trays	2.5 cm
Magnetic field	∼ 1.3 Tesla
RPC	
RPC unit dimension	2 m × 2 m
Readout strip width	3 cm
No. of RPCs/Road/Layer	8
No. of Roads/Layer/Module	8
No. of RPC units/Layer	192
Total no of RPC units	∼ 27000
No. of electronic readout channels	3.6×10^6

along the X-direction (2 m) and 512 strips along the YCdirection (16 m). The specifications of the ICAL detector and the RPC modules are summarized in Table 1.4.

The whole detector, as described above, will be surrounded by an external layer of scintillators or gas proportional counters. This will act as a veto layer and will be used to identify muons entering the detector from outside as well as to identify partially confined events with the vertex inside the detector.

1.9 Objective of the thesis

Resistive Plate Chamber (RPC) [26] is a gas filled detector utilizing a constant and uniform electric field produced between two parallel electrode plates made of a material with high bulk

resistivity ($\rho \sim 10^9$ - 10^{12} Ω cm) $e.g.$ bakelite, glass. RPC is introduced by R. Santonico and R. Cardarelli in the early 1980s. Currently three large CERN LHC experiments, ALICE, ATLAS and CMS, are using RPC-based muon triggering systems. The OPERA experiment at Gran Sasso is building RPC-based detector system. BaBar at SLAC and Belle at KEK both use RPCs for muon triggering and identification.

In the proposed India-based Neutrino Observatory (INO), the RPCs have been chosen as the prime active detector for the detection of muons (produced through the interaction of neutrinos) in an Iron Calorimeter (ICAL) [17]. The India-based Neutrino Observatory is being planned to determine the neutrino oscillation parameters precisely using atmospheric neutrinos. As proposed presently, ICAL is a sampling calorimeter consisting of 140 layers of magnetized iron, each of 6 cm thickness, using RPCs of 2 m $\times$ 2 m area as active media sandwiched between them. A 50 kton ICAL is expected to consist of about 27000 RPC modules. The RPC is chosen as the active detector for ICAL since (a) RPCs are built from simple and common materials ($e.g.$ bakelite, glass) (b) it has low fabrication cost per unit area (c) it is easy to construct and operate (d) signal pick up and readout system, used for RPC is relatively simple (e) it has large detector area coverage (f) RPC gives high efficiency ($> 90\%$) and good time resolution ($\sim$ 2 ns for single gap and $\sim$ 50 ps for multi-gap) (g) it has the particle tracking capability and good position resolution (h) two dimensional (x and y) readout from the same chamber can be used and most importantly (i) RPCs are operated stably for a long period. For ICAL-RPCs, main design criteria are (a) good position resolution ($\sim$ 1-2 cm), (b) good timing resolution ($\sim$ 1-2 ns) (c) ease of fabrication in large scale with modular structure and most importantly (d) low cost.

In INO about 27000 RPC modules of dimension 2 m $\times$ 2 m will be used for the detection of neutrino and the experiment will run for a long time. It is necessary that each RPC module should work stably for a long period. So the study on the development of these detectors and its material is very essential for INO.

Phenolic paper laminates commonly referred as bakelite have been the standard resistive plate material since the invention of RPC. In INO, RPCs made from both glass and bakelite will likely to be used. R&D on bakelites are chosen parallel to glass for building of RPC since (a) surface smoothness of glossy-finish melamine coated bakelite sheet is comparable to glass (b)

bakelite sheets are more flexible than glass and it is less breakable (c) large bakelite sheets can be made in India on a commercial basis (d) bulk resistivity of bakelite can be controlled by adjusting the ratio of the phenol and melamine and most importantly bakelite RPCs are cheaper in cost and easier to handle. So a systematic study on bakelite RPC is important.

The RPCs can be operated in two modes namely avalanche mode (pulse height is small) and streamer mode (pulse height is large). The avalanche mode corresponds to the generation of a Townsend avalanche following the release of primary charge due to the passage of an ionising radiation through the gas volume. In the streamer mode, the avalanche is followed by a 'streamer' discharge. The RPCs working in the avalanche mode mostly use mixtures of tetrafluoroethane ($C_2H_2F_4$ - also known as R-134a) with 2-5% of isobutane (iso-C_4H_{10}). In the streamer mode, mixtures of argon with isobutane and tetrafluoroethane in widely varying proportions are used. Typical signal amplitudes in the avalanche and streamer modes are $\sim$ 5-10 mV and 100-200 mV (across a 50 Ω load), respectively. The streamer mode of operation reduces the number of electronic components (*e.g.* preamplifiers) significantly. So it will find useful application, if these bakelite RPCs can be operated in streamer mode for a long period. In this respect also a systematic study is necessary.

A detail and systematic study on the development of bakelite resistive plate chamber is presented in this thesis. The thesis has five chapters besides this introductory one. In chapter 2, a general discussion on resistive plate chamber is presented.

Details of the development of resistive plate chamber using bakelite available in the local market in India is described in chapter 3. In this chapter fabrication of the modules, modification, details of testing and test results are discussed.

Chapter 4 deals with the ICAL prototype development at VECC, Kolkata.

Finally, a summary of the work and outlooks have been drawn in chapter 5 based on various studies reported in previous chapters.

Chapter 2

Resistive Plate Chamber

2.1　Introduction

In experimental high energy physics the radiation detector is a device used to detect the charged particles and/or the electromagnetic radiation produced in high energy collision experiments or in cosmic radiation. Detectors can also measure energy, momentum, life time and other properties of the particles produced in an experiment.

Gas filled detectors were the first measuring instrument developed for the detection of the radiation [27, 28]. Gas filled detectors are being used in all the large high energy physics experiments (e.g. STAR, CMS, ATLAS, ALICE, OPERA, BaBar, Belle, BESIII) since they are cheap and simple to fabricate and to operate. The composition of the fill gas, operating conditions, mode of operation, detector material, shape of the detector depend on the require-ments of a particular experiment. The gas filled detectors are also vary in their parameters e.g. efficiency, rate, particle identification capability, time and position resolution. Based on the requirements, conditions are varied. Different types of gaseous detectors presently used are Multi-Wire Proportional Counter (MWPC), Time Projection Chamber (TPC), parallel plate avalanche chamber (PPAC), Gas Electron Multiplier (GEM), micromegas etc.

The position resolution i.e. the capability of localizing particle trajectory in a small region, the time resolution i.e. how small is the time interval of detection of two particles separately falling on the detector and efficiency i.e. what fraction of particles falling on it can be detected, are some important properties of the detector. In high energy physics (HEP) experiments the

position resolution from $\sim$ a few cm to $\sim$ a few μm and the time resolution from $\sim$ 1-2 ns to $<$ 50 ps are necessary depending on the requirements. In some experiments high efficiency ($>$ 95%), high rate handling capacity ($\sim$ 1 kHz/cm^2) and in addition, the capability of working in high multiplicity is essential. Other challenges of the HEP detectors are the use of large number of cells and the cost.

Resistive Plate Chamber (RPC) is a gas filled detector utilizing a constant and uniform electric field produced between two parallel electrode plates made of a material with high bulk resistivity e.g. glass, bakelite [26]. Since such a detector has very good timing ($\sigma \sim$ 1-2 ns) and spatial resolution, it is well suited for a tracking calorimeter. The first resistive spark chambers were developed by Fedotovich et al. [29], using semi-conductive glass and a gas gap of 100 μm. A planar chamber with gaps of 1.52 mm, simple in construction and having gas mixtures at atmospheric pressure was then developed [26, 30, 31] using Bakelite ($\rho \approx 10^{11}$ Ω cm) as resistive electrodes. This technique, although economical, had some difficulties in operation at that time. To overcome some of these difficulties Anelli et al. [32] developed a new type of RPC based on low cost resistive glass plate electrodes. In RPC the high resistance of the plates limits the intensity of the spark created by a through going charged particle. Currently three large CERN LHC experiments, ALICE, ATLAS and CMS, are using RPC-based muon triggering systems. The OPERA experiment at Gran Saso are building RPC-based detector system. BaBar at SLAC and Belle at KEK both use RPCs for muon triggering and identification. For INO, we require the single particle efficiency $>$90% and time resolution $\sim$ 2 ns.

The RPCs are made up of highly resistive (bulk resistivity $\sim 10^9$ - 10^{12} Ω cm) plates (e.g. glass, bakelite etc.) as electrodes, which help to contain the discharge created by the passage of a charged particle or an ionizing radiation in a gas volume, and pick-up strips are used to collect the resulting signals. Typical time resolution for a single gap RPC is $\sim$ 1-2 ns. By reducing the gaps between the electrodes or by using multi-gap configuration, time resolution can be improved to $<$ 50 ps [33, 34, 35].

The RPCs are operated in two modes, viz., the avalanche mode and the streamer mode [36]. Over the years, one of the main concerns with the use of RPCs is their long term stability. In the avalanche mode, a small amount of charge is produced in the gas, which allows the RPC to recover in a relatively shorter time to handle high counting rates ($\sim$ 1 kHz/cm^2). Ageing effects

caused by the accumulated charge is also relatively less in this mode. In the streamer mode, the amount of charge produced is considerably larger creating induced signals of larger magnitude. But, the recovery time is larger and the irreversible damage caused by the accumulated charge reduces the life of the RPC. However, several remedial measures can be taken to prolong its life under streamer mode of operation. Careful choice of materials, smoothness of surfaces to avoid localization of excess charges, surface treatment to reduce the surface resistivity or providing alternate leakage path for post-streamer recovery are adopted in the major high energy physics experiments. Prolonged stable operation in the streamer mode of the BELLE RPCs, though made of glass, is a testimony to many serious efforts taken for the above cause [37]. The main advantage of the streamer mode is that it needs relatively less number of electronic components.

The glass-based RPCs are found to be more stable mainly for low rate applications, even though some erosion effects are found for such cases, particularly when these are operated in the streamer mode [36]. This has been attributed to the corroding of the glass surface due to the large charge build up in the streamer mode of operation. However, in the avalanche mode of operation, the detectors can be operated for longer periods. At the end of nineties, it was found that the RPCs based on bakelites with linseed oil coating show serious ageing effects reducing the efficiency drastically in particular at high rate [38]. Detailed investigations revealed that the use of linseed oil for the surface treatment in such cases was the main reason for this ageing effect [39, 40]. Efforts were subsequently made to look for alternatives to linseed oil treatment, or to develop bakelite sheets which can be used without the application of linseed oil [41]. It has, however, been found that for several ongoing and future applications (e.g. CMS detectors), bakelite based RPCs are chosen as preferred options mainly due to cheaper cost of fabrication and easy to handle. Still researches are going on to solve the ageing problem of bakelite RPC.

2.2   Working principle of RPC

A single gap RPC, shown in Figure 2.1, is made of two parallel electrode plates with high bulk resistivity of the order of 10^9 - 10^{12} Ω cm (e.g. Glass, Bakelite) separated by spacers made of even higher resistive materials like polycarbonate. The detector is filled with a mixture of suitable gases e.g. argon, isobutane and tetrafluroethane (R-134a). Inner surface of resistive electrodes are charged from a d.c. high voltage power supply which produce an electric field between two
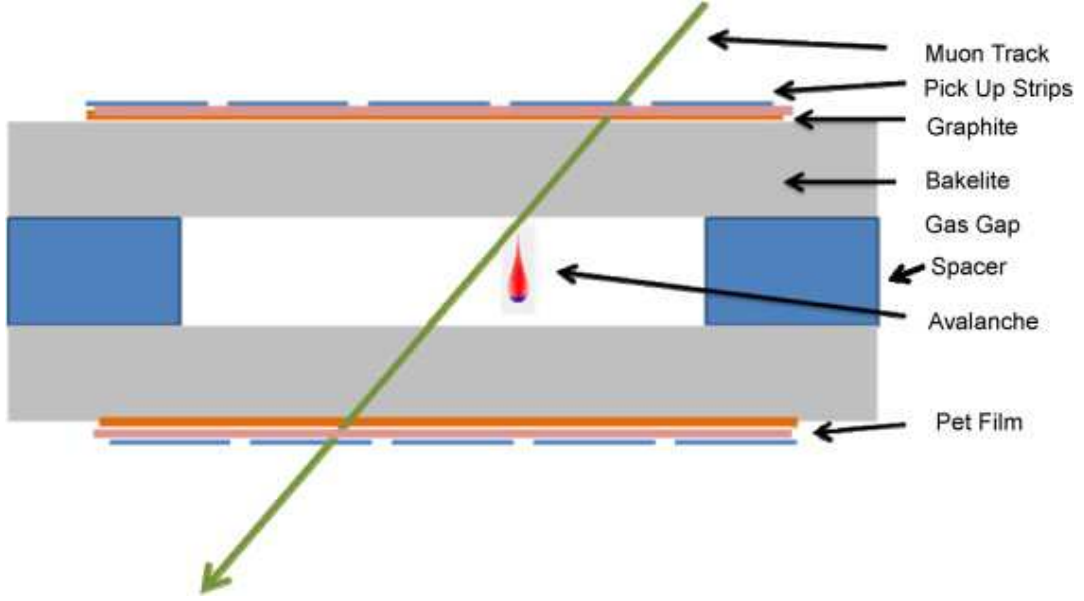
Figure 2.1: Schematic representation of a RPC. (The Figure is adopted from Ref. [42]).

plates. Charge-up process is slow due to high resistivity of the material. A passing charged particle induces an avalanche, which develops into a spark. The discharge stops when the local charge is used up. The isobutane is used to prevent the secondary streamer by quenching the photon and R-134a is used to limit the streamer size from spreading in transverse direction. The electric field is reduced suddenly in that region where the discharge occurs and the region is dead until re-charged through the bulk resistivity of the plates ($\sim 10^9$ - 10^{12} Ω cm). The discharge is also prevented from spreading through the whole gas due to the high resistivity of the plates. When readout strips are placed on the outer surface of the electrodes, induced charges are either drawn in or drawn out from the readout strips, generating voltage signals of opposite polarities on the two sides of a RPC. The charge-up time after each discharge is given by

$$
\begin{aligned}
\tau &= R_{bakelite}C \simeq \left(\frac{\rho_{bakelite}d_{bakelite}}{A}\right)\left(\frac{\kappa_{gas}\epsilon_0 A}{d_{gas}}\right) \\
&= \rho_{bakelite}\kappa_{gas}\epsilon_0 \\
&\simeq (5 \times 10^{10}\Omega\ m)(\sim 4)(8.85 \times 10^{-12}) \simeq 2\ sec
\end{aligned}
\tag{2.1}
$$

where $R_{bakelite}$ and $\rho_{bakelite}$ are respectively the resistance and the bulk resistivity of the bakelite plate and C is the chamber capacitance. Here the thickness of the bakelite plate ($d_{bakelite}$) and

31

the gas gap (d_{gas}) are same. κ_{gas}, ϵ_0 and A are the dielectric constant of the gas, permittivity of free space and the area of the chamber respectively.

Each discharge is localized to ~ 0.1 cm^2. Therefore, RPC with 0.2 Hz/cm^2 count rate suffers dead time fraction of $0.2 \times 0.1 \times 2 = 0.04$[1]. So one should aim to build and operate RPC with less than 0.2 Hz/cm^2 in order to keep the dead time fraction below 5% [43, 44].

2.3 Modes of operation

The RPCs are operated in two modes, viz., the avalanche mode and the streamer mode. These two modes are explained below.

Let at any particular point inside the gas gap n_0 be the number of electrons in a cluster. If α is the first Townsend coefficient i.e. the number of ionisations per unit length and β is the attachment coefficient i.e the number of electrons captured by the gas per unit length then the number of electrons reaching the anode,

$$n = n_0 e^{(\alpha - \beta)x} \tag{2.2}$$

where x is the distance between anode and the point where the cluster is produced. The gain of the chamber is defined by

$$M = \frac{n}{n_0} \tag{2.3}$$

The gain M decides the mode of the RPC operation. If M $> 10^8$ the mode is called the streamer mode and if M $<< 10^8$ the mode is avalanche mode.

The two modes can also be explained from another point of view. A planar detector with resistive electrodes (e.g. RPC) can be considered as a set of independent discharge cells. From the expression for the capacitance of a planar condenser, the area of such cell is proportional to the total average charge Q, that is produced in the gas gap. The area of such a cell is given by

$$S = \frac{Qd}{\epsilon V} \tag{2.4}$$

---

[1]The dead time fraction is calculated as:

$$\frac{0.2 \; particles}{cm^2 \; sec} \times 0.1 \; cm^2 \times 2 \; sec$$

So, 0.04 particles in each discharge is lost.

where, d is the gap thickness, V is the voltage applied to the electrodes and ϵ is the permittivity of the gas. If Q is ~ 100 pC, the mode is streamer mode and if Q is ~ 1 pC the mode of operation is called avalanche mode.

In streamer mode of operation, the efficiency of the RPC decreases quickly with the rate [45, 46, 47] since the surface of the resistive plates becomes charged and reduces the electric field across the gas gap. The full electric field is restored by current flowing through the resistive plates.

A possible way to handle high rate is to operate the RPCs in avalanche mode using some sensitive preamplifiers. But there are still some possibilities of discharge in avalanche mode too, which may damage the preamplifiers. There are two methods to reduce the effect of sparks. The first one is to quench the spark by using a high fraction of u.v. photon-absorbing gas, such as freon [48, 49]. The second method is to increase the size of the gas gap [50], which decreases the probability of a spark.

2.4 RPC gas and surface finish of the electrode

In the RPC the gap between the electrodes is filled with a gas of a high absorption coefficient for ultraviolet light. In the streamer mode of operation, mixtures of argon with isobutane (iso-C_4H_{10}) and tetrafluoroethane ($C_2H_2F_4$/R-134a) in widely varying ratios are used whereas in the avalanche mode mostly use mixtures of tetrafluoroethane with 2-5% of isobutane. In the avalanche mode, sometimes a small fraction of SF_6 is also used as quencher. When the gas is ionized by a charged particle crossing the detector a discharge is originated by the electric field. The discharge, however, is prevented from propagating through the whole gas because, due to the high resistivity of the electrode plates, the electric field is suddenly switched off in a limited area around the point where the discharge occurred. Out of this region the sensitivity of the chamber remains unaffected. On the other hand, due to the ultra-violet absorbing component of the gas (iso-C_4H_{10}), the photons produced by the discharge are not allowed to propagate in the gas, thus avoiding the possibility to originate secondary discharges in other points of the detector. R-134a is used as electron quencher i.e. to limit the streamer size from spreading in transverse direction.

Smooth inner surface is an important factor for steady operation of the RPC [51]. Due to surface roughness, particularly the sharp pin like edge in the surface morphological structure the electric field inside the RPC may vary $\sim$ 5-12% [52]. Rough surface is very sensitive to the field emission which is a source of high dark current and high counting rates. That is why rough inner surfaces of the bakelite electrodes were coated by 2-propanol (or similar chemical solution) diluted Linseed oil, otherwise its huge noise rate prohibits the chamber from any practical application.

Another point is that the strong electric field presented on the surface of the RPC helps to enhance the photoelectric efficiency. The UV photon created in every avalanche or streamer can hit the large surface of the cathode. To reduce the afterpulse/noise rate the least UV sensitive material for the electrode is very essential. The study of the Surface UV sensitivity for various Bakelite samples with a VUV photospectrometer reveals that the Linseed oil coating plays big roll in reducing the surface UV sensitivity [51].

HF, produced by fluorine with the interaction of water vapour is notoriously chemical reactive, it can attack many different materials and has corrosive action. Several tests show that the Linseed oil coating on Bakelite surface can effectively protect the surface from HF vapor attack [51].

2.5 Different types of RPC

2.5.1 Classification by application

According to the application, RPCs are classified into two categories: trigger and timing RPC.

2.5.1.1 Trigger RPC

The type of RPC used for triggering the Minimum Ionising Particles (MIPs) such as muons in the muon detector systems are referred as the Trigger RPC. Single gap (gas gap $\sim$ 2 mm) or double gap RPCs with large area, operated in streamer or avalanche mode are used as trigger RPC. These types of RPCs provide an efficiency $\sim$ 98% with a time resolution of $\sim$ 1-1.5 ns (σ).

2.5.1.2 Timing RPC

Large area Resistive Plate Chambers with gas gaps of 0.2 to 0.3 mm are widely used in multi gap configurations for Time-Of-Flight (TOF) measurements. These type of RPCs are operated in avalanche mode with an electric field of 100 kV/cm. This type of RPCs provide an efficiency $\sim 99\%$ with a time resolution of ~ 50 ps (σ) or better. The time resolution of the timing RPC is much better than the trigger RPC.

2.5.2 Classification by design

There are several classes of RPC in accordance to their design, material used etc. a brief description of various designs of RPC is given below.

2.5.2.1 Single-gap RPC

The single gap RPC, first developed by R. Santonico and R. Cardarelli is a charged particle detector consisting of two parallel plates electrodes made of resistive material such as bakelite or glass (bulk resistivity $\sim 10^{10}$ - 10^{11} Ω cm) enclosing a gas volume [26]. A uniform gap of 2 mm is maintained by spacers made by a material such as polycarbonate whose resistivity is more than the resistivity of the electrode plates. By applying a d.c. high voltage to these electrodes, an electric field is generated across the gas gap. A passing charged particle creates an avalanche in the gas. The discharge is prevented from spreading through the whole gas due to the high resistivity of the plates. The created electron and positive ion pairs while traveling towards the respective electrodes induces signal on the pickup strips placed over the electrode plates. The generated charge is deposited on a small region of the electrode plate; this spot is slowly recharged by current flowing through the plate. If the electric field is even more intense, a 'spark' breakdown can be initiated by the avalanche.

In the conventional single gap RPC a gas mixture of argon, isobutane and tetrafluoroethane (R134a) in widely varying proportions is used at atmospheric pressure in the streamer mode of operation. The isobutane is used to prevent the secondary streamer by quenching the photon and R134a is used to limit the streamer size from spreading in transverse direction. In the avalanche mode of operation mixtures of tetrafluoroethane (R134a) with 2-5% of isobutane

(iso-C_4H_{10}) are used. The single gap RPC first developed has been replaced by its variants, where electrode materials, gap thickness and geometry have been changed.

2.5.2.2   Wide-gap RPC

In the RPC the gas gap is used for two purposes, first one is to produce the primary ionisation cluster and the second one is for the gas gain. The accumulated charge in a RPC signal depends on the gas gap. Two types of detector can be chosen, the first one is single (gas gap: $\sim$ 2 mm) gap RPC (sometimes it is called as narrow gap RPC) as discussed in section 2.5.2.1 and the second one is wide gap RPC (gas gap: 8 mm or 9 mm) [53]. The main advantage of the wide gap RPC is the lower dynamic range of signal; this leads to the smaller current flowing through the gas gap and resistive plates. Wide gap helps to produce large signal amplitude particularly in avalanche mode. But in this case the time resolution is poor since the larger path produces larger fluctuation in signal arrival time.

2.5.2.3   Multi-gap RPC

The Multigap Resistive Plate Chamber (MRPC) which is operated at atmospheric pressure and consists of several small gas gaps (0.2 mm to 1 mm for each step) [53]. Small gap improves the time resolution. In MRPC the total gas volume is divided into a number of small gas gaps with equal width by inserting intermediate resistive plates (bulk resistivity $\sim 10^{11}$ - 10^{12} Ω cm) between the two outermost resistive plates. The high voltages (HV) are applied only to the external surfaces of each stack of plates and the intermediate plates are electrically floating, thus one can build the detector by stacking plates separated by suitable spacers. Pickup strips are located outside the stack and insulated from the high voltage electrodes. A passing charged particle creates an avalanche in the gas. Signals on the pickup electrodes are induced by the movement of charge in the gas; in case of the RPC, the fast signal is generated by the fast movement of electrons towards the anode. Since the resistive plates act as dielectrics, the induced signals can be caused by the movement of charge in any of the gas gaps between the anode and the cathode pickup strips. In this way the observed induced signal on the pickup strip becomes the sum of the individual avalanche signal in any of the gaps making up the MRPC, but the time jitter in the rise time is expected to reduce due to the smaller subgap

of the MRPC [54]. It is shown by simulation that efficiency increases and time resolution improves with the increase of number of gap [55]. Though for a multigap RPC of n number of gaps the time resolution does not scale with $\sigma_t/\sqrt{n}$, however, the efficiency does scale with $1-(1-\varepsilon)^n$, where σ_t and ε are the time resolution and efficiency respectively of the single gap RPC. Schematic representation of a 24 gap MRPC is shown in Figure 2.2. It whole detector is divided into four stacks, each with six gas gaps of 160 μm [35]. The best time resolution obtained from this detector was 20 ps.
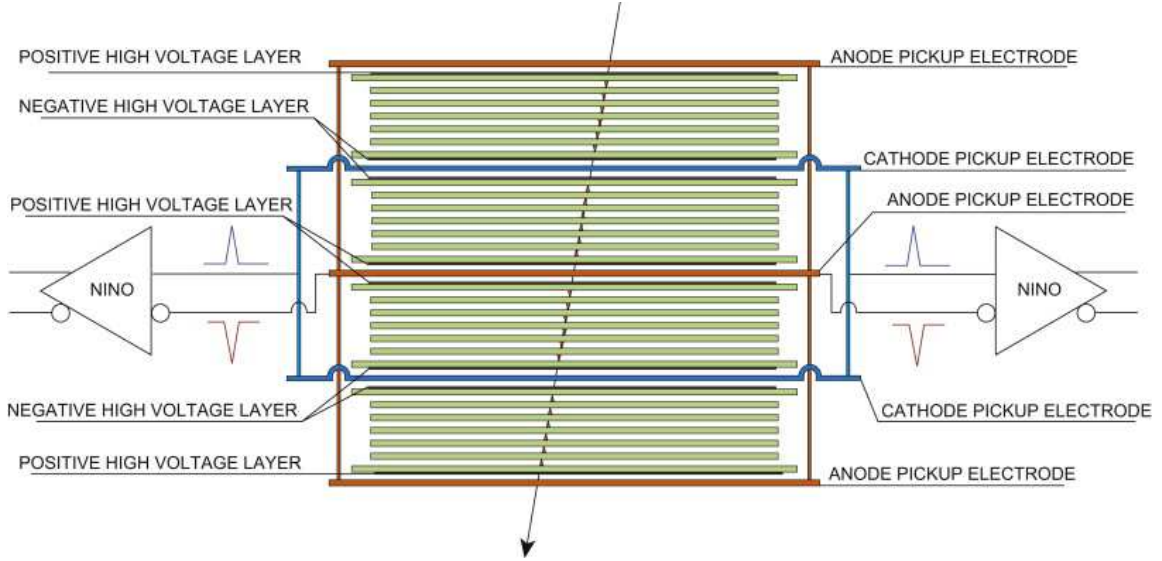
Figure 2.2: Schematic representation of a MRPC. (The Figure is adopted from Ref. [35]).

2.5.2.4 Hybrid RPC

RPCs made with a combination of resistive and metallic electrodes are hybrid type RPC. Such a hybrid type RPC, presented in Ref. [33] are built by a pair of identical double-gap chambers, each one having 2 mm thick aluminium anode and cathode and a central resistive electrode plate operated at floating potential. The cathodes are connected to the high voltage of negative polarity and the anodes, kept at ground potential, are connected together and feed the pre-amplifier. The resistive electrodes were made with 3 mm thick glass of bulk resistivity $\rho \approx 2 \times 10^{12}$ Ω cm. The main features of these detectors, are simple and mechanically stable construction, very good time resolution (< 50 ps σ) and detection efficiency ($> 95\%$), large

plateau and high discriminating threshold. This type of RPCs can be used in TOF and PET imaging. A schematic diagram of hybrid RPC is shown in Figure 2.3.
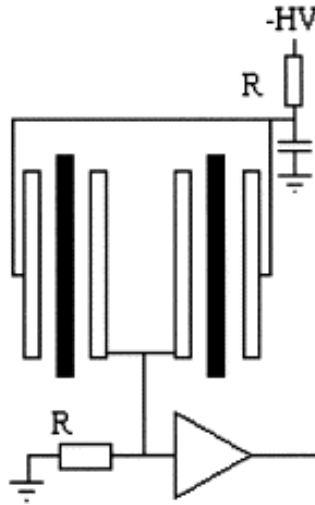
Figure 2.3: Schematic representation of a hybrid RPC. White electrodes are metallic and black black electrodes are resistive. (The Figure is adopted from Ref. [33]).

2.6 Application of RPC

The Resistive Plate Chambers (RPCs), first developed by Santonico et. al. [26] using bakelite are used extensively in high energy physics experiments for spacetime particle tracking. Primarily used for generating fast trigger for muon detection [56], time of flight (TOF) [30, 57] measurement, and tracking capabilities in multi layer configurations, they are successfully used in BELLE [37], BaBar [58], BESIII [59], and several LHC experiments (ALICE, ATLAS, CMS etc.) [60, 61, 62]. RPCs are used in neutrino experiments like OPERA where its excellent time resolution and tracking capabilities are exploited [63]. The RPCs are also being explored for use in PET imaging with TOF-PET [64], detection of γ-rays [65] and neutrons [66, 67] over a large area. The RPCs are being considered for the following reasons: a) good time resolution ($\sim$ 1-2 ns in single gap and a few hundred or less ps in multigap RPC) and good position resolution ($\sim$ 1 cm or better) b) relatively low cost of materials used in making RPCs and c) robust fabrication procedure and handling. A list of some present and future experiments where RPCs are used is given in Table 2.1.

38

Table 2.1: Summary of RPC application in some past and current experiments

Experiment	Application	Area (m^2)	Electrode material	Volume resistivity (Ω cm)	No. of gaps	Gap (mm)	Mode of operation
BaBar	Trigger	2000	Bakelite	10^{11} - 10^{12}	1	2	Streamer
Belle	Trigger	2000	Glass	$> 10^{12}$	2	2	Streamer
ALICE-Muon	Trigger	140	Bakelite	3×10^9	1	2	Streamer
ALICE-TOF	Timing	150	Glass	10^{13}	10	0.25	Avalanche
ATLAS	Trigger	6550	Bakelite	$(1-4) \times 10^{10}$	1	2	Avalanche
CMS	Trigger	4000	Bakelite	$\sim 10^{10}$	2	2	Avalanche
STAR	Timing	60	Glass	10^{12} - 10^{13}	6	0.22	Avalanche
PHENIX	Trigger	-	Bakelite	10^{10}	2	2	Avalanche
OPERA	Trigger	3200	Bakelite	$>5 \times 10^{11}$	1	2	Streamer
BESIII	Trigger	1200	Bakelite	10^9 - 10^{13}	1	2	Streamer
YBJ-ARGO	Trigger	5600	Bakelite	$(0.5-1) \times 10^{12}$	1	2	Streamer
HARP	Timing	10	Glass	10×10^{12}	4	0.3	Avalanche
HADES	Timing	8	Glass	5×10^{12}	4	0.3	Avalanche
FOPI	Timing	5	Glass	10^{12}	6	0.3	Avalanche
CBM-TOF	Timing	120	Glass	$(3-4) \times 10^{10}$	6	0.22	Avalanche
NeuLAND	Timing	4	Glass	-	3	0.3	Avalanche

In the proposed India-based Neutrino Observatory (INO) in Southern India, the neutrino oscillation will be studied. In INO the proposed detector is a magnetised Iron CALorimeter (ICAL), which will consist of a stack of 140 horizontal layers of $\sim$ 6 cm thick magnetised iron plates separated by 2.5 cm gaps to house the active detector layers. The ICAL will consist of 3 modules each of dimension 16 m $\times$ 16 m $\times$ 12 m. Considering the overall size of the apparatus and the large active detector area of $\sim$ 108,000 m^2, it is desirable that the active detector should be of low cost, modular in construction with elements of a size suitable for mass production and having a time resolution better than 2 ns and spatial resolution < 1 cm. Considering all these factors the resistive plate chamber (RPC) seems to be most appropriate choice as the active detector medium in INO [17].

2.7   Summary and outlooks

Presently RPCs of several types are being used in several high energy physics experiments. RPCs are operated in two modes: avalanche and streamer mode. The experimental groups of

different experiments select the mode according to their requirements. Still researches is going on the improvement of RPC performance, ageing problem, gas mixture etc.

RPC will be used as the active detector in the 50 kton ICAL detector in INO. Detailed R&D programme has been undertaken by the INO collaboration for the development of RPCs satisfying the criteria mentioned in the previous sections. The works presented in this thesis contains the description of RPC-R&D using bakelite procured from local market as electrodes.

Chapter 3

Bakelite-based RPC: Fabrication, testing & results

3.1 Introduction

The proposed India-based Neutrino Observatory (INO) [17] is being planned with the aim to determine precisely the oscillation parameters using atmospheric neutrinos. In INO, the RPC has been chosen as the active detector for the detection of muons (produced through the interaction of neutrinos) in a 50 kton Iron CALorimeter (ICAL). As proposed, ICAL is a sampling calorimeter consisting of a stack of 140 horizontal layers of 6 cm thick magnetized iron plates separated by 2.5 cm gaps to house the RPCs. A 50 kton detector having 3 modules each of dimension 16 m $\times$ 16 m $\times$ 12 m will require $\sim$ 27000 RPCs of size 2m $\times$ 2m each i.e. a total active detector area of $\sim$ 108,000 m^2. For ICAL RPCs, main design criteria are (a) good position resolution ($\sim$ 1 cm) (b) good timing resolution (better than 2 ns) (c) ease of fabrication in a large scale with modular structure and most importantly (d) low cost. Detailed R&D are being performed on glass RPCs for this application [68].

In this work, we report a parallel effort of building and testing of the RPC modules made of bakelite paper laminates commercially available in India. These RPCs are operated in the streamer mode as opposed to the avalanche mode in glass RPCs. Main goal of this R&D is to achieve high efficiency, good time resolution over a prolonged operation period.

The work was initiated by testing two 30 cm × 30 cm RPC modules, obtained from the Institute of High Energy Physics, China [69] where thousands of such modules of different dimensions have been built for the BESIII [41] experiment. One special feature of these bakelite plates is that the linseed oil was not used for surface preparation of these bakelite based modules. After obtaining the satisfactory performance of those Chinese RPCs the fabrication and testing of RPC modules using bakelite commercially available in India was started.

Several single gap (gap of 2 mm) prototype RPCs of different dimensions (10 cm × 10 cm, 30 cm × 30 cm, and 100 cm × 100 cm) were fabricated using high resistive ($\rho \sim 10^{10}$ - 10^{12} Ω cm) bakelite paper laminates produced and commercially available in India and a series of systematic studies have been performed both in streamer and avalanche mode using the cosmic rays to characterise those modules. The bakelites of P-120, NEMA LI-1989 Grade XXX, commonly used for high voltage (HV) insulation under humid conditions, were found to be most suitable for the RPC application. A thin coating of silicone fluid on the inner surfaces of the modules have been found to be necessary for the stable operation of the detector. Different types of silicone coating have been studied along with the base silicone fluid mixed with an accelerator to fabricate the modules. While the RPCs coated with only base component of silicone are referred to as the unpolymerised silicone coated modules in the following text, the base components with an accelerator are referred to as the polymerised coating. P-120 grade bakelite with better surface finish and without any coating have also been tried.

3.2 Electrical properties of the electrodes

The bakelite sheets are phenolic resin bonded paper laminates. In the present work, three types of bakelite sheets have been used to build as many modules. They are (a) mechanical grade bakelite (P-1001), (b) Superhylam grade and (c) electrical grade (P-120).

The P-1001 and P-120 grade bakelites are manufactured by Bakelite Hylam, India and the Superhylam grade is obtained from the other manufacturer Super Hylam, India. The sheets of P-1001 and P-120 were obtained as matt-finished whereas the superhylam grade was glossy finished. The P-1001 has good mechanical properties whereas the P-120 has good mechanical
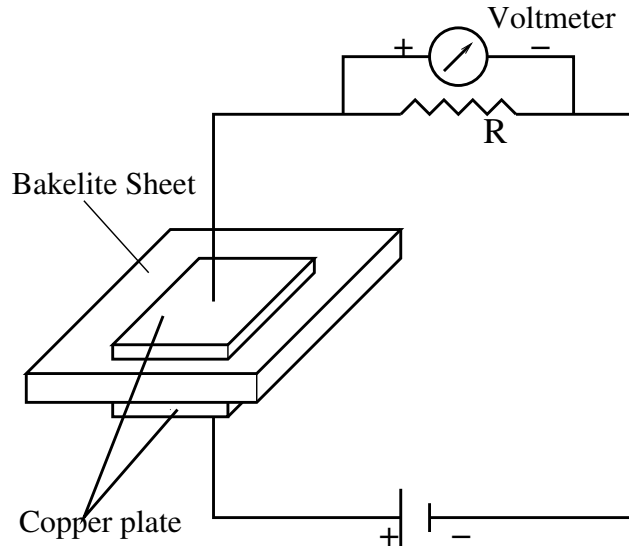
Figure 3.1: Schematic diagram of the bulk resistivity measurement setup.

and electrical properties under humid conditions prevalent in India. All the bakelite sheets are 2 mm thick unless otherwise stated.

The bulk resistivity (volume resistivity) of the electrode plates of the RPC is an important parameter [70, 71]. The high resistivity helps in controlling the time resolution, counting rate and also prevents the discharge from spreading through the entire gas volume [26, 72, 73]. We have measured the bulk resistivities of the bakelite sheets via the measurement of leakage current. Figure 3.1 shows the schematic diagram of the set up for the bulk resistivity measurement. Bakelite samples are cut into 3 cm × 3 cm sizes. The sample was sandwiched between two copper plates of dimension 2 cm × 2 cm and thickness of 1.5 mm. The copper sheets are pressed on to the bakelite plates using two 10 cm × 10 cm glass epoxy pieces with a hole at the centre and screwed at the 4 corners (for tightening and not shown in the picture). Two cables have been soldered on to the copper plates and connected to the LeCroy 1458 high voltage power supply and a 33 MΩ resistance (R) in series. By varying the applied voltage from the power supply, measured voltages across R are used to obtain the leakage current and the bulk resistivity of the bakelite sheet.

This measurement has been performed in a temperature and humidity controlled room where the RPCs have also been tested. These two parameters have been monitored during the measurement and were kept almost constant during the entire period of experiment. The bulk

43

Table 3.1: Mechanical and electrical properties of different grades of bakelite.

Trade Name	NEMA LI-1989 Grade	BS-2572 Grade	Density (g/cc)	Electrical strength (kV/mm)	Surface finish	Bulk resistivity (Ω cm)
P-1001	X	P1	1.38	3.5	Matt	6.13×10^{10}
Superhylam	-	P2	1.72	9.5	Glossy	1.25×10^{11}
P-120	XXX	P3	1.22	9.5	Matt	3.67×10^{12}
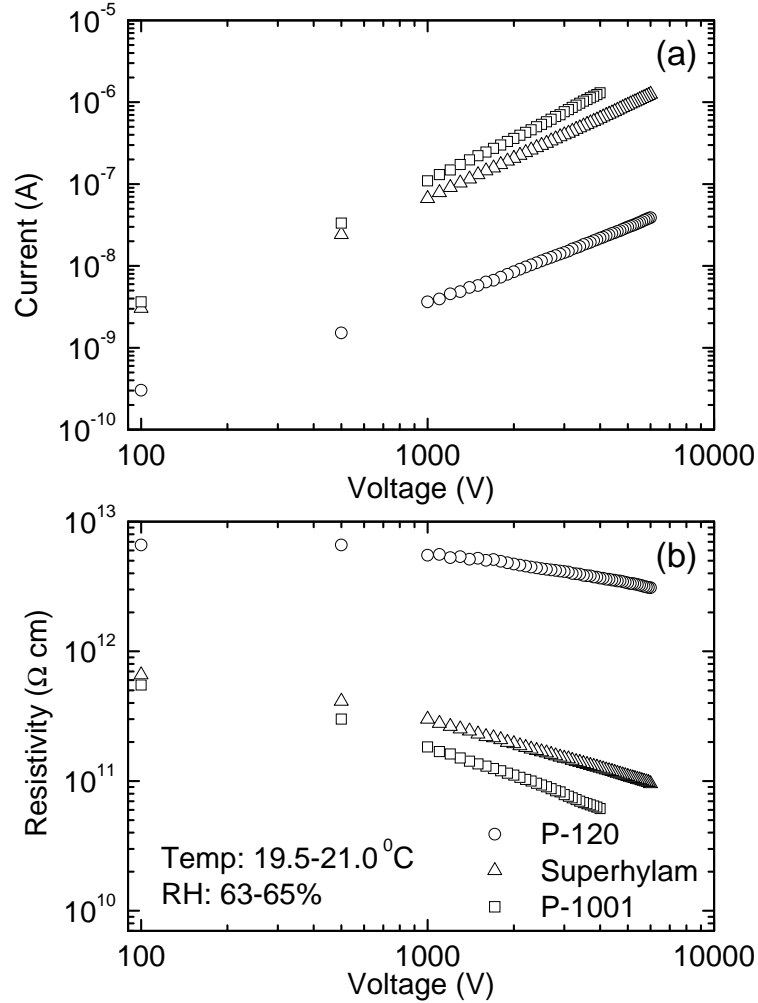
Figure 3.2: (a) The current & (b) the volume resistivity (ρ) as a function of the applied voltage for three grades of bakelite.

resistivities of different grade materials at 4 kV are tabulated in Table 3.1. The variation of current and volume resistivity (ρ) with applied voltage of different grade materials are shown in

44

Figure 3.2 (a) and (b) respectively. It is clear from the figures that the bulk resistivity is considerably higher for the P-120 grade bakelite. For the P-1001 grade, resistivity is much lower and it cannot sustain the high voltage above 4 kV. Therefore, the P-1001 grade is not considered for further use in the fabrication of RPC. The superhylam grade, though having lower bulk resistivity than P-120, would stand high voltages up to 6 kV, and was also considered for the fabrication of RPC detector [74, 75, 76].
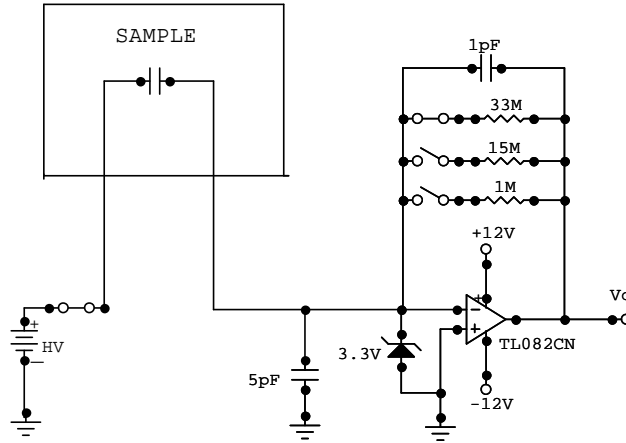
Figure 3.3: Block diagram of the surface resistivity measurement setup.

Figure 3.4: Experimental setup for surface resistivity measurement. The inset shows the figure of the aluminium jig.

A setup shown schematically in Figure 3.3 has been made to measure the surface resistivity of the bakelite surface with and without silicone coating. For various reasons different

45

types of silicone coating were applied on the bakelite surface as discussed in detail in Section 3.5.1 and 3.5.13. The actual experimental setup is shown in Figure 3.4.

The circuit shown in Figure 3.4 is basically a current to voltage converter, designed to measure the surface resistivity ($\sim 10^{11}$ $\Omega/\square$)). A bakelite sample (silicone coated or uncoated) of 30 cm $\times$ 30 cm size has been taken. A jig with sides made by aluminium bar having V-shape at the bottom (see the inset to Figure 3.4) is used. A double-stick foam tape is pasted and an aluminium foil is attached onto the jig to avoid any surface damage. The length of the aluminium bar and their separation were same (5 cm). The bars were separated by glass epoxy.
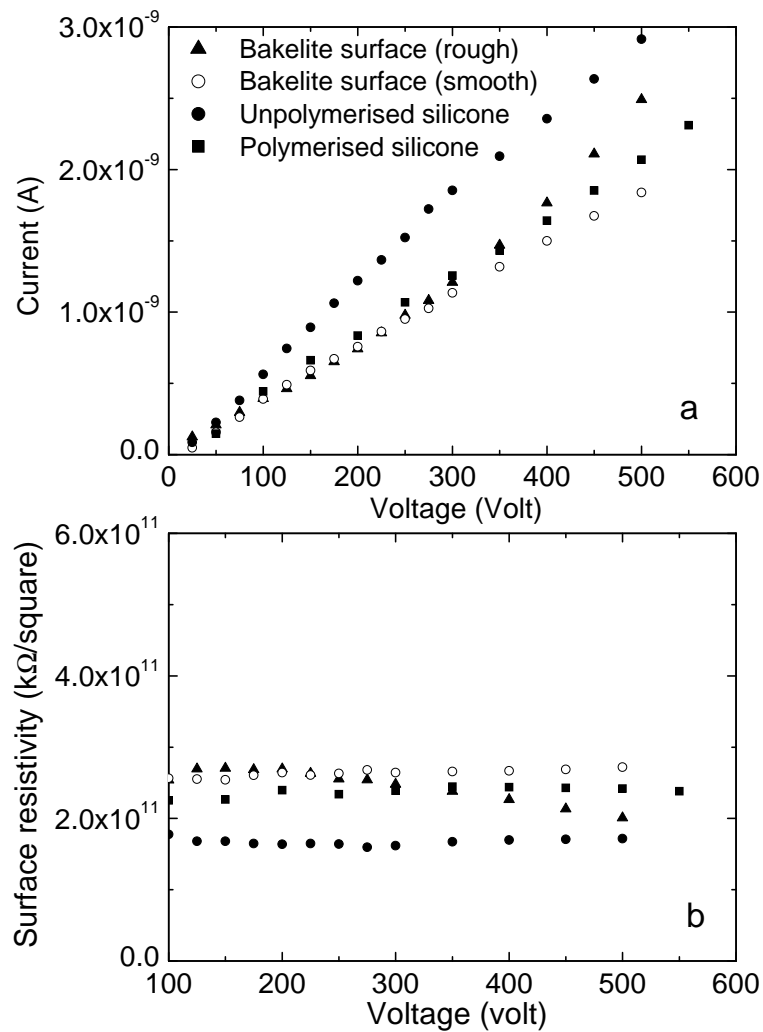
Figure 3.5: (a) The surface current & (b) the surface resistivity versus the applied voltage for different samples.

46

The jig is placed on a particular surface of the bakelite sample. Voltage ~ 600 Volt is applied to the sample through the jig. Since the resistivity of glass epoxy is very high with respect to the bakelite, the current ($\sim$ nA/pA) will flow through the bakelite. The output voltage is then measured. The surface resistivity is obtained from the current which in turn is calculated from the measured output voltage.

The variation of surface current and surface resistivity with the applied voltage are shown in Figure 3.5 (a) and 3.5 (b) respectively. The surface resistivity of the silicone coated (unpolymerised) surface was found to be less by a factor of 2 compared to the uncoated surface. Lower value of surface resistivity helps to reduce the space charge effect because of quicker dissipation of accumulated charge through the surface layer.

3.3 Construction of RPC
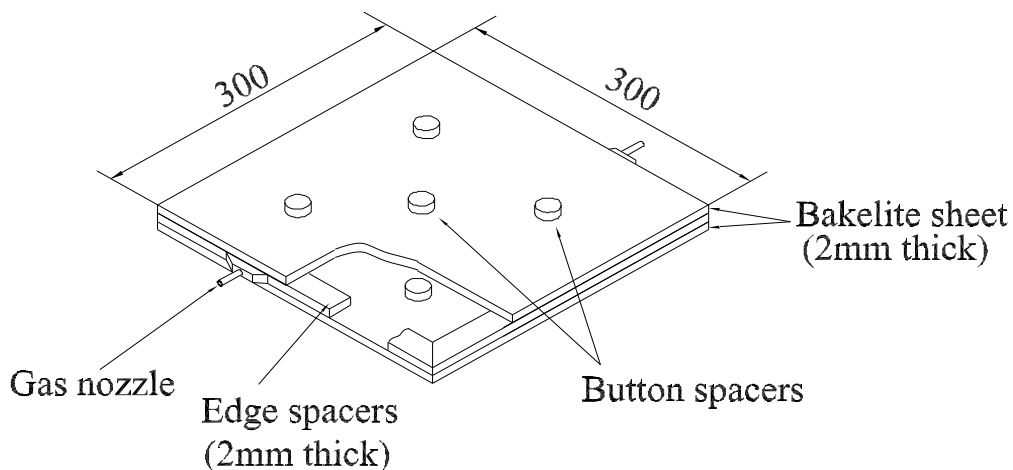
Figure 3.6: Schematic diagram of a resistive plate chamber.

In this work RPCs of different dimensions (10 cm × 10 cm, 30 cm × 30 cm, and 100 cm × 100 cm) have been fabricated. A schematic view of the assembled RPC modules is shown in Figure 3.6. Two bakelite sheets of same thickness are used as electrodes [75]. Bakelite sheets of thickness 2 mm, 1.6 mm and 3.2 mm are used to build as many RPC prototypes. Inner surfaces of two sheets are separated by a gap of 2 mm. Uniform separation of the electrodes are ensured by using button spacers (5 buttons for 30 cm × 30 cm RPC, 49

47

buttons for 100 cm × 100 cm and 1 button for 10 cm × 10 cm) of 1 cm diameter and 2 mm thickness, and edge spacers of 8 mm width, both being made of polycarbonate. Two nozzles for gas inlet and outlet, also made of polycarbonate, are placed diagonally as part of the edge spacers for the 30 cm × 30 cm RPC and 10 cm × 10 cm RPC while four such nozzles are used for the 100 cm × 100 cm RPC (gas nozzles, edge spacers and button spacers, used initially for 30 cm × 30 cm RPC are shown in Figure 3.7). All the spacers and nozzles are glued to the bakelite sheets using Araldite® epoxy adhesive. 2 mm thick active gas gaps of the RPC modules are leak-checked using argon and helium sniffer probes. The edges of the bakelite sheets are sealed by applying a layer of the epoxy adhesive to prevent permeation of moisture. Gluing of spacers and gas nozzles on a 30 cm × 30 cm bakelite plate is shown in Figure 3.8 while a few steps of 1 m × 1 m RPC fabrication is illustrated in Figure 3.9.
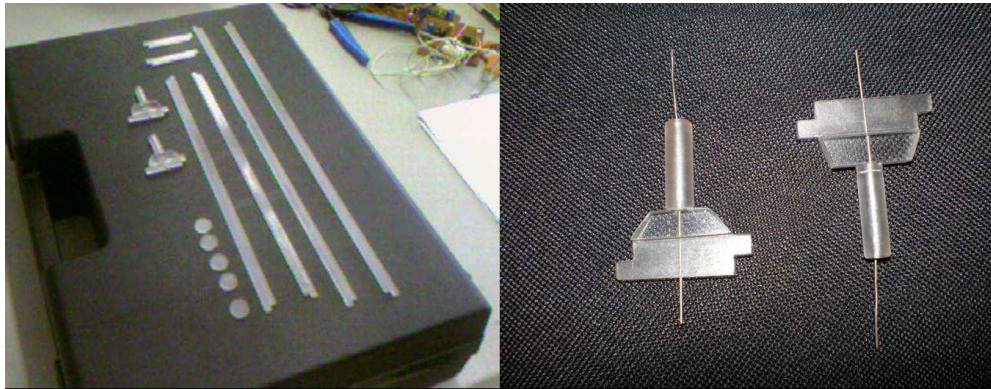
Figure 3.7: Polycarbonate gas nozzles, edge spacers and button spacers used for 30 cm × 30 cm RPC.

Figure 3.8: Gluing of spacers and gas nozzles on bakelite plates of 30 cm × 30 cm size.
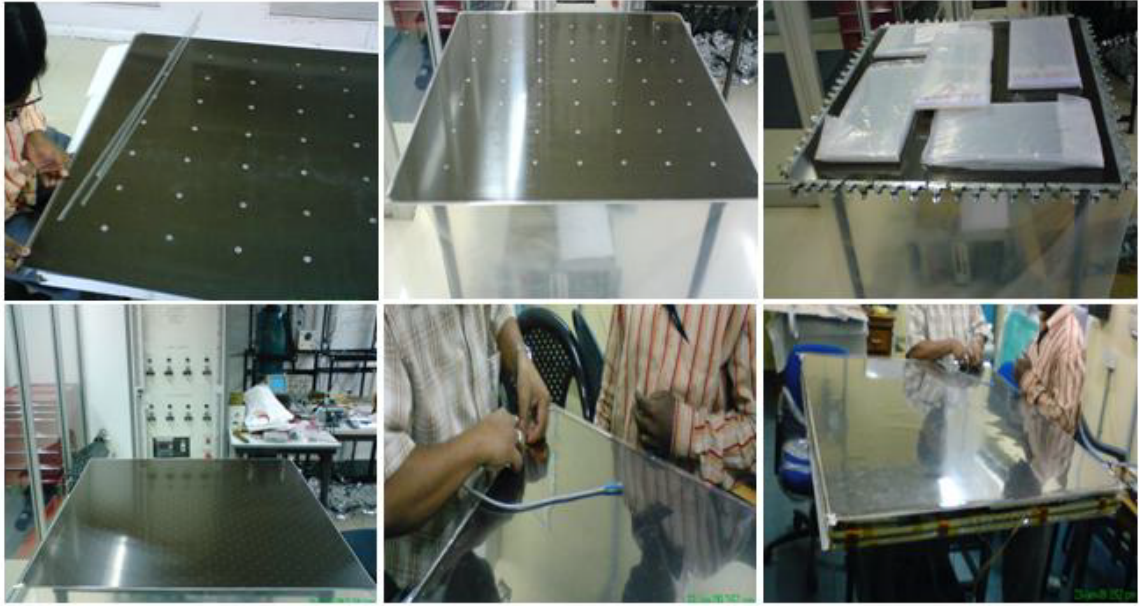
Figure 3.9: A few steps of 1 m × 1 m RPC fabrication.

After proper cleaning, a graphite coating (surface resistivity $\sim$ 1 MΩ/□) is made on the outer surfaces of the RPC to distribute the applied voltage uniformly over the entire RPC. A gap of 1 cm is maintained from the edges to the graphite layer to avoid external discharge. The graphite coating, applied by using a spray gun, however, results in a non-uniformity (typically less than 20%) for a coated surface. Two small (20 mm × 10 mm) $\sim$ 20 μm thick copper foils are pasted by kapton tapes on both the outer surfaces for application of high voltages. The high voltage connectors are soldered on these copper strips. Equal high voltages with opposite polarities are applied on both the surfaces. A complete 30 cm × 30 cm RPC module with gas tubes and high voltage connection is shown in Figure 3.10.

In order to collect the induced signals, pick-up strips are placed above the graphite coated surfaces. The pick-up strips are made of copper (20 μm thick), pasted on one side of 10 mm thick foam used as dielectric. The ground plane, made of aluminium, is pasted on the other side of the foam. The area of each strip is 300 mm × 30 mm (it was changed to 300 mm × 25 mm at a later stage) with a separation of 2 mm between two adjacent strips for the 30 cm × 30 cm RPCs. For the large RPCs, pick-up strips of 1000 mm × 30 mm area, made with plastic honeycomb dielectric between the copper strips and the ground plane are used. For the 10 cm × 10 cm RPC, G-10 based copper pick-up strips with air dielectric between the strips and

49
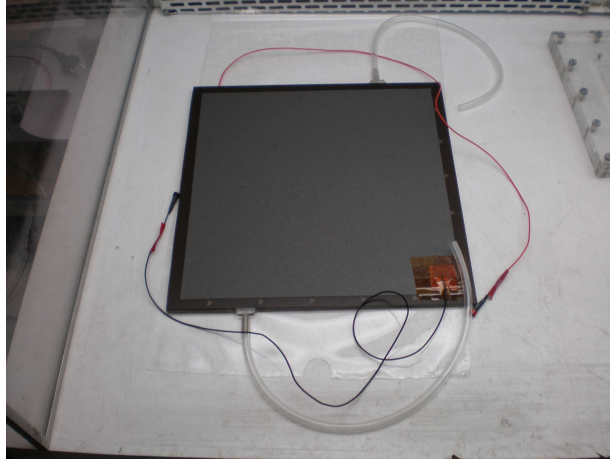
Figure 3.10: A 30 cm × 30 cm complete bakelite RPC.

the ground plane are used. In this case the area of each strip is 100 mm × 5 mm with 1 mm separation. The pick-up strips are covered with 100 μm thick kapton/mylar sheets to isolate them from the graphite layers. The signals from different strips are sent through a ribbon cable, followed by RG-174/U coaxial cables using proper impedance matching. For the 10 cm × 10 cm RPC, signals are collected by a flat ribbon cable. Pick-up strips with ribbon cable for the 30 cm × 30 cm RPC is shown in Figure 3.11.

Figure 3.11: 30 cm long pick-up strip with ribbon cable.

In the initial stage of fabrication, three modules each of area 30 cm × 30 cm are constructed with P-120 grade and these are referred to as IB1, IB2 & IB3 in the following text whereas one module is made using superhylam grade and is referred to as SH. Name, electrode materials and surface resistivity of graphite coating of different RPCs are given in Table 3.2.

Table 3.2: Name and materials of different RPCs

Detector name	Electrode material	Surface resistivity of graphite coating kΩ/□	
		Anode	Cathode
SH	Superhylam	500	500
IB1	P-120	2000	2000
IB2	P-120	1600	1000
IB3	P-120	1300	1000

3.4 Cosmic ray test setup

Figure 3.12 shows the schematic of the setup for testing the RPC modules using cosmic rays. Three scintillators, two placed above the RPC plane and one placed below are used for obtaining the trigger from the incidence of the cosmic rays. The coincidence between scintillator I (350 mm × 250 mm size), scintillator II (350 mm × 250 mm size) and the finger scintillator(III) (200 mm × 40 mm size) is taken as the Master trigger. Finally, the ORed signal obtained from two adjacent pick-up strips of the chamber is put in coincidence with the master trigger obtained above. This is referred to as the coincidence trigger of the RPC. The window of the cosmic ray telescope is therefore of the area of 200 mm × 40 mm. The width of the finger scintillator is made smaller than the total width of the two adjacent readout strips. A correction has been applied for dead zones (of area 200 mm × 2 mm) in between two adjacent readout strips while
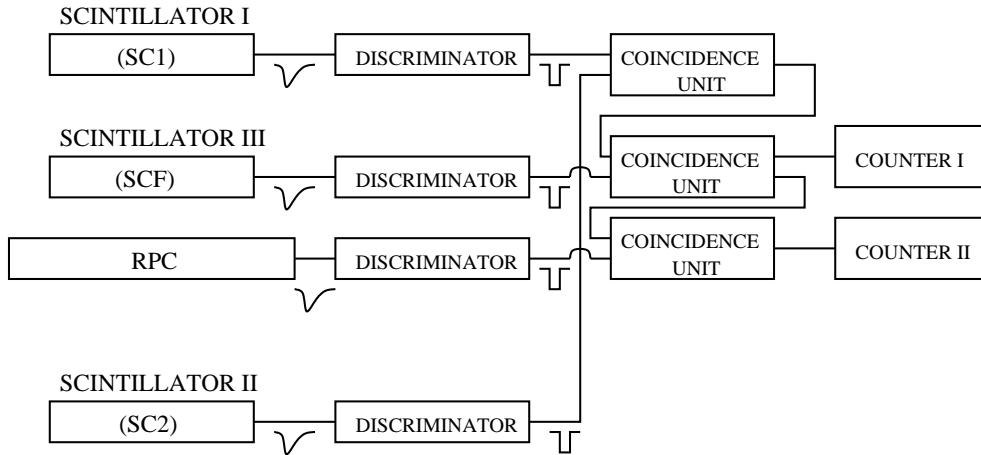
Figure 3.12: Schematic representation of the cosmic ray test setup.

obtaining the efficiency [75]. The arrangement of the scintillators and the RPC is shown in Figure 3.13.

Figure 3.13: Arrangement of the scintillators and the RPC.

The high voltages are applied to the RPC at the ramping rate of 5 V/s on both the electrodes. The streamer pulses are obtained starting from the high voltage of 5 kV ($\pm$ 2.5 kV) across the RPC. A typical screen dump of the oscilloscope pulse at 8 kV is shown in Figure 3.14. The figure shows the rise time is about 6 ns, which indicates the fastness of the pulse. The leakage current as measured by the high voltage system is recorded for further study.
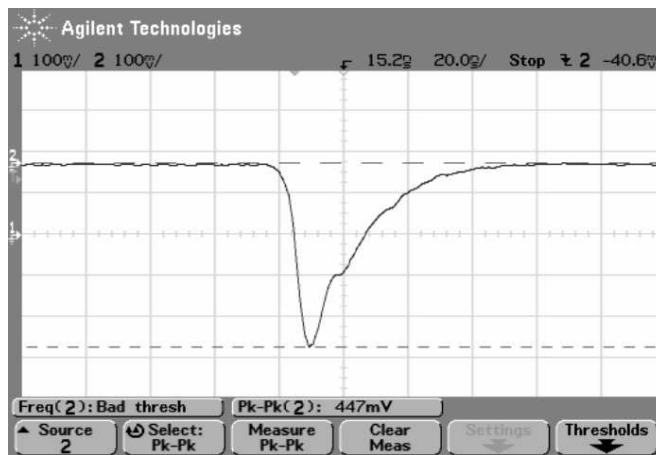
Figure 3.14: Typical induced pulse on a pick-up strip at 8 kV (100 mV/Div, 20 ns/Div, 50 Ω load) of a silicone coated P-120 grade bakelite RPC operated in streamer mode.

Figure 3.15: Arrangement of the power supply, front-end electronics and DAQ.

The leading edge discriminators are used for the scintillators and the RPC pulses. Thresholds in the discriminators are optimised to reduce the noise. For our final results, a threshold of -40 mV is used on the RPC signal unless otherwise stated. We have used a CAMAC-based data acquisition system LAMPS, developed by the Electronics Division, Bhabha Atomic Research Centre, Trombay, India [77]. The counts accumulated in a scalar over a fixed time period are recorded at regular intervals, and saved in a periodic log database. The temperature and the humidity are monitored at the time of measurement. The arrangement of the power supply, front-end electronics and DAQ is shown in Figure 3.15.

The gases used in the RPC are mixtures of Argon, Isobutane and Tetrafluroethane (R-134a) in 34:7:59 (mass) mixing ratio (equivalent to 55/7.5/37.5 volume ratio)[1]. The gases are pre-

---

[1]See Appendix A.

mixed, stored in a stainless steel container and sent to the detector using stainless steel tubes. A typical flow rate of 0.4 ml per minute was maintained by the gas delivery system, as mentioned in Ref. [78], resulting in $\sim$ 3 changes of gap volume per day.

Figure 3.16: Gas mixing and delivery system.
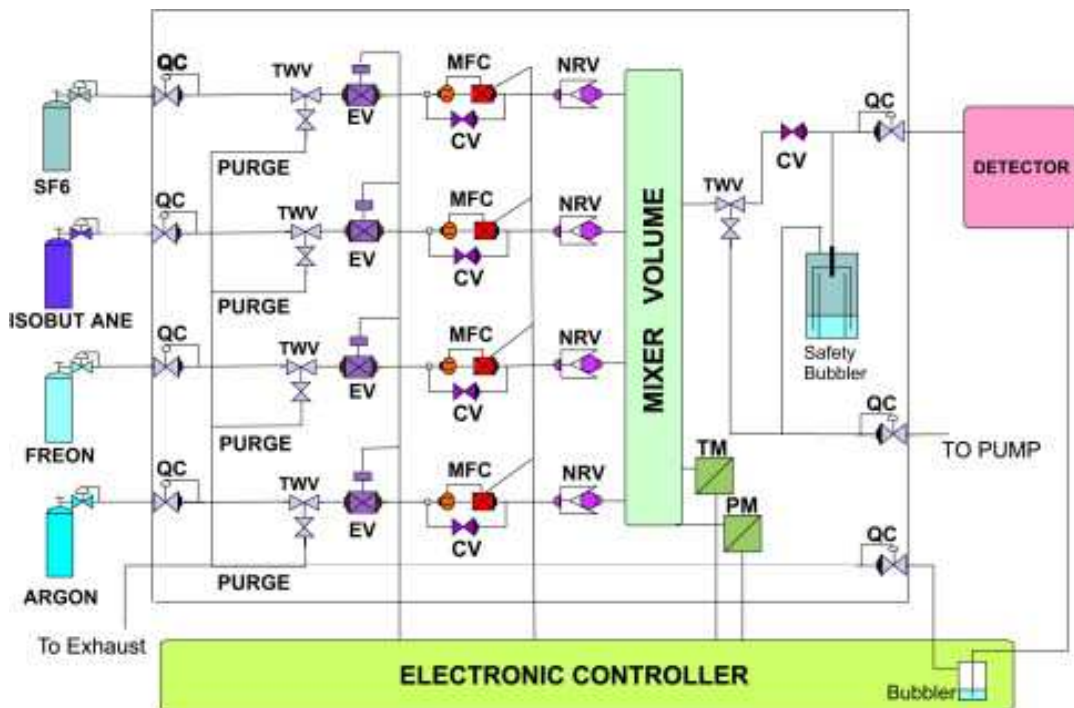
Figure 3.17: Schematic layout of the gas mixing system.

The gas mixing and delivery system is illustrated in Figure 3.16 and a schematic layout is given in Figure 3.17. The whole system consists of two parts: the first one is a gas control hardware (GCH) unit containing pressure regulators, filters, valves, flow controllers, and associated plumbing, and the second one is an electronic controller and display (ECD) unit. The system contains a stainless steel mixing vessel (MV) which has 10 cascaded mixing volumes, inter-connected to enhance mixing while passing through an elongated path of gas flow. The temperature and pressure inside the four-input mixing vessel are monitored and displayed electronically. Four different gas cylinders are connected to the system through pressure regulators and quick-connector (QC) valves in each channel. The gases, after passing through active silica gel drying columns and 0.5 μm filters, pass through three way valves (TWV), and normally closed (NC) electromagnetic valves (EV). The alternate ports of the TWVs are used for gas purging and evacuation of the inlet side to maintain purity. The four lines are then connected to the mass flow controllers (MFC), with optional by-pass lines through the manual control valves (CV) for the static mode (pre-mixed mode) of operation. Non-return valves (NRV) to the mixing vessel are also provided for safety, reliability and stability of gas flow. All the rigid connections between the gas flow components are done using $\frac{1}{4}$ OD SS-304L tubes and compression fittings to ensure leak tightness of the joints. All these connections are leak-checked using helium sniffer probe. The flexible connections, though only $\sim$5% of the total plumbing length, are made using Tygon^{TM} tubings.

The auto-lock feature of the quick-connector valves isolates the systems from the ambient when the input line is disconnected. One three way valve in the output line of the mixing vessel connects it either to the RPC detector through CV and QC, or to a vacuum pump for evacuation of the system, which is needed when the gas mixing ratio has to be changed. A safety bubbler, connected parallel to the output QC releases the mixed gas to the exhaust line in case of occasional increase of pressure in the inlet side of the RPC. The return line from the RPC is connected to the exhaust through a safety bubbler placed in the ECD unit. Diffusion pump fluid (DC-704) is used inside the bubblers.
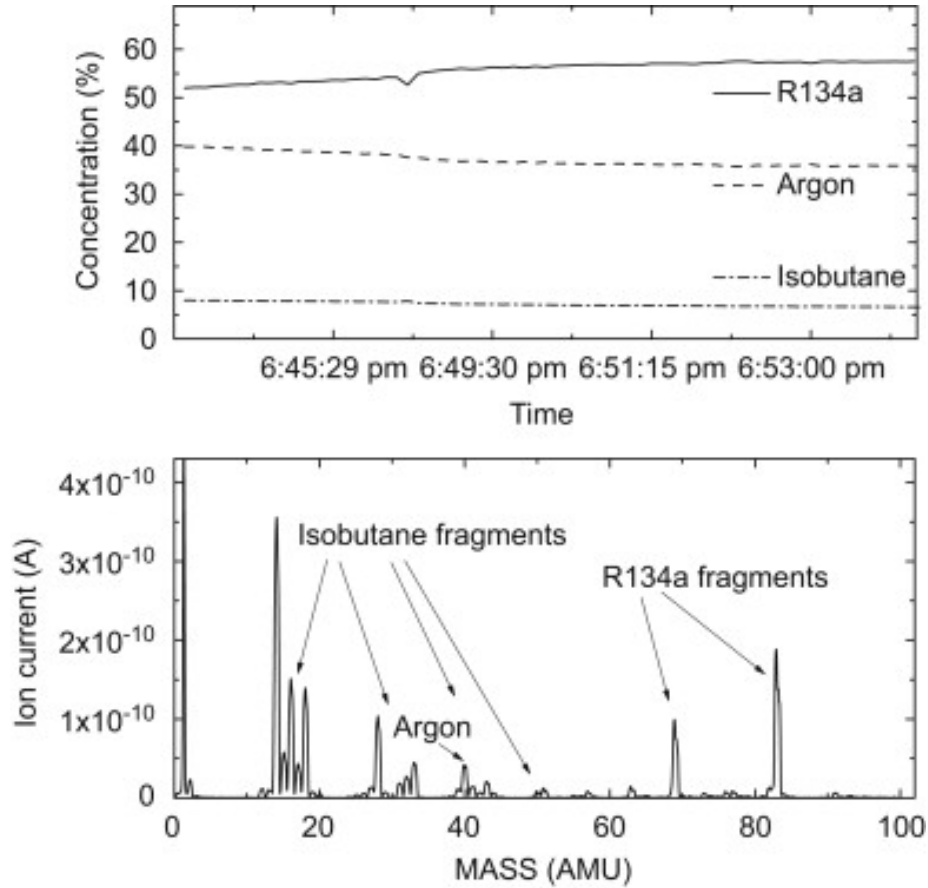
Figure 3.18: Results of residual gas analysis (RGA) of the mixed gas for streamer mode of operation.

The component gases of the pre-mixed samples from the detector inlet, was analyzed using a Prisma^{TM} QMS 200 quadrupole mass spectrometer-based Residual Gas Analyzer (RGA), with residual mass sensitivity of 1050 ppm over a mass range of 0200 amu. The sampled gas, taken in a previously evacuated glass enclosure, baked at 150°C, was fed into the vacuum test chamber where the RGA was mounted. The chamber was evacuated by a turbo pump to maintain a dynamical high vacuum of $<10^{-5}$ for the RGA system, in order to avoid damaging the sensitive channeltron device inside. The results of these measurements are given in Figure 3.18. The average concentrations, measured by the RGA set up for the streamer ratio of gas (used in our RPC operation) are: Argon: 37.1±1.4%, Isobutane: 7.2±0.5%, and R134A: 55.7±1.9%, which agree reasonably well within the quoted systematic uncertainties. Variation in concentrations of the gases with time as seen in Figure 3.18 is an artifact of the different pumping speeds of the turbo pump for different gas components.

3.5 Results in streamer mode of operation

The long term stability with high efficiency and good time resolution are important goals of any RPC detector development. In that spirit, the following studies are performed in the streamer mode of operation using cosmic rays for all the RPC modules by varying different parameters *e.g.* high voltage, discriminator threshold etc.: (a) efficiency of the chambers, (b) counting rate, (c) leakage current, (d) time resolution, (e) induced charge and (f) long term stability. Though our main goal is to operate those RPCs in the streamer mode, we have also measured the efficiency, time resolution, induced charge of those modules in the avalanche mode for comparative studies and the results are described in Section 3.6.

3.5.1 R&D on RPC based on efficiency and counting rate

The efficiency of the RPC, taken as the ratio between the coincidence trigger counts of the RPC modules and the master trigger counts of the 3-element plastic scintillator telescope as mentioned in Sec.3.4, is studied by varying the applied high voltage for each detector [75]. Counting is done over 30 minutes duration for each high voltage setting. The average master trigger rate is $\simeq 0.005$ Hz/cm^2.

One 30 cm × 30 cm RPC module made with the Superhylam grade bakelite has been tested initially in the cosmic ray test bench and the threshold of the RPC signal has been set at -50 mV in this case. The variation of efficiency with the applied high voltage is shown in the Figure 3.19 (a) for that particular RPC and that of the counting rates with the high voltage is shown in the Figure 3.19 (b). It is seen that the efficiency gradually increases from 20% to 75% as the high voltage is ramped up from 6.5 kV to 6.8 kV and reaches the plateau at > 90% at 7.5 kV. The counting rate has increased more or less exponentially with sudden jumps around 6.5-7.0 kV (see Figure 3.19 (b)), i.e. near the points where the efficiency saturates at > 90%.

The long term stability of the SH bakelite RPCs has also been studied using the same cosmic ray test set-up at 8 kV. The efficiency and counting rate of the RPC have been measured using the data accumulated over every 2 hours. The variation of efficiency and counting rate as a function of the period of operation are shown in Figure 3.20 (a) and 3.20 (b) respectively. The SH RPC had worked with an efficiency of > 95% and remained steady for 25 days, but beyond
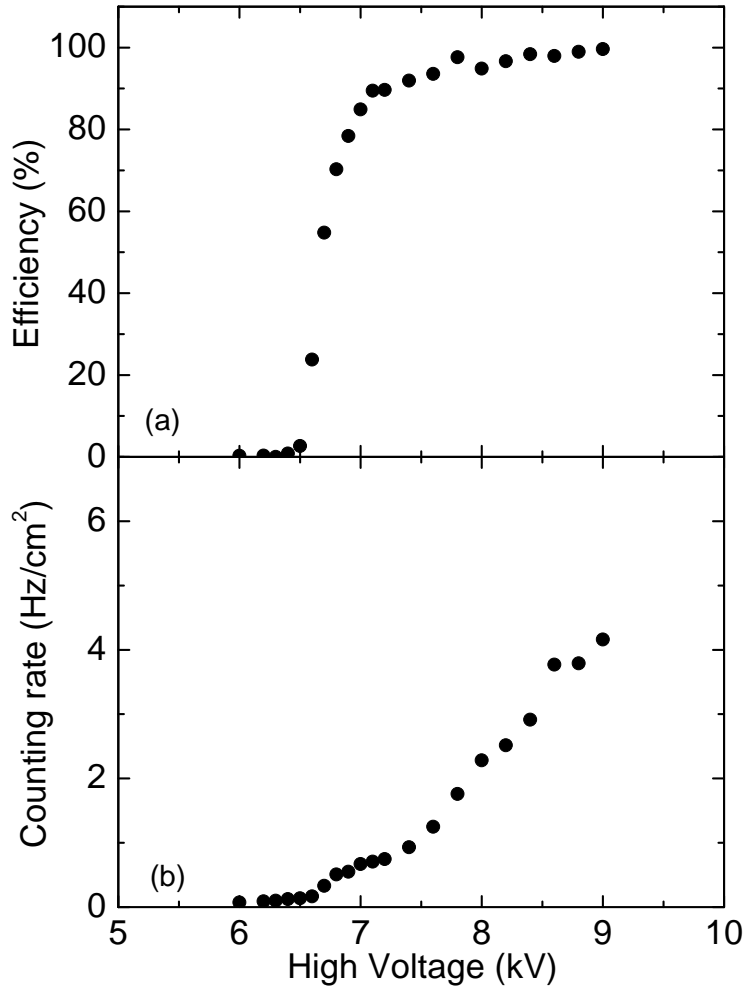
Figure 3.19: (a) Efficiency & (b) counting rate as a function of the high voltage for RPC made with Superhylam grade bakelite obtained with a gas mixture of Argon (55%) + Isobutane (7.5%) + R-134a (37.5%).

that, the efficiency deteriorated gradually to $\sim 86\%$ within next 13 days. On the other hand the count rate increased from 1 Hz/cm^2 to 10 Hz/cm^2 within 10 days, and then it increased slowly over the next 28 days. After that period, the count rate suddenly shot up to a value > 30 Hz/cm^2. The leakage current gradually increased from 3-4 μA to > 10 μA within that period. The test on this RPC was discontinued after 38 days and the RPC made with P-120 grade bakelite (IB1) RPC was mounted for testing with the same gas mixture.

The SH RPC has also been tested again after a gap of a few months. It showed same high leakage current (> 10 μA) and lower efficiency ($\sim 86\%$) indicating that some intrinsic breakdown of the bulk material must have taken place.
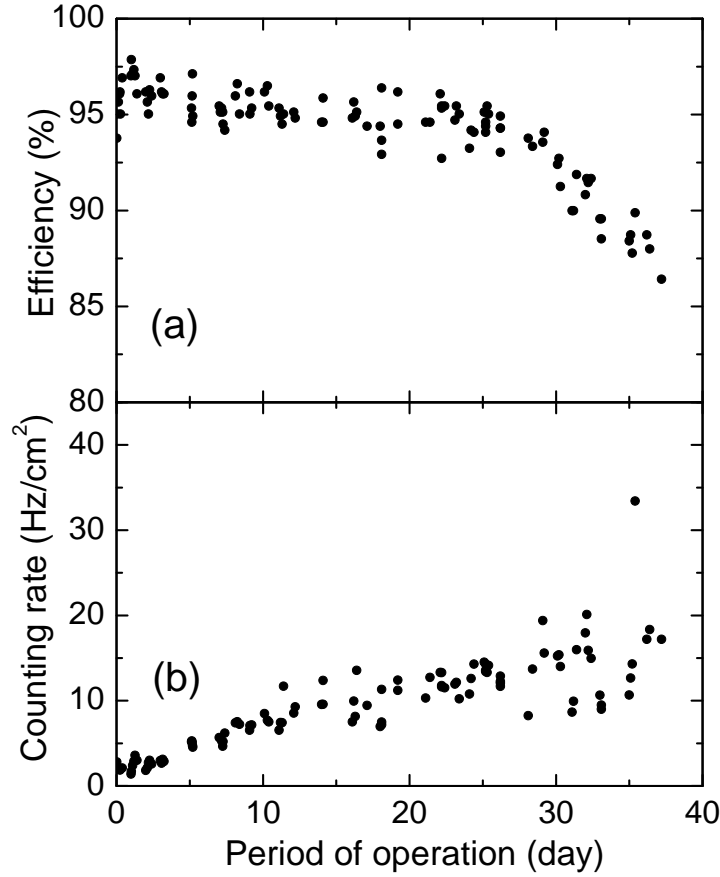
Figure 3.20: (a) Efficiency & (b) counting rate as a function of the period of operation for SH RPC. The RPC has been operated in streamer mode. Operating voltage was 8 kV.

The variation of efficiency and counting rate of the RPCs made by P-120 grade bakelite are shown in Figure 3.21 (a) and Figure 3.21 (b) respectively. It is seen that like SH, the efficiency increased from 20% to 75% as high voltage is ramped up from 6.5 kV to 6.8 kV, but unlike SH, the efficiency of the IB1 RPC reaches a maximum of $\sim 79\%$ at 7.2 kV and then decreases steadily up to $\sim 35\%$ as the high voltage is increased to 9 kV. The counting rates also increased more or less exponentially with sudden jumps around 6.5-7.0 kV (see Figure 3.21 (b)), i.e. near the points where the efficiency starts to decrease. This possibly indicates the onset of a breakdown regime that dose not recover in a reasonable time for the IB1 but works the other way for the SH. Similar behavior is observed also for IB2 and IB3. IB2 and IB3 which are made to establish the consistency of the results. It should, however, be noted that the counting rate and the leakage current of the SH are both larger than those of the IB1, IB2 & IB3, which are expected on the basis of smaller bulk resistivity of the superhylam grade bakelite [56].

59
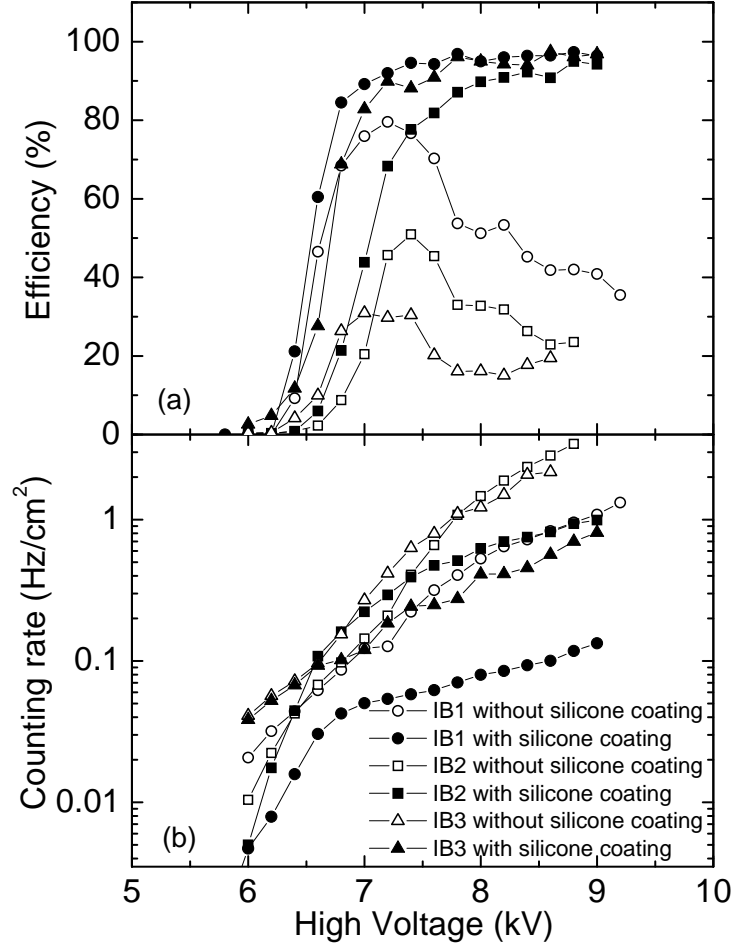
Figure 3.21: (a) Efficiency & (b) counting rate as a function of the high voltage for three RPCs made with P-120 grade bakelite (with & without silicone coating) obtained in streamer mode with Ar/Isobutane/R-134a in 55/7.5/37.5 ratio. The thresholds are set at -40 mV.

In order to investigate the reason for the reduction of efficiency in the IB1 (made by P-120 grade bakelite) above $\sim$ 7.2 kV, and taking cue from the fact that superhylam surfaces are glossy finished while the P-120 surfaces are matt finished, we have dismantled the detectors and made surface profile scan over a 5 mm span of the surfaces using DekTak 117 Profilometer [75]. These scans are shown in Figure 3.22. It is clearly seen that all the surfaces have a short range variation (typically $\sim$ 0.1 μm length scale) and a long range variation (typically $\sim$ 1 μm length scale). The long range surface fluctuation, which is a measure of non - uniformity, averaged over several scans are: 0.84 $\pm$ 0.12 μm (P-120), 0.49 $\pm$ 0.17 μm (superhylam) and 0.88 $\pm$ 0.09 μm (P-1001). On the other hand, the short range fluctuations, a measure of surface roughness, are: 0.64 $\pm$ 0.06 μm (P-120), 0.17 $\pm$ 0.02 μm (superhylam), and 0.63 $\pm$ 0.13 μm
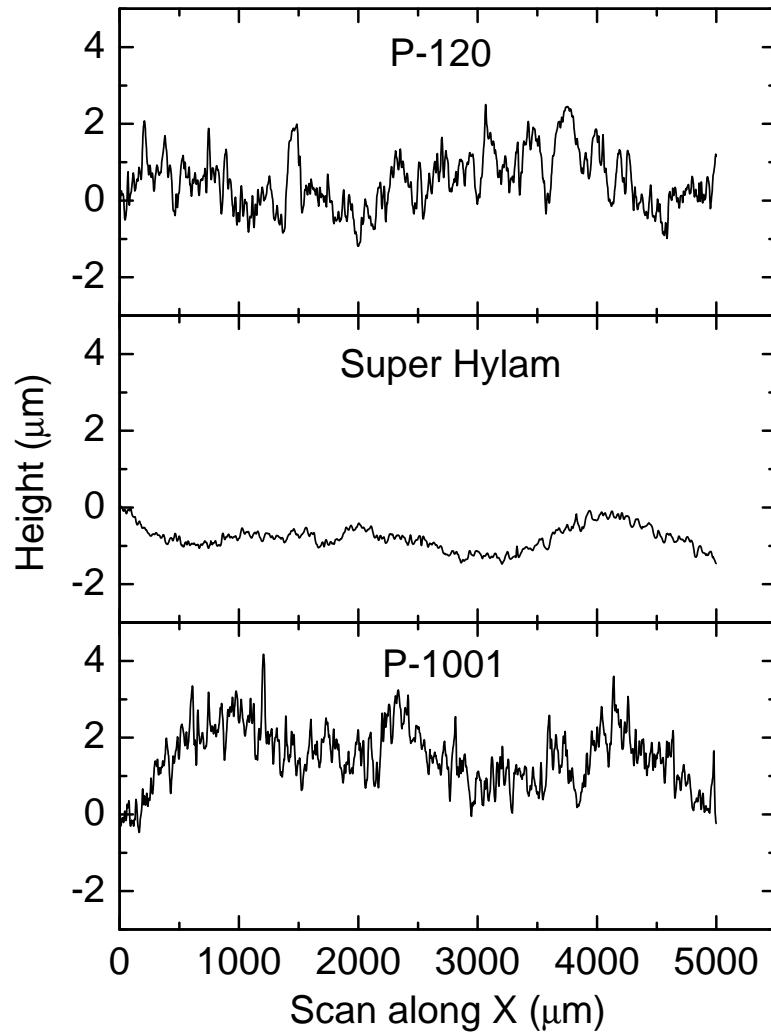
Figure 3.22: Linear surface profile scans of three grades of bakelite sheets.

(P-1001). Thus the long range fluctuations, within the limits of experimental uncertainties, are nearly same in all the grades but taking the short range fluctuations only the superhylam grade

Table 3.3: Average surface roughness of different grade of bakelite

Grade	Long range variation (μm)	Short range variation (μm)
P-120	0.84 ± 0.12	0.64 ± 0.06
Superhylam	0.49 ± 0.17	0.17 ± 0.02
P-1001	0.88 ± 0.09	0.63 ± 0.13

61

has a superior surface quality. The value of surface roughnesses of different bakelite grades are tabulated in Table 3.3.

An Atomic Force Microscope (AFM) is also used to study the surface morphological structure of the P-120 grade bakelite sheet. 3-D image of AFM scan of 2 mm thick P-120 grade bakelite surface over an area of 16μm $\times$ 16μm at two different places of the sample are shown in Figure 3.23. The topography of AFM data for the P-120 grade bakelite surface morphological structure is shown in Figure 3.24. It is clear from Figure 3.24 that the average roughness, R_a, expressed in units of height, [defined as $R_a = \frac{1}{n} \sum_{i=1}^{n} | y_i |$, where the roughness profile contains n number of ordered, equally spaced points along the trace, and y_i is the vertical distance from the mean line to the ith data point. Height is assumed to be positive in the up direction, away from the bulk material. The typical length scan interval of the AFM is $\sim$ 10 nm] was obtained in the AFM for the P-120 sample is $\sim$ 0.13 μm.

This is smaller by a factor of 5 as compared to short range variation of the surface profile, as obtained by the profilometer measurement. This clearly indicates that while the bakelite surface is relatively smoother at the submicron scale, it has larger wavyness of the surface at the micron scale. Preliminary neBEM [52] calculations indicate that the micron scale roughness of the surface, as obtained in our measurement, may cause a field variation of $\sim$ 5-12% across the surface. Detailed simulation calculations of avalanche or streamer propagation will be necessary to understand the effect of the surface roughness.
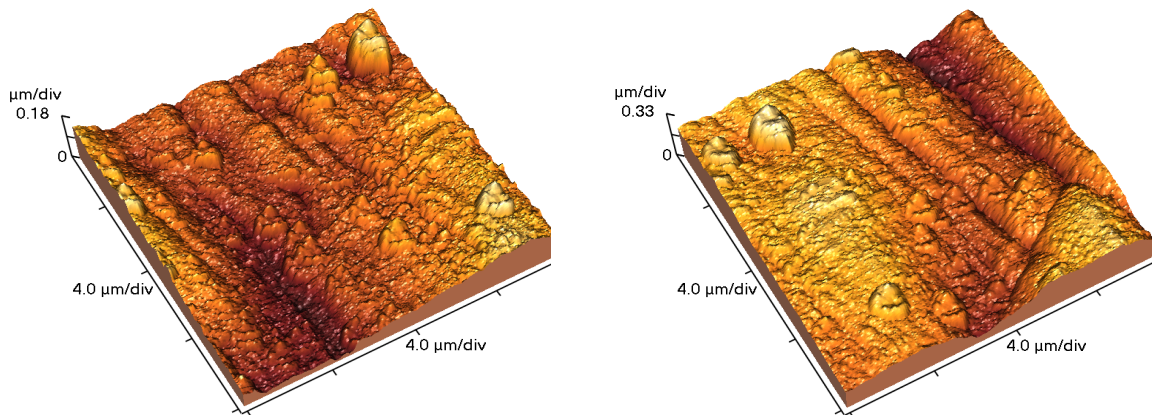
Figure 3.23: AFM image of the P-120 grade bakelite surface morphological structure.

AutoProbe Image
Topography

Results for Line 2

Histogram
Height: 385. nm

96.5 nm   482. nm

Line 2

0.20 µm/Div

0.00   4.00   8.00   12.00 µm

50   250   450 nm

Ra: 269.7 nm
Rq: 156.3 nm

Height Profile

Rp: 260.3 nm
Rv: -221.4 nm

nm
450.0

250.0

50.00
0.00   4.00   8.00   12.00 µm

Power Spectrum

dc   117. nm

0   4   8 (1/µm)
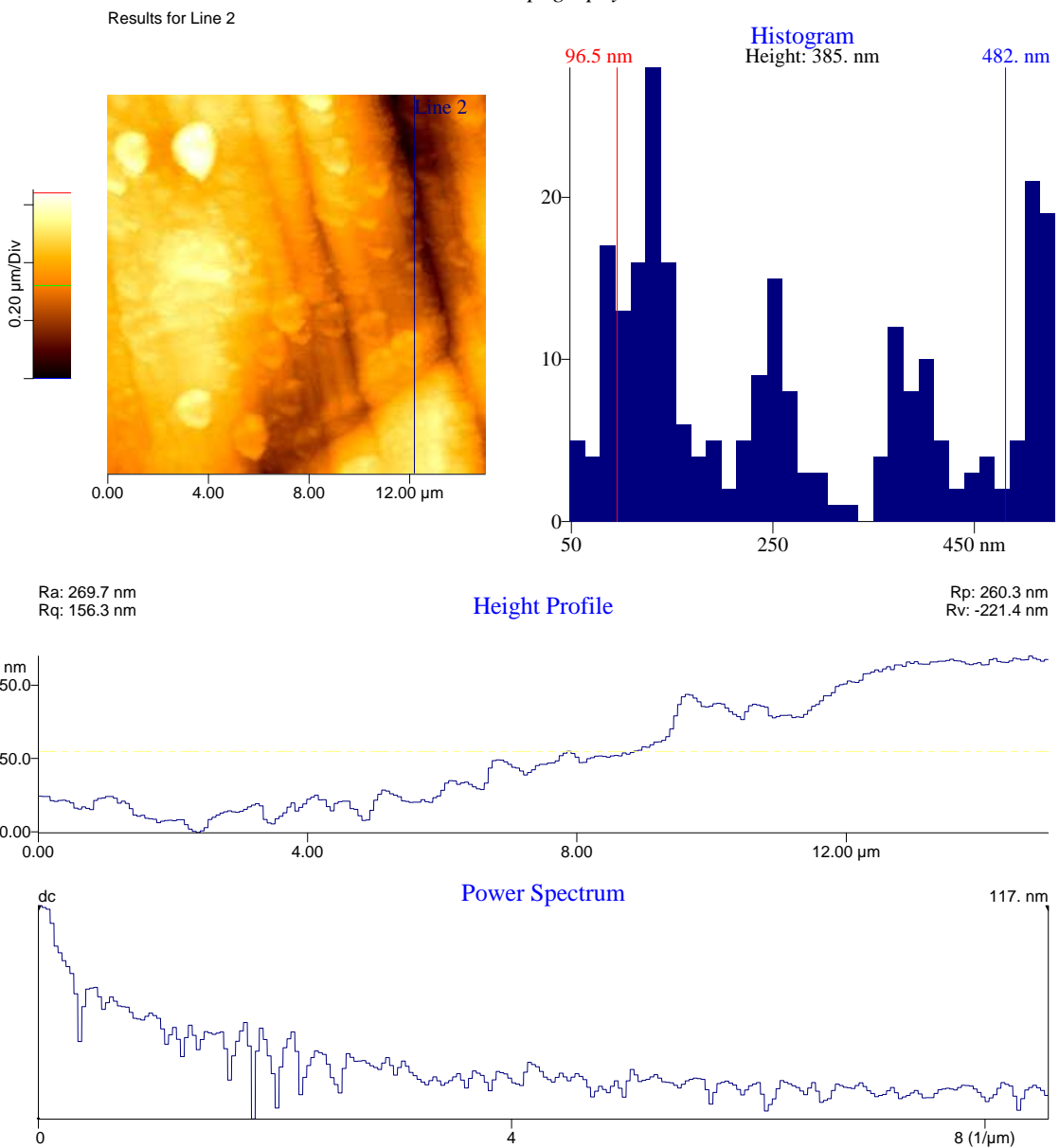
Rp-v	Rms Rough (Rq)	Ave Rough (Ra)	Mean Ht	Median Ht	Arc length	Bearing Ratio
481.7 nm	156.3 nm	138.8 nm	269.7 nm	239.7 nm	15.30 µm	@30.0% 389.40 nm

Bearing Ratio	Peak (Rp)	Valley (Rv)
@80.0% 119.06 nm	260.3 nm	-221.4 nm

Figure 3.24: Topography of AFM data of the P-120 grade bakelite surface morphological structure.

63

Smooth inner surface is an important factor for steady operation of the RPC [51]. Rough surface particularly the sharp pin like edge in the surface morphological structure is very sensitive to the field emission which is a source of high dark current and high counting rates.

To explore the remedial measure for the IB1 RPC, we have applied a thin layer of viscous fluid, Polydimethylsiloxane (PDMS) commonly known as silicone, manufactured by Metroark Limited, Kolkata, India, on the inner surfaces of the P-120 bakelite sheets. The chemical formula of silicone is $[R_2SiO]_n$, where R is an organic groups such as methyl, ethyl, or phenyl and have the coefficient of viscosity about 5.5 Pa.s at 23°C. About 1 g of the fluid is applied over 300 mm × 300 mm area. Based on the specific gravity (1.02 at 23°C) of the fluid, the estimated coating thickness would be ~ 10 μm. This material is chosen for the following reasons: a) very low chemical reactivity with the gases used, b) good thermal stability over a wide temperature range (from -100 to 250 °C), c) very good electrical insulator, d) excellent adhesion to most of the solid materials, and e) low vapour pressure, which is essential for stable operation over a reasonable time period. The silicone treated surfaces are kept under infrared lamp for 2 hours to allow the viscous fluid to fill all the micro-crevices on the surface. The reassembled detector is tested at the same set-up. The results of efficiency and count rate measurements, shown in the Figure 3.21 (a) and 3.21 (b), indicate a remarkable improvement in the performance of the P-120 detector. The efficiency increases from 20% to 75% as the high voltage is increased from 5.7 kV to 6.2 kV, while the singles count rate, as a whole has decreased by a factor of 5. This indicates quenching of micro-discharge after silicone treatment, which is very much desirable for functioning of the detector. The efficiency in this case reaches > 95% plateau at 7 kV. Improvement on performances is also observed for the IB2 and IB3 after the application of silicone fluid on the inner surfaces as shown in Figure 3.21 (a) and 3.21 (b).

It is worth noting that the surface treatment with insulating/non-polar liquid as a remedial measure was first demonstrated for the BaBar RPCs. However, it was observed that the formation of stalagmites by polymerisation of uncured linseed oil droplets had created conducting paths through the gap, thereby causing irreversible damage to the bakelite plates [39]. The process of linseed oil treatment was later changed by increasing the proportion of eptane as a solvent to produce a thinner coating (10-30 μm) on the inner surface [79]. Our observation that

silicone coating of the inner surfaces aides the proper functioning of our P-120 bakelite RPC detector once again confirms the importance of smooth surface finish of the inner surfaces.

At a later stage of work silicone fluid made by Dow Corning (USA) has been used to build several RPC modules. Details of this type of coating and the results of those RPCs are described in Section 3.5.13.

3.5.2   Leakage current
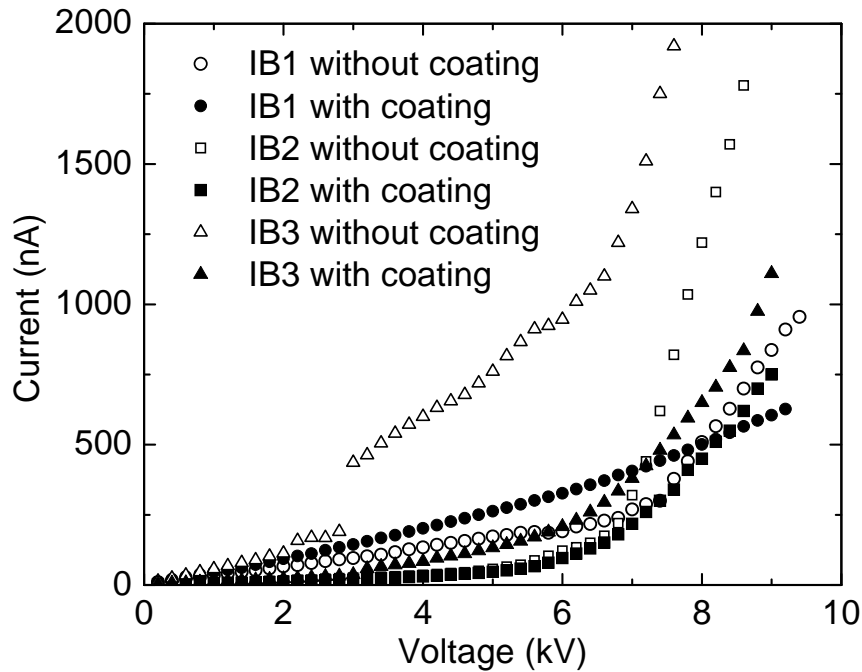
Figure 3.25: Current as a function of the applied voltage for RPC made by P-120 grade bakelite, operated in streamer mode.

To judge the improvement in the overall performance of the RPC detector, we have measured the leakage current through the RPC detector with and without silicone coating as shown in the Figure 3.25 [75]. The plots show a common feature that the current-voltage curves have two distinctly different slopes as it has been shown earlier [41]. The reason is explained below by the equivalent circuit of RPC (Figure 3.26).
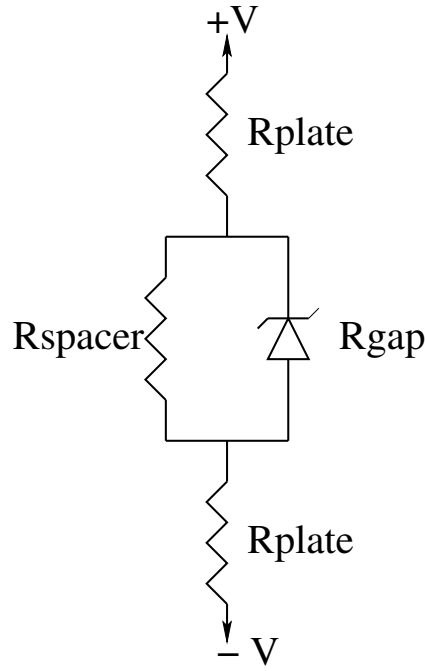
Figure 3.26: Equivalent circuit of RPC.

At a voltage below discharge (low voltage):

$$R_{gap} \simeq \infty \quad , \quad R_{spacer} \gg R_{plate}$$
$$\frac{dV}{dI} = R_{spacer} \tag{3.1}$$

i.e. the gas gap behaves as an insulator in the lower range of applied voltage and hence the slope over this span scales as the conductance of the polycarbonate spacers.

At a voltage above discharge (high voltage):

$$R_{gap} \approx 0$$
$$\frac{dV}{dI} = R_{plate} \tag{3.2}$$

i.e. at the higher range of voltage, the gas behaves as a conducting medium due to the formation of streamers. Therefore, the slope over this range scales as the conductance of the gas gap.

It is seen that the slope in the higher range of voltage is much steeper for the RPC without silicone coating and hence it points to the fact that some sort of uncontrolled streamers are being formed in the gas gap causing a degradation of the efficiency [80]. This possibly does not happen in the RPC detectors with silicone coating.

3.5.3 Long term stability test

Long term stability of one silicone coated bakelite RPC (IB1) has been studied using the same cosmic ray test set-up. In this case the coincidence trigger counts of the RPCs and the master trigger counts, accumulated over every 2 hours, have been recorded continuously for more than 4 months at a high voltage of 8 kV. The average room temperature and the relative humidity have been recorded to be 22-25°C and 63-65%, respectively. The count rates of the RPCs have also been recorded simultaneously. Figure 3.27(a) and 3.27(b) depict the variation of efficiency and count rates over the above mentioned period for the silicone coated RPC. The efficiency measured was $\sim 96\%$ and above and remained steady for the period of measurement of more than 130 days. The count rate also remained steady around 0.1 Hz/cm^2. The leakage current was found to be marginally dependent on temperature and humidity, though it remained steady
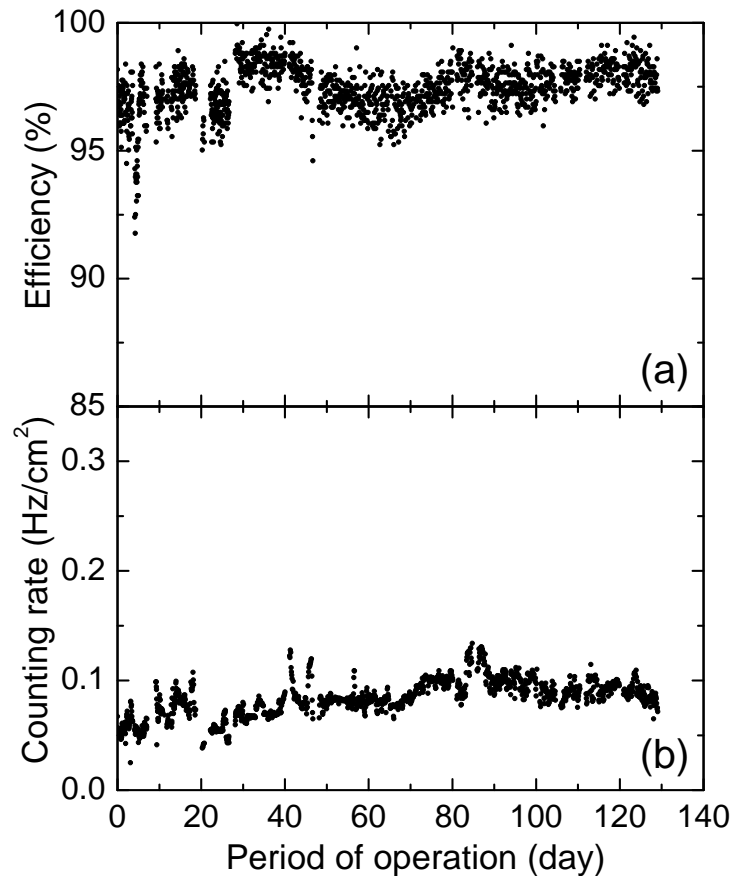
Figure 3.27: (a) Efficiency & (b) counting rate as a function of the period of operation for silicone coated RPC prototype operated in streamer mode. Operating voltage was 8 kV.
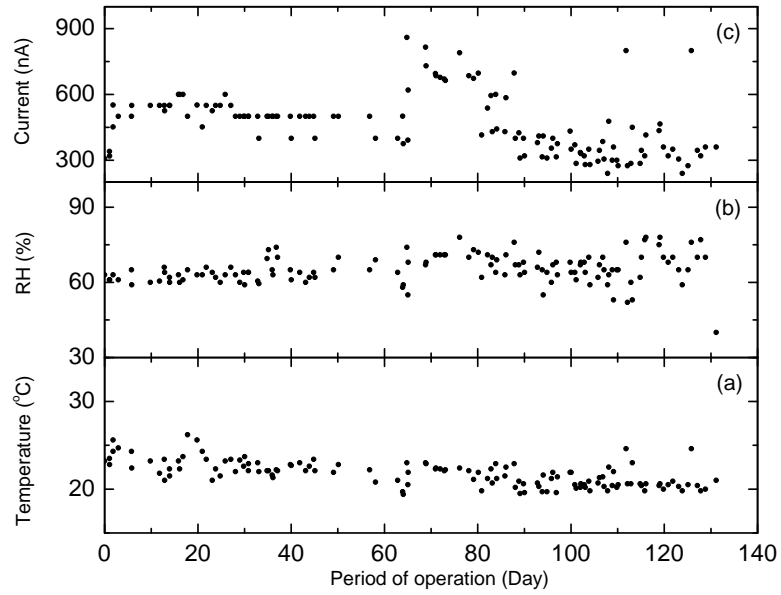
Figure 3.28: (a) Temperature, (b) relative humidity, and (c) current as a function of the period of operation at the time of long term operation of IB1.

at $\sim$ 400 - 500 nA during the operation. Variations of the average values of temperature, relative humidity (RH) and current over the above mentioned period are shown in Figure 3.28 (a), (b) and (c) respectively. During the period of 60th to 80th day the average current was relatively higher. This jump was due to sudden change of the environmental condition because of frequent power trip of the AC.

3.5.4 Effect of environmental humidity

The effect of the environmental humidity on the efficiency curves has also been studied. This measurement was done at relative humidities of 58% and 67% of the laboratory environment and at the room temperature of $\sim$ 22-25°C. These curves, plotted in Figure 3.29, indicate that there is no significant effect of humidity on the efficiency, except that the efficiency plateau is marginally higher at lower humidity. However, the counting rate (shown in Figure 3.29) and the leakage currents, measured simultaneously and plotted in Figure 3.30, are larger at higher humidity. These observations indicate that at higher humidity, charge leakage through the exterior surfaces produce micro discharges which in turn induce signals to the pick-up strips and the counting rate increases. Due to this continuous discharge through the surface at higher humidity leakage current also increases.

68
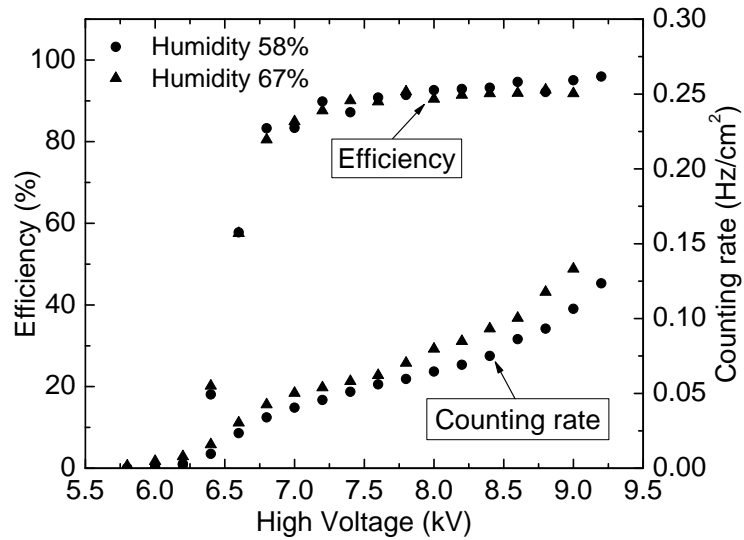
Figure 3.29: The efficiency and the counting rate versus high voltage for different humidities for a silicone coated P-120 grade bakelite RPC operated in streamer mode.
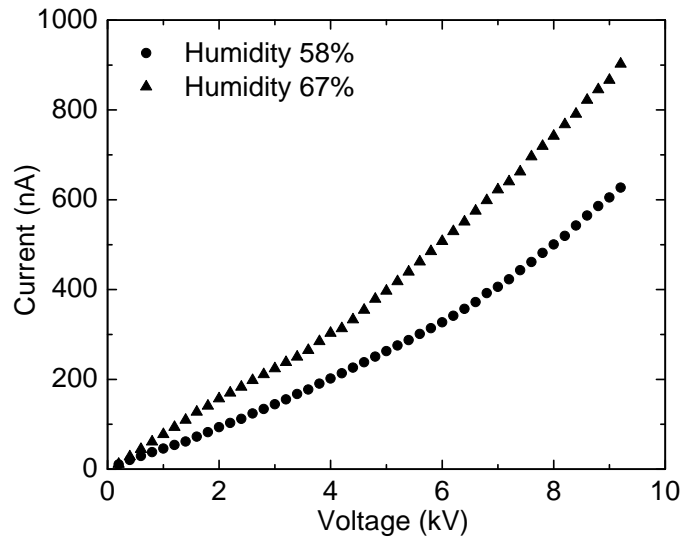
Figure 3.30: Current versus high voltage for different humidities for a silicone coated RPC operated in streamer mode.

3.5.5 Effect of RPC threshold

The efficiency and the counting rate, which is also known as the noise rate, of the RPCs have been studied by varying the applied high voltage and setting different discriminator thresholds [81]. The variation of efficiency and counting rates with the applied high voltage for the three discriminator thresholds of a silicone coated RPC is shown in Figure 3.31. It is seen that

the counting rate of the RPC decreases with increase of threshold which is expected with the suppression of noise at a higher threshold. However, the efficiency curves do not depend much on the threshold setting varying between 20 mV to 80 mV, except that the efficiency plateau is marginally higher at the lowest threshold setting of 20 mV. The variation of efficiency and counting rate of a RPC module with the threshold at a particular high voltage of 8.5 kV is
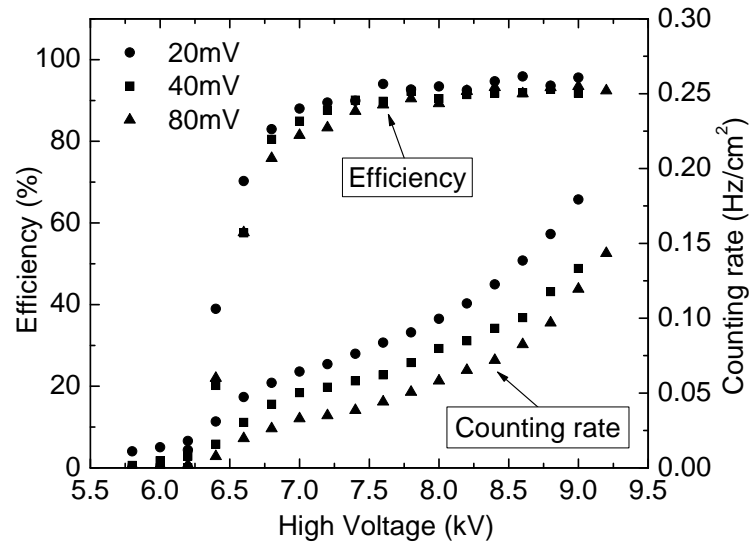
Figure 3.31: The efficiency and the counting rate as a function of the high voltage for a silicone coated bakelite RPC operated in streamer mode with discriminator threshold values of 20 mV, 40 mV and 80 mV.
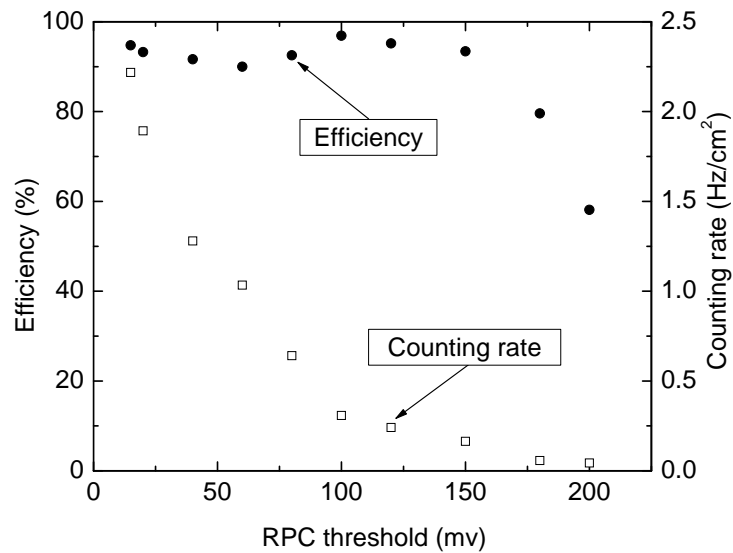
Figure 3.32: Variation of the efficiency and the counting rate with the threshold.

70

shown in Figure 3.32. The efficiency remains steady over 90% with low counting rate up to 150 mV threshold. The counting rate decreases exponentially with the increase of the threshold as more and more noise are suppressed with the increase of the threshold.

3.5.6 Strip multiplicity and Crosstalk

The average strip multiplicity of a RPC to the minimum ionising cosmic muons is obtained by measuring the amplitudes of two, three and four consecutive strips by external trigger in the oscilloscope. The data are analysed for different RPC thresholds. In Figure 3.33 the variation of average strip multiplicity as a function of RPC threshold is shown. It is clear from the plot that the strip multiplicity decreases with increasing RPC threshold. RPC threshold can be increased to a few tens of mV as efficiency remains over 90% with low counting rate up to 150 mV. After 150 mV the efficiency decreases with threshold as shown in Figure 3.32.
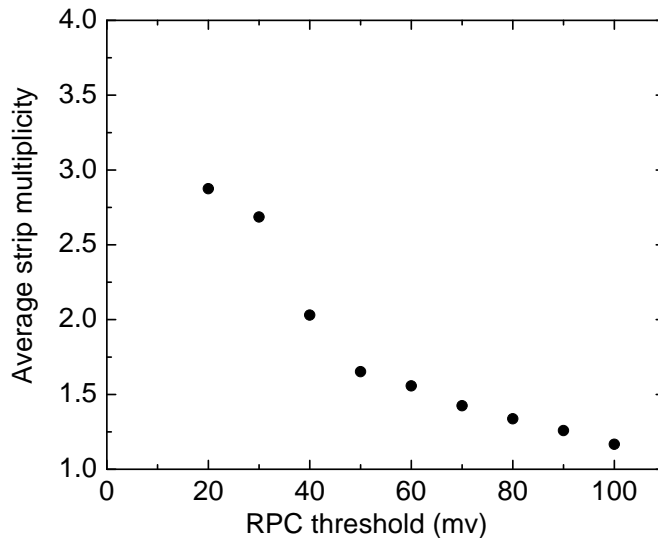
Figure 3.33: The average strip multiplicity of an RPC as a function of high voltage.

When a single particle induces signal on two or more strips then the term crosstalk comes into the picture. The measurement of the crosstalk (CT) for a silicone coated RPC was carried out rigorously. Figure 3.34 shows the schematic of the crosstalk measurement setup. The width of the finger scintillator is such that it covers one pick-up strip completely and two adjacent strips
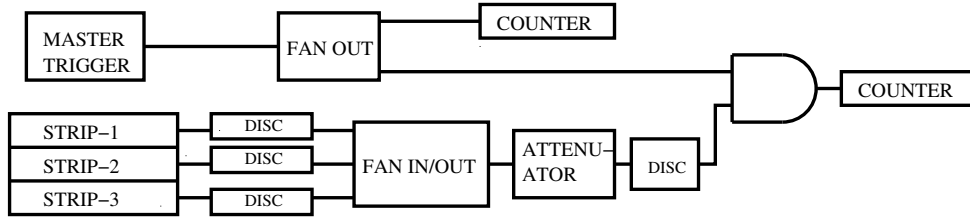
Figure 3.34: Schematic representation of the crosstalk measurement setup.

partially. The signals from these three strips after leading edge discriminator (LED threshold : 40 mV) were sent to the inputs of a FAN-IN-FAN-OUT (FI/FO) module. The output signal from the FI/FO after attenuation was again put to another discriminator. The signal from this discriminator was taken in coincidence with the master trigger. The crosstalk was defined by the ratio of this coincidence count and the master trigger. The attenuation factor was set at 0.3. The fan out signal after attenuation, observed in the oscilloscope, was ~ 250 mV when one strip fires. The resulting pulse heights were ~ 440 mV and 630 mV respectively, when signals from two strips and three strips came simultaneously. In order to measure the crosstalk between two and three adjacent strips, the discriminator threshold to the fan out signal was set at 280 mV and 520 mV, respectively.
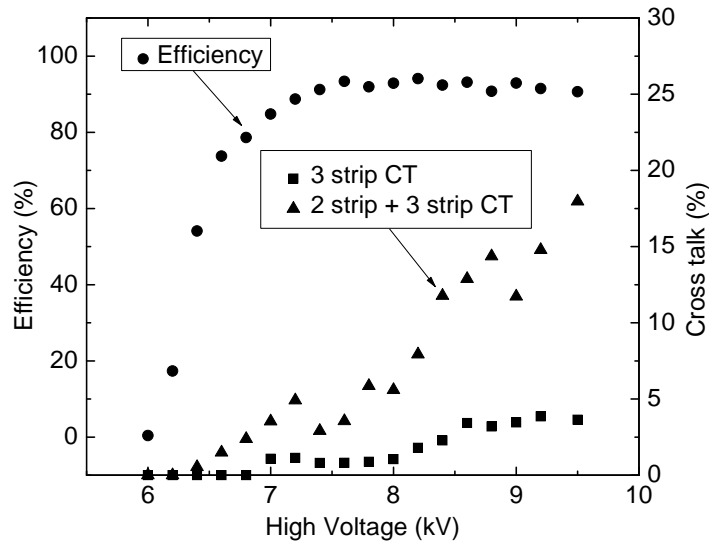
Figure 3.35: Variation of the crosstalk with the high voltage in comparison with the efficiency for a silicone coated P-120 grade bakelite RPC.

The crosstalk between the two and three RPC strips, defined in the last paragraph, had been measured by varying the applied high voltage as shown in Figure 3.35. When the discrimination threshold after attenuation was set at 280 mV as stated above, the signals from the two adjacent strips as well as three adjacent strips simultaneously contributed to the crosstalk and it was found to be < 20% (Figure 3.35). The crosstalk between the three adjacent strips was found to be < 5%, when the discrimination threshold after attenuation was set at 520 mV [81, 82]. These values of the crosstalk have been taken into account while estimating the final efficiency.

3.5.7 Test of signal attenuation

The long cable drive of RPC streamer pulse has been tested using RG-174/U coaxial cables. A maximum of 40 m RG-174/U coaxial cable has been used. The average pulse height of RPC in streamer mode was $\sim$ 300-500 mV as shown in Figure 3.14. After 40 m cable drive the signal amplitude was attenuated to $\sim$ 80% of the signal amplitude obtained at 2 m cable. The rise time increases slightly at that length of cable. The variation of normalised pulse height and rise time are shown in Figure 3.36. Here normalised pulse height and rise time means the ratio of those values obtained after a particular cable length to that obtained after 2 m cable.
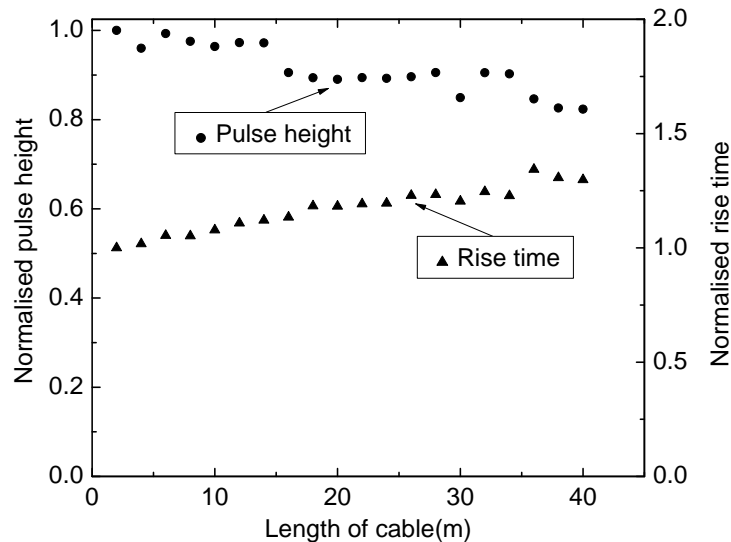
Figure 3.36: Variation of the normalised pulse height and rise time with the cable length for a silicone coated P-120 grade bakelite RPC.

3.5.8 Induced Charge
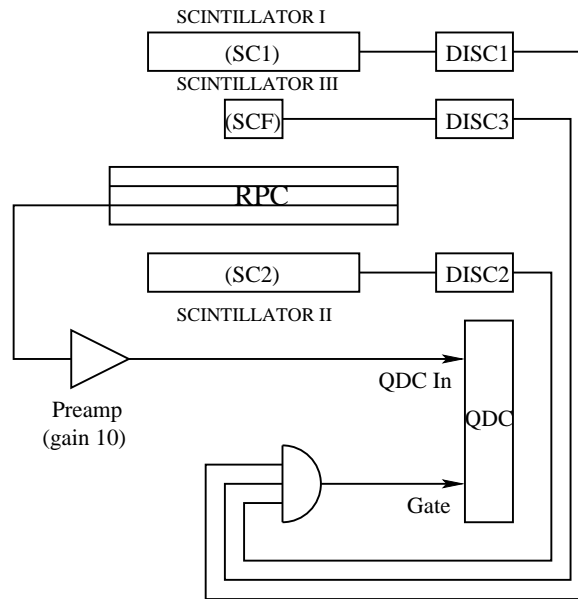
Figure 3.37: Schematic representation of the charge spectrum measurement setup. Phillips 7166 Charge to Digital Converter (QDC) was used.

Charge content of the pulses were measured using a charge to digital converter, referred to as QDC (Phillips 7166 16-channel QDC). [52]. The set-up is shown in Figure 3.37, which is very similar to that used in Ref. [83]. First the QDC was calibrated by using a Phillips 7120 charge-time generator. The calibration curve is shown in Figure 3.38. The master trigger of the
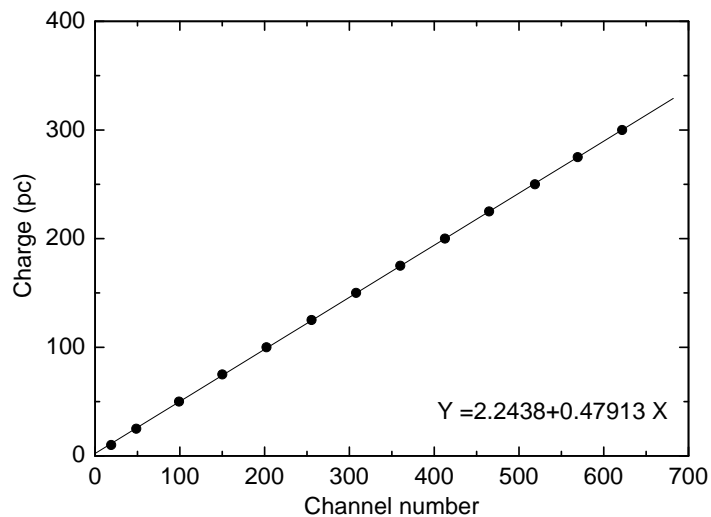
Figure 3.38: The calibration curve of QDC.

3-element plastic scintillator telescope was used as gate to the QDC. The width of the gate was 1.5 μs. The pulse height in the streamer mode was noted to be a few hundred mV, while that in the avalanche mode was found to be < 10 mV (Details of avalanche mode operation is discussed in Section 3.6. A 10X voltage pre-amplifier was used for the avalanche mode operation of the RPCs.
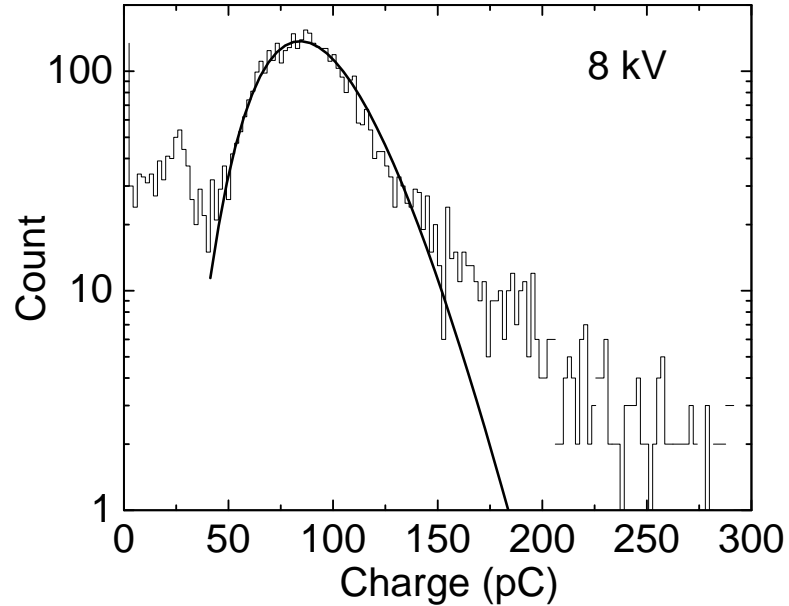
Figure 3.39: The charge distribution spectrum in the streamer mode with a gas mixture of Argon/isobutane/R-134a in 55/7.5/37.5 ratio.

The charge distribution spectrum in the streamer mode operation at 8 kV with a gas mixture of Ar, isobutane and R-134a in 55/7.5/37.5 ratio is shown in Figure 3.39. Corresponding best-fit Polya distribution curve to the streamer charge spectrum is also shown in the same plot [83, 84]. It is clear that the fitted curve underpredicts the tail of the charge spectrum. This possibly indicates the onset of a breakdown responsible for excess streamer charge beyond that can be predicted by the clustering model.

The Polya distribution [55, 85, 86] describes the distribution of the signal generated starting from a single electron. Its formal expression is:

$$Q \;=\; a\left(\frac{b}{c}x\right)^{b-1} e^{-\left(\frac{b}{c}x\right)} \tag{3.3}$$

where, a,b and c are three parameters.

75

The charge distribution spectra in streamer mode for a 30 cm × 30 cm RPC with a gas mixture of argon, isobutane and R-134a in 55/7.5/37.5 ratio are shown in Figure 3.40 for different high voltages and that for a 10 cm × 10 cm module are shown in Figure 3.41. In case of 30 cm × 30 cm module area of each pick-up strip was 30 cm × 2.5 cm while that was 10 cm × 0.5 cm for the 10 cm × 10 cm RPC. Charge induced on a pick-up strip of area 10 cm × 2.5 cm was also measured for the 10 cm × 10 cm module. The charge distribution spectra for this case is shown in Figure 3.42 for different high voltages. The charge distributions show broadening with the increase of the applied voltage for both the chambers.
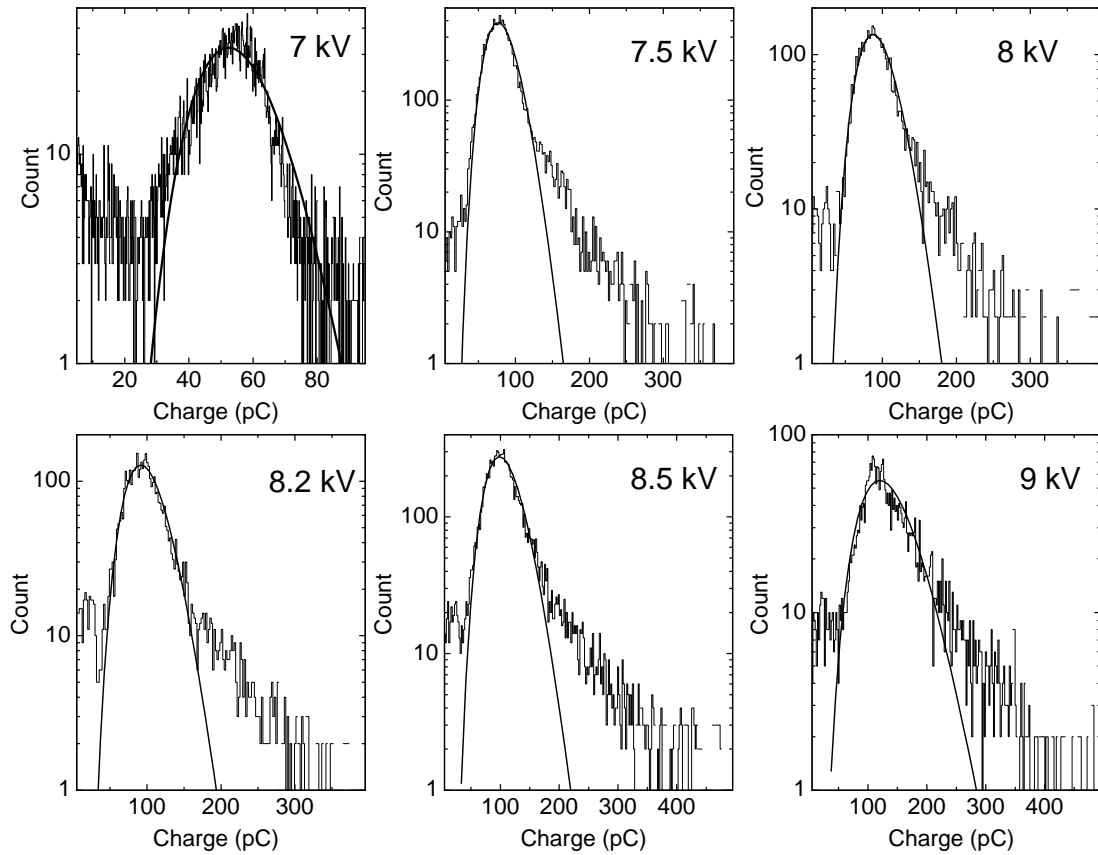
Figure 3.40: The distribution of charge in streamer mode of operation for different high voltages for a 30 cm × 30 cm RPC. Area of each pick-up strip is 30 cm × 2.5 cm. The gas mixture Argon/Isobutane/R-134a=55/7.5/37.5

The average induced charge as a function of the applied high voltage is shown in Figure 3.43. It is clear from the Figure 3.43 that the streamer charge is ∼ 100 pC at the plateau region (at ∼ 8 kV) for the 30 cm × 30 cm RPC measured with a pick-up strip of dimension 30 cm × 2.5 cm
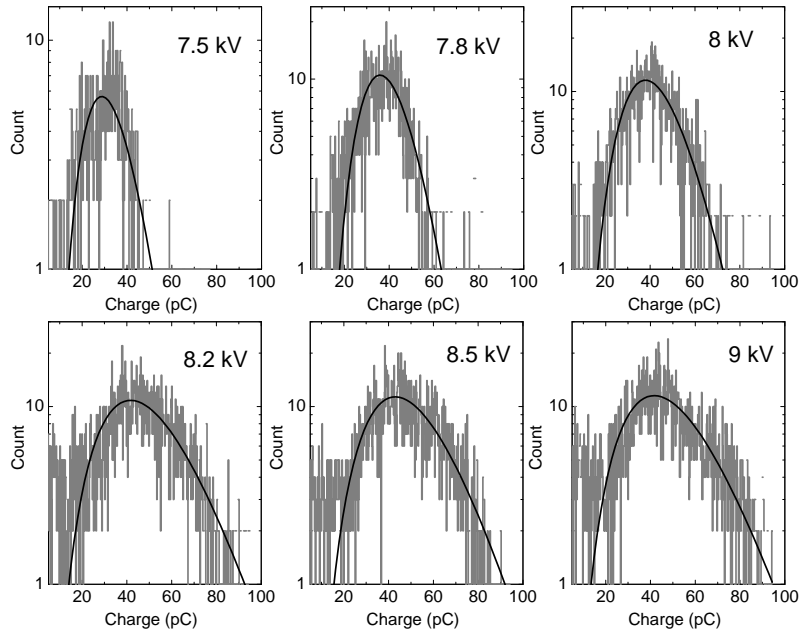
Figure 3.41: The distribution of charge in streamer mode of operation for different high voltages for a 10 cm × 10 cm RPC. Area of each pick-up strip is 10 cm × 0.5 cm. The gas mixture Argon/Isobutane/R-134a=55/7.5/37.5
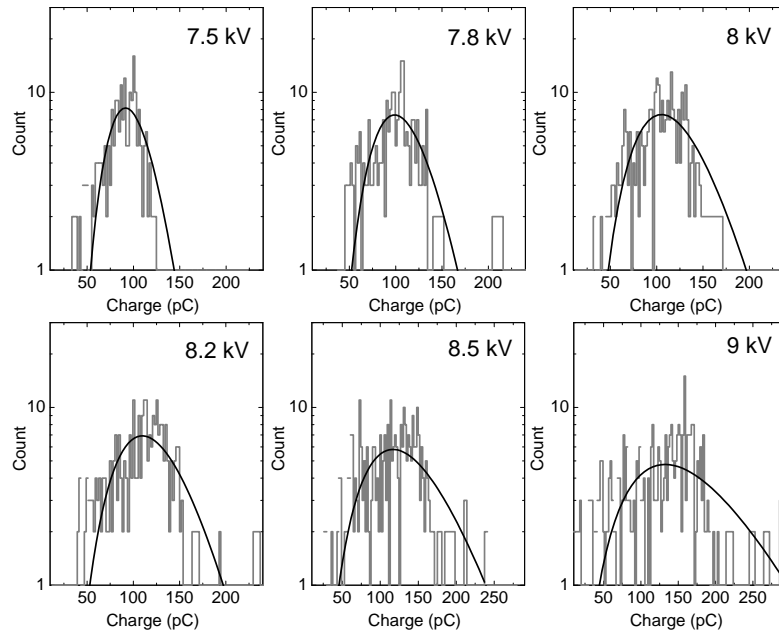
Figure 3.42: The distribution of charge in streamer mode of operation for different high voltages for a 10 cm × 10 cm RPC. Area of each pick-up strip is 10 cm × 2.5 cm. The gas mixture Argon/Isobutane/R-134a=55/7.5/37.5

77

and that for the 10 cm × 10 cm module is ∼ 45 pC when it is measured by using pick-up strip of area 10 cm × 0.5 cm and ∼ 100 pC when it is measured by using pick-up strip of area 10 cm × 2.5 cm. There is a difference between the charges for 30 cm × 30 cm and 10 cm × 10 cm RPCs when measured by strip of width of 2.5 cm. This is due to the fact that the pick-up strips were not exactly same for the two RPCs in accordance to their dielectric constants, impedance etc.
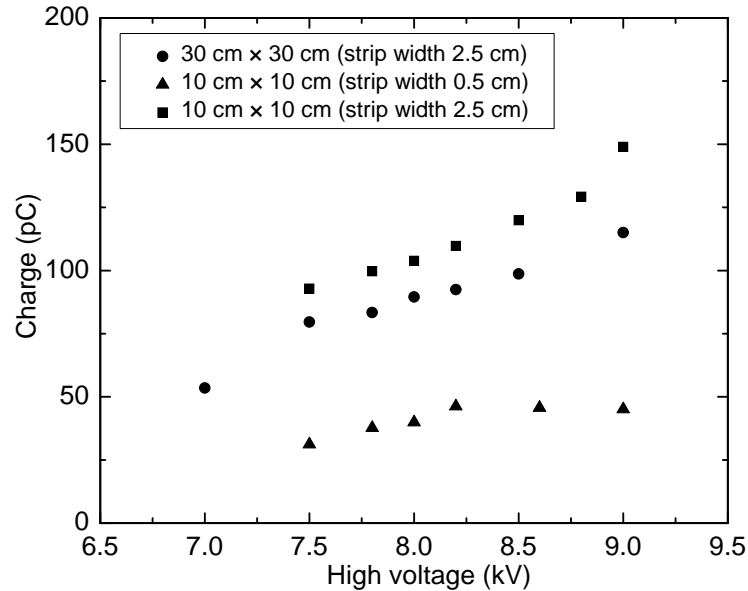
Figure 3.43: Average charge as a function of the applied high voltage in the streamer mode.

When a charged particle passes trough a RPC it ionizes the gas and when the pick-up strips are placed on the outer surface of the electrodes, induced charges are either drawn in or drawn out from the readout strips, generating voltage or current pulses of opposite polarities on the two sides of a RPC as mentioned in Section 2.2. There should be a correlation between the charges measured by integration of pulse The correlation between the charge induced on the pick-up strip placed over the positive electrode (charge1) and that induced on the pick-up strip placed over the negative electrode (charge2) is studied for a 10 cm × 10 cm RPC using the pick up strip of width 0.5 cm and 2.5 cm. The correlation in this two cases are shown in Figure 3.44 and Figure 3.45 respectively. The negative and positive induced charges are proportional to each other. The negative signal is directly fed to one QDC input whereas the positive signal is first inverted by an inverting transformer and then enters to another QDC input. Due to the bandwidth limitation the positive signal (charge 2) attenuates. So the total induced charge is more for charge 1 than charge 2.

78
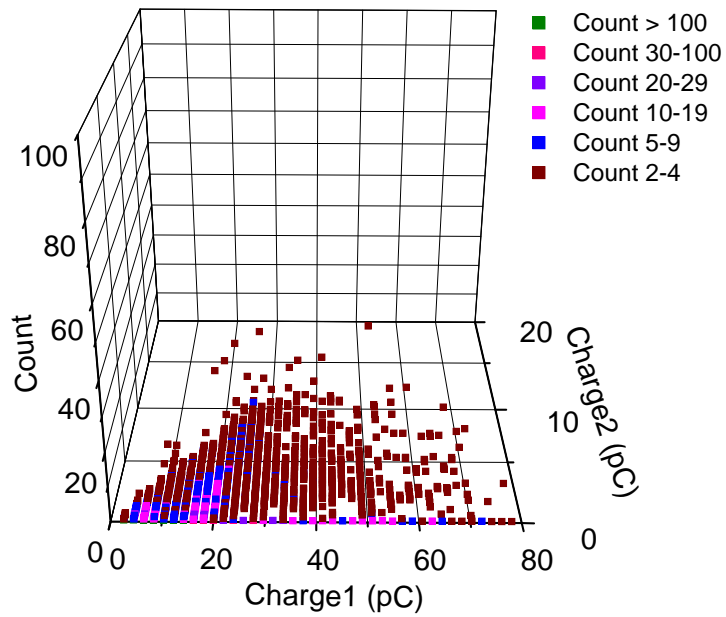
Figure 3.44: Correlation between the charges induced on the pick-up strip placed over the positive electrode (charge1) and that induced on the pick-up strip placed over the negative electrode (charge2). Width of the pick-up strip is 5 mm.
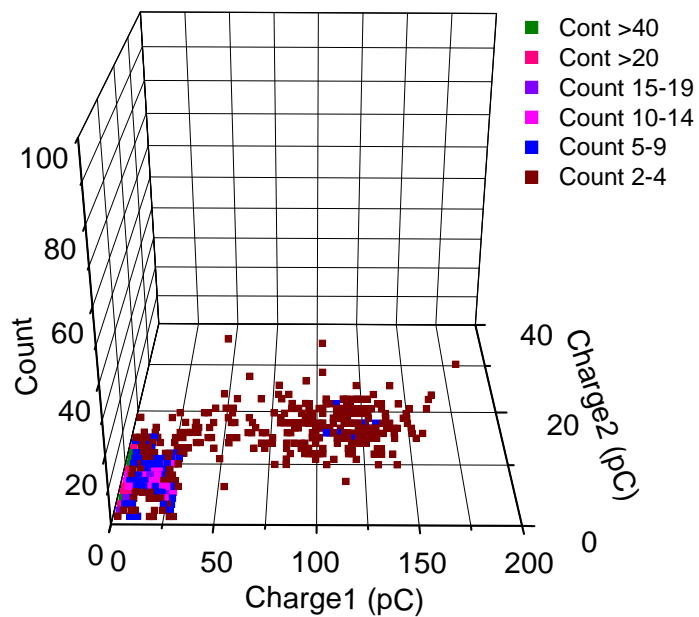
Figure 3.45: Correlation between the charges induced on the pick-up strip placed over the positive electrode (charge1) and that induced on the pick-up strip placed over the negative electrode (charge2). Width of the pick-up strip is 2.5 cm.

3.5.9   Time resolution

The time resolutions of the RPC modules were measured in the same cosmic ray test bench described in section 3.4 using a common start in Phillips Scientific 7186 Time to Digital Converter (TDC). The cosmic ray telescope was constructed using three scintillators, two placed above the RPC and one below. The individual time resolution of each RPC was estimated as follows. The triple coincidence of the signals obtained from the three scintillators was taken as the START signal (master trigger) for the TDC. The STOP signal was taken from a single RPC strip. Figure 3.46 shows the schematic of the time resolution measurement setup [87]. Time calibration was measured as 0.1 ns/channel. The TDC calibration curve is shown in Figure 3.47. There was a offset of 10.7 ns, which was incorporated in all timing measurement.
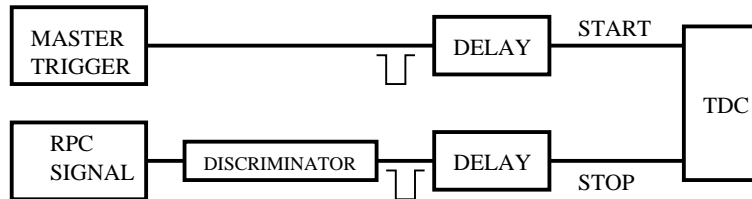
Figure 3.46: Schematic representation of the time resolution measurement setup. A common start in Phillips Scientific 7186 Time to Digital Converter (TDC) was used.
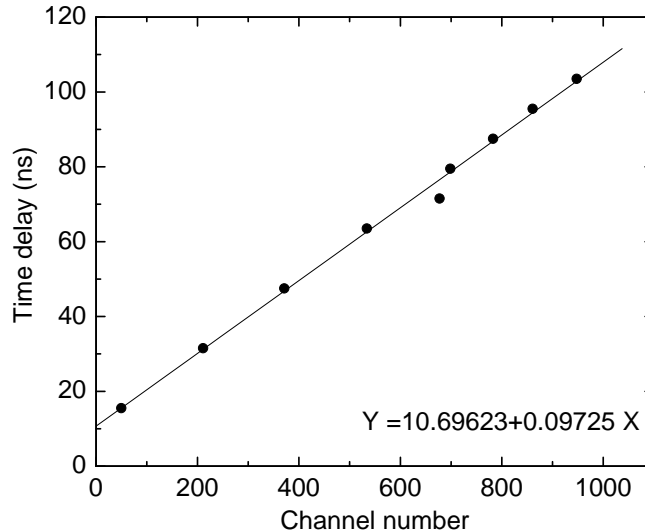
Figure 3.47: The calibration curve of TDC.

80
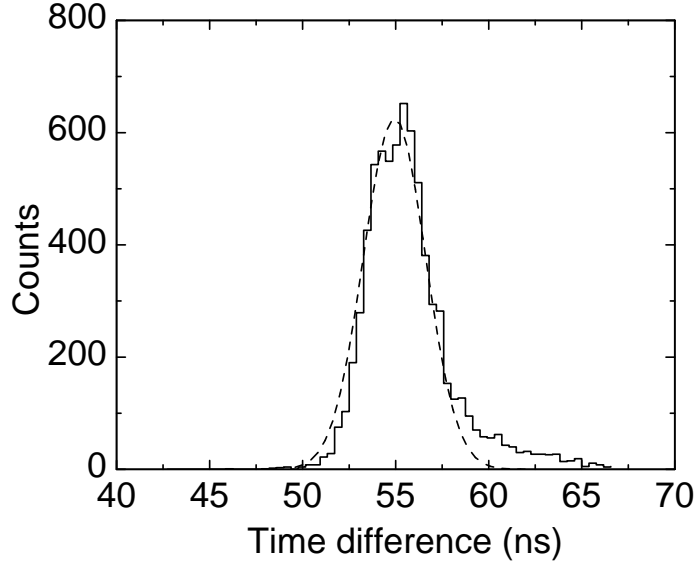
Figure 3.48: The distribution of the time difference between the RPC and the master trigger.

The distribution of the time difference between the master trigger and the signal from one RPC strip is shown in Figure 3.48. From the time difference spectrum, the full width at half maximum (FWHM) and the corresponding standard deviation (σ_{ij}), where i and j refer to scintillators and the RPC, were obtained by fitting a Gaussian function. σ_{ij}'s were similarly obtained for 3 different pairs of the scintillators I, II and III, taking START signal from one and STOP signal from the other. The intrinsic time resolutions of the RPC and the scintillators were obtained from the individual standard deviations σ_i, σ_j, which were extracted by solving the equations: $\sigma_{ij}^2 = \sigma_i^2 + \sigma_j^2$ [33]. Time resolution (FWHM) of the individual scintillators were obtained as: 3.20 ± 0.07 ns (scintillator I), 3.39 ± 0.08 ns (scintillator II) and 1.98 ± 0.02 ns (scintillator III), where the quoted uncertainties include statistical and fitting errors. The extracted time resolution (FWHM) of the RPC at 8 kV operating voltage for a typical run was: 2.48 ± 0.08 ns.

The average signal arrival time (T), taken as the mean position of the fitted Gaussian peak in the time difference spectrum (such as in Figure 3.48) and the time resolution (FWHM) τ of the RPC as a function of the applied high voltage for three 30 cm $\times$ 30 cm RPCs are shown in Figure 3.49 (a) and Figure 3.49 (b) respectively. The measured values of T include the delays introduced in both the START and STOP channels by the electronics shown in Figure 3.46. The time resolution for all the modules improve and the average signal arrival time decreases

81
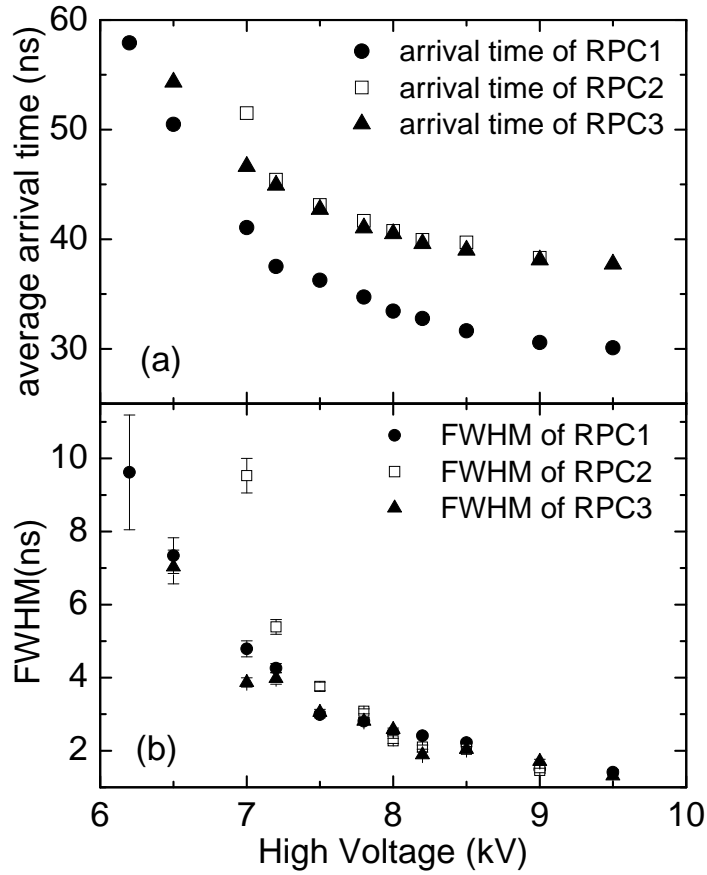
Figure 3.49: (a) The average signal arrival time with respect to the master trigger & (b) the time resolution (FWHM) as a function of the high voltage for three silicone coated RPC modules.

with the increase of high voltage which is common to any gas filled detector. At the plateau region, the time resolution has been found to be ~ 2 ns [87]. The time difference spectra obtained when voltage is gradually increased are shown in Figure 3.50.

Data taken at the time of long term test for the previously mentioned period of more than 130 days at a constant high voltage of 8 kV showed nearly constant values of the time resolution (~ 2-3 ns) and the average signal arrival time (~ 55 ns) as shown in Figure 3.51.

The time resolution between two RPCs was also measured by taking the START signal from one RPC operated at constant voltage (8 kV), while the voltage of the other RPC was varied. The time difference spectra for two different voltages are shown in Figure 3.52. The results are shown in Figure 3.53. In this case, the average time resolution is found to be ~ 3 ns in the plateau region.
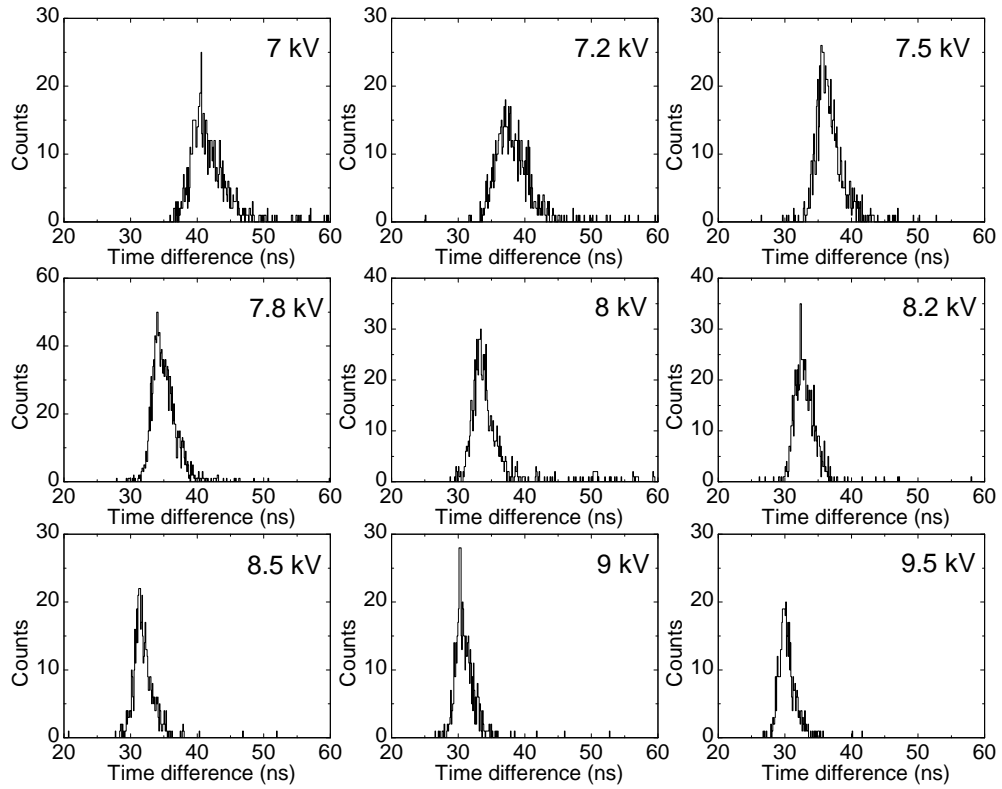
Figure 3.50: The distribution of the time difference between the RPC and the master trigger at different high voltages.
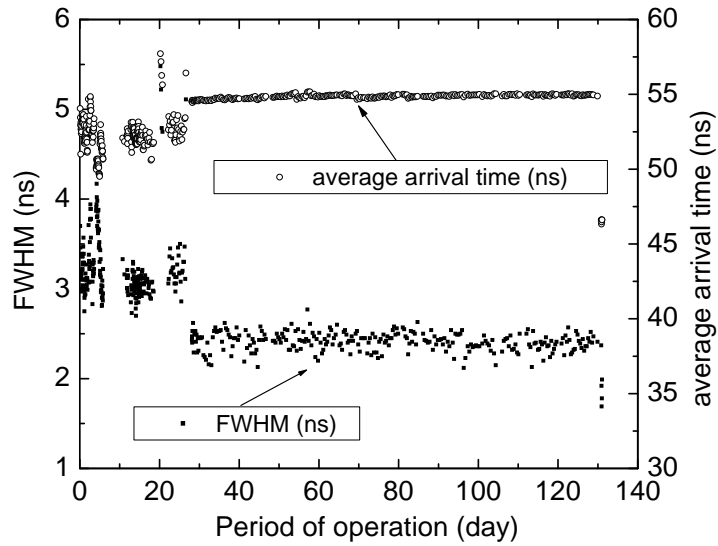
Figure 3.51: The time resolution (FWHM) and the average signal arrival time as a function of period of operation at 8 kV.

83
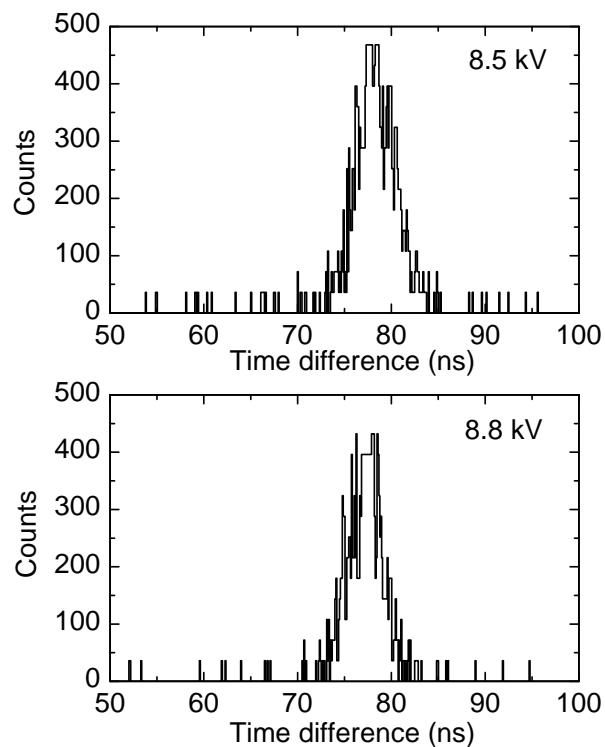
Figure 3.52: The distribution of the time difference between two RPCs at two different high voltages.
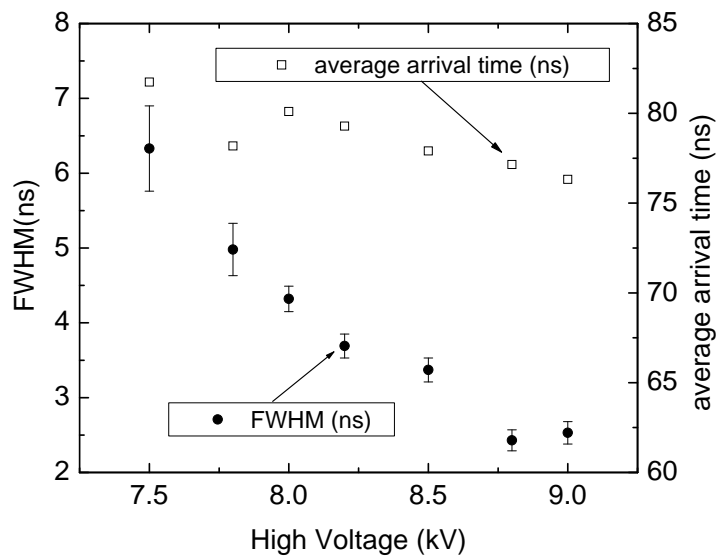
Figure 3.53: The time resolutions (FWHM) and the average signal arrival time of one RPC with respect to another RPC as a function of applied high voltage.

84
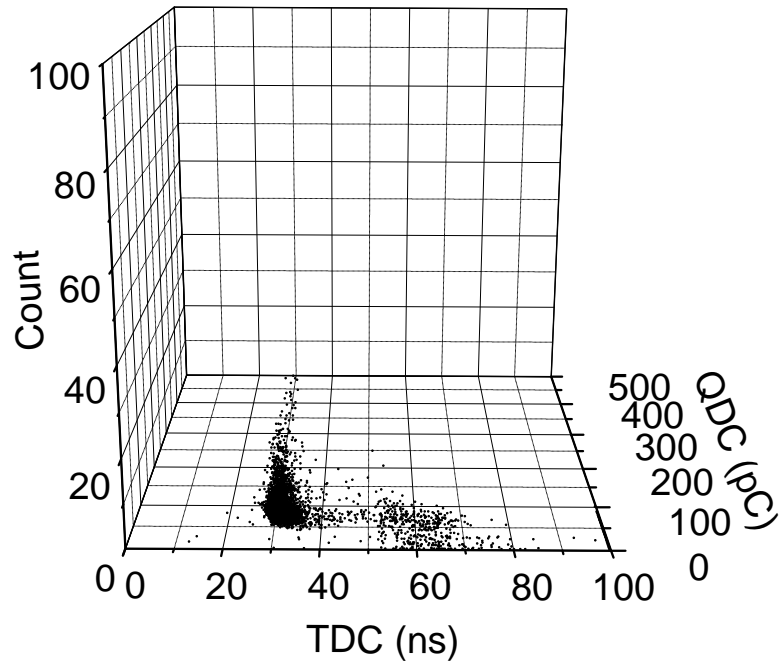
Figure 3.54: X-Y projection of the two dimensional histogram of time and charge correlation for the 30 cm × 30 cm RPC in the streamer mode.
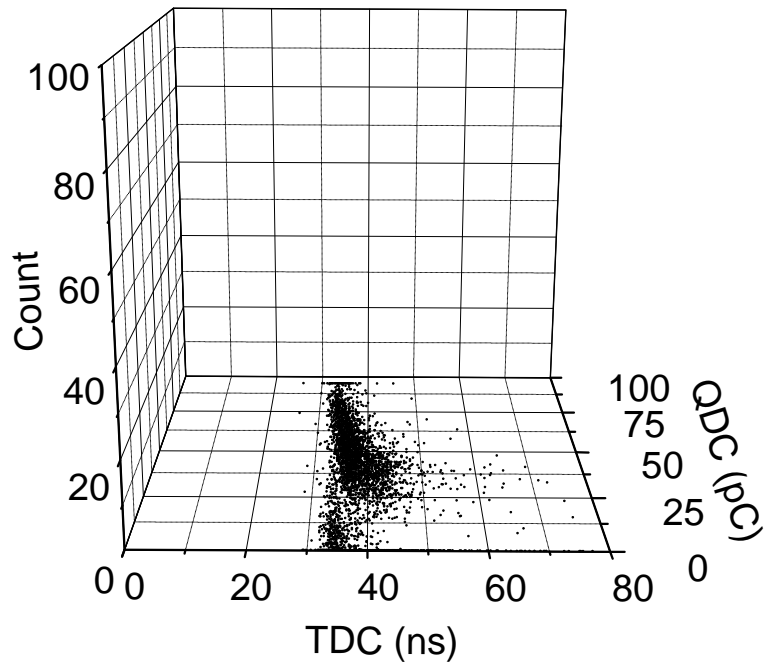
Figure 3.55: X-Y projection of the 2-dimensional histogram of time-charge correlation for the 10 cm × 10 cm RPC.

The time correlated charge spectrum for the 30 cm × 30 cm module at an applied voltage of 8 kV is shown in Figure 3.54. It is clear from the Figure 3.54 that the larger pulses i.e. pulse developed with large induced charges are coming early in time. This effect is also visible in the 10 cm × 10 cm RPC as shown in Figure 3.55 at 9 kV.

The charge correlated time spectrum at 9 kV for the small RPC (10 cm × 10 cm) is shown in Figure 3.56. The time resolution (FWHM) in this particular case is 4.40 ± 0.26 ns and the spectrum shows a tail. From the charge-time correlation data the time spectra are drawn taking different charge slices. The spectra are shown in Figure 3.57. It is clear from the figure that the tail is absent in the time spectrum for larger pulses, as shown in Figure 3.56. The time resolution are also better for the larger pulses as shown in Figure 3.58. In other words the broadening of the time spectrum and the worse time resolution are due to smaller pulses of larger fluctuation.
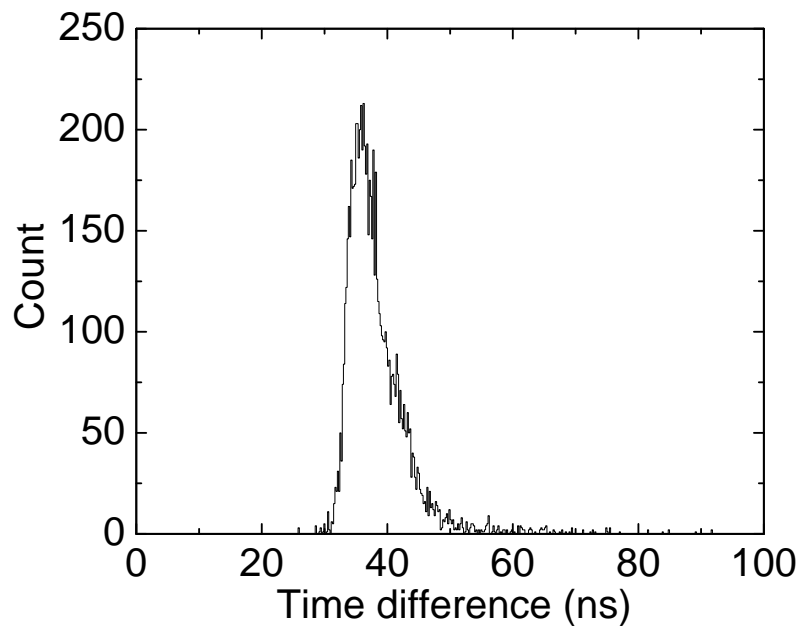
Figure 3.56: Charge correlated time difference spectrum for the 10 cm × 10 cm RPC.
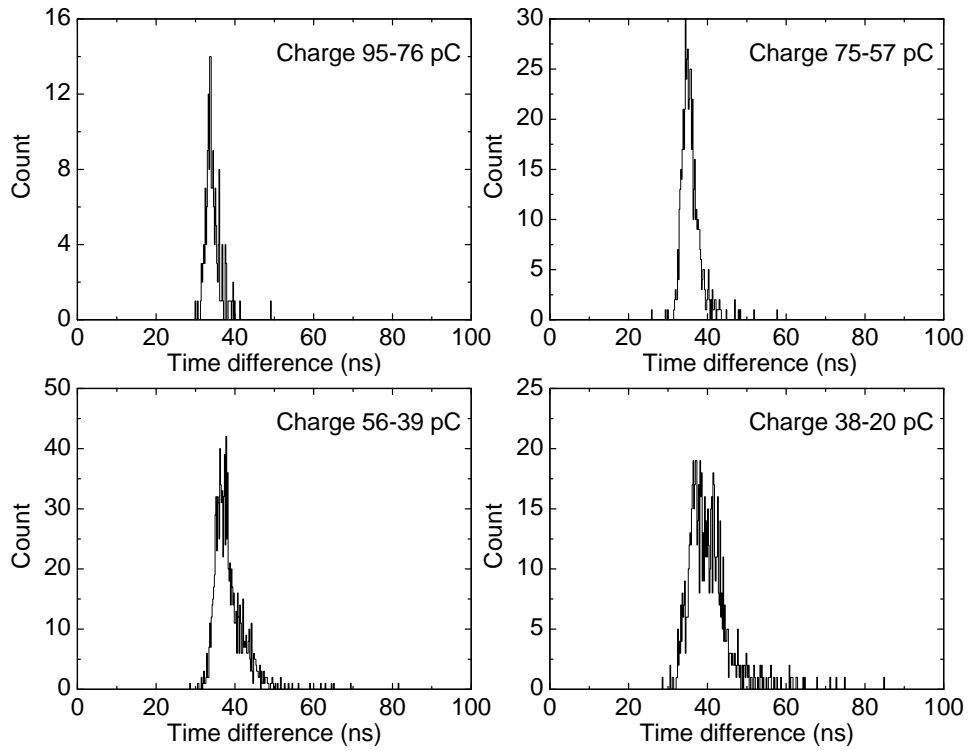
Figure 3.57: Time spectrum taking different charge slice from the 2-dimensional histogram of time-charge correlation for the 10 cm × 10 cm RPC.
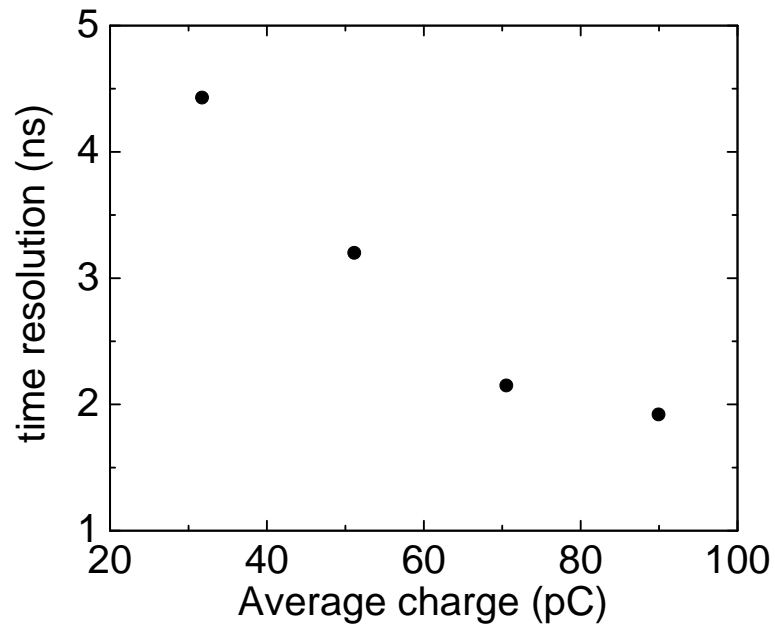
Figure 3.58: Time resolution as function of charge for the 10 cm × 10 cm RPC.

3.5.10   Uniformity of results

The test was performed on different strips of one RPC module at 9.5 kV to study the uniformity of results. The result is shown in Figure 3.59. The figure shows that the efficiency varies between 90-95% or above for different strips while the best time resolution is obtained at the middle of the RPC. The noise rate is different for different strips.
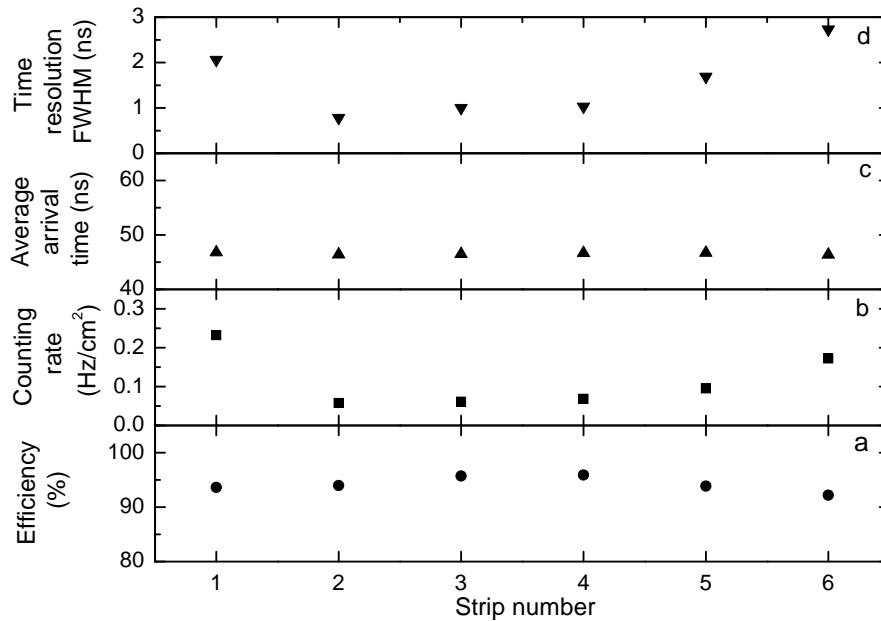
Figure 3.59: (a) Efficiency (b) counting rate, (c) average signal arrival time, and (d) time resolution (FWHM) in six different strips of an RPC at 9.5 kV.

3.5.11   Performance at higher operating voltage

One silicone coated module has been tested for more than 20 days continuously at a voltage of 9.5 kV (higher than normal operating voltage of 8 kV) to test the degradation of performance due to polymerisation of silicone. The result is shown in Figure 3.60. The efficiency and time resolution remained steady at $>95\%$ and <2 ns respectively while the counting rate, though high at the initial stage, gradually stabilized at ~ 0.1 Hz/cm^2.
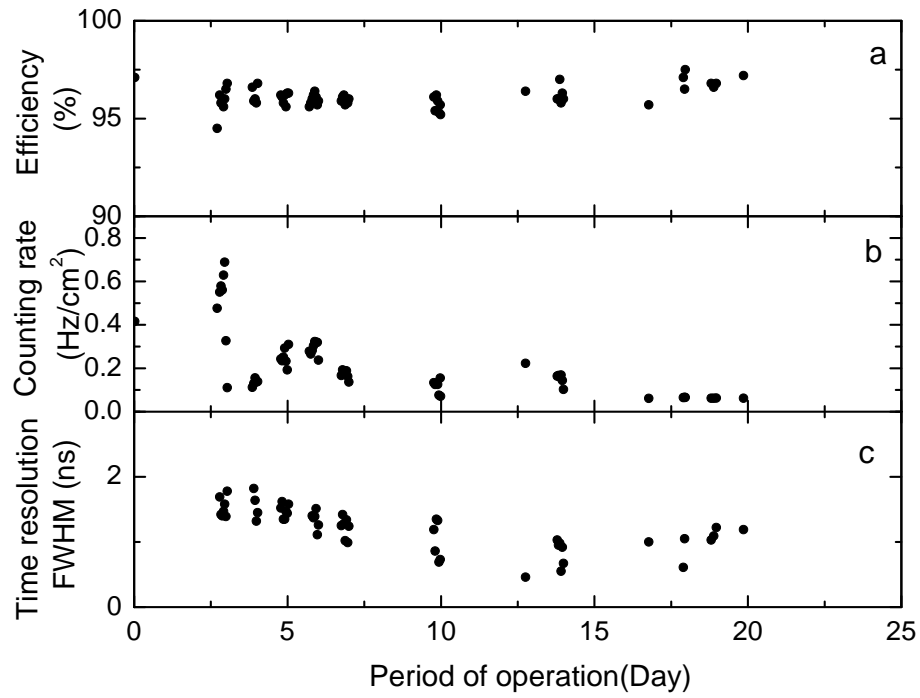
Figure 3.60: (a) Efficiency, (b) counting rate & (c) time resolution (FWHM) as a function of the period of operation for a silicone coated RPC operated at 9.5 kV.

3.5.12 RPC without coating

One module made of 1.6 mm thick P-120 grade bakelite sheets having better surface finish at production has been studied. A 3-D image of AFM scan of 1.6 mm thick P-120 grade bakelite
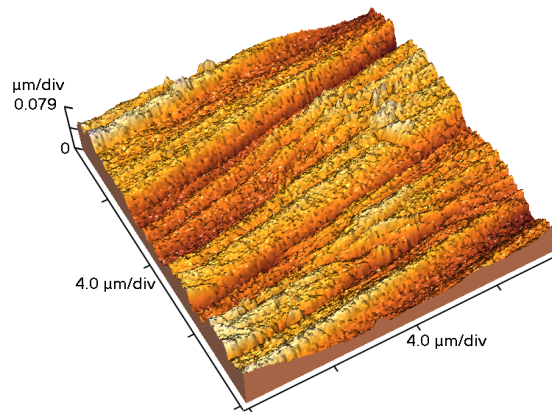
Figure 3.61: AFM image of the P-120 grade bakelite (thickness 1.6 mm) surface morphological structure.

89

Results for Line 6

Line 6

40.0 nm/Div

0.00   4.00   8.00   12.00 µm

Histogram
Height: 78.1 nm

49.0 nm

127. nm

20

10

0

40.0   80.0   120.0 nm

Ra: 90.08 nm
Rq: 25.24 nm

Rp: 46.80 nm
Rv: -50.83 nm

Height Profile

nm
120.0

80.00

40.00

0.00   4.00   8.00   12.00 µm

Power Spectrum

dc

117. nm

0   4   8 (1/µm)
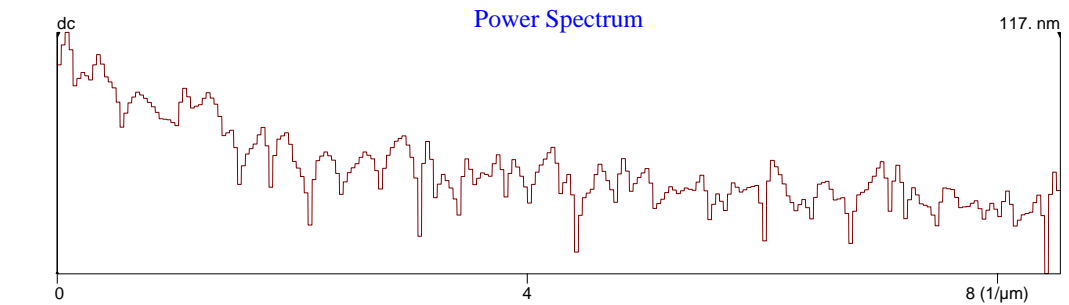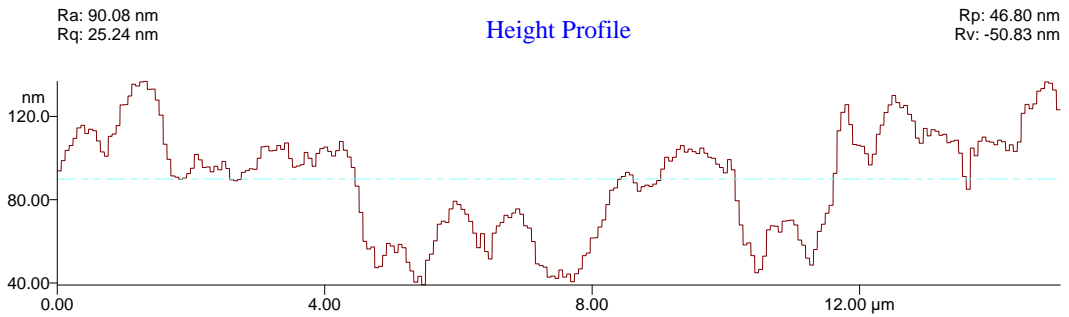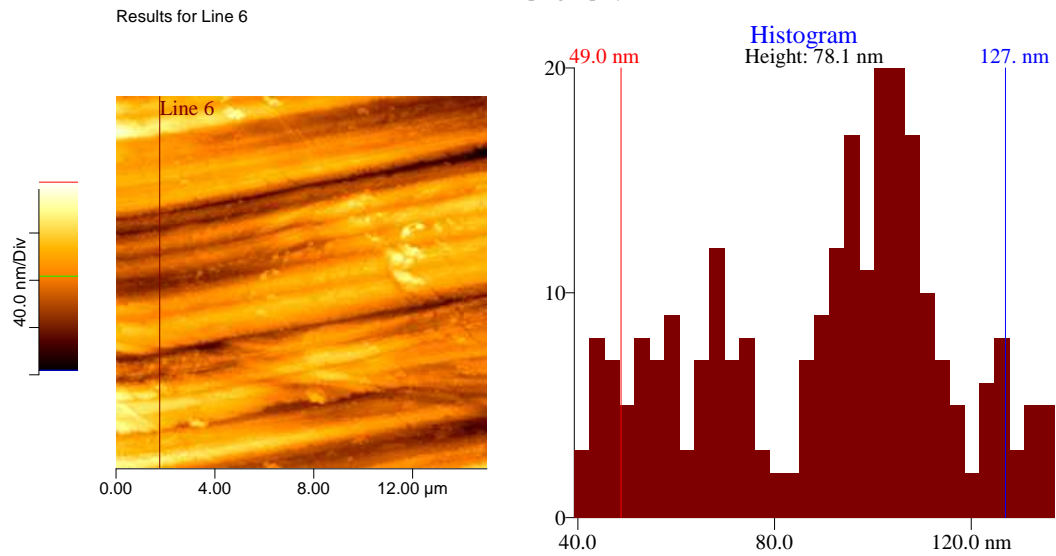
Rp-v	Rms Rough (Rq)	Ave Rough (Ra)	Mean Ht	Median Ht	Arc length	Bearing Ratio
97.62 nm	25.24 nm	21.25 nm	90.08 nm	95.56 nm	15.07 µm	@30.0% 105.18 nm

Bearing Ratio	Peak (Rp)	Valley (Rv)
@80.0% 64.05 nm	46.80 nm	-50.83 nm

Figure 3.62: Topography of AFM data of the P-120 grade bakelite (thickness 1.6 mm) surface morphological structure.

surface is shown in Figure 3.61. The topography of AFM data for the this P-120 grade bakelite surface morphological structure is shown in Figure 3.62. It is clear from Figure 3.62 that the average roughness obtained in the AFM for this 1.6 mm thick P-120 sample is ~ 0.02 μm which is much better than the 2 mm thick P-120 sample as shown in Figure 3.24 of Section 3.5.1. No coating was applied to that RPC [88]. The efficiency curve and the variation of the counting rate with high voltage are plotted in Figure 3.63 (a) and that of the time resolution and the average arrival time with the high voltage are drawn in Figure 3.63 (b). Figure 3.63 (a) shows that an efficiency plateau is obtained at efficiency >90% from 7.5 kV onwards with counting rate comparable to that of the silicone coated RPC. Figure 3.63 shows a time resolution ~ 2 ns at the plateau region. The current (2 μA at 8 kV) for this particular RPC was found to be higher than that of the silicone coated one.
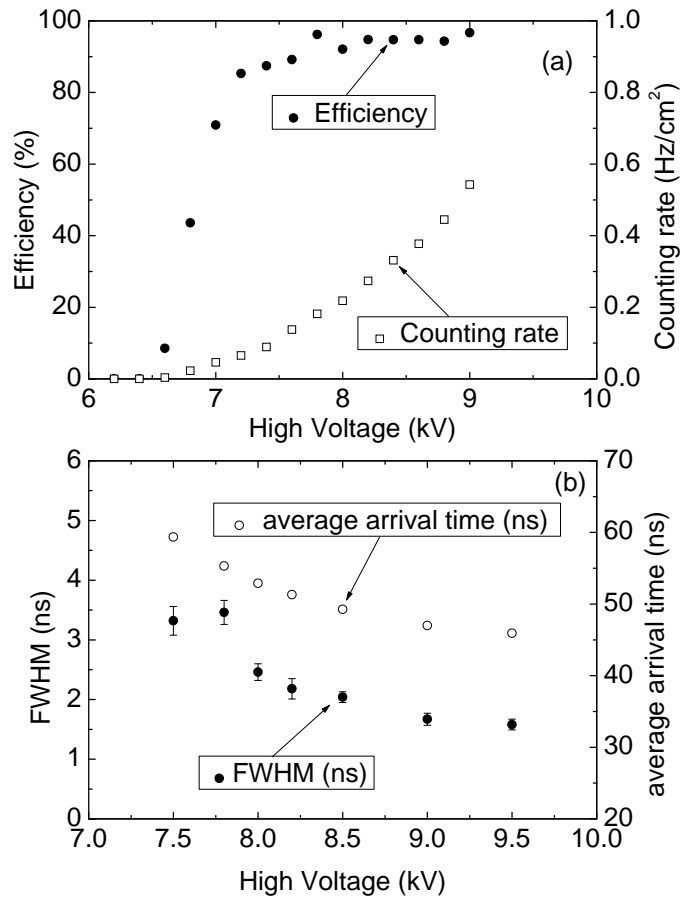
Figure 3.63: (a) The efficiency and the counting rate & (b) the time resolution (FWHM) and the average signal arrival time as a function of high voltage for uncoated P-120 grade bakelite RPC.

91
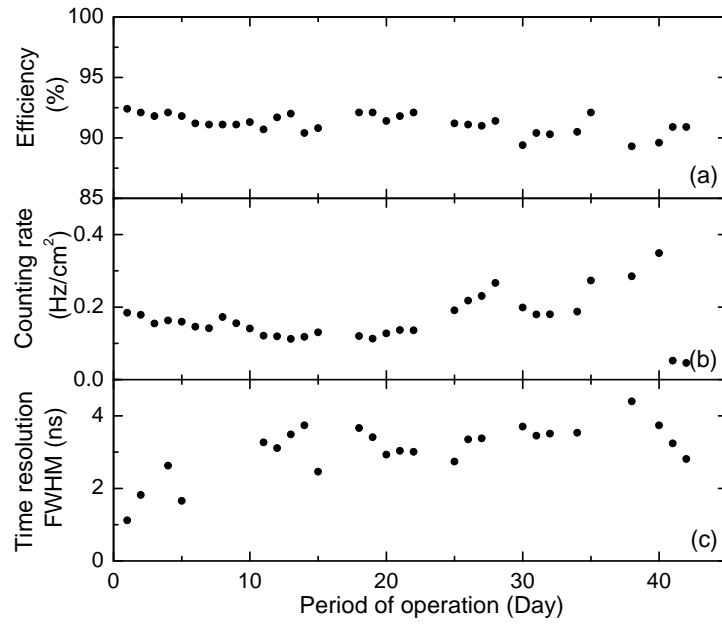
Figure 3.64: (a) Efficiency, (b) counting rate & (c) time resolution (FWHM) as a function of the period of operation for the uncoated RPC. Operating voltage was 8 kV.
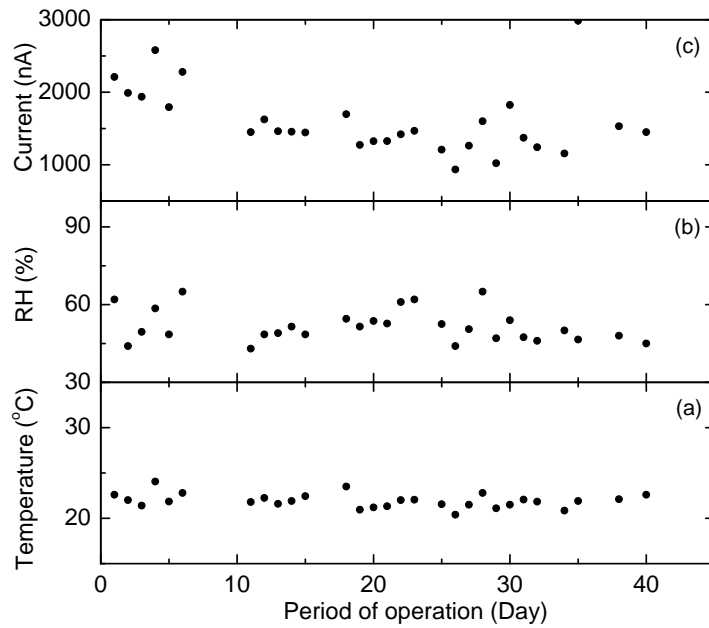
Figure 3.65: (a) Temperature, (b) relative humidity, and (c) current as a function of the period of operation at the time of long term test of the uncoated RPC.

The long term stability test has also been performed for this uncoated RPC in the same cosmic ray test set-up at a high voltage of 8 kV. The test was carried out for a period of more than 40

92

days. The variation of efficiency, counting rate and time resolution (FWHM) with the period of operation are shown in Figure 3.64 (a), Figure 3.64 (b) and Figure 3.64 (c) respectively. The uncoated RPC had worked with an efficiency of $> 90\%$ and remained steady for the above mentioned period. The count rate, was steady at 0.1-0.2 Hz/cm^2. The time resolution varied from 2 ns to 4 ns in this period. The test on this RPC was discontinued after 42 days. Variations of temperature, relative humidity (RH) and current over the above mentioned period are shown in Figure 3.65 (a), (b) and (c) respectively. Current in this module was higher than all the silicone coated modules operated at 8 kV. The operation of this detector for longer period might open up the possibility of developing the RPC without coating.

3.5.13 Variety of silicone coating

Very recently silicone fluid made by Dow Corning (USA) has been used to build the RPC modules and the results such as efficiency, were similar to those obtained from the locally made silicone coated RPC. Dow Corning silicone is a two component material, with one base component and one accelerator. We made one module (dimension: 10 cm $\times$ 10 cm) with only base component (marked unpolymerised) which is similar to the one used in our previous RPC. We have also build a few modules (dimension: 10 cm $\times$ 10 cm) using both the components (marked polymerised) of silicone. The polymerised modules are also giving similar kind of efficiency plateau. Only difference is that the efficiency plateau is reached at a somewhat higher voltage (from 8.2 kV). The variation of current with voltage of one unpolymerised RPC and one polymerised RPC are shown in Figure 3.66 (a) and the variation of efficiency and counting rate as a function of the applied high voltage are shown in Figure 3.66 (b). In both the cases efficiency plateau are obtained above 90%. The current for these Dow Corning silicone coated RPCs were relatively higher than that obtained from the locally made silicone coated RPCs. In this case the count rate was also higher. The variation of time resolution (FWHM) and average signal arrival time as a function of the applied high voltage are shown in Figure 3.66 (c). In both the cases the arrival time is decreasing with the high voltage, but the time resolution is somewhat better in unpolymerised sample.

The long term stability of the unpolymerised RPC and one polymerised RPC were tested using the same cosmic ray stand at 8.5 kV. The average pulse height for both the modules were $\sim$ 100-150 mV. The threshold of the RPC signals were set at -20 mV for both the modules.
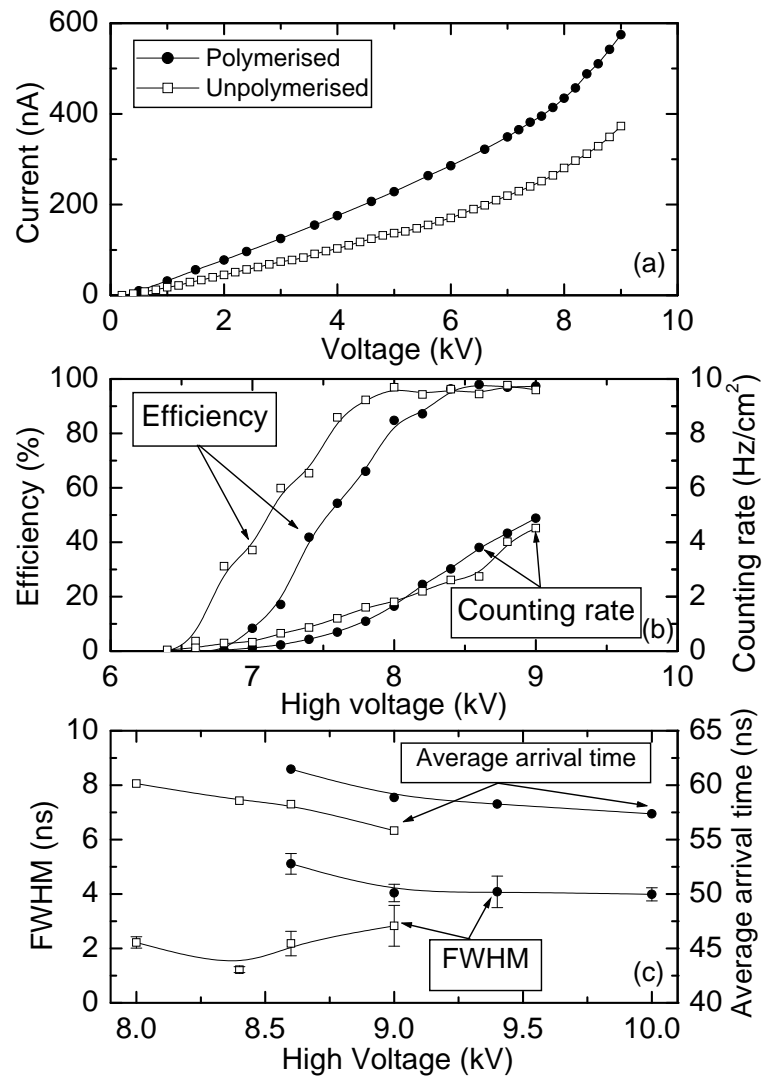
Figure 3.66: (a) Current as a function of the applied voltage, (b) efficiency and counting rate & c) time resolution (FWHM) and average signal arrival time as a function of high voltage for one unpolymerised and one polymerised RPC modules.

The unpolymerised module was tested for more than 70 days. The results (efficiency, counting rate, time resolution) of long term stability test of the unpolymerised RPC are shown in Figure 3.67 (a), (b), and (c) whereas the temperature, relative humidity and current recorded during the period of operation are shown in Figure 3.68 (a), (b), and (c).
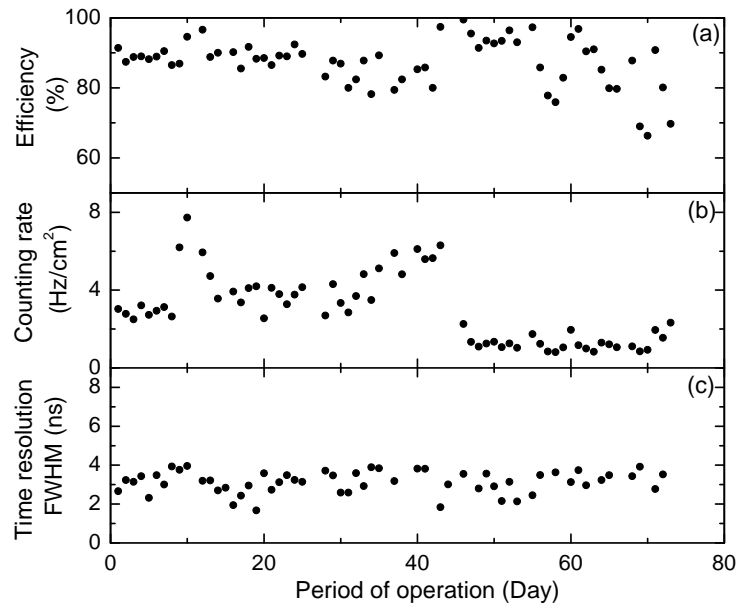
Figure 3.67: (a) Efficiency, (b) counting rate & (c) time resolution (FWHM) as a function of the period of operation for the unpolymerised RPC. Operating voltage was 8.5 kV.
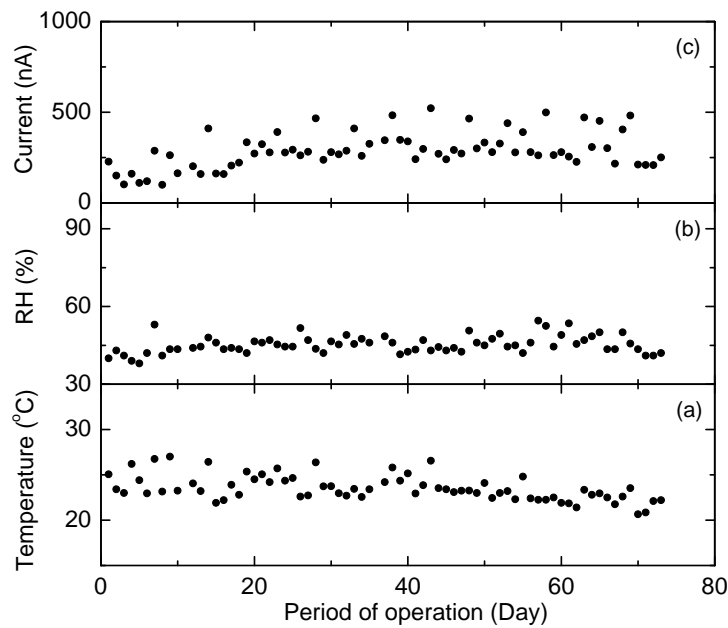
Figure 3.68: (a) Temperature, (b) relative humidity, and (c) current as a function of the period of operation at the time of long term test of the unpolymerised RPC.

The polymerised module was operated for more than 40 days. The results (efficiency, counting rate, time resolution) of long term stability test of the polymerised RPC are shown in Figure 3.69 (a), (b), and (c) while the temperature, relative humidity and current recorded during
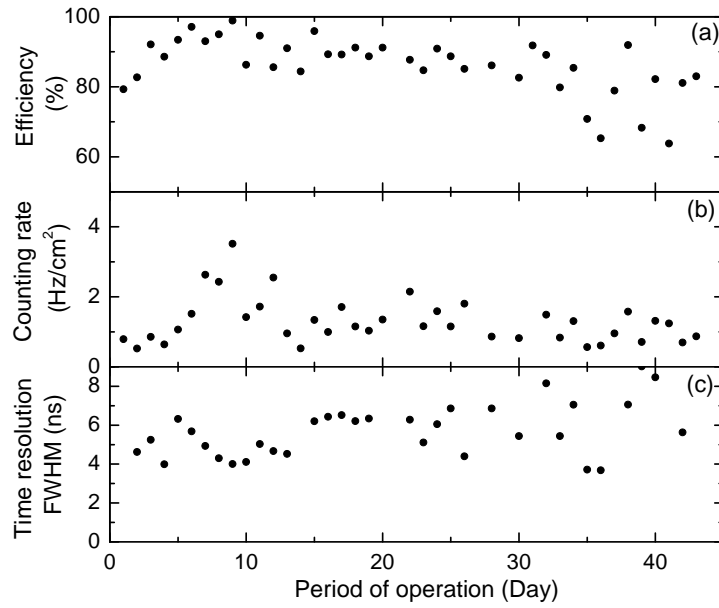
Figure 3.69: (a) Efficiency, (b) counting rate & (c) time resolution (FWHM) as a function of the period of operation for the polymerised RPC. Operating voltage was 8.5 kV.
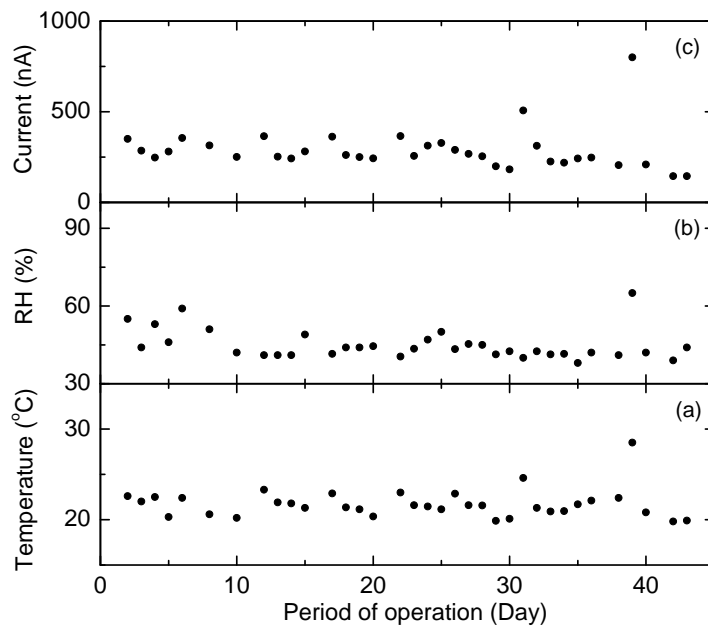
Figure 3.70: (a) Temperature, (b) relative humidity, and (c) current as a function of the period of operation at the time of long term test of the polymerised RPC.

the period of operation are shown in Figure 3.70 (a), (b), and (c). In the long term test the average efficiency obtained in both the modules were $\sim 87\%$ and also the efficiency decreased a little at the last part of the measurement. It has been observed that the efficiency recovered

with proper conditioning of both the detectors such as slowly increase of the bias, operation at proper environmental condition etc. A systematic long term study is still necessary in order to fully characterize these two modules.

3.6 Results in avalanche mode of operation

Though our main goal is to operate the RPCs in streamer mode, we have also tested one 10 cm × 10 cm and one 30 cm × 30 cm silicone coated modules in avalanche mode for comparing the performance. Silicone used in these two modules was manufactured by Metroark Limited. In avalanche mode, a passing charged particle produces a small amount of charge (~ 1 pC) in the gas, which allows the RPC to recover in a relatively shorter time to handle high counting
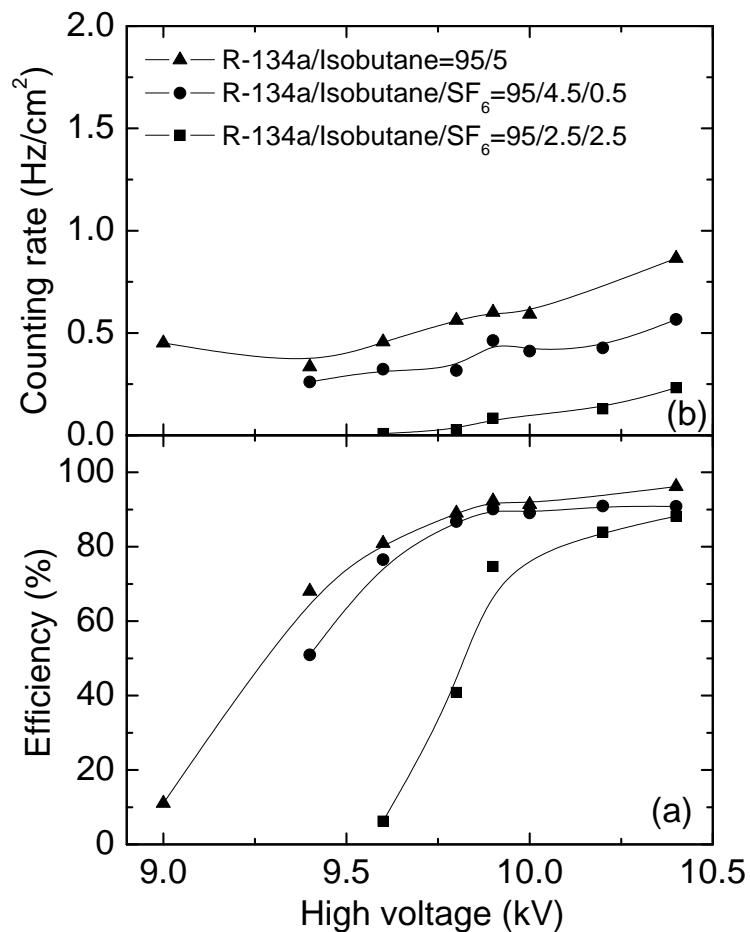
Figure 3.71: (a) Efficiency & (b) counting rate as a function of the applied high voltage for a silicone coated RPC, operated in avalanche mode using three different gas mixtures.

rates ($\sim$ 1 kHz/cm^2). Ageing effects caused by the accumulated charge is also relatively less in this mode.

Several gas mixtures such as R-134a/Isobutane in 95/5 and R-134a/Isobutane/SF$_6$ in 95/4.5/0.5, 95/2.5/2.5, 92/3/5 ratio have been used in the avalanche mode. The effect of streamer quenching by SF$_6$ was also studied.

The efficiency and the counting rate (noise rate) of the RPCs are studied by varying the applied high voltage. The variation of the efficiency and counting rate with the applied high voltage for the gas mixtures of R-134a/Isobutane in 95/5 and R-134a/Isobutane/SF$_6$ in 95/4.5/0.5, 95/2.5/2.5 ratio are shown in Figure 3.71 (a) and 3.71 (b) respectively for the 30 cm $\times$ 30 cm
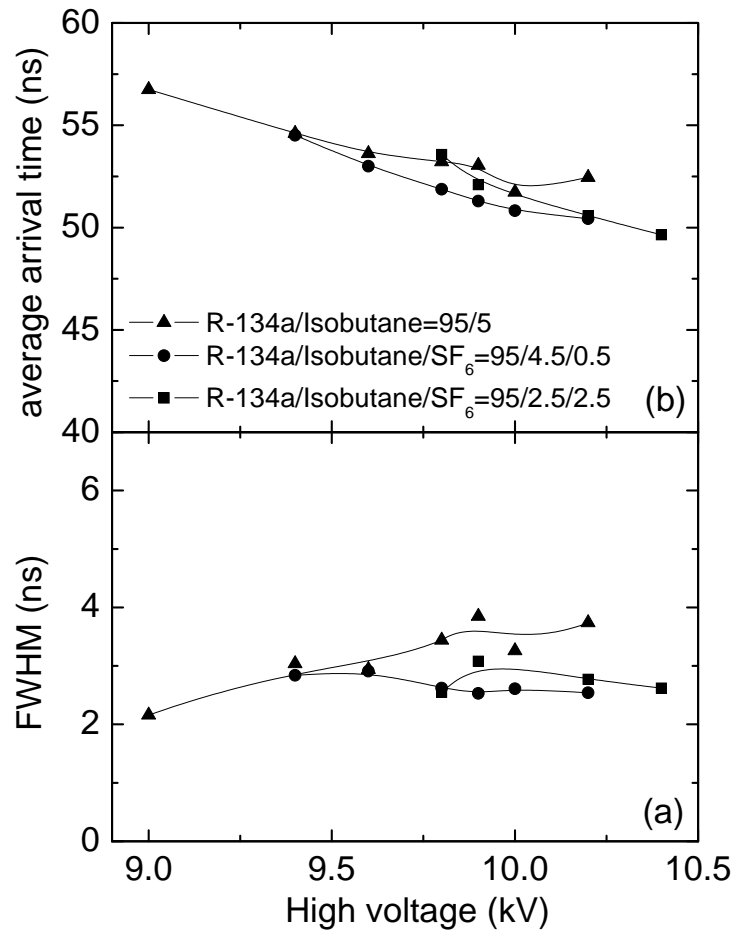
Figure 3.72: (a) Time resolution (FWHM) & (b) average signal arrival time with respect to the master trigger as a function of applied high voltage for a silicone coated RPC in avalanche mode using three different gas mixtures.

98

RPC. While the efficiency plateau was obtained at around 90% or more for all the gas mixtures and the value was marginally higher for a gas mixture with less amount of SF_6. The count rate decreases with the increase of the fraction of SF_6 as it quenches the streamer more.

The time resolution (FWHM) of the RPC operated in avalanche mode was measured for cosmic rays. The average signal arrival time (T) with respect to the master trigger and the time resolution (FWHM) τ of the RPC as a function of the applied high voltage are shown in Figure 3.72 for three gas mixtures. For all the gas mixtures the average signal arrival time decreases and the time resolution improves with the increase of applied high voltage. The time resolution (FWHM) was found to be around 2-3 ns.

In Figure 3.73, a typical charge spectrum of the RPC operated in the avalanche mode (HV = 9.6 kV) using the gas mixture of R-134a/Isobutane/SF_6 in 95/4.5/0.5 ratio, together with the Polya distribution fitting curve is shown. Figure 3.74 shows the charge distributions at different high voltages for a gas mixture of R-134a/Isobutane in 95/5 ratio whereas in Figure 3.75 and Figure 3.76 those distributions are shown for the gas mixtures of R-134a/Isobutane/SF_6 in 95/4.5/0.5 and 95/2.5/2.5 mixing ratio respectively.
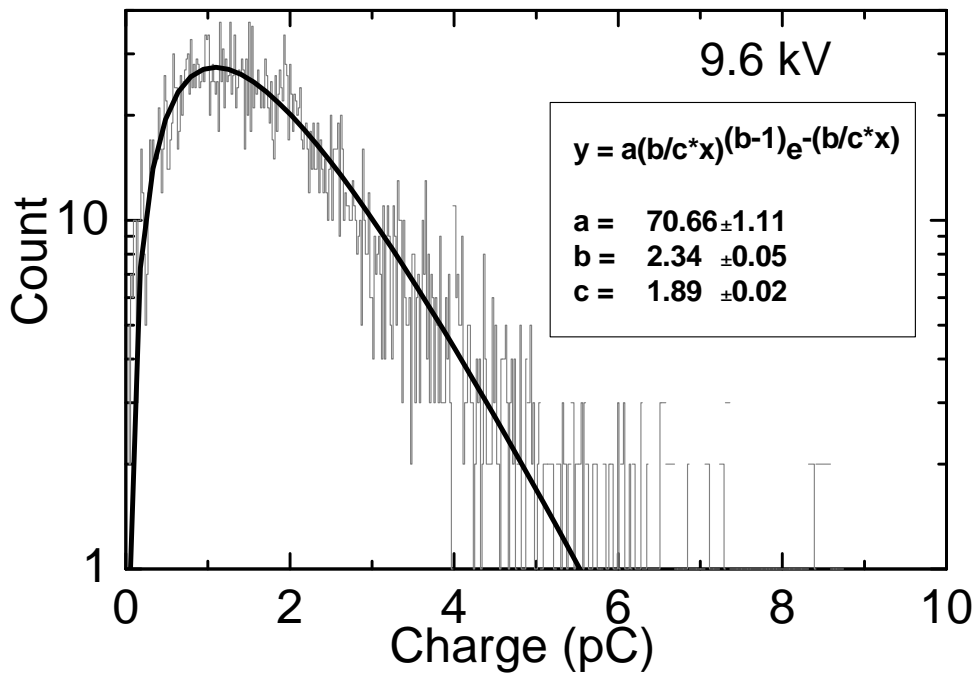
Figure 3.73: The charge spectrum of the RPC operated in the avalanche mode using the gas mixture of R-134a/Isobutane/SF_6 in 95/4.5/0.5 ratio, at 9.6 kV.
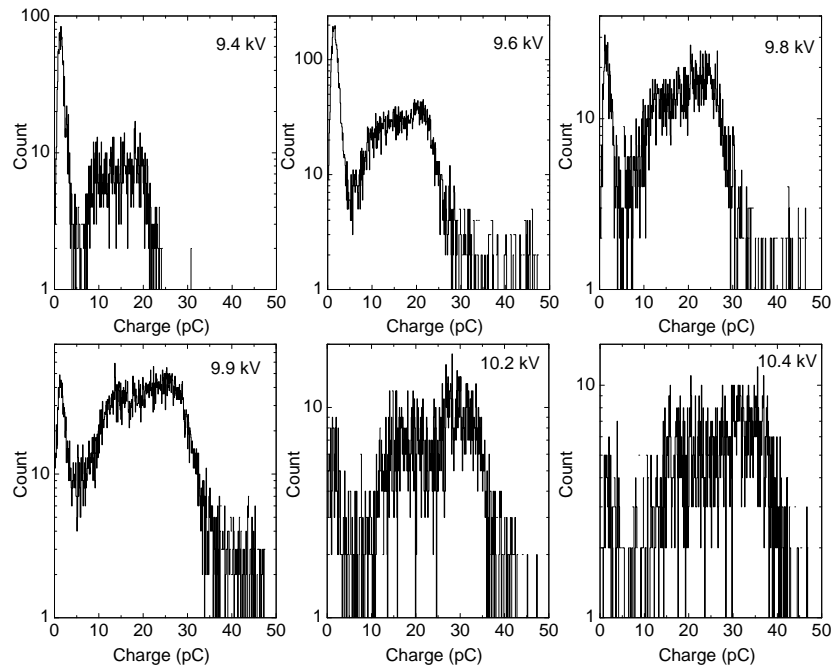
Figure 3.74: The distribution of charge at different high voltages for the gas mixture R-134a/Isobutane =95/5.
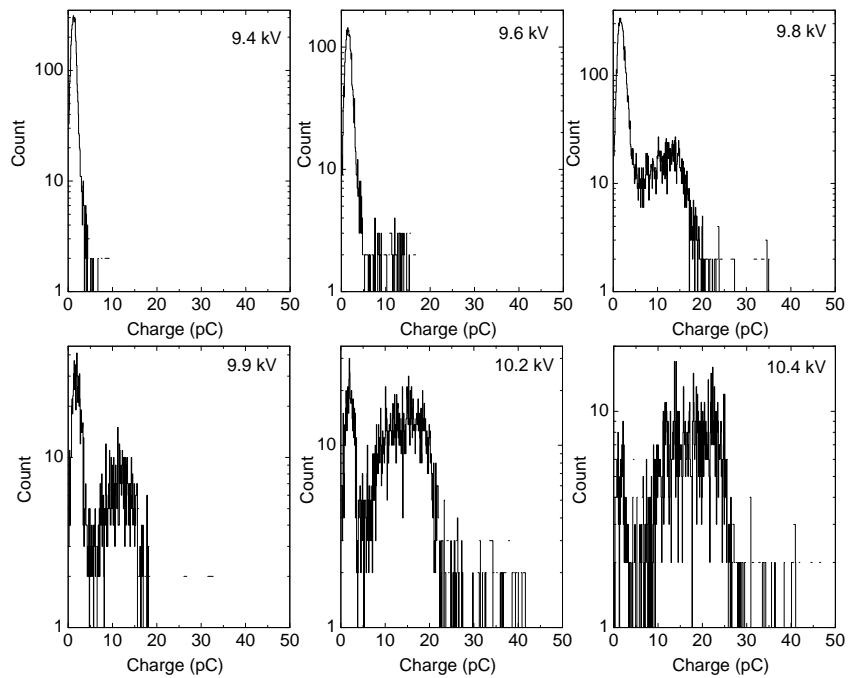
Figure 3.75: The distribution of charge at different high voltages for the gas mixture R-134a/Isobutane/SF$_6$=95/4.5/0.5.
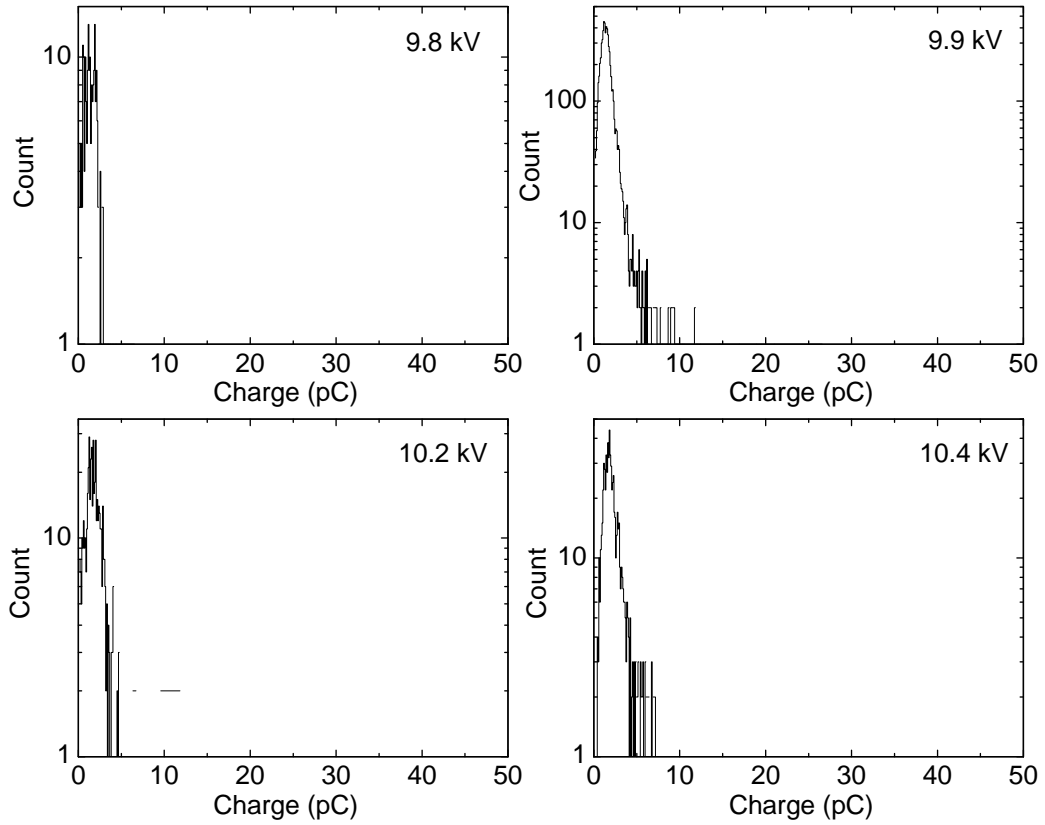
Figure 3.76: The distribution of charge at different high voltages for the gas mixture R-134a/Isobutane/SF$_6$=95/2.5/2.5.

In Figure 3.77, the variation of the induced charge in avalanche mode as a function of the applied high voltage is shown for the gas mixtures of R-134a/Isobutane in 95/5 and R-134a/Isobutane/SF$_6$ in 95/4.5/0.5, 95/2.5/2.5 ratio. It is clear from the figure that in all cases avalanche charges saturate at $\sim$ 1.5 pC. It is also noted from Figure 3.74 and Figure 3.75 that with the increase of the applied high voltage a streamer signal is coming after the avalanche and the streamer pulse is the most dominant at the higher voltages. The variation of the amount of streamer charges with the applied high voltage for those two gas mixtures are shown in Figure 3.78. The amount of streamer charge decreases i.e. the streamer quenches with the introduction of SF$_6$. The variation of the ratio of the area under the streamer peak and the avalanche peak as a function of the applied high voltage is shown in Figure 3.79. This ratio also decreases with the introduction of SF$_6$.
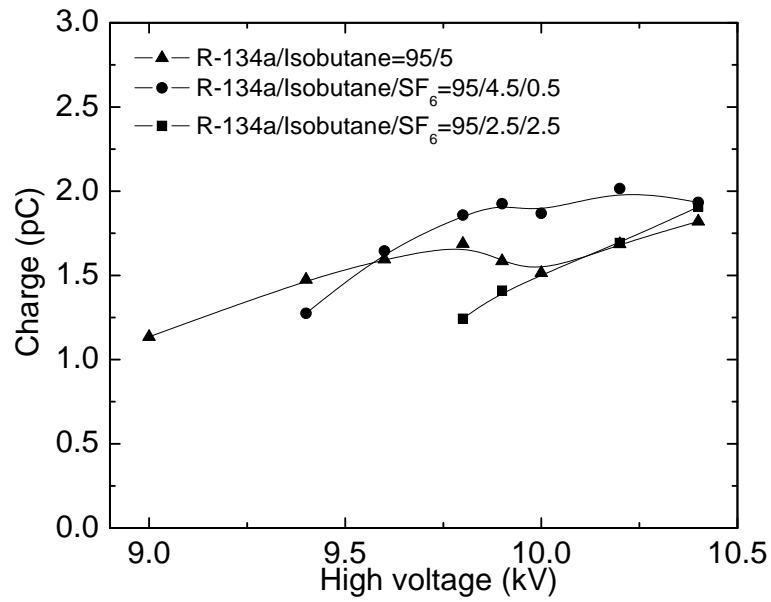
Figure 3.77: Average charge as a function of the applied high voltage in the avalanche mode for three different gas mixtures.
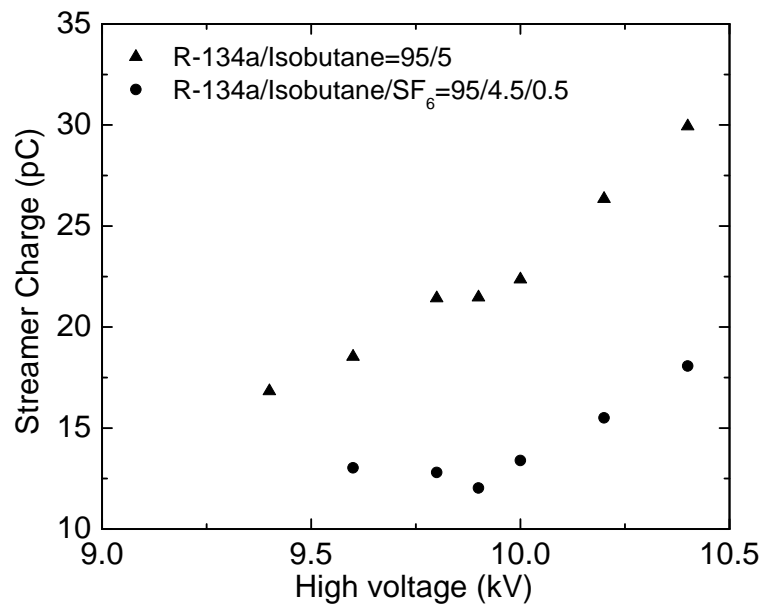
Figure 3.78: Charge from streamer fraction as a function of the applied high voltage in the avalanche mode for the gas mixtures R-134a/Isobutane =95/5 and R-134a/Isobutane/SF$_6$=95/4.5/0.5.
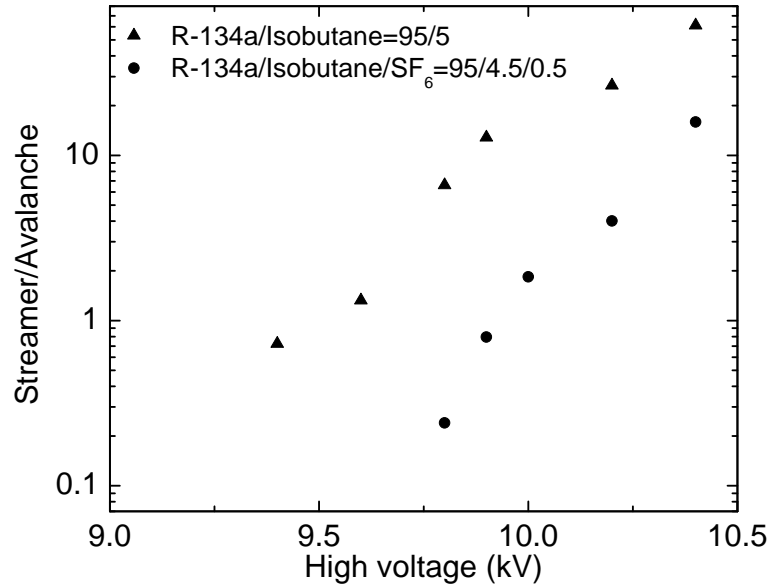
Figure 3.79: The ratio of the area under the streamer peak and the avalanche peak as a function of the applied high voltage in the avalanche mode for the gas mixtures of R-134a/Isobutane =95/5 and R-134a/Isobutane/SF$_6$=95/4.5/0.5.

A gas mixture of R-134a/Isobutane/SF$_6$=92/3/5 has also been used to see the effect of quenching by SF$_6$. For this typical gas mixture the variation of the efficiency and counting rate with the applied high voltage are shown in Figure 3.80 (a) and 3.80 (b) respectively. In this case efficiency above 90% comes only after 11.5 kV.

In the voltage range of 11.5 to 12 kV the measured average signal arrival time with respect to the master trigger and the time resolution (FWHM) of the RPC as a function of the applied high voltage are shown in Figure 3.81 for the gas mixture of R-134a/Isobutane/SF$_6$=92/3/5. Like the previous case the average signal arrival time decreases and the time resolution improves with the increase of applied high voltage. The time resolution (FWHM) was found to be around $\sim$2 ns.

The charge distributions at high voltages above which it attaining efficiency $>$ 80% for this gas mixture are shown in Figure 3.82 and the variation of the induced charge as a function of the applied high voltage is shown in Figure 3.83. The charge spectra shown in Figure 3.82 are very similar to Figure 3.76, except that the spectra for the gas mixture of R-134a/Isobutane/SF$_6$=92/3/5 shown in Figure 3.82 come at higher voltages where also high efficiency is achievable. That is most of the signals are quenched by SF$_6$ and at lower voltage not many signals are in coincidence with the trigger.

103
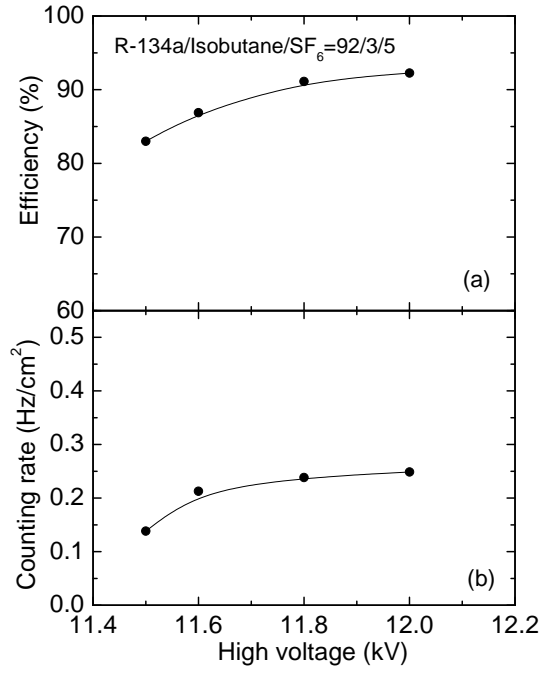
Figure 3.80: (a) Efficiency & (b) counting rate as a function of the applied high voltage for a silicone coated RPC, operated in avalanche mode using R-134a/Isobutane/SF$_6$=92/3/5 ratio.
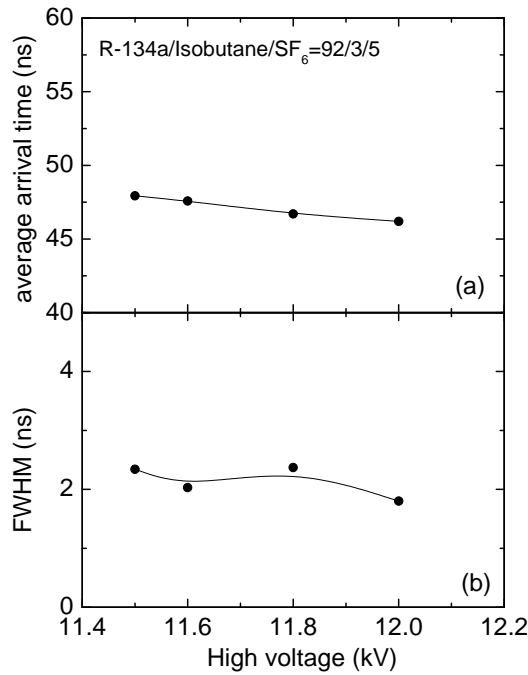
Figure 3.81: (a) Time resolution (FWHM) & (b) average signal arrival time with respect to the master trigger as a function of applied high voltage for a silicone coated RPC, operated in avalanche mode using R-134a/Isobutane/SF$_6$=92/3/5 ratio.
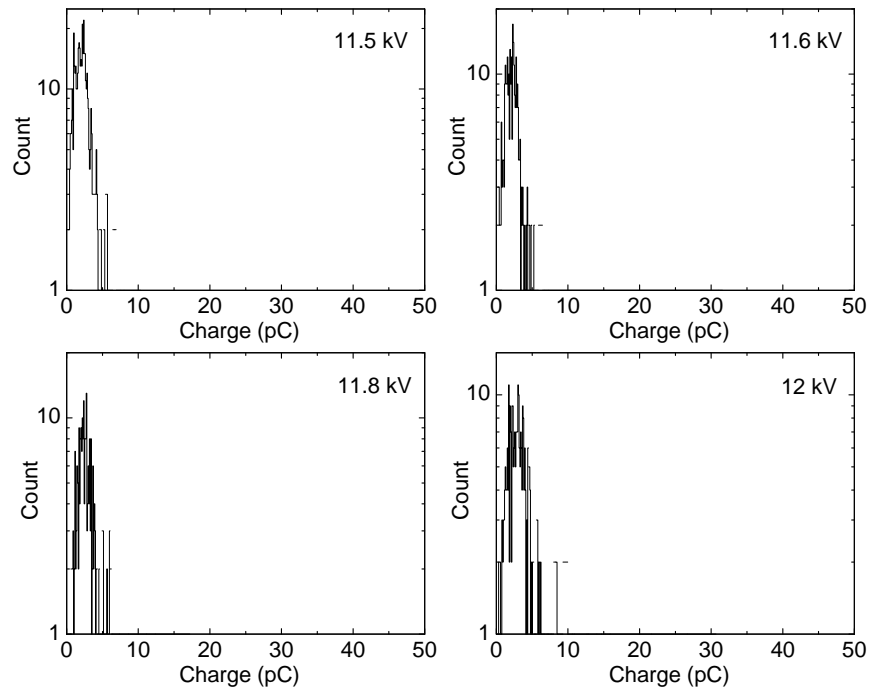
Figure 3.82: The distribution of charge at different high voltages for the gas mixture R-134a/Isobutane/SF$_6$=92/3/5.
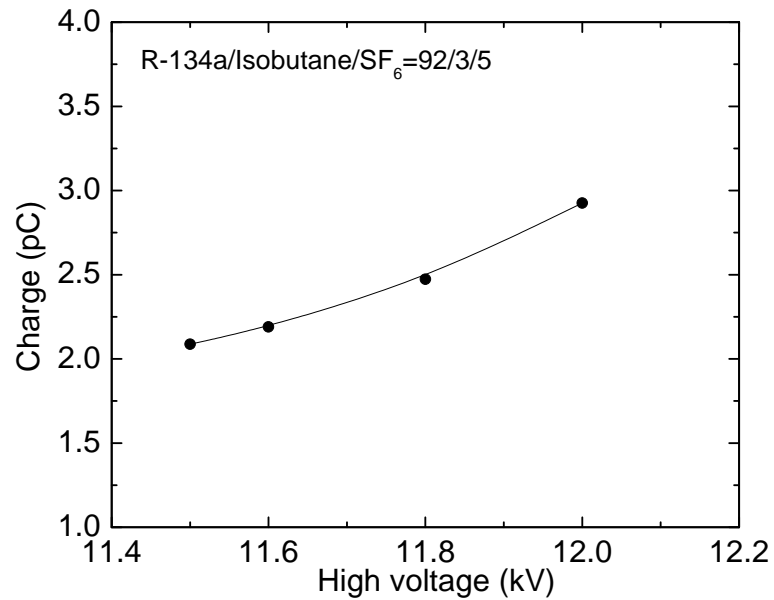
Figure 3.83: Average charge as a function of the applied high voltage in the avalanche mode for the gas mixture R-134a/Isobutane/SF$_6$=92/3/5.

3.6.1 Tests in GIF at CERN in avalanche mode

After preliminarily tests in both streamer mode (with a gas mixture of argon, R-134a and isobutane in 55/37.5/7.5 volume ratio) and avalanche mode (with a gas mixture of R-134a/Isobutane/SF_6 in 95/4.5/0.5 volume ratio) in India one 10 cm $\times$ 10 cm silicone coated chamber was shipped to CERN where new tests have been carried out [89]. The module was sent to CERN to test the effect of high rate. A separate cosmic stand has been built (Figure 3.84), using two little scintillators in coincidence. At CERN the CMS standard gas mixture (95.7% $C_2H_2F_4$ - 4.0% Iso-C_4H_{10} - 0.3% SF_6 humidified at about 40%) has been used and a high voltage of 10 kV has been applied. An online current monitoring and recording system was also set up in order to test the long term stability. After these preliminary tests at the ISR (Intersecting Storage Ring) cosmic stand, the small prototype was moved to the GIF (Gamma Irradiation Facility, CERN) where a 137 Cesium source was irradiating the environment. During this installation the mechanical support for the chamber and set up for online monitoring of radiation, current and environmental parameters such as temperature, pressure, humidity etc. were developed in order to keep track of the chamber performance and environmental changes.

Figure 3.84: Experimental setup at CERN.

This prototype has readout strips in x-y axis, this means that one is able to locate in the two dimensional space where the chamber was fired by the muons. A software that is able to reproduce a coincidence between two readout strips was developed, in order to obtain the lego plot as shown in (Figure 3.85). Though the event distribution is not constant, there are no dead zone, so the efficiency is homogeneous all over the chamber.
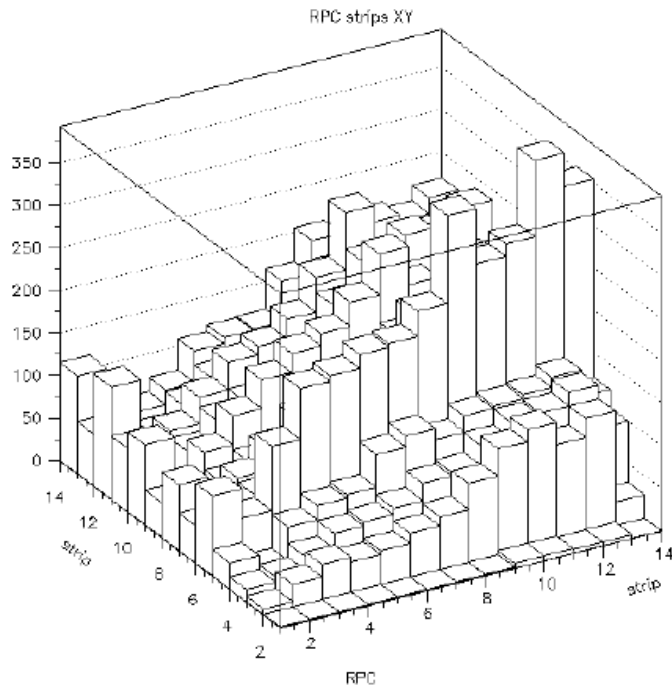
Figure 3.85: Surface plot of the small prototype.

An efficiency scan performed earlier in India, reached full efficiency at around 10 kV as as shown in Figure 3.86. The same test has been performed with CMS standard gas mixture once the chamber arrived at CERN.

At the ISR Forward RPC Lab, the chamber, in the cosmic stand reached full efficiency as we can see in Figure 3.87. The prototype chamber is then installed in the CERN GIF experimental area, in order to irradiate with a gamma source and the chamber performances are monitored. During two months the chamber was irradiated with a nominal photon flux of $5.109m^-2s^-1$. The current and high voltage as well as environmental parameters and gas parameters were
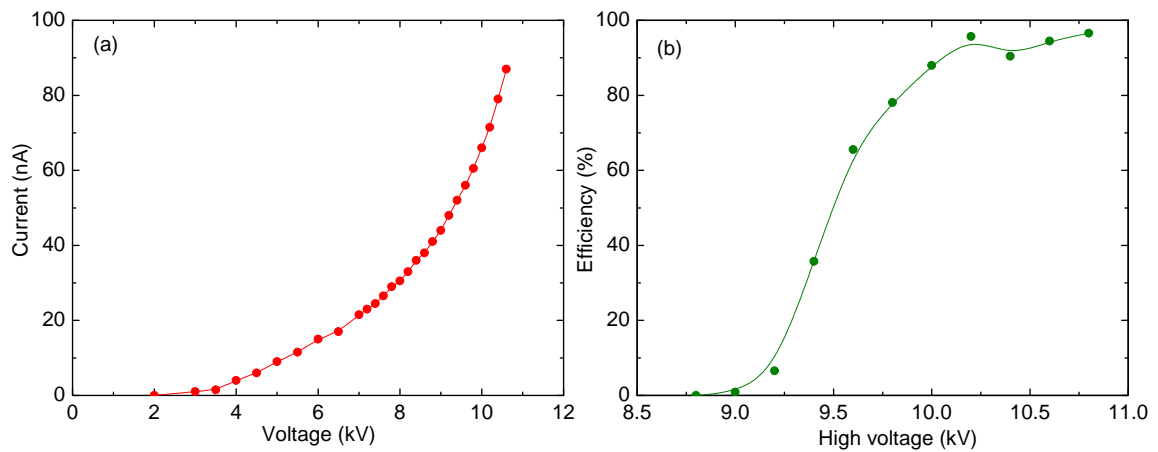
Figure 3.86: (a) I-V plot and (b) efficiency plot with a gas mixture of R-134a/Isobutane/SF_6 in 95/4.5/0.5 ratio.
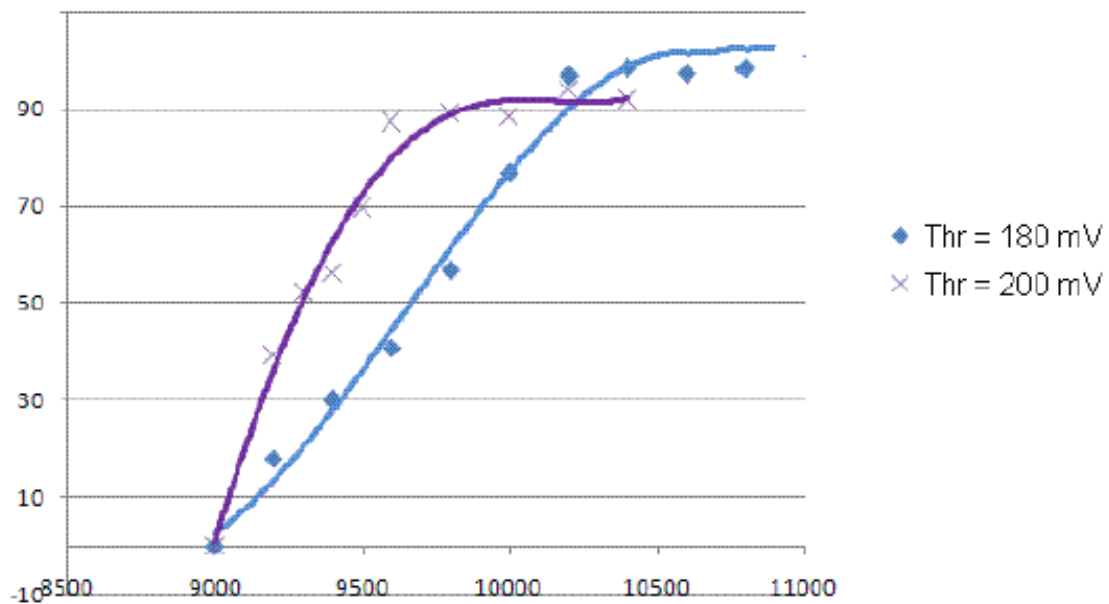
Figure 3.87: Efficiency as a function of high voltage with CMS standard gas mixture.

recorded. After the irradiation, the chamber was reinstalled in the CERN ISR cosmic stand in order to compare the performances before and after the irradiation. Preliminary results show that chamber behavior did not change with radiation exposure. A systematic long term study has to be done in order to fully characterize this promising new kind of silicone coated bakelite RPC.

3.7 Summary and outlooks

In summary, the locally made bakelite pieces are used to build RPCs of different size (10 cm × 10 cm, 30 cm × 30 cm). Well defined procedures are laid down on RPC construction. It appeared that study of surface properties lead better understanding of the performance of the detectors. The RPC which can satisfy required criteria to be used in ICAL needs several characteristics. Those properties of the bakelite RPCs are studied in a systematic way. The characteristic features of the study are as follows: (a) For a matt-finished P-120 grade bakelite, a thin coating of silicone fluid is necessary for stable performance, for glossy finished surface, the detector seems to be stable even without coating. The decrease of the surface resistivity is helping to replenish the field after each ionisation cluster formation by reducing the effect of space charge, which is another reason behind this kind of coating on bakelite. The decrease of the surface resistivity is helping to replenish the field after each ionisation cluster formation by reducing the effect of space charge, which is another reason behind this kind of coating on bakelite. (b) The gas mixture of argon, tetrafluroethane (R134a) and isobutane in 55/37.5/7.5 volume ratios allows streamer mode operation with > 90% efficiency at around a high voltage of 8 kV. (c) The threshold, environmental conditions are optimized for long term operation. The current as well as the counting rate increases with the increase of environmental humidity. The strip multiplicity of the RPC decreases with the increase of the threshold. The crosstalk between two neighboring strips (which may be due to some real event) is found to be about 15% and that between three neighboring strips is about 5% (d) The charge content in the streamer mode of operation are found to be $\sim$ 100 pC. Operating at $\sim$ 8-9 kV is suggested for avoiding generation of uncontrolled streamers, thereby increasing the induced charge. (e) The timing properties are on expected line $e.g.$, arrival time and time resolution decreases with high voltage. The time resolution reaches $\sim$ 2 ns (FWHM) at $\sim$ 8 kV. (f) The detector, if operated in avalanche mode, giving similar performance but inducing less charge ($\sim$ 1-2 pC) and presence of SF_6 is important from the streamer quenching point of view.

In spite of these features of the silicone coated bakelite RPC, there are still some points to be studied in future. The points are as follows: (a) There is a variation of the counting rate in different modules. One of the reasons behind this is the variation in the surface resistivity of the graphite coating of electrodes. So the value of the graphite surface resistivity should be

optimized and uniformity should be maintained. (b) UV sensitivity of the silicone layer is an important property. It should be studied systematically. (c) Test of bakelite surface protection property of silicone should also be studied.

Chapter 4

ICAL prototype

4.1   Introduction

As a part of the extensive R&D programme undertaken on building the ICAL detector, it was decided to build a prototype consisting of layers of iron plates, magnetic coils and gaps for testing RPCs. The entire process of design, installation and operation of the prototype is aimed to give enough experience to be useful for building the ICAL detector. A 35 ton prototype of the INO-ICAL detector has therefore, been built and installed at VECC, Kolkata. In this work, we discuss details of design, installation and operation of the prototype detector.

The prototype detector should be such that

- The shape should be similar to ICAL.

- The active area, where magnetic field will be uniform should be large enough to test non uniformity if any. We have taken an area of 1 m × 1 m where the magnetic field is uniform.

- The size, shape, placement and materials of the iron should be such that magnetization of iron will be tested and measured in the context of ICAL.

- Loss of flux due to gaps etc. can be studied.

- The placement, operation and dependence of detectors in the magnetic field to be tested.

- The effect of environmental condition on the detectors and maintenance of proper environmental condition to be studied.

Figure 4.1: ICAL prototype detector magnet with electronics rack.

4.2 Design of the prototype detector

The prototype detector is built with 13 layers each of 50 mm thick low carbon iron (Tata A-grade) plates and gaps of 50 mm each for installing 12 RPCs (both bakelite and glass) each of 1m × 1m area sandwiched between the iron plates [90]. Each layer is assembled by joining a 'T' and a 'C' shaped iron plates. The iron plates will be magnetized to about 1.5 Tesla which is below the saturation magnetic field of 2 Tesla of iron, making the momentum measurement and charge separation of cosmic muons incident on the detector. To magnetize the iron plates, four sets of copper coils of 5 turns each, made from electrolytic copper conductor tubing having a central bore for flowing low conductivity water, are used. The power supply (PS) for the magnet coils is a thyristor controlled, three phase low voltage constant current type and has a stabilised reference to regulate the current. It is a twin power supply with provision of working either independently or in client-serve mode. The maximum current rating is 500 ampere. The prototype will provide an active volume of uniform magnetic field of about 1 m^3. The prototype detector magnet in the assembled state is shown in Figure 4.1.

It should be noted that, as per design, the current flowing through the coil will magnetize the iron plates only and almost no field present in the gap. It was found that while installing the

'T' & 'C' sections together, air-gaps up to several mm were created and the flux tends to bypass the gap thereby requiring about 4 times larger current compared to the designed value for a configuration of no air-gap. It is, therefore, utmost important that the effects of gaps etc. are simulated properly. It should be mentioned here that even though the physical dimension of the iron plates are $\sim$ 2m $\times$ 2m, the area of uniform magnetic field is $\sim$ 1m $\times$ 1m at the centre of the magnet.

Depending on the direction of the flow of currents in the coils, a mutual force is created in between coils. Special arrangement was therefore necessary to arrest the movement of the coils due to these forces.

4.3 Installation and operation of prototype magnet at VECC

The iron plates were installed one above the other separated by spacers with a provision of the first layer placed on a concrete base suitable for a load of 35 ton. A box made of 1 cm thick stainless steel wall base was filled with concrete (step-a in Figure 4.2) and then the concrete box is reversed (step-b in Figure 4.2) such that the iron plates are placed on the stainless steel sheet. A provision is made for a central valley (step-c in Figure 4.2) in the base to place the current carrying copper coils properly. On the base plate, first the 'T' shape iron plates are stacked (step-d in Figure 4.2) and then four sets of copper coils are placed (step-e in Figure 4.2). Finally the 'C' shape iron plates are stacked to give the final form of the magnet (step-f in Figure 4.2). The magnet is finally painted by using spray painting.

The magnet is to run with a current of $\sim$ 500 A and even with extremely low resistance, a rise in temperature is expected and therefore the coils are equipped with a central channel for passing low conductivity water (LCW). A chiller unit is in place to keep the water temperature at $\sim$ 20°C and the compressor maintains a water pressure of 6 kg/cm^2 as measured near the coil. The compressor, LCW tank and chiller units are placed in a room about 40 m away from the prototype labs. The water flow rate is set at $\sim$ 35-40 liter per minute (LPM). An interlock system is in place on the power supply so that the PS is switched off when the water temparature is $>$ 70°C and/or the water flow rate is $<$ 5 LPM.
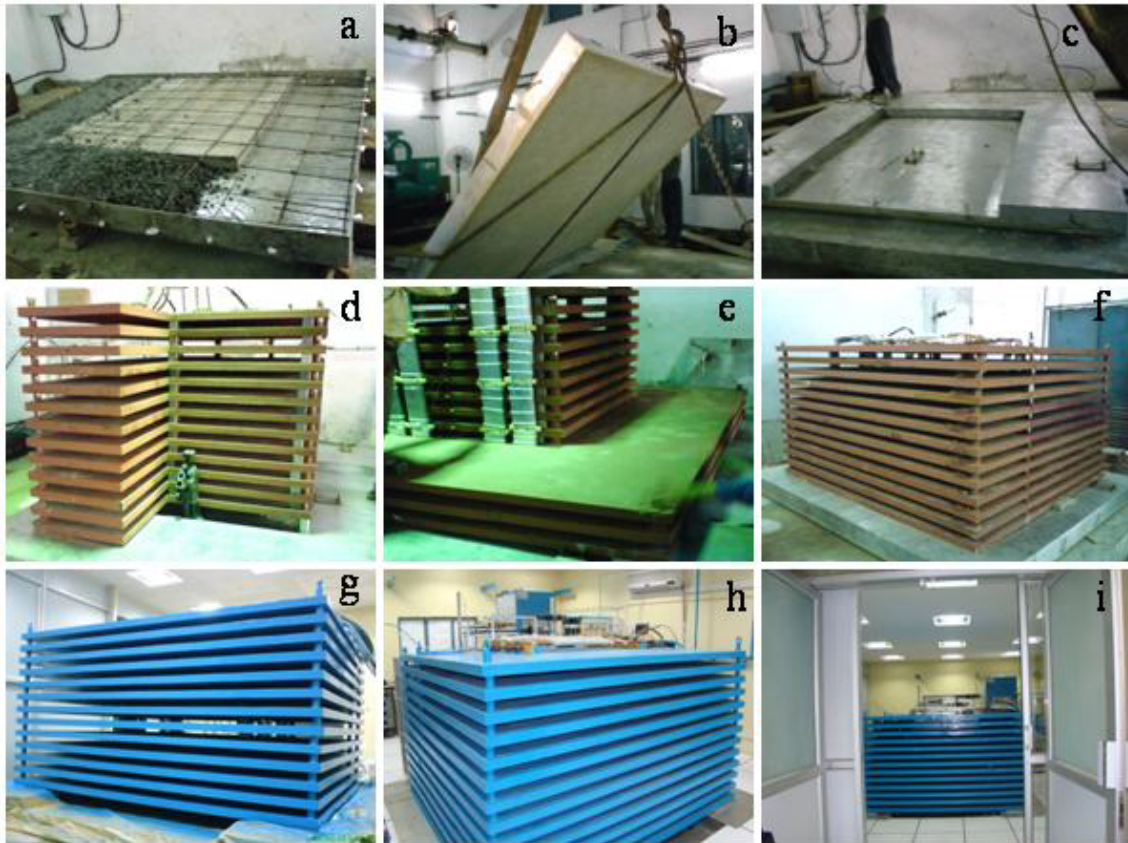
Figure 4.2: (a) Concrete base under construction, (b) concrete box is being reversed, (c) central valley in the base, (d) 'T' shape iron plates are stacked, (e) four sets of copper coils are placed, (f) 'C' shape iron plates are stacked to give the final form of the magnet, (g) the magnet is painted, (h) side view of the assembled prototype, (i) front view of the assembled prototype.

The magnet was switched on by ramping current at a step of 50 amp and the arresters were arranged properly to stop the movement of the coils. Magnetic fields in the iron were measured using a flux meter and by Hall probe in the gaps between 'C' and 'T' section of the iron plates. It was found that the field in the edge of the iron plates is about 25 gauss. The B-H curve is shown in Figure 4.3 [90, 91].

4.4 The electronics and data acquisition system

In the prototype calorimeter, both types of RPCs, a few made of glass and others made of bakelite will be used. Each RPC has 32 X-strips and 32 Y-strips. Data from these 64 channels are to be read out from each of the 12 RPCs [90]. Role of the data acquisition system is to
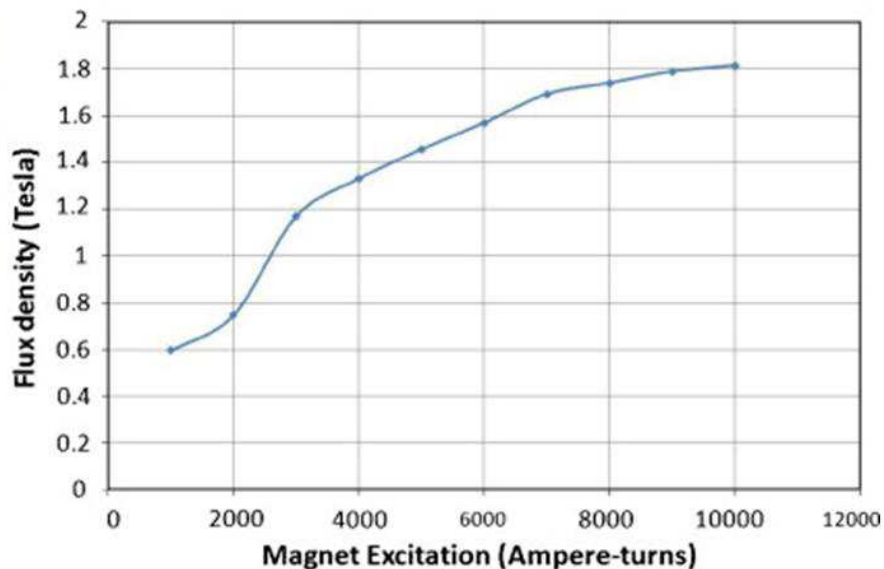
Figure 4.3: The B-H curve. (The Figure is adopted from Ref. [90]).

generate the trigger, based on the hit pattern of the RPC pickup strips and to record strip hit patterns as well as timing of the individual RPCs with reference to the trigger. As an alternative arrangement, signals from two large scintillators (35 cm × 35 cm) placed at the top and bottom of the magnet were taken in coincidence to generate trigger. The strips placed in between provide the hits for cosmic tracks. Monitoring the stability of the detector as well as laboratory ambient parameters, such as temperature, relative humidity and barometric pressure, is another important task of the on-line data acquisition system.

The signal readout chain essentially consists of a front-end fast high gain HMC (Hybrid Micro Circuits) based preamplifier and low level threshold discriminator followed by the digital front-end (DFE) for the glass RPCs operated in avalanche mode. For the bakelite RPC operated in streamer mode no preamplifier is used. The digital front-end built around a couple of CPLD chips handles important tasks of latching the strip hit pattern on master trigger as well as serially transferring the data to back-end. It is also here that the pre-trigger signals are generated, which are used by the back-end trigger module built using combinatorial circuits and produces master trigger. Finally, the digital front-end system handles the entire signal multiplexing required both during the event data acquisition as well as during strip signal rate monitoring. The timing data are acquired using the commercial TDC modules. The data acquisition is done using a CAMAC backend, employing many custom built modules, such as

115

control and readout modules. The multiplexed signals from the front-end are sent to the back-end through appropriate router modules. Monitoring of strip signal rates is done as a cyclic background job using the scaler module in the back-end. A schematic of the data acquisition system for the INO-ICAL prototype detector is shown in Figure 4.4.
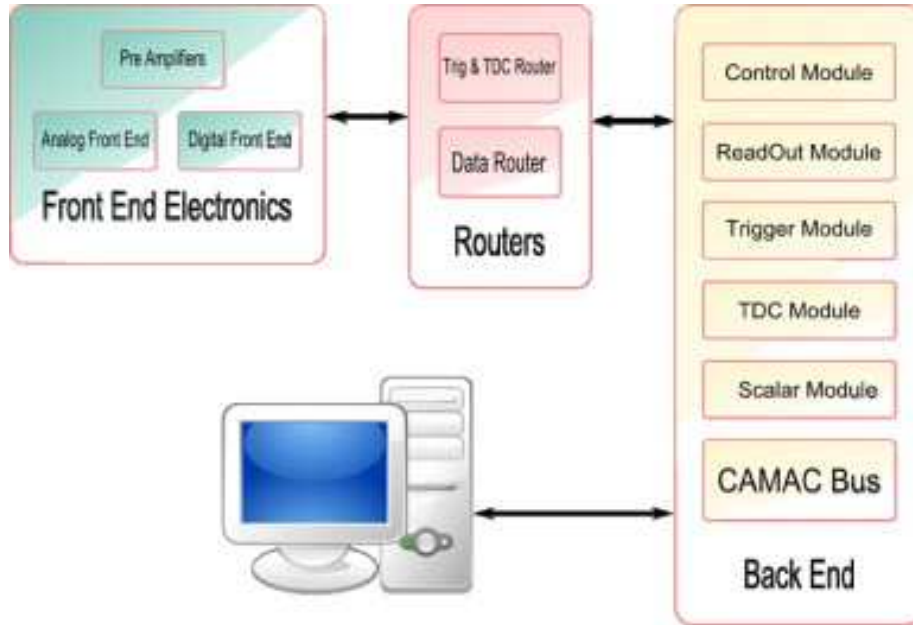
Figure 4.4: Schematic of the data acquisition system for the INO-ICAL prototype detector. (The Figure is adopted from Ref. [90]).

The electronics (AFE, DFE, CDR, TTR etc.) and the data acquisition system for the prototype detector have been designed and fabricated by the TIFR group and some modules have been tested at VECC. The cabling for both the high voltage and low voltage has been done at VECC whereas the preamplifiers with G I frame for both the positive and negative channels are made at SINP.

4.5   Gas mixing and distribution system

One 4-channel and one 8-channel gas dryer and mixer units, with flow dividers for the respective number of channels have been installed in the INO-ICAL prototype lab at VECC. There is a provision to use 4 gases (Argon, Isobutane, SF_6, R134-a i.e 4 inputs) in proper ratio (adjustable)
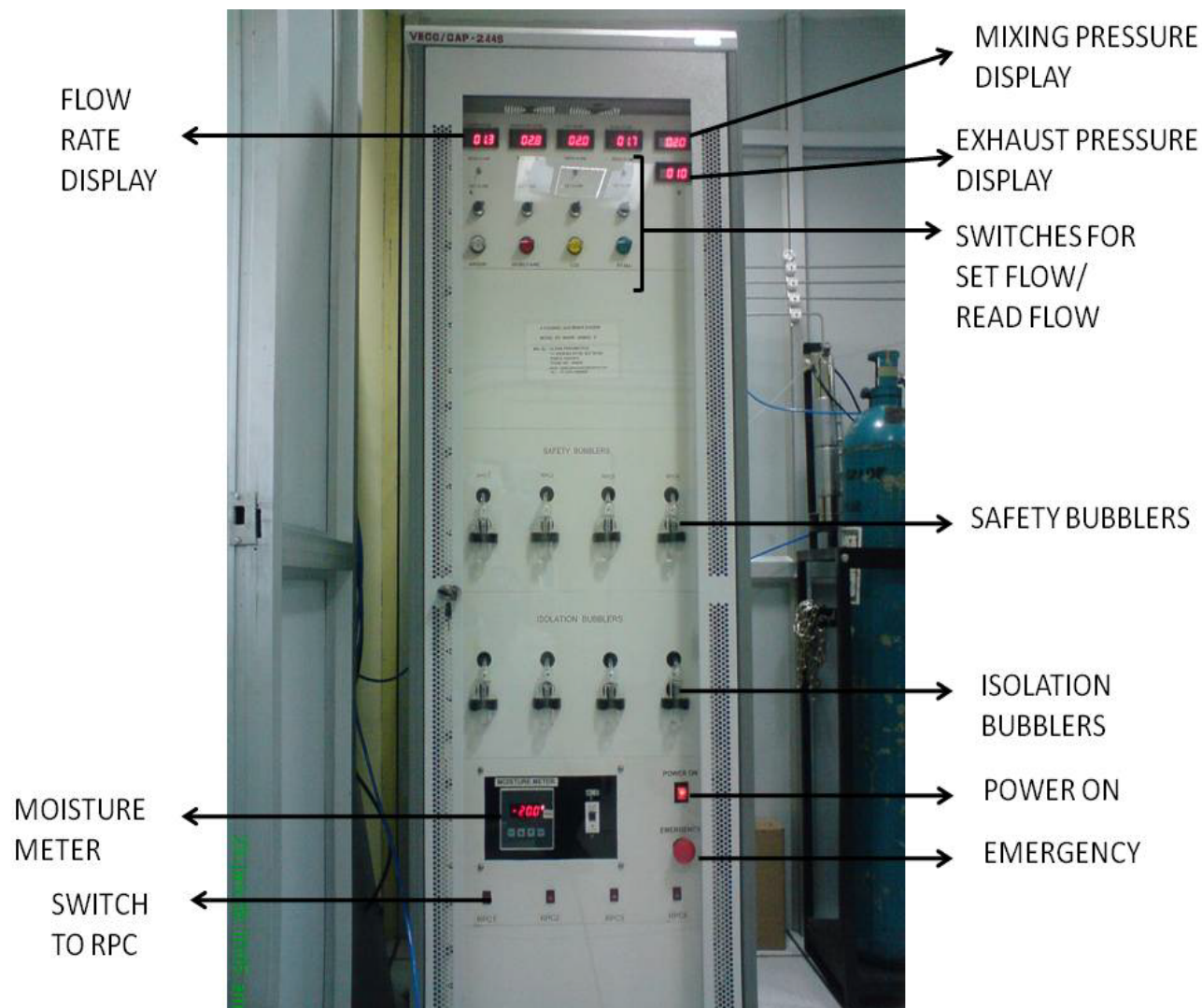
Figure 4.5: On-line gas mixing and distribution system.

using mass flow controllers (MFC), connected to each line. The MFCs have been calibrated using water displacement method. The gasses are mixed online according to proper ratio (set value) in a stainless steel cylinder and are delivered to the respective number of RPCs. The front panel of the 4-channel gas system is shown in Figure 4.5. Two mixing systems are installed for delivering mixed gases to glass RPCs and bakelite RPCs separately operating in avalanche and streamer mode respectively. The systems were procured from Alpha Pneumatics, Thane, India.

4.5.1 Calibration of Mass Flow Controllers (MFC)

Mass Flow Controllers for all the gases (Argon, Isobutane and R-134a) were calibrated using water displacement method. In case of bakelite RPCs SF_6 was not used. The procedure for calibration was as per following:

a) Firstly a flow rate was set up on MFC using the proper gas. It was taken as the "set value" in SCCM (Standard Cubic Centimeters per Minute).

b) The measuring cylinder was filled with water and inverted in a bowl containing water. The bubbling into water column started but the stopwatch was not started at this stage to measure the time.

c) Water level starts dropping at steady rate. When it reaches a certain level (say X cc), the stopwatch was started for timing measurement.

d) When the water level drops to another point (say Y cc), the stopwatch was stopped. The elapsed time (say t minutes) between these two events (start and stop) was measured.

e) Flow rate $Q_v = \frac{(Y-X)}{t}$ cc/min .

f) SCCM flow rate $Q_m = Q_v \times \left(\frac{P}{101.3}\right) \times \left(\frac{273}{273+T}\right)$,
Where P is the pressure in kPa and T is the temperature in °C.

g) If the above calibration is done using a gas other than the proper gas then we convert the flow from test gas to actual gas by using proper multiplying constant.

We made sure that the time t is at least in range of 200 sec or/and the collected gas volume is more than 40 cc.

The MFCs for the argon, isobutane and R-134a, used for the streamer mode of operation of the bakelite RPC were calibrated by the method described above. The calibration curves are shown in Figure 4.6. The set value of the flow for the respective gases in SCCM are taken along X-axis and the measured flow rate is taken along Y-axis. All the plots are linear with a very small offset.
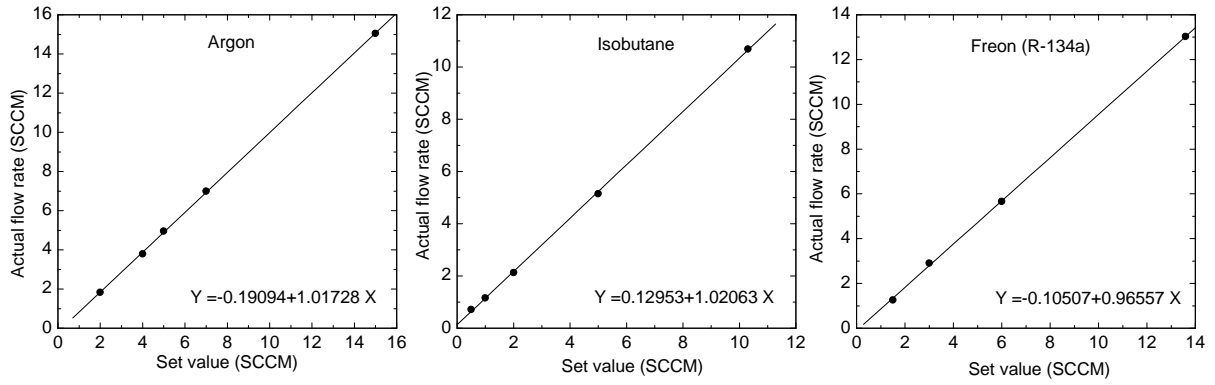
Figure 4.6: Calibration curve for the MFCs of argon, isobutane and R-134a.

4.6   1m × 1m bakelite RPC for ICAL prototype

Till now two 1 m^2 modules have been fabricated, one using 3.2 mm thick bakelite (referred as ib09 in the following text) and other with 1.6 mm (referred as ib10 in the following text) thick sheets for the prototype [92]. The fabrication procedure is discussed in section 3.3. Both the modules are silicone coated chambers. The assembled RPC equipped with pick up strips is placed on an aluminium honeycomb tray for the mechanical support and the whole system is put inside the prototype iron.
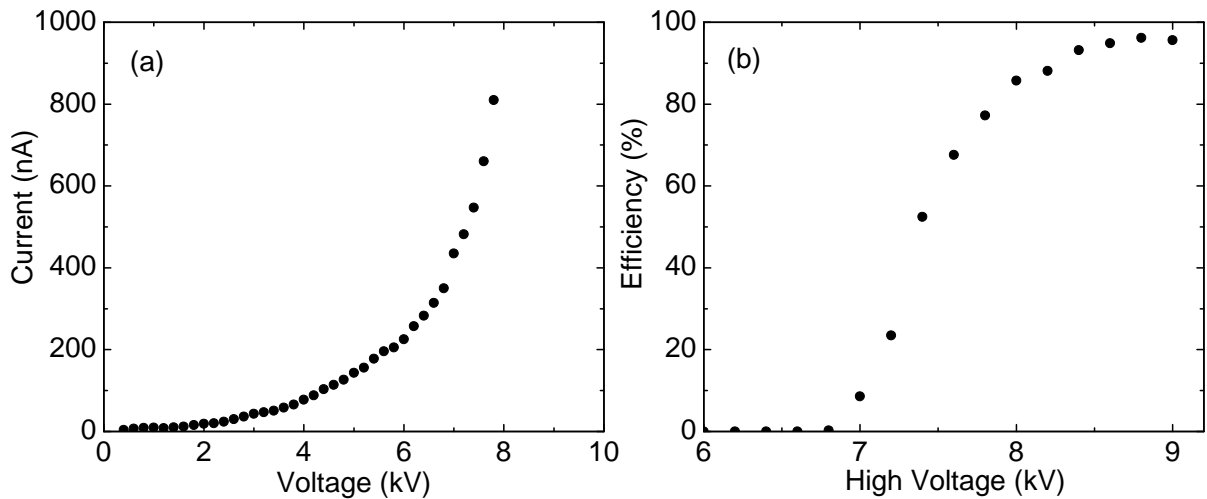
Figure 4.7: (a) Leakage current & (b) efficiency as a function of the high voltage for a 1m × 1m RPC (ib09) obtained in streamer mode.
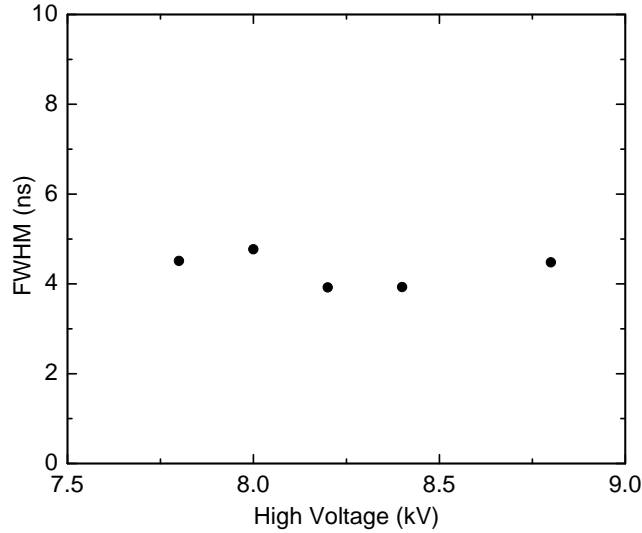
Figure 4.8: Time resolution (FWHM) as a function of the high voltage for a 1m × 1m RPC (ib09) module.

We report here some of the results obtained from these RPCs placed inside the iron plates but keeping the magnet in off condition. Initially the variation of the leakage current, efficiency, and time resolution with the high voltage (HV), are studied in streamer mode using premixed gas of argon, tetrafluroethane (R134a) and isobutane in 55:37.5:7.5 volume mixing ratio, for all the RPCs in the cosmic ray stand as described in section 3.4. Typical results of leakage current and efficiency as a function of the high voltage for a 1m × 1m RPC (ib09) module are shown in Figure 4.7 (a) and (b) respectively. The efficiency for the RPC gradually increases and reaches the plateau at > 90% as shown in the Figure 4.7 (b). The efficiency plateau is reached at relatively higher voltages for the RPC made with thicker (3.2 mm) bakelite sheet, than modules with 2 mm bakelite sheet as shown in Figure 3.21. The time resolution for the module as a function of the applied high voltage is shown in Figure 4.8 and at the plateau region the time resolution (FWHM) has been found to be ∼ 4 ns. Efficiency > 90% with time resolution ∼ 4 ns was also obtained for ib10.

After the initial measurement in the cosmic ray stand the chambers are shifted to INO-ICAL prototype laboratory where new tests have been carried out. The 1 m² RPC (ib09) is placed in the 4th slot of the magnet and the cosmic ray master trigger is made with signals from two scintillators one placed above and the other placed below the RPC. Finally, the ORed signal

120

obtained from the adjacent pick-up strips of the chamber, under the coincidence area of two scintillators is put in coincidence with the master trigger obtained above. The RPC has been tested in the streamer mode at the prototype laboratory using the same ratio of gas. The leakage current as a function of the applied voltage is shown in Figure 4.9 (a). The curve shows two distinct slopes (as obtained previously). Intitially the current was about 4 times higher in the prototype lab, and stabilized with time. The variation of efficiency with applied high voltage is shown in Figure 4.9 (b). The efficiency increases with the increase of the applied voltage and reaches a plateau at >90%.
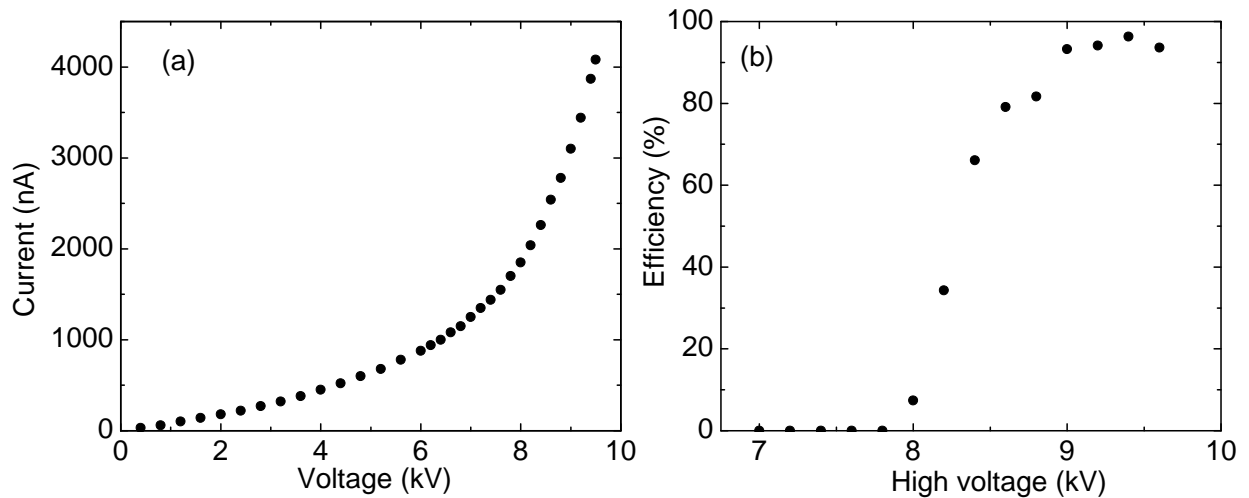
Figure 4.9: (a) Leakage current & (b) efficiency as a function of the high voltage for a 1m × 1m RPC (ib09) obtained in streamer mode at ICAL prototype laboratory.

4.7 Operation of the prototype calorimeter using 6 RPCs

The prototype calorimeter is finally operational with 2 bakelite RPCs and 4 glass RPCs. The bakelite RPCs are operated in streamer mode with a gas mixture of argon, isobutane and R-134a in 55/7.5/37.5 volume mixing ratio while the glass RPCs are operated in avalanche mode with a mixture of R-134a and isobutane in 94.7/5.3 volume mixing ratio. The gas flow rate for glass RPCs is 3 SCCM and that for bakelite RPC is 4 SCCM. The bakelite RPCs are operated at 8.5 kV whereas the glass RPCs are operated at 9.6 kV. The trigger is generated from the RPCs as well as with the scintillators. Two typical tracks for event no. 12 and 296 of run no.
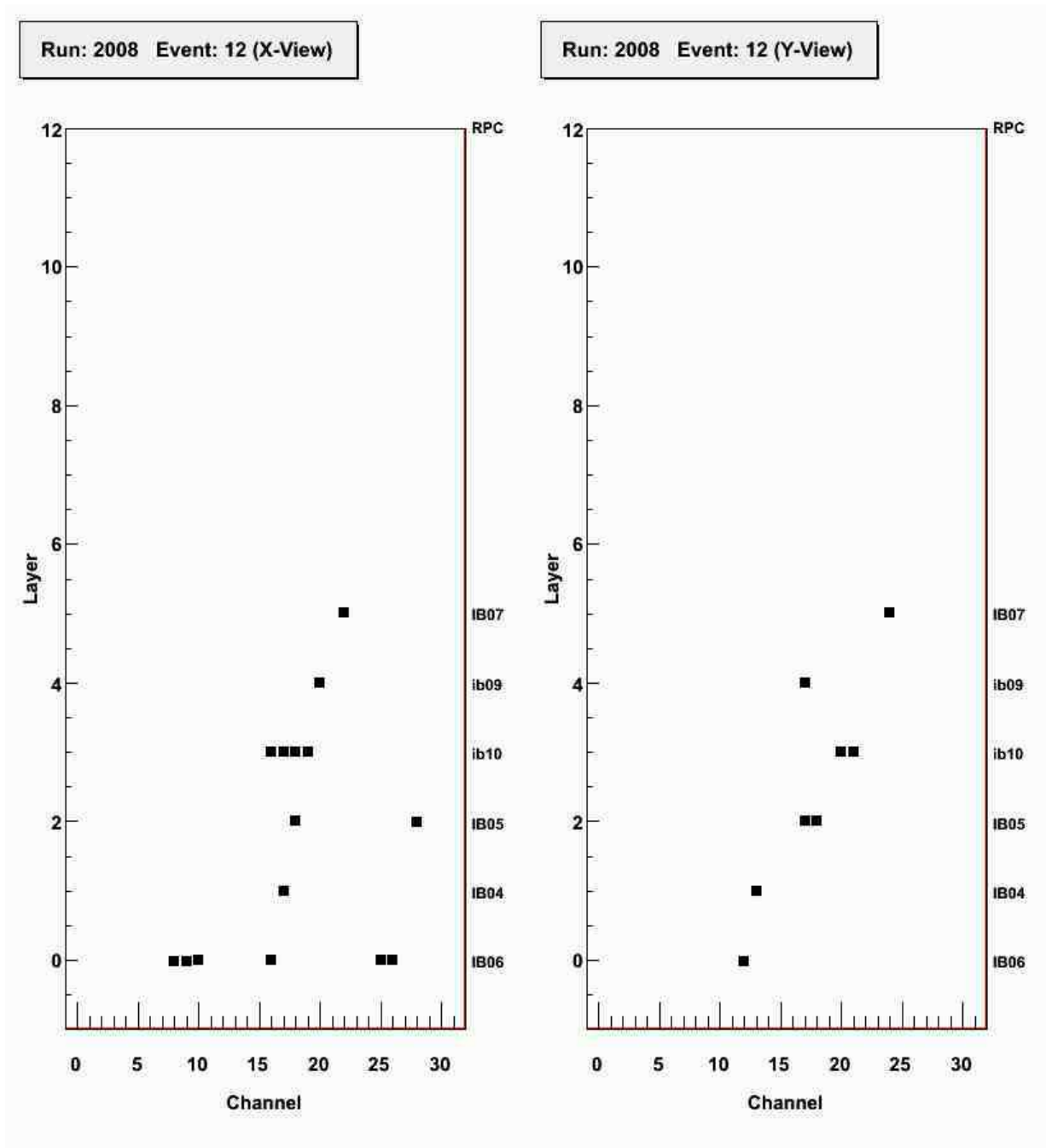
Figure 4.10: Track for Run No:2008 Event No:12.

2008 are shown in Figure 4.10 and 4.11 respectively. The glass RPCs are marked as IB04, IB05, IB06 and IB07 while the bakelite RPCs are marked as ib09 and ib10. In the figures the X-view and Y-view of the tracks are shown. One single spot corresponds one hit point on a strip. In Figure 4.10, ib09 gives single hit both in X-strip and Y-strip while in ib10 multiple hit comes which is the effect of crosstalk. In Figure 4.11, ib09 missed to give hit in the Y-strip.
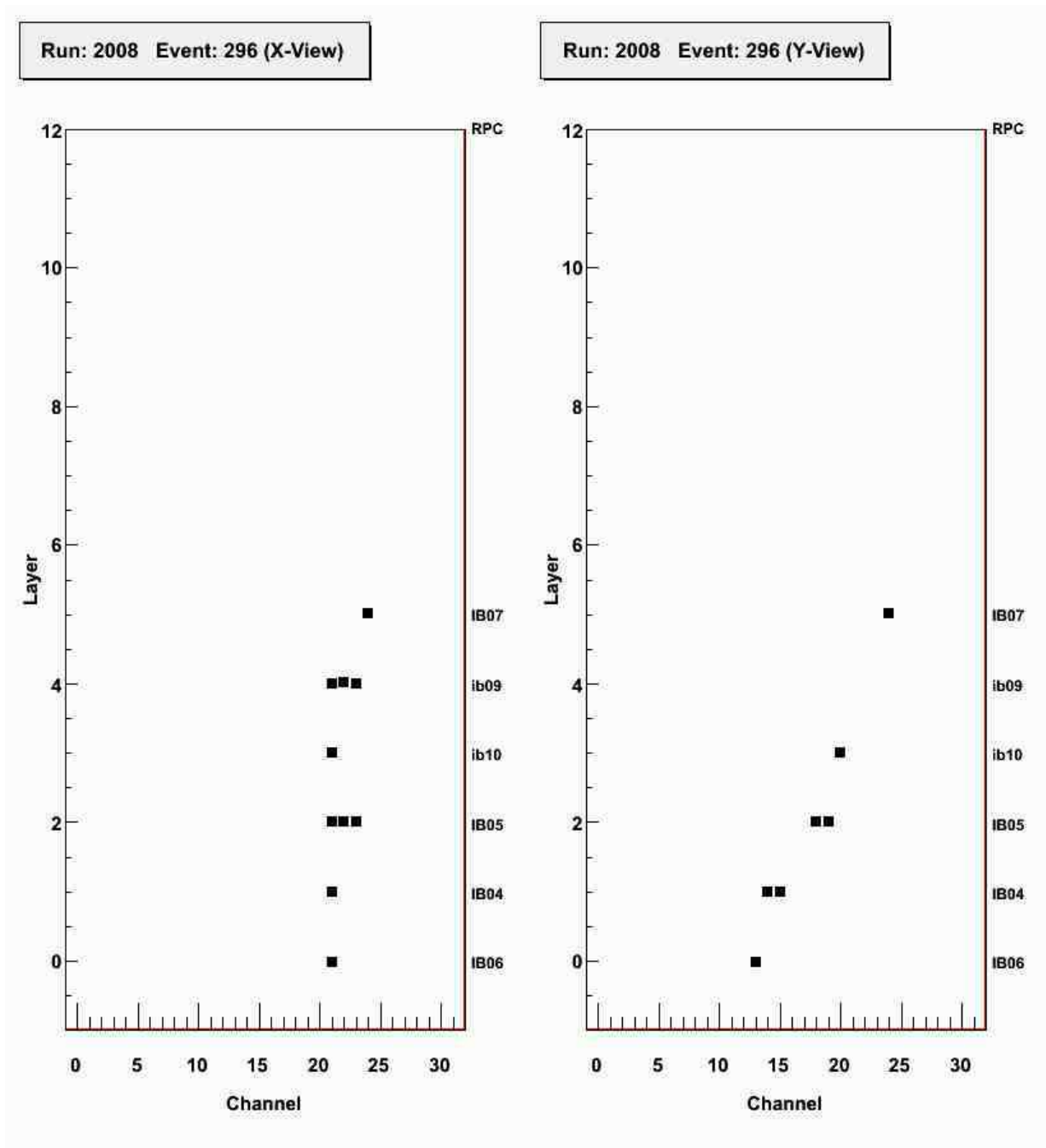
Figure 4.11: Track for Run No:2008 Event No:296.

4.8   Summary and outlook

The INO-ICAL prototype is ready for 24×7 operation. The mechanical work is completed. One
4 channel and one 8 channel gas mixing units are ready with all the stainless steel tubings. Four
glass RPCs and two bakelite RPCs are placed inside the magnet. Glass RPCs are operational

123

in avalanche mode whereas the bakelite RPCs are being operated in streamer mode. Track is obtained without the magnetic field with 6 RPCs in position and initial results are presented. As per plan, magnet will run with full strength shortly thereby making the system completed for full-fledged operation.

Chapter 5

Summary and Discussions

Resistive Plate Chamber (RPC) is one of the most widely used large area gas filled detectors in experimental high energy physics with a potential to be used in PET imaging. Main characteristics of RPC, which have made it highly attractive are excellent time resolution ($\sim$ 1-2 ns for single-gap and $\sim$ 50 ps for multi-gap) and position resolution (1 cm to $\sim$ 100 μm) coupled with the low cost of fabrication. Till now, RPCs have found their applications in HEP experiments like STAR, ALICE, ATLAS, CMS, BELLE, BaBar, BESIII and neutrino experiments *e.g.* OPERA.

The main topic of this thesis is R&D on bakelite based RPC for the Iron Calorimeter (ICAL) in INO. From the considerations of up/down separation of the interacting neutrinos and background rejection, ICAL requires highly efficient sensitive detectors with $\sim$ 2 ns time resolution. Current effort is a development complimentary to the development of glass-based RPCs in other collaborating institutes.

Starting from a 30 cm $\times$ 30 cm Chinese made bakelite-based RPC, we have developed a number of RPCs making use of the bakelites available locally. Entire effort can be divided into following steps: (a) Characterization of different grades of bakelite in terms of resistivity (bulk and surface) and other electrical properties and thereby choosing the electrically suitable bakelite for RPC-building (b) Building of RPCs (10 cm $\times$ 10 cm and 30 cm $\times$ 30 cm), detailed procedure involved building of components like button and edge spacers, gas nozzles, pick-up strips, graphite coating arrangement by adjusting the resistivity, connection of high voltage leads (c) Testing of the RPCs in a cosmic ray stand by measuring the efficiency, count rate,

time resolution and long term stability in the streamer mode of operation. It was observed that for a grade of bakelite (Superhylam) even though an efficiency $> 90\%$ is reached, but it reduces slowly with time coupled by increase in count rate while in some other grade (P-120) efficiency increases with high voltage, reaches a maximum and then start to decrease with continuous increase of count rate. (d) As an effort to improve the performance, a thin layer of silicone coating is applied in the inner surfaces of the electrodes, towards maintaining the surface smoothness. (e) One such silicone coated RPC is tested for a long duration showing $\sim 96\%$ efficiency for a period of operation of more than 130 days. The time resolution measured for the RPCs reaches ~ 2 ns and the measured charge content is ~ 100 pC at a high voltage of 8 kV. (f) Consistency of results are established making several such RPC modules. (g) Operating the detectors in avalanche mode and studying the properties like efficiency, time resolution, charge content. Various composition of gases are also used for further study (h) Finally, building of the 1m $\times$ 1m RPC for use in a prototype calorimeter.

The work started from a scratch and at the end silicone-coated bakelite-based RPCs even working in streamer mode have been established as alternatives to glass-based RPC working in avalanche mode. Apart from being less expensive, larger pulses and less number of electronic components in streamer mode of operation makes bakelite-based RPCs even more attractive.

In addition to the RPC development, this work describes the installation and operation of a 35 ton prototype magnet for ICAL. The ICAL-prototype is installed at VECC as a facility for testing different types of RPC (bakelite and glass) in a ~ 1.5 Tesla magnetic field.

All the activities are part of the R&D effort towards building ICAL detector in INO. In this context, the development and satisfactory performance of bakelite-based RPCs open up new avenue for the sensitive detectors in ICAL. ICAL needs about 27000 RPCs and there is always a possibility of using more than one types of electrode materials. Bakelite-based RPCs are attractive from the point of view that the materials are locally made. The work presented in this thesis is likely to open up the horizon for the active detectors for ICAL.

Appendix A

Relation between volume ratio and mass ratio of gas

In the cosmic muon test set up, most of the time pre-mixed gas was used. The gases were mixed in a cylinder by filling the gases serially according to their partial pressure. It can be shown that their partial pressure ratio and their volume ratio at atmospheric pressure are the same. Initially, the cylinder was evacuated by a pump and then using proper gases in proper partial pressure ratio, the cylinder was filled to a certain pressure. Finally the mixed gas was sent to the RPC.

Let us consider, that three gases are used. The partial pressure ratio (%) is $p_1 : p_2 : p_3$. The total pressure of the cylinder will be P (say).

Let the partial pressure of gas 1, 2 and 3 respectively are:

$$P_1 = P\frac{p_1}{100} \tag{A.1}$$

$$P_2 = P\frac{p_2}{100} \tag{A.2}$$

$$P_3 = P\frac{p_3}{100} \tag{A.3}$$

such that

$$P = P_1 + P_2 + P_3 \tag{A.4}$$

So, the cylinder is filled with the first gas from vacuum to a pressure P_1, then the pressure is raised from P_1 to P_1+P_2 by filling the second gas, and finally the last gas is filled to raise the pressure from P_1+P_2 to $P_1+P_2+P_3$ i.e. P.

A.1 Partial pressure ratio and volume ratio

In a mixture of ideal gases, each gas has a partial pressure which is the pressure the gas would have if it occupies the whole volume. Let the volume of the cylinder is V in our system. So, at pressure P_1 the first gas occupies a volume V. The same amount of gas at pressure P' (say, at one atmospheric pressure) will occupy a volume V_1 which according to Boyle's law is,

$$V_1 = \frac{P_1 V}{P'} \tag{A.5}$$

assuming that the temperature remains constant.

Similarly the volumes of the second and the third gas at pressure P' are

$$V_2 = \frac{P_2 V}{P'} \tag{A.6}$$

and

$$V_3 = \frac{P_3 V}{P'} \tag{A.7}$$

respectively.

Therefore,

$$V_1 : V_2 : V_3 = P_1 : P_2 : P_3 = p_1 : p_2 : p_3 \tag{A.8}$$

So, the volume ratio in which the gases are mixed are same as the partial pressure ratio.

A.2 Conversion from partial pressure ratio to mass ratio

Let partial pressure ratio of gas 1, 2 and 3, expressed in percentage are p_1:p_2:p_3 and their partial pressures P_1, P_2 and P_3, are calculated from equations A.1, A.2 and A.3 respectively. Here P is the total pressure of the cylinder. So,

$$\begin{aligned} P_1 &= n_1 \frac{RT}{V} \\ &= \frac{m_1}{M_1} \frac{RT}{V} \end{aligned} \tag{A.9}$$

$$\begin{aligned} P_2 &= n_2 \frac{RT}{V} \\ &= \frac{m_2}{M_2} \frac{RT}{V} \end{aligned} \tag{A.10}$$

$$P_3 = n_3 \frac{RT}{V}$$

$$= \frac{m_3}{M_3} \frac{RT}{V} \tag{A.11}$$

with

$$P = P_1 + P_2 + P_3$$

Where n_1, n_2 and n_3 are the mole fractions, m_1, m_2 and m_3 are the masses and M_1, M_2 and M_3 are the molecular weights of three gases respectively. R is the universal gas constant, T is the absolute temperature and V is the volume of the cylinder.

Therefore,

$$P_1 : P_2 : P_3 = \frac{m_1}{M_1} : \frac{m_2}{M_2} : \frac{m_3}{M_3} \tag{A.12}$$

or,

$$m_1 : m_2 : m_3 = P_1 M_1 : P_2 M_2 : P_3 M_3 \tag{A.13}$$

To get the mass ratio $m_1':m_2':m_3'$ in percent, we calculate

$$m_1' : m_2' : m_3' = \frac{P_1 M_1}{M} 100 : \frac{P_2 M_2}{M} 100 : \frac{P_3 M_3}{M} 100 \tag{A.14}$$

such that

$$m_1' + m_2' + m_3' = 100 \tag{A.15}$$

where

$$M = P_1 M_1 + P_2 M_2 + P_3 M_3 \tag{A.16}$$

A.3   Conversion from mass ratio to partial pressure ratio

If the mass ratio $m_1':m_2':m_3'$ is given, the corresponding partial pressure ratio $p_1:p_2:p_3$ can be calculated by combining eqs. (A.8) and (A.12) as

$$p_1 : p_2 : p_3 = \frac{m_1'}{M_1} \frac{100}{M'} : \frac{m_2'}{M_2} \frac{100}{M'} : \frac{m_3'}{M_3} \frac{100}{M'} \tag{A.17}$$

such that

$$p_1 + p_2 + p_3 = 100 \tag{A.18}$$

where

$$M' = \frac{m'_1}{M_1} + \frac{m'_2}{M_2} + \frac{m'_3}{M_3} \tag{A.19}$$

Bibliography

[1] Claus Grupen: Astroparticle Physics, (Springer-Verlag Berlin Heidelberg, 2005).

[2] Y. Fukuda et al., (Super-Kamiokande Collaboration), Phys. Rev. Lett. 81 1562 (1998) hep-ex/9807003.

[3] Y. Fukuda et al., (Super-Kamiokande Collaboration), Phys. Rev. Lett. 82 2644 (1999) hep-ex/9812014.

[4] S. Fukuda et al., (Super-Kamiokande Collaboration), Phys. Rev. Lett. 85 3999 (2000) hep-ex/0009001.

[5] Y. Fukuda et al., (Super-Kamiokande collaboration), Phys Rev. Lett. 82, 2430 (1999); 86 5651 (2001).

[6] M. B. Smy et al., (Super-Kamiokande Collaboration), Phys. Rev. D 69, 011104(2004) hep-ex/0309011.

[7] J. Yoo et al., (Super-Kamiokande Collaboration), Phys. Rev. D 68, 092002(2003) hep-ex/0307070.

[8] K. Eguchi et al., [KamLAND Collaboration], Phys. Rev. Lett. 90, 021802 (2003)hepex/ 0212021.

[9] Q. R. Ahmad et al., (SNO collaboration), ibid. 87, 071301 (2001).

[10] B. Aharmim et al., (SNO Collaboration) hep-ex/0407029.

[11] S. N. Ahmed et al., (SNO Collaboration), Phys. Rev. Lett. 92, 181301 (2004)nuclex/ 0309004.

[12] David Griffiths: Introduction to Elementary Particles, (Second, Revised Edition, WILEY-VCH Verlag GmbH & Co. KGaA, 2009).

[13] J. N. Bahcall, A.M. Serenelli, and S. Basu, Astrophysical Journal 621, L85 (2005).

[14] Raymond Davis, Jr., Don S. Harmer, and Kenneth C. Hoffman, (1968) Physical Review Letters, 20, 1205.

[15] John N. Bahcall, Neta A. Bahcall and Giora Shaviv, (1968) Physical Review Letters, 20, 1209.

[16] V. Gribov and B. Pontekorvo, Physics Letters B 28 (1969) 493.

[17] INO Project Report, INO/2006/01, June 2006, ⟨http://www.imsc.res.in/∼ino/⟩.

[18] Y. Totsuka, IEEE conference, Portland, 2003.

[19] S. Goswami, talk at Neutrino 2004, see S. Goswami, A. Bandyopadhyay and S. Choubey, hep-ph/0409224.

[20] T. Schwetz, Acta Phys. Polon. B 36, 3203 (2005), Talk given at the XXIX International Conference of Theoretical Physics, September 2005, Ustron, Poland: hep-ph/0510331.

[21] L. Wolfenstein, Phys. Rev. D 17, 2369 (1978); S. P. Mikheev and A. Y. Smirnov, Sov. J. Nucl. Phys. 42, 913 (1985) [Yad. Fiz. 42, 1441 (1985)].

[22] M. Maltoni, T. Schwetz, M.A. Tortola, J.W.F. Valle New J.Phys. 6, 122 (2004); hepph/ 0405172.

[23] CHOOZ Collaboration: M. Appolonio et al, Phys. Lett. 420B, 397 (1998), Phys. Lett. 466B, 415 (1999).

[24] C. Athanassopoulos, et al. (LSND Collaboration), Phys. Rev. Lett. 81, 1774 (1998); Phys. Rev. C58, 2489 (1998).

[25] P. Picchi and F. Pietropaolo, ICGF RAP. INT. 344/1997, Torino 1997 (CERN preprint SCAN-9710037).

[26] R. Santonico, R. Cardarelli, Nucl. Instr. and Meth. 187 (1981) 377.

[27] W. R. Leo: Techniques for Nuclear and Particle Physics Experiments, (2nd Edition, Springer-Verlag Berlin Heidelberg, 1994).

[28] G. F. Knoll: Radiation Detection and Measurement, (3rd Edition, John Wiley & Sons, Inc.).

[29] G.V. Fedotovich et al., Proc. Int. Conf. on Instrumentation for Colliding Beam Physics, Stanford, 1982.

[30] R. Cardarelli, et al., Nucl. Instr. and Meth. A 263 (1988) 20.

[31] R. Santonico, Nucl. Instr. and Meth. A 456 (2000) 1.

[32] G. Anelli et al., Nucl. Instr. and Meth. A 300 (1991) 572.

[33] P. Fonte et al., Nucl. Instr. and Meth. A 449 (2000) 295.

[34] A. Blanco et al., Nucl. Instr. and Meth. A 535 (2004) 272.

[35] S. An et al., Nucl. Instr. and Meth. A 594 (2008) 39.

[36] G. Bruno, Eur Phys. J. C 33 (2004) s1032.

[37] A. Abashian, et al., Nucl. Instr. and Meth. A 479 (2002) 117.

[38] J. Va'vra, Nucl. Instr. and Meth. A 515 (2003) 354.

[39] F.Anulli, et al., Nucl. Instr. and Meth. A 508 (2003) 128.

[40] F. Anulli et al., Nucl. Instr. and Meth. A 515 (2003) 322.

[41] J. Zhang et al., Nucl. Instr. and Meth. A 540 (2005) 102.

[42] A.Sharma, Nucl. Instr. and Meth. A 602 (2009) 854.

[43] K. Abe, Talk given at Saha Institute of Nuclear Physics, India, 2007.

[44] S. Biswas, et al., Proceedings of the National seminar on New Era in Nuclear and Particle Physics, November 2008 (To be published).

[45] M. Iori, F. Massa, Nucl. Instr. and Meth. A 306 (1991) 159.

[46] I. Crotty et al., Nucl. Instr. and Meth. A 329 (1993) 133.

[47] E. Cerron Zeballos et al., Nucl. Instr. and Meth. A 373 (1996) 35.

[48] R. Cardarelli, A. Di Ciaccio, R. Santonico, Nucl. Instr. and Meth. A 333 (1993) 399.

[49] I. Duerdoth et al., Nucl. Instr. and Meth. A 348 (1994) 303.

[50] I. Crotty et al., Nucl. Instr. and Meth. A 337 (1994) 370.

[51] Changguo Lu, Nucl. Instr. and Meth. A 602 (2009) 761.

[52] S. Biswas, Talk given at X. Workshop on Resistive Plate Chambers and Related Detectors, GSI, Darmstadt, Germany, February 2010.

[53] E. Cerron Zeballos, et al., Nucl. Instr. and Meth. A 374 (1996) 132.

[54] S. Narita, et al., Nucl. Instr. and Meth. A 602 (2009) 814.

[55] W. Riegler et al., Nucl. Instr. and Meth. A 500 (2003) 144.

[56] Gy. L. Bencze, et al., Nucl. Instr. and Meth. A 340 (1994) 466.

[57] A. Blanco, et al., Nucl. Instr. and Meth. A 513 (2003) 8.

[58] BaBar Technical Design Report, BaBar Collaboration, SLAC Report SLAC-R-95-457, March 1995.

[59] The BESIII Detector, IHEP-BEPCII-SB-13, IHEP, Beijing.

[60] ALICE Collaboration, Technical Design Report of the Time-Of-Flight Detector CERN/LHCC/2000-12; Addendum CERN/LHCC/2002-16.

[61] ATLAS Technical Design Report, Muon Spectrometer, CERN/LHCC/97-22, Geneva, 1997.

[62] CMS - Technical Proposal, CERN/LHCC/94-38, December 1994.

[63] M. Guler, et al., OPERA, an appearance experiment to search for ν_μ-ν_τ oscillations in the CNGS beam, CERN/SPSC 2000-028.

[64] M. Couceiro, et al., Nucl. Instr. and Meth. A 580 (2007) 915.

[65] P. Camarri, Nucl. Instr. and Meth. A 572 (2007) 476.

[66] M. Abbrescia, et al., Nucl. Phys. B (Proc. Suppl.) 125 (2003) 43.

[67] M. Abbrescia, et al., Nucl. Instr. and Meth. A 506 (2003) 101.

[68] V. M. Datar, et al., Nucl. Instr. and Meth. A 602 (2009) 744.

[69] Saikat Biswas, et al., Proceedings of the XVII DAE-BRNS High Energy Physics Symposium, December 2006, 335.

[70] G. Aielli, et al., Nucl. Instr. and Meth. A 533, (2004) 86.

[71] G. Bencivenni, et al., Nuclr. Inst. and Meth. A 332, (1993) 368.

[72] R. Cardarelli, A. Di Ciaccio and R. Santonico, Nucl. Instr. and Meth. A 333, (1993) 399.

[73] H. Czyrkowski, et al., Nucl. Instr. and Meth. A 419, (1998) 490.

[74] S. Biswas, et al., arXiv:0802.2766.

[75] S. Biswas, et al., Nucl. Instr. and Meth. A 602 (2009) 749.

[76] S. Biswas, et al., Proceedings of the DAE Symposium on Nuclear Physics, Volume 52, (2007), 593.

[77] Data Acquisition and Analysis Package LAMPS. (http://www.tifr.res.in/~pell/lamps.html).

[78] S.Bose, et al., Nucl. Instr. and Meth. A 602 (2009) 839.

[79] F.Anulli, et al., Nucl. Inst. and Meth. A 539, (2005) 155.

[80] I. Crotty, et al., Nucl. Inst. and Meth. A 337, (1994) 370.

[81] S. Biswas, et al., Nucl. Instr. and Meth. A 604 (2009) 310.

[82] S. Biswas, et al., Proceedings of the DAE Symposium on Nuclear Physics, Volume 53, (2008), 687.

[83] C. Lu, SNIC Symposium, Stanford, California -3-6 April 2006.

[84] Elena Rocco , CERN-THESIS-2010-053, 16/02/2010.

[85] H. Genz, Nucl. Instr. and Meth. 112 (1973) 83.

[86] M. Abbrescia et al., Nucl. Instr. and Meth. A 431 (1999) 413.

[87] S. Biswas, et al., Nucl. Instr. and Meth. A 617 (2010) 138.

[88] S. Biswas et al., Proceedings of the XVIII DAE-BRNS High Energy Physics Symposium, December 2008 (To be published).

[89] A. Sharma, IEEE Nuclear Science Symposium, Florida, USA,2009..

[90] A.Behere, et al., Nucl. Instr. and Meth. A 602 (2009) 784.

[91] M. S. Bhatia, et al.,Fabrication and testing of the magnet of the prototype Iron calorimetric detector, in: Proceedings of the DAE Symposium on Nuclear Physics, vol.52, Sambalpur University, 2007, p.609.

[92] S. Biswas et al., Proceedings of the National Symposium on Nuclear Instrumentation. BARC, Mumbai, (2010), 269.

List of Publications

- **Performances of linseed oil-free bakelite RPC prototypes with cosmic ray muons.**
  Authors: S. Biswas, S. Bhattacharya, S. Bose, S. Chattopadhyay, S. Saha, M.K. Sharan, Y.P. Viyogi
  Published in **Nucl. Instr. and Meth. A 602 (2009) 749-753.**
  e-Print: **arXiv:0907.2976** [physics.ins-det, hep-ex]

- **Control system for a four-component gas mixing unit.**
  Authors: S. Bose, S. Biswas, S. Saha, M.K. Sharan, S. Bhattacharya
  Published in **Nucl. Instr. and Meth. A 602 (2009) 839-841.**

- **INO prototype detector and data acquisition system.**
  Authors: Anita Behere, M.S. Bhatia, V.B. Chandratre, V.M. Datar, P.K. Mukhopadhyay, Satyajit Jena, Y.P. Viyogi, Sudeb Bhattacharya, Satyajit Saha, Sarika Bhide, S.D. Kalmani, N.K. Mondal, P. Nagraj, B.K. Nagesh, Shobha K. Rao, L.V. Reddy, M. Saraf, B. Satyanarayana, R.R. Shinde, S.S. Upadhya, P. Verma, Saikat Biswas, Subhasish Chattopadhyay, P.R. Sarma
  Published in **Nucl. Instr. and Meth. A 602 (2009) 784-787.**

- **Development of linseed oil-free Bakelite Resistive Plate Chambers.**
  Authors: S. Biswas, S. Bhattacharya, S. Bose, S. Chattopadhyay, S. Saha, Y.P. Viyogi
  Published in **Nucl. Instr. and Meth. A 604 (2009) 310-313.**
  e-Print: **arXiv:0907.2978** [physics.ins-det, hep-ex]

- **Study of timing properties of single gap high-resistive bakelite RPC.**
  Authors: S. Biswas, S. Bhattacharya, S. Bose, S. Chattopadhyay, S. Saha, Y.P. Viyogi
  Published in **Nucl. Instr. and Meth. A 617 (2010) 138-140.**
  e-Print: **arXiv:0907.2982** [physics.ins-det, hep-ex]

National Conference Proceedings

- **Study of bakelite-based RPC detector performance with cosmic ray muons.**
  Authors: Saikat Biswas, S. Bhattacharya, S. Chattopadhyay, S. Saha, M.K. Sharan, Y.P. Viyogi
  Proceedings of the XVII DAE-BRNS High Energy Physics Symposium.
  December 2006, 335.

- **Development of Resistive Plate Chamber using Bakelite.**
  Authors: S. Biswas, S. Bhattacharya, S. Chattopadhyay, S. Saha, M.K. Sharan, Y.P. Viyogi
  Proceedings of the DAE Symposium on Nuclear Physics.
  Volume 52, (2007), 593.

- **Resistive Plate Chamber for Neutrino Oscillation Experiment.**
  Authors: S. Biswas, S. Bhattacharya, S. Bose, S. Chattopadhyay, S. Saha, Y.P. Viyogi
  Proceedings of the National seminar on New Era in Nuclear and Particle Physics.
  (To be published)
  November 2008.

- **RPC with high-resistive Indian-bakelite electrodes for low-rate operation.**
  Authors: S. Biswas, S. Bhattacharya, S. Bose, S. Chattopadhyay, S. Saha, Y.P. Viyogi
  Proceedings of the XVIII DAE-BRNS High Energy Physics Symposium.
  Volume 18, (2008), 289.

- **Development of silicone-coated Bakelite RPC.**
  Authors: S. Biswas, S. Bhattacharya, S. Bose, S. Chattopadhyay, S. Saha, Y.P. Viyogi
  Proceedings of the DAE Symposium on Nuclear Physics.
  Volume 53, (2008), 687.

- **Time resolution measurement of silicone coated bakelite Resistive Plate Chamber.**
  Authors: S. Biswas, S. Bhattacharya, S. Bose, S. Chattopadhyay, S. Saha, Y.P. Viyogi
  Proceedings of the International Symposium on Nuclear Physics.
  Volume 54, (2009), 660.

- **Development of multigap RPC.**
  Authors: A. Banerjee, A. M. Ghosh, S. Biswas, S. Bhattacharya, S. Bose, S. Chattopadhyay, M. R. Dutta Majumdar, S. Saha, Y.P. Viyogi
  Proceedings of the International Symposium on Nuclear Physics.
  Volume 54, (2009), 662.

- **Development of 1m × 1m bakelite Resistive Plate Chamber for INO-ICAL prototype.**
  Authors: S. Biswas, S. Bhattacharya, S. Bose, S. Chattopadhyay, S. Saha, Y.P. Viyogi
  Proceedings of the National Symposium on Nuclear Instrumentation.
  February, (2010), 269.

  Other relevant publications

- **Development of bakelite based Resistive Plate Chambers.**
  Authors: S. Biswas, S. Bhattacharya, S. Bose, S. Chattopadhyay, S. Saha, M.K. Sharan, Y.P. Viyogi
  e-Print: **arXiv:0802.2766v1** [nucl-ex]

Reprints

Performances of linseed oil-free bakelite RPC prototypes with cosmic ray muons

S. Biswas [a,*], S. Bhattacharya [b], S. Bose [b], S. Chattopadhyay [a], S. Saha [b], M.K. Sharan [b], Y.P. Viyogi [c]

[a] Variable Energy Cyclotron Centre, 1/AF Bidhan Nagar, Kolkata 700 064, India
[b] Saha Institute of Nuclear Physics, 1/AF Bidhan Nagar, Kolkata 700 064, India
[c] Institute of Physics, Sachivalaya Marg, Bhubaneswar, Orissa 751 005, India

ARTICLE INFO

ABSTRACT

A comparative study has been performed on Resistive Plate Chambers (RPC) made of two different grades of bakelite paper laminates, produced and commercially available in India. The chambers, operated in the streamer mode using argon, tetrafluroethane and isobutane in 34:59:7 mixing ratio, are tested for the efficiency and the stability with cosmic rays. A particular grade of bakelite (P-120, NEMA LI-1989 Grade XXX), used for high voltage insulation in humid conditions, was found to give satisfactory performance with stable efficiency of $>96\%$ continuously for more than 130 days. A thin coating of silicone fluid on the inner surfaces of the bakelite RPC is found to be necessary for the operation of the detector.

1. Introduction

In the proposed India-based Neutrino Observatory (INO), the Resistive Plate Chambers (RPCs) [1] have been chosen as the prime active detector for muon detection in an Iron Calorimeter (ICAL), which will be used for studying atmospheric neutrinos [2]. Detailed studies are being performed on glass RPCs for INO [3]. In this article, we report a parallel effort on building and testing of the RPC modules using the bakelite obtained from the local industries in India. The aim of this study is to achieve stable performance of such a RPC detector for prolonged operation in streamer mode.

2. Construction of the RPC modules

Two $300\,\text{mm} \times 300\,\text{mm} \times 2\,\text{mm}$ bakelite sheets are used as electrodes. The inner surfaces of the two sheets are separated by a 2 mm gap. Uniform separation of the electrodes is ensured by using five button spacers of 10 mm diameter and 2 mm thickness, and edge spacers of $300\,\text{mm} \times 8\,\text{mm} \times 2\,\text{mm}$ dimension, both being made of polycarbonate. Two nozzles for gas inlet and outlet, also made of polycarbonate, are placed as part of the edge spacers. The edges of the modules are sealed by applying a layer of the epoxy adhesive to prevent permeation of moisture. The 2 mm thick active gas gap of the RPC modules are leak-checked using argon and helium sniffer probes.

After cleaning, a graphite coating is made on the outer surfaces of bakelite sheets to form the electrodes. A gap of 10 mm from the edges to the graphite layer is maintained to avoid external sparking. The surface resistivity varies from $500\,\text{K}\Omega/\square$ to $2\,\text{M}\Omega/\square$ for different electrode surfaces. The graphite coating, applied by using a spray gun, however, results in a non-uniformity (less than 20%) for a particular coated surface. Two small ($20\,\text{mm} \times 10\,\text{mm}$) copper foils $\sim 20\,\mu\text{m}$ thick are pasted by kapton tape on both the outer surfaces for the application of high voltage (HV). The HV connectors are soldered on these copper strips. Equal HVs with opposite polarities are applied on both the surfaces.

In order to collect the accumulated induced charges, pick-up strips are placed above the graphite coated surfaces. The pick-up strips are made of copper ($20\,\mu\text{m}$ thick), pasted on one side of 10 mm thick foam. The area of each strip is $300\,\text{mm} \times 30\,\text{mm}$ with a separation of 2 mm between two adjacent strips. The pick-up strips are covered with $100\,\mu\text{m}$ thick kapton foils to insulate them from the graphite layers. The ground plane, made of aluminium, is pasted on the other side of the foam. The signals from different strips are sent through a ribbon cable, followed by RG-174/U coaxial cables using proper impedance matching.

3. Measurement of bulk resistivity of bakelite

The bakelite sheets are phenolic resin bonded paper laminates. In the present work, two types of bakelite sheets have been used

to build several detector modules. They are (a) Superhylam and (b) P-120.

The P-120 grade bakelite is manufactured by Bakelite Hylam, India, and the Superhylam grade is obtained from the other manufacturer Super Hylam, India. The surfaces of P-120 are matt finished whereas Superhylam is glossy finished. Specifications are given in Table 1.

The bulk resistivity of the electrode plates of the RPC is an important parameter [4,5]. The high resistivity helps in controlling the time resolution, counting rate and also prevents the discharge from spreading through the whole gas [1,6,7]. We have measured the bulk resistivities of the bakelite sheets via the measurement of the leakage current.

This measurement is performed at the same place and the same environment where the RPCs have been tested. The test setup is kept in an air-conditioned room. The temperature and humidity have been monitored during the experiment. The bulk resistivities of different grade materials at 4 kV are presented in Table 1. The bulk resistivity (ρ) vs. voltage (V) characteristics of different grade materials are shown in Fig. 1. It is clear from the

Table 1
Mechanical and electrical properties of different grades of bakelites.

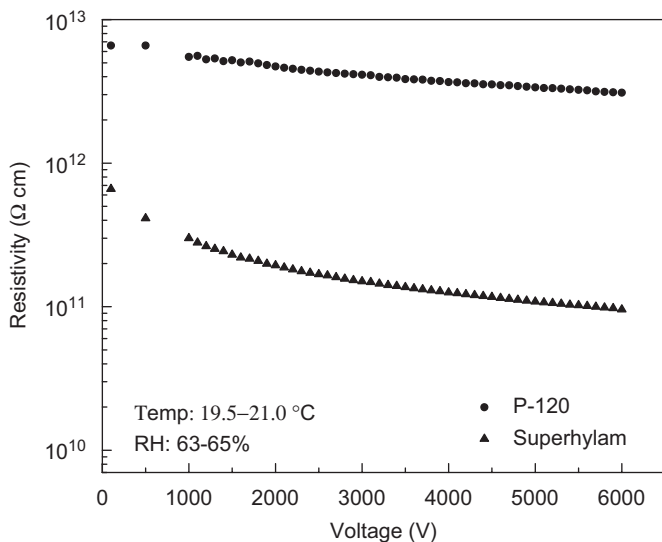| Trade name	NEMA LI-1989 Grade	BS-2572 Grade	Density (g/cc)	Electrical strength (kV/mm)	Surface finish	Bulk resistivity (Ω cm)
Superhylam	–	P2	1.72	9.5	Glossy	1.25×10^{11}
P-120	XXX	P3	1.22	9.5	Matt	3.67×10^{12}

Fig. 1. The bulk resistivity (ρ) as a function of the applied voltage for the two grades of bakelites.

Table 2
Name and materials of different RPC.

Detector name	Electrode material	Surface resistivity kΩ/□	
		Anode	Cathode
SH	Superhylam	500	500
IB1	P-120	2000	2000
IB2	P-120	1600	1000
IB3	P-120	1300	1000

figure that the bulk resistivity is considerably higher for the P-120 grade bakelite. Three modules are constructed with P-120 grade and these are referred to as IB1, IB2 and IB3 in the following text whereas one module is made using Superhylam grade and is referred to as SH. The name, electrode materials and graphite surface resistivity of different RPCs are given in Table 2.

4. Cosmic ray test setup

Fig. 2 shows the schematic of the setup for testing the RPC modules using cosmic rays. Three scintillators, two placed above the RPC plane and one placed below, are used for obtaining the trigger from the incidence of the cosmic rays. The coincidence between scintillator I ($350\,mm \times 250\,mm$ size), scintillator II ($350\,mm \times 250\,mm$ size) and the finger scintillator(III) ($200\,mm \times 40\,mm$ size) is taken as the Master trigger. Finally, the ORed signal obtained from two adjacent pick-up strips of the chamber is put in coincidence with the master trigger obtained above. This is referred to as the coincidence trigger of the RPC. The window of the cosmic ray telescope is of the area $200\,mm \times 40\,mm$. The width of the finger scintillator is made smaller than the total width of the two adjacent readout strips. A correction has been applied for dead zones (of area $200\,mm \times 2\,mm$) in between two adjacent readout strips.

The HVs to the RPC are applied at the ramping rate of 5 V/s on both the electrodes. The streamer pulses are obtained starting from the HV of 5 kV across the RPC. The leakage current as measured by the HV system is recorded for further study.

The leading edge discriminators are used for the scintillators and the RPC pulses. Various thresholds are used on the discriminators to reduce the noise. For our final results, a threshold of 40 mV is used on the RPC signal. We have used a CAMAC-based data acquisition system. Counts accumulated in a scalar over a fixed time period are recorded at regular intervals, and saved in a periodic log database. The temperature and the humidity are monitored at the time of measurement.

The gases used in the RPC are mixtures of Argon, Isobutane and Tetrafluroethane (R-134a) in 34:7:59 mixing ratio. The gases are pre-mixed, stored in a stainless steel container and sent to the detector using stainless steel tubes. A typical flow rate of 0.4 ml/min resulting in $\sim$3 changes of gap volume per day is maintained by the gas delivery system. Variation of less than 4% is found in the mixing ratio for Argon, Isobutane and R-134a in a systematic analysis by a Residual Gas Analyzer.

5. Results

An important and obvious goal of any RPC detector development is to study the long-term stability with high efficiency. In that spirit, the following studies are performed in the cosmic ray test bench of the RPC detectors.

The efficiency of the RPC detector, taken as the ratio between the coincidence trigger rates of the RPC and the master trigger rates of the 3-element plastic scintillator telescope as mentioned in Section 4, is studied by varying the applied HV for each detector. The rates are calculated from the data taken over 30 min duration for each HV setting. The temperature and humidity during these measurements are recorded to be about $22-25\,°C$ and 63–65%, respectively. The average master trigger rate is $\simeq 0.005\,Hz/cm^2$. The variation of efficiency with applied HV is shown in Fig. 3(a) and that of the counting rates with the HV is shown in Fig. 3(b). It is seen that for both the bakelite grades, the efficiency has increased from 20% to 75% as HV is ramped up from 6.5 to 6.8 kV. The efficiency for the SH RPC gradually
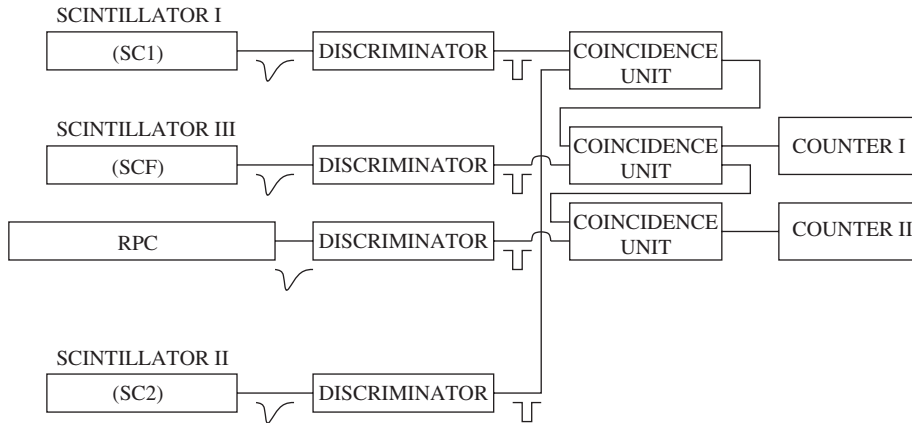
Fig. 2. Schematic representation of the cosmic ray test setup.
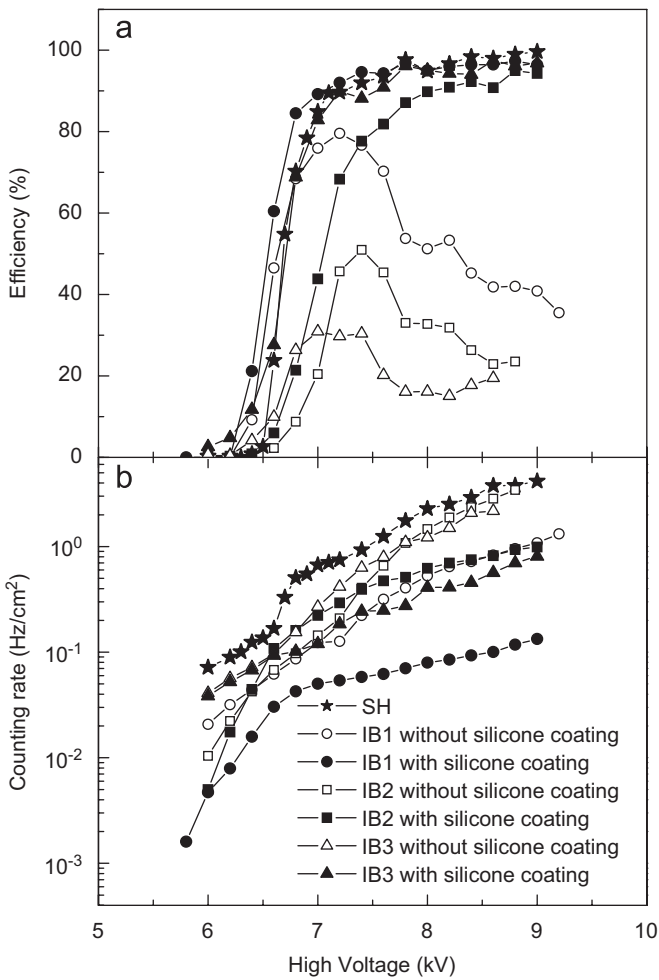
Fig. 3. (a) The efficiency as a function of high voltage for RPCs [three RPCs made with P-120 grade bakelite (with and without silicone coating) and one made with Superhylam grade bakelite] obtained with a gas mixture of Argon (34%) + Isobutane (7%) + R-134a (59%). The thresholds are set at 40 mV for IB1, IB2 and IB3 and 50 mV for SH. (b) Counting rate as a function of high voltage.

Fig. 4. Linear surface profile scans of the two grades of bakelite sheets.

increases and reaches the plateau at ~96% from 7.5 kV, while that of the IB1 RPC reaches a maximum of ~79% at 7.2 kV and then decreases steadily up to ~35% as the HV is increased to 9 kV. The counting rates in both the cases, however, have increased more or less exponentially with sudden jumps around 6.5–7.0 kV

(see Fig. 3(b)), i.e. near the points where the efficiency becomes uniform (in the case of SH) or starts to decrease (in the case of IB1). This possibly indicates the onset of a breakdown regime that recovers in a reasonable time for the SH but works the other way for the IB1. Similar behavior is observed also for IB2 and IB3. IB2 and IB3 are made to study the consistency of the results. It should, however, be noted that both the counting rate and the leakage current of the SH are larger than those of the IB1, IB2 and IB3, which are expected on the basis of smaller bulk resistivity of the Superhylam grade bakelite [8].

In order to investigate the reason for the phenomena of reduction of efficiency in the IB1 above ~7.2 kV, and taking cue from the fact that Superhylam surfaces are glossy finished while the P-120 surfaces are matt finished, we have dismantled the detectors and made surface profile scan over a 5 mm span of the surfaces using DekTak 117 Profilometer. These scans are shown in Fig. 4. It is clearly seen that both the surfaces have a short range variation (typically ~0.1 μm length scale) and a long range variation (typically ~1 μm length scale). The long range surface

fluctuation, which is a measure of non-uniformity, averaged over several scans are $0.84 \pm 0.12\,\mu m$ (P-120) and $0.49 \pm 0.17\,\mu m$ (Superhylam). Thus the long range fluctuations, within the limits of experimental uncertainties, are nearly the same. On the other hand the short range fluctuations, a measure of surface roughness, are $0.64 \pm 0.06\,\mu m$ (P-120) and $0.17 \pm 0.02\,\mu m$ (Superhylam), and thus indicate a superior surface quality of the Superhylam grade.

To explore a remedial measure for the IB1 RPC, we have applied a thin layer of viscous silicone fluid (chemical formula: $[R_2SiO]_n$, where R = organic groups such as methyl, ethyl, or phenyl) [coefficient of viscosity = $5.5\,Pa\,s$ at $23\,°C$, manufactured by Metroark Limited, Kolkata, India] on the inner surfaces of the P-120 bakelite sheets. About $1\,g$ of the fluid is applied over $300\,mm \times 300\,mm$ area. Based on the specific gravity (1.02 at $23\,°C$) of the fluid, the estimated coating thickness would be $\sim 10\,\mu m$. This material is chosen for the following reasons: (a) very low chemical reactivity with the gases used; (b) good thermal stability over a wide temperature range (from -100 to $250\,°C$); (c) very good electrical insulator; (d) excellent adhesion to most of the solid materials, and (e) low vapour pressure, which is essential for stable operation over a reasonable time period. The silicone treated surfaces are kept under infrared lamp for 2 hours to allow the viscous fluid to fill all the micro-crevices on the surface. The reassembled detector is tested at the same setup. The results of efficiency and count rate measurements, shown in Figs. 3(a) and (b), respectively, indicate a remarkable improvement in the performance of the P-120 detector. The efficiency increases from 20% to 75% as the HV is increased from 5.7 to 6.2 kV, while the single count rate as a whole has decreased by a factor of 5. This indicates quenching of micro-discharge after silicone treatment, which is very much desirable for the functioning of the detector. The efficiency in this case reaches $>95\%$ plateau at 7 kV. Improvement on performances is also observed for the IB2 and IB3 after the application of silicone fluid on the inner surfaces as shown in Figs. 3(a) and (b).

It is worth noting that surface treatment with insulating/non-polar liquid as a remedial measure was first demonstrated for the BaBar RPCs. However, it was observed that the formation of stalagmites by the polymerisation of uncured linseed oil droplets had created conducting paths through the gap, thereby causing irreversible damage to the bakelite plates [9]. The process of linseed oil treatment was later changed by increasing the proportion of eptane as a solvent to produce a thinner coating ($10-30\,\mu m$) on the inner surface [10]. Our observation that silicone coating of the inner surfaces aides the proper functioning of our P-120 bakelite RPC detector once again confirms the importance of smooth surface finish of the inner surfaces.

To judge the improvement in the overall performance of the RPC detector, we have measured the leakage current through the RPC detector with and without silicone coating and the plot of these as a function of the applied HV is shown in Fig. 5. Both the plots show a common feature that the current–voltage curves have two distinctly different slopes as it has been shown earlier [11]. While the gas gap behaves as an insulator in the lower range of applied voltage and hence the slope over this span scales as the conductance of the polycarbonate spacers, at higher range of voltage, the gas behaves as a conducting medium due to the formation of the streamers. Therefore, the slope over this range scales as the conductance of the gas gap. It is seen that the slope in the higher range of voltage is much steeper for the RPC without silicone coating and hence it points to the fact that some sort of uncontrolled streamers are being formed in the gas gap causing a degradation of the efficiency [12]. This possibly does not happen in the RPC detectors with silicone coating.
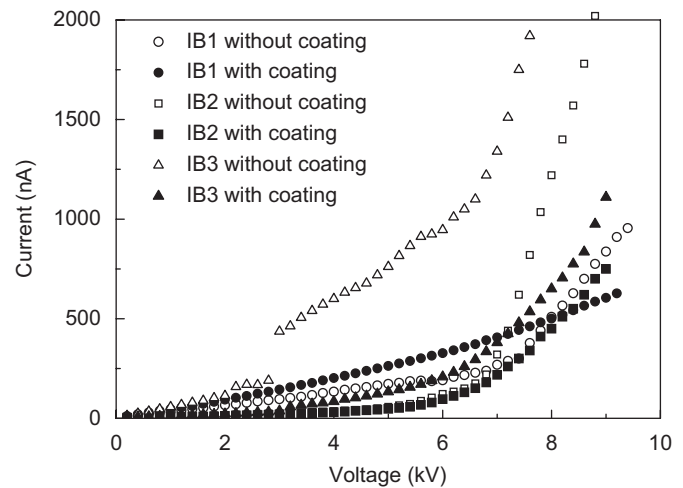
Fig. 5. Current as a function of the applied voltage for RPC made by P-120 grade bakelite.
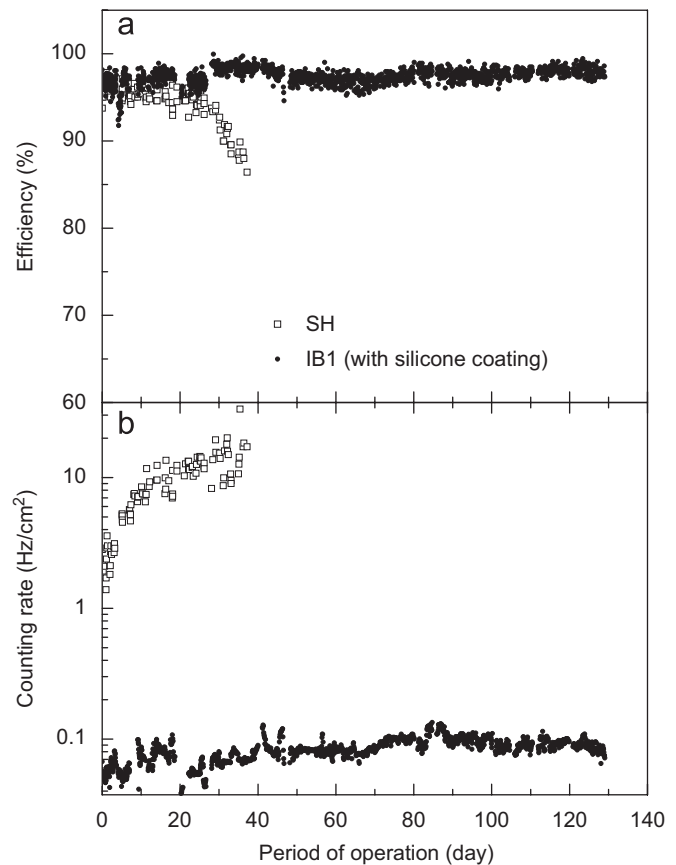
Fig. 6. (a) Efficiency as a function of period of operation for two RPC prototypes. Operating voltage is 8 kV for both the RPC. (b) The counting rate as a function of the period of operation for the two RPC prototypes.

The long-term stability of the bakelite RPCs has been studied using the same cosmic ray test setup. The coincidence trigger counts of the RPCs and the master trigger counts, accumulated over every 2 hours, have been recorded continuously for more than 4 months at a HV of 8 kV. The average room temperature and the relative humidity have been recorded to be $22-25\,°C$ and 63–65%, respectively. The count rates of the RPCs have also been recorded simultaneously. Figs. 6(a) and (b) depict the variation of

efficiency and count rates over the above-mentioned period for both the grades of RPCs. The SH RPC had worked with an efficiency of $>95\%$ which remained steady for 25 days, but beyond that it deteriorated gradually to $\sim86\%$ efficiency within the next 13 days. The count rate, however, had increased from 1 to $10\,Hz/cm^2$ within 10 days, and then it increased slowly over the next 28 days. After that period, the count rate shot up to $>30\,Hz/cm^2$. The leakage current gradually increased from 3–4 to $>10\,\mu A$ within that period. The test on this RPC was discontinued after 38 days and the silicone coated IB1 RPC was mounted. The efficiency measured was $\sim96\%$ and above and has remained steady for more than 130 days. The count rate also has remained steady around $0.1\,Hz/cm^2$. The leakage current was found to be marginally dependent on temperature and humidity, though it has remained steady at $\sim400\,nA$ during the operation.

The SH RPC has also been tested again after a gap of a few months. It has shown the same higher leakage current ($>10\,\mu A$) and lower efficiency ($\sim86\%$) indicating that some intrinsic breakdown of the bulk material may have taken place.

6. Conclusions and outlook

In conclusion, a comparative study of bakelite RPCs made from two different grades of bakelites commercially available in India is performed. The RPC, made of Superhylam grade bakelite with glossy finished surface, is found to have a shorter life. On the other hand, the RPCs made from P-120 grade bakelite with matt finished surfaces, which are coated with a thin layer of viscous silicone fluid, are found to work steadily for more than 130 days showing a constant efficiency of $>96\%$ without any degradation. The detector is found to be less immune to variation in humidity which makes it a viable alternative to semiconductive glass based RPC for use in the ICAL detector of the INO.

Application of silicone fluid on the surface shows improved performance, suggesting the making of a smoother surface. As a future plan, we will perform in detail the study of the properties of the surfaces after silicone coating. A detailed analysis will be performed on the exhaust gas to understand the effect of silicone, if any. Further studies include the performance of RPCs at higher rate and of larger size.

References

[1] R. Santonico, R. Cardarelli, Nucl. Instr. and Meth. 187 (1981) 377.
[2] INO Project Report, INO/2006/01, June 2006 ⟨http://www.imsc.res.in/~ino/⟩.
[3] V.M. Datar, et.al., Nucl. Instr. and Meth. A (2009), this issue.
[4] G. Aielli, et al., Nucl. Instr. and Meth. A 533 (2004) 86.
[5] G. Bencivenni, et al., Nucl. Instr. and Meth. A 332 (1993) 368.
[6] R. Cardarelli, A. Di Ciaccio, R. Santonico, Nucl. Instr. and Meth. A 333 (1993) 399.
[7] H. Czyrkowski, et al., Nucl. Instr. and Meth. A 419 (1998) 490.
[8] Gy. L. Bencze, et al., Nucl. Instr. and Meth. A 340 (1994) 466.
[9] F. Anulli, et al., Nucl. Instr. and Meth. A 508 (2003) 128.
[10] F. Anulli, et al., Nucl. Instr. and Meth. A 539 (2005) 155.
[11] J. Zhang, et al., Nucl. Instr. and Meth. A 540 (2005) 102.
[12] I. Crotty, et al., Nucl. Instr. and Meth. A 337 (1994) 370.

Control system for a four-component gas mixing unit

S. Bose [a,*], S. Biswas [b], S. Saha [a], M.K. Sharan [a], S. Bhattacharya [a]

[a] *Saha Institute of Nuclear Physics, I/AF Bidhan Nagar, Kolkata 700064, India*
[b] *Variable Energy Cyclotron Centre, I/AF Bidhan Nagar, Kolkata 700064, India*

ARTICLE INFO

ABSTRACT

Resistive Plate Chambers (RPC), planned to be used in the ICAL detector of the Indian Neutrino Observatory (INO) project, need precise mixing of four different gases, as well as precise control of the flow rate of the mixed gas. The designed system has the capability to pre-mix the gases (static mode), which can be stored in a pressurized vessel for subsequent use. The unit can also dynamically control the ratio of the four constituent gases (dynamic mode) and deliver it at a controlled flow rate through the mixing volume to the RPC.

© 2009 Elsevier B.V. All rights reserved.

1. Introduction

The Resistive Plate Chamber (RPC) detectors operate with a mixture of argon, isobutane, tetrafluoroethane and sulfur hexafluoride as active gas. These detectors are operated at 1 bar pressure, but the mixed gas has to be pure, free of dust particles, and maintained at a constant mixing ratio of the component gases. The detector has to be operated in the uniform flow mode to renew the gas in the detector volume approximately at the rate of 2–3 volume changes per day. Such a gas mixing system was developed for the prototyping of RPC detectors of the massive magnetized iron calorimeter of the proposed Indian Neutrino Observatory (INO) [1]. Description of the gas mixing system and its performance are reported in this paper.

2. Description

A photograph of the four-component gas mixing system is shown in Fig. 1, and a schematic layout is given in Fig. 2. It consists of two parts: a gas control hardware (GCH) unit containing pressure regulators, filters, valves, flow controllers, and associated plumbing, and an electronic controller and display (ECD) unit. The system contains a stainless steel mixing vessel (MV) which has 10 cascaded mixing volumes, inter-connected to enhance mixing while passing through an elongated path of gas flow. The pressure and temperature inside the four-input mixing vessel are monitored and displayed electronically. Four different gas cylinders are connected to the system through pressure regulators and quick-connect (QC) valves in each channel. The gases, after passing through active silica gel drying columns and $0.5\,\mu m$ filters, pass

through three way valves (TWV), and normally closed electromagnetic valves (EV). The alternate ports of the TWVs are used for gas purging and evacuation of the inlet side to maintain purity. The four lines are then connected to the mass flow controllers (MFC), with optional by-pass lines through the manual control valves (CV) for the static mode of operation. Non-return valves (NRV) to the MV are also provided for safety, reliability and stability of gas flow. All the rigid connections between the gas flow components are done using $\frac{1}{4}$ in. OD SS-304L tubings and compression fittings to ensure leak tightness of the joints. All these connections are leak-checked using helium sniffer probe. The flexible connections, though only ~5% of the total plumbing length, are made using Tygon[TM] tubings.

The auto-lock feature of the QC isolates the systems from the ambient when the input line is disconnected. One TWV in the output line of the MV connects it either to the RPC detector through CV and QC, or to a vacuum pump for evacuation of the system, which is needed when the gas mixing ratio has to be changed. A safety bubbler, connected parallel to the output QC releases the mixed gas to the exhaust line in case of occasional increase of pressure in the inlet side of the RPC. The return line from the RPC is connected to the exhaust through a safety bubbler placed in the ECD unit. Diffusion pump fluid (DC-704) is used inside the bubblers.

3. Control circuit principle for gas mixing

The electronic controller and display operates the EV, displays the percentage setting of the component gases and the final volume flow rate for every channel, as well as the pressure monitor (PM) and temperature monitor (TM) readings. It also controls the percentage setting of each gas component, and the final flow rate of the mixed gas.

*Corresponding author.
E-mail address:* suvendunath.bose@saha.ac.in (S. Bose).

In the static mixing mode, the component gases are sequentially filled using the known partial pressure of each of the components in the mixed gas. The control switch for EV in each channel is operated to select the channel, and the displays for PM and TM are used for mixing the gases in the desired proportion. The MFCs are bypassed through CVs for sequential filling of the component gases. The final flow rate is controlled by the CV at the output line, and the other displays are not used. The absolute flow rate of the mixed gas to the RPC is measured from the safety bubbler at the RPC output, which is pre-calibrated by volume displacement of water column held in a measuring cylinder.

In the dynamic mixing mode, the gases are mixed in the ratio of their individual mass flow rates (MFR). The control signals to the MFCs to preset the flow rates are obtained from the calibration data of the individual MFCs. Relevant details of the four MFCs used in the system are given in Table 1. The control signals for each MFC are generated electronically using the formula

$$R = K(P_{Ar} + P_{R134a} + P_{IB} + P_{SF_6}),\qquad(1)$$

where R is the flow rate of the mixed gas, and K is the desired total flow rate (in % of maximum flow rate), P_{Ar}, P_{R134a}, P_{IB}, and P_{SF_6} are the mass flow rates of Argon, Isobutane, R-134a, and SF_6 in percent of their maximum flow rates.
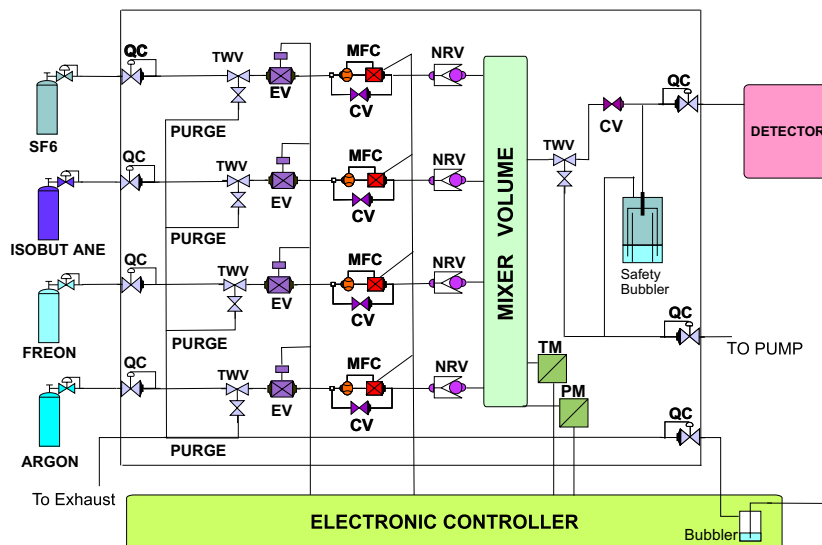

Fig. 1. Photograph of the gas mixing system.

Control scheme of the gas mixing system is shown in Fig. 3. The potentiometer P0 sets the value of K in terms of the voltage derived from the drop across a temperature compensated zener, and P1, P2, P3 and P4 set the flow rates of the MFC used for argon, R134a, isobutane and SF_6, respectively. R1 to R4 set the minimum flow rates in each channel. Each potentiometer drives a voltage to current converter for converting the generated control voltage to the current required to drive the 4–20 mA control current loop of each MFC. The control voltages thus generated are summed up and used to display the percentage flow with the help of the analog divider A/B as shown. The output current from each MFC, indicating the actual volume flow rate, through the 4–20 mA current loop, is again converted to voltage by current to voltage converter and are displayed in litres per hour.

4. Results

Each digital voltmeter used in the display and the converters (V to I and I to V) have been tested and calibrated using Fluke 8865 calibrator. The errors in the converters are less than 0.5% and temperature coefficients are ~100 ppm/°C. Before commissioning, the MFCs were first tested with clean air to check the calibration supplied by the manufacturer. The flow rates and the final ratio settings indicate good agreement with the MFC specifications for different gases within systematic uncertainties of less than 5%.

The gas mixing system was then used either in the static or in the dynamic mixing mode to feed the mixed gas to the RPC detectors. In most of the test runs, the detectors were operated in the streamer mode using three gases in the ratio Ar: Isobutane: R134a = 34 : 59 : 7. Performance and long term stability of the bakelite RPC detectors operated with the gas mixing system has

Table 1
Specifications of the mass flow controllers used.

Gas	Maximum flow rate (l/h)	Range of MFC to preset (percent of maximum flow rate)
Argon	2.5	40–50
R-134a	2.5	40–50
Isobutane	0.5	1–10
SF$_6$	0.1	0.1–2

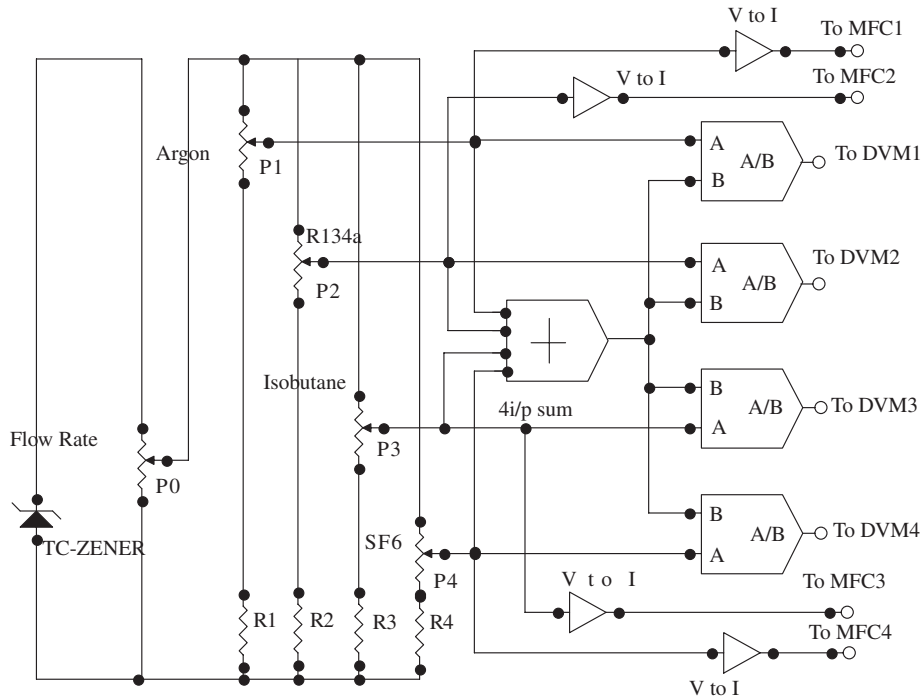**Fig. 2.** Schematic layout of the gas mixing system.

Fig. 3. Schematic of the control electronics used for the gas mixing system.

Fig. 4. Results of residual gas analysis (RGA) of the mixed gas for streamer mode of operation.

quadrupole mass spectrometer-based residual gas analyzer (RGA), with residual mass sensitivity of 10–50 ppm over a mass range of 0–200 amu. The sampled gas, taken in a previously evacuated glass enclosure, baked at 150 °C, was fed into the vacuum test chamber where the RGA was mounted. The chamber was evacuated by a turbo pump to maintain a dynamical high vacuum of $< 10^{-5}$ mbar for the RGA system, in order to avoid damaging the sensitive channeltron device inside. The results of these measurements are given in Fig. 4. The average concentrations, measured by the RGA set up for the streamer ratio as mentioned above are: Argon: $37.1 \pm 1.4\%$, Isobutane: $7.2 \pm 0.5\%$, and R134A: $55.7 \pm 1.9\%$, which agree reasonably well within the quoted systematic uncertainties. Variation in concentrations of the gases with time as seen in Fig. 4 is an artifact of the different pumping speeds of the turbo pump for different gas components. Further measurements of the short term and long term stability of the gas mixing system are in progress.

Acknowledgments

been reported elsewhere [2]. The performance of the RPC detector was also studied by varying the gas mixing ratio, and the behavior was found to be similar to the data reported by other groups working on the bakelite and glass RPCs [3,4].

We have also analyzed the component gases of the pre-mixed samples from the detector inlet using a Prisma™ QMS 200

References

[1] INO Project Report, 2006.
[2] S. Biswas, et al., Nucl. Instr. and Meth. A (2009), doi:10.1016/j.nima.2008.12.131.
[3] J. Zhang, et al., Nucl. Instr. and Meth. A 540 (2005) 102.
[4] V.M. Datar, et al., Nucl. Instr. and Meth. A (2009), doi:10.1016/j.nima.2008.12.129.

INO prototype detector and data acquisition system

Anita Behere [a], M.S. Bhatia [a], V.B. Chandratre [a], V.M. Datar [a], P.K. Mukhopadhyay [a], Satyajit Jena [b],
Y.P. Viyogi [c], Sudeb Bhattacharya [d], Satyajit Saha [d], Sarika Bhide [e], S.D. Kalmani [e], N.K. Mondal [e],
P. Nagaraj [e], B.K. Nagesh [e], Shobha K. Rao [e], L.V. Reddy [e], M. Saraf [e], B. Satyanarayana [e,*], R.R. Shinde [e],
S.S. Upadhya [e], P. Verma [e], Saikat Biswas [f], Subhasish Chattopadhyay [f], P.R. Sarma [f]

[a] Bhabha Atomic Research Centre, Mumbai, India
[b] Indian Institute of Technology Bombay, Mumbai, India
[c] Institute of Physics, Bhubaneswar, India
[d] Saha Institute of Nuclear Physics, Kolkata, India
[e] Tata Institute of Fundamental Research, Mumbai, India
[f] Variable Energy Cyclotron Centre, Kolkata, India

ARTICLE INFO

ABSTRACT

India-based Neutrino Observatory (INO) collaboration is proposing to build a 50 kton magnetised iron calorimetric (ICAL) detector in an underground laboratory to be located in South India. Glass resistive plate chambers (RPCs) of about $2\,m \times 2\,m$ in size will be used as active elements for the ICAL detector. As a first step towards building the ICAL detector, a 35 ton prototype of the same is being set up over ground to track cosmic muons. Design and construction details of the prototype detector and its data acquisition system will be discussed. Some of the preliminary results from the detector stack will also be highlighted.

1. Introduction

ICAL is a 50 kton magnetised iron tracking calorimeter, comprising about 140 layers of low carbon 56 mm thick iron plates [1]. Sandwiched between these layers are glass RPCs, which are used as the active detector elements. Lateral dimensions of this cubical geometry detector are $48\,m \times 16\,m \times 12\,m$. About 27,000 RPCs of dimensions $2\,m \times 2\,m$ will be deployed in this detector. The geometry and structure of INO magnet is largely fixed by the principle of ICAL detector. Its purpose is twofold: providing target nucleons for neutrino interactions and also a medium in which secondary charged particles can be separated on the basis of their magnetic rigidity. The iron absorber will be magnetised to a strong field of about 1.5 T. Some of the primary goals of the ICAL detector are to precisely determine oscillation parameters of the atmospheric neutrinos, to study matter effects on the oscillations and finally to use it as a long baseline detector for the neutrino beams from factories in future. It was proposed that we build on surface a modest 35 ton prototype of the ICAL detector. Experience with the prototype will be very useful in planning for the much bigger ICAL detector.

2. Prototype detector design

The structure of the prototype detector is built in the form of a 13 layer sandwich of 50 mm thick low carbon iron (*Tata A-grade*) plates and 12 glass RPCs of $1\,m \times 1\,m$ in area. Each layer is assembled by joining a 'T' and a 'C' shaped iron plate. The prototype detector will provide an active volume of about $1\,m^3$. The overall design of prototype magnet was kept close to the conceived design of the full scale INO magnet. As the prototype magnet detects muons, it serves as the medium in which secondary charged particles can be separated on the basis of their magnetic rigidity. The detector is magnetised to 1.5 T, which enables momentum measurement of 1–10 GeV muons produced by ν_μ interactions within the detector. Four sets of copper coils of 5 turns each, which were made from electrolytic copper conductor tubing having a central bore for flowing low conductivity water, are used for this purpose. The power supply for the magnet coils is a thyristor controlled, three phase low voltage constant current type and has a stabilised reference to regulate the current. Shown on the left in Fig. 1 is the prototype detector magnet in the assembled state and on the right is its B–H curve [2].

RPC gas gaps required for the detector were fabricated using 3 mm thick Asahi float glass sheets procured from the local market [3]. The glass sheets were coated with a semi-resistive paint developed in collaboration with a local paint industry [4].
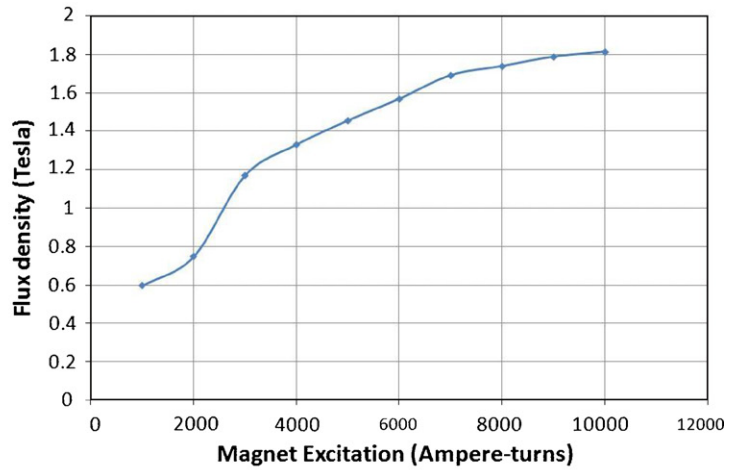
Fig. 1. ICAL prototype detector magnet.

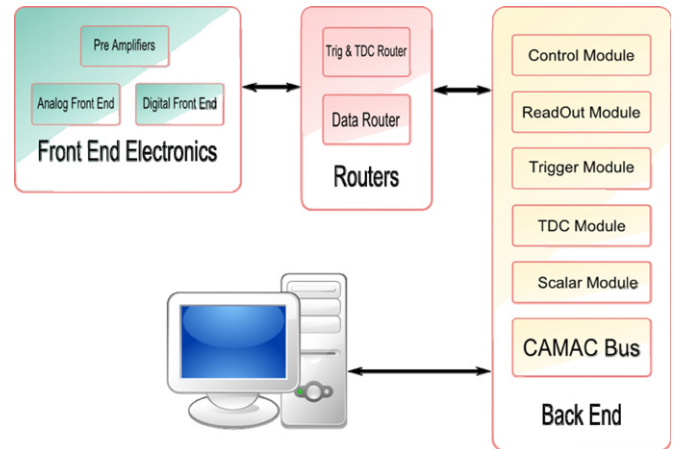Fig. 2. On-line gas mixing and distribution system.

Fig. 3. Schematic of the data acquisition system for the INO prototype detector.

on either side with copper sheets were used for signal pickup as well as for providing rigidity to the assembled chamber. Two panels, each grooved with 30 mm signal pickup strips, were mounted on either side of the gas gap and orthogonal to each other in order to record particle hit coordinates in a plane. The required field across the glass electrodes was set up by applying a differential high voltage using contacts on the semi-resistive coat. There are 64 signal channels in all to be read out from an RPC-32 each on either side.

3. Gas mixing and distribution system

A sophisticated gas mixing and distribution system, which works on four different input gases, has been designed and fabricated [5]. It features molecular sieve based filter columns on the input gas lines, Nippon Tylan made model FC–760 Mass Flow Controllers to precisely mix the gases to required proportion, Parker made fine filters and on-line moister readout on the mixed gas manifold. Mixed gas flow into 16 pneumatically controlled output channels is controlled by 0.3 mm diameter stainless steel capillaries. Each of the output gas channels is equipped with a pair of bubblers, one on the detector input side for protecting the RPC in case of a gas channel block and the other on the output to isolate the chamber from the atmosphere. The gas system also features a facility to add controlled moister into the gas mixture,

Polycarbonate buttons, spacers and gas nozzles, which were developed indigenously and fabricated by local industry, were used to assemble the gas gaps. The gaps were fabricated with the help of a pneumatic jig, which has ensured that the gap between the glass sheets is uniform throughout the gas volume and all the joints are glued well. The RPCs are operated in the avalanche mode using a gas mixture of R134:Isobutane:SF6 in the proportion 95.5:5.0:0.5. Plastic honeycomb based panels padded

which is useful while working with the bakelite RPCs. The entire operation of control and monitoring of gas system is controlled by a PC using a dedicated hardware interface. All the input gas channels have been precisely calibrated over their entire dynamic range by water displacement and other methods. Shown in Fig. 2 is a front view of the gas system.
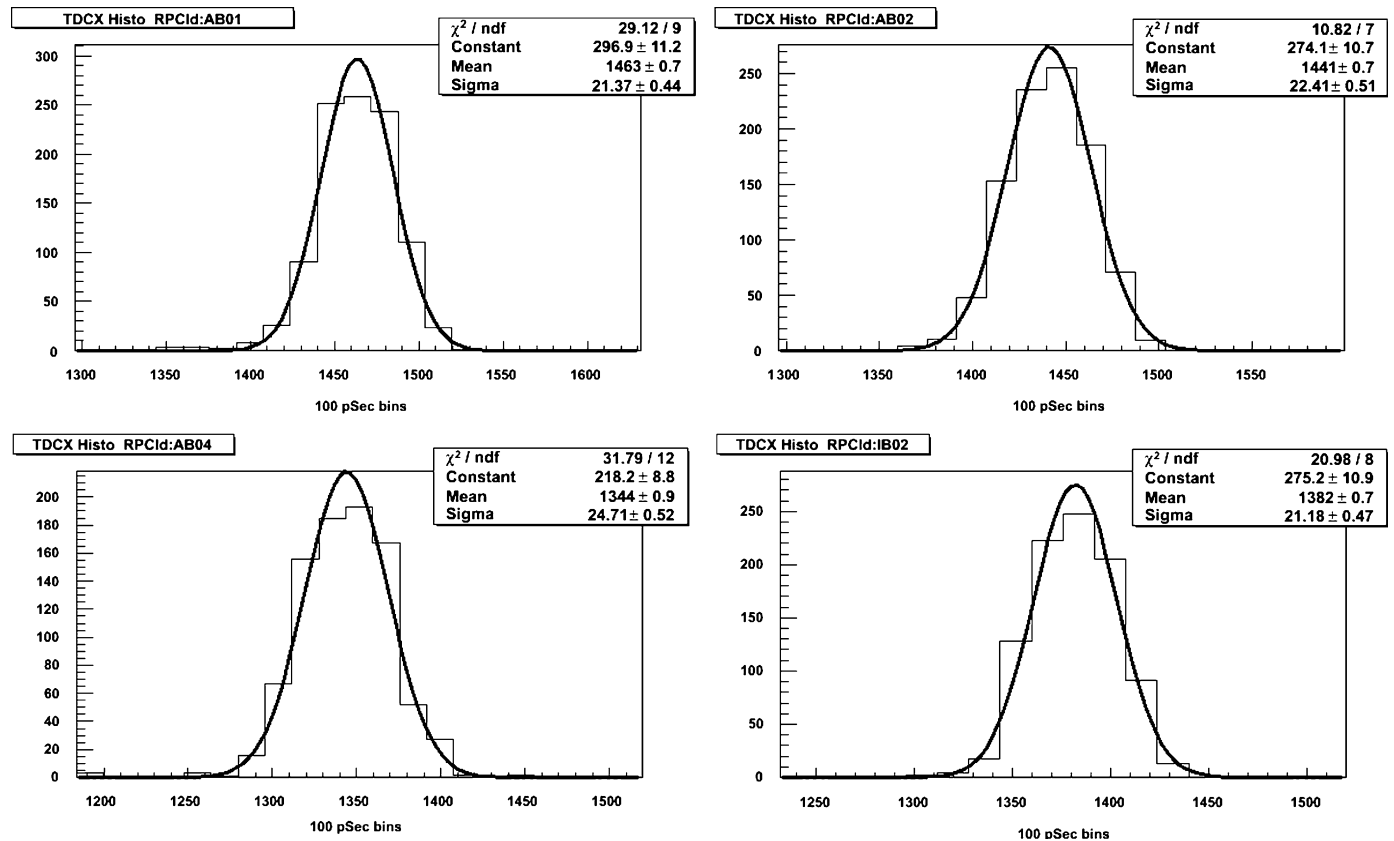

Fig. 4. Stack of INO prototype detector RPCs.

4. Electronics and data acquisition systems

As mentioned above, 64 data channels are to be read out from each of the 12 RPCs. Role of the data acquisition system then is to generate the trigger, based on the hit pattern of the RPC pickup strips and to record strip hit patterns as well as timing of individual RPCs with reference to the trigger. Monitoring the stability of the detector as well as laboratory ambient parameters, such as temperature, relative humidity and barometric pressure, is another important task of the on-line data acquisition system.

The signal readout chain essentially consists of a front-end fast high gain HMC based preamplifier and low level threshold discriminator followed by the digital front-end. The digital front-end built around a couple of CPLD chips handles important tasks of latching the strip hit pattern on master trigger as well as serially transferring the data to back-end. It is also here that the pre-trigger signals are generated, which are used by the back-end trigger module built using combinatorial circuits and produces master trigger. Finally, the digital front-end system also handles the entire signal multiplexing required both during the event data acquisition as well as during strip signal rate monitoring. The timing data are acquired using the commercial TDC modules. The data acquisition is done using a CAMAC backend, employing many custom built modules, such as control and readout modules. The multiplexed signals from the front-end are sent to the back-end through appropriate router modules. Monitoring of strip signal rates is done as a cyclic background job using the scaler module in the back-end. Monitoring of ambient laboratory parameters such as temperature, relative humidity and barometric pressure along with important operating parameters of the RPCs such as high voltage and current is also routinely done and made available on-line on web. Shown in Fig. 3 is a schematic of the data acquisition system for the INO prototype detector.
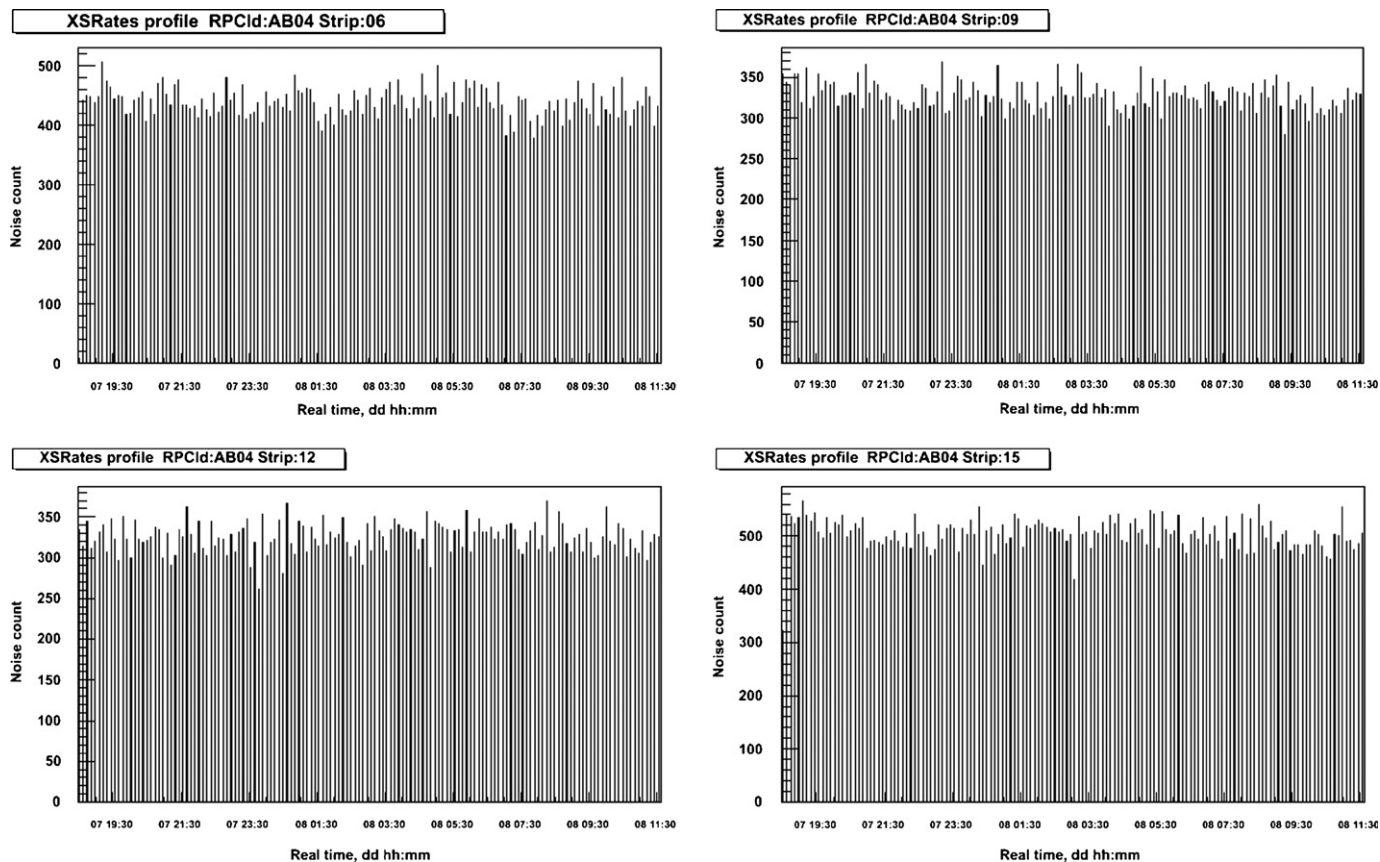

Fig. 5. Time resolution plots of RPCs.

Fig. 6. Noise rate monitor profiles of an RPC.

5. Results

Fig. 4 is a picture of the stack of 12 RPCs of $1\,m \times 1\,m$ in area, along with the front-end electronics mounted in the racks installed on either side of the stack. The stack is in un-interrupted operation now for about a year and the data are being acquired using the on-line system described above. The recorded data are stored in a customised format by the on-line software and is analysed off-line in detail using sophisticated ROOT based analysis software. Some of the aspects that are analysed on a day to day basis are the RPC efficiencies for cosmic ray muons, absolute and relative timing resolutions and the stability of RPCs based on the monitoring data of the individual strip rates.

Timing resolution plots for four individual RPCs is shown in Fig. 5. These RPCs show timing resolutions of about 2 nS with reference to scintillator paddle based trigger signal.

Shown in Fig. 6 are the strip rate monitor profiles of an RPC. As can be seen from the plots, the noise rates are very stable over the period of monitoring inferring the stability of operation of the RPCs under test.

6. Conclusions and outlook

Large area RPCs of dimensions $1\,m \times 1\,m$ required for the ICAL prototype detector were successfully developed, built and characterised. They were operated stably in avalanche mode for a long period of time without any signs of aging and other problems. Electronics, trigger, data acquisition and monitoring system hardware required to operate the detector have been designed and developed indigenously and commissioned. Necessary data analysis tools have also been developed. The prototype detector magnet has been designed, fabricated, installed and was found to produce the designed field. Final integration of the magnet, the active detector elements and the electronics systems is in progress and we expect to start acquiring the data from the prototype detector soon.

References

[1] INO Project Report, INO/2006/01, May 2006.
[2] M.S. Bhatia, et al., Fabrication and testing of the magnet of the prototype Iron calorimetric detector, in: Proceedings of the DAE Symposium on Nuclear Physics, vol. 52, Sambalpur University, 2007, p. 609.
[3] V.M. Datar, et al., Nucl. Instr. and Meth. A (2009), these proceedings, doi:10.1016/j.nima.2008.12.129.
[4] S.D. Kalmani, et al., Nucl. Instr. and Meth. A (2009), these proceedings, doi:10.1016/j.nima.2008.12.150.
[5] S.D. Kalmani, et al., Nucl. Instr. and Meth. A (2009), these proceedings, doi:10.1016/j.nima.2008.12.153.

Development of linseed oil-free bakelite resistive plate chambers

S. Biswas [a], S. Bhattacharya [b,*], S. Bose [b], S. Chattopadhyay [a], S. Saha [b], Y.P. Viyogi [c]

[a] Variable Energy Cyclotron Centre, 1/AF Bidhan Nagar, Kolkata 700 064, India
[b] Saha Institute of Nuclear Physics, 1/AF Bidhan Nagar, Kolkata 700 064, India
[c] Institute of Physics, Sachivalaya Marg, Bhubaneswar, Orissa 751 005, India

ARTICLE INFO

ABSTRACT

In this paper we would like to present a few characteristics of the Resistive Plate Chambers (RPCs) made of a particular grade of bakelite paper laminates (P-120, NEMA LI-1989 Grade XXX), produced and commercially available in India. This particular grade is used for high voltage insulation in humid conditions. The chambers are tested with cosmic rays in the streamer mode using argon, tetrafluroethane and isobutane in 34:59:7 mixing ratio. In the first set of detectors made with such grade, a thin coating of silicone fluid on the inner surfaces of the bakelite was found to be necessary for operation of the detector. Those silicone coated RPCs were found to give satisfactory performance with stable efficiency of >90% continuously for a long period as reported earlier. Results of the crosstalk measurement of these silicone coated RPC will be presented in this paper. Very recently RPCs made with the same grade of bakelite but having better surface finish are found to give equivalent performance even without any coating inside. Preliminary results of this type of RPCs are also being presented.

© 2009 Elsevier B.V. All rights reserved.

1. Introduction

In the proposed India-based Neutrino Observatory (INO), the Resistive Plate Chambers (RPCs) [1] have been chosen as the active detector for muon detection in an Iron Calorimeter (ICAL) [2]. As proposed presently, the ICAL is a sampling calorimeter consisting of 140 layers of magnetized iron, each of 60 mm thickness, using RPCs of 2 m × 2 m area as active media sandwiched between them. A 50 kton ICAL is expected to consist of about 27 000 RPC modules. For the ICAL-RPCs, main design criteria are: (a) moderate position resolution (~1 cm), (b) good timing resolution (~1−2 ns), (c) ease of fabrication in large scale with modular structure and most importantly (d) low cost. The detailed R&D are being performed on the glass RPCs for INO [3]. A parallel effort on building and testing of the RPC modules using the bakelite obtained from the local industries in India is also going on.

At the end of nineties, it was found that the RPCs based on bakelite show serious ageing effects reducing the efficiency drastically [4]. Detailed investigations revealed that the use of linseed oil for the surface treatment in such cases was the main reason for this ageing effect [5,6]. Efforts were subsequently made to look for alternatives to linseed oil treatment, or to develop bakelite sheets which can be used without the application of linseed oil [7].

The aim of the present study is to achieve stable performance of the bakelite RPC detector without linseed oil for prolonged operation. The method of construction of these RPCs and the results of the long term test has been reported earlier [8,10]. In this article we report some other characteristics of the silicone coated bakelite RPC and the initial results of the RPC fabricated without any coating.

2. Design of the prototype RPCS

The RPCs were made of two 300 mm × 300 mm × 2 mm bakelite sheets, used as electrodes, separated by a 2 mm gas gap. A uniform separation of the electrodes was ensured by using five polycarbonate button spacers of 10 mm diameter and 2 mm thickness, and edge spacers of 300 mm × 8 mm × 2 mm dimension. Two polycarbonate made nozzles were used for gas inlet and outlet [9,10].

The high voltages (HV) to the RPC were applied on the graphite coating (surface resistivity ~1 MΩ/□) made over the outer surfaces of the bakelite. The induced RPC signals were collected using copper and foam based pick-up strips, each of area 300 mm × 25 mm with a separation of 2 mm between two adjacent strips. The pick-up strips were covered with 100 μm thick kapton foils to isolate them from the graphite layers.

Premixed gas of Argon, Isobutane and Tetrafluroethane (R-134a) was used in 34:7:59 mixing ratio. A typical flow rate of 0.4 ml per minute was maintained by the gas delivery system, [11], resulting in ~3 changes of gap volume per day.

E-mail address: sudeb.bhattacharya@saha.ac.in (S. Bhattacharya).

3. Cosmic ray test set-up

The RPCs were tested in the same cosmic ray test bench described in Ref. [10]. The coincidence between the signals obtained from the scintillator I (350 mm × 250 mm size), the finger scintillator (III) (200 mm × 40 mm size) which was placed above the RPC plane and the scintillator II (350 mm × 250 mm size) which was placed below, was taken as the Master trigger. Finally, the ORed signal obtained from two adjacent pick-up strips of the chamber was put in coincidence with the master trigger obtained above. This was referred to as the coincidence trigger of the RPC. The efficiency of the RPC detector, taken as the ratio between the coincidence trigger rates of the RPC and the master trigger rates of the 3-element plastic scintillator telescope was measured over an area of 200 mm × 40 mm which was the window of the cosmic ray telescope. The average master trigger rate was $\simeq 0.005\,\text{Hz/cm}^2$.

Fig. 1 shows the schematic of the crosstalk (CT) measurement set-up. The width of the finger scintillator covered one pick-up strip completely and two adjacent strips partially. The signals from these three strips after leading edge discriminator (LED threshold: 40 mV) were sent to the input of a fan in module. The output signal of the previous stage after attenuation was again put to another discriminator. The signal from this discriminator was taken in coincidence with the master trigger. The crosstalk was defined by the ratio of this coincidence count and the master trigger. The attenuation factor was set at 0.3. The fan out signal after attenuation, observed in the oscilloscope, was ~250 mV when one strip fires. The resulting pulse heights were ~440 and 630 mV, respectively, when signals from two strips and three strips came simultaneously. In order to measure the crosstalk between two and three adjacent strips, the discriminator threshold to the fan out signal was set at 280 and 520 mV, respectively.

4. Results

The following properties have been studied in the test set-up for all the chambers: (a) the efficiency of the chambers and their variation with change in different parameters, e.g. HV, gas composition, laboratory environment, etc., (b) the variation of the counting rate, (c) the leakage current and their variation and (d) the long term stability in the streamer mode. The long term behavior of the silicone coated RPCs in the streamer mode has been reported earlier [10]. Some more results are presented in this section.

The efficiency and the counting rate, which is also known as the noise rate, of the RPCs have been studied by varying the applied HV and setting different discriminator threshold values. The variation of the efficiency and the counting rates with the applied HV for three discriminator threshold value of a silicone coated RPC is shown in Fig. 2. It is seen that the counting rate of the RPC decreases with the increase of the threshold value which

is expected with the suppression of noise at a higher threshold value. However, the efficiency curves do not depend much on the threshold setting varying between 20 and 80 mV, except that the efficiency plateau is marginally higher at the lowest threshold setting of 20 mV. A typical screen dump of the oscilloscope pulse at 8 kV is shown in Fig. 3. The figure shows the rise time is about 6 ns, which indicates the fastness of the pulse.

The effect of the environmental humidity on the efficiency curves has also been studied. This measurement was done at relative humidities of 58% and 67% of the laboratory environment and at the room temperature of ~22−25 °C. These curves, plotted in Fig. 4, indicate no effect of humidity on the efficiency. However, the
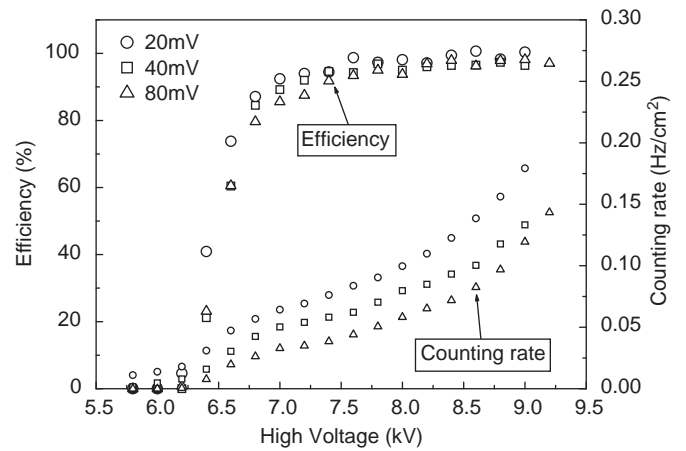

Fig. 2. The efficiency and the counting rate as a function of high voltage for a silicone coated RPC made of P-120 grade bakelite with discriminator threshold values of 20, 40 and 80 mV. The gas mixture used was Argon (34%) + Isobutane (7%) + R-134a (59%).
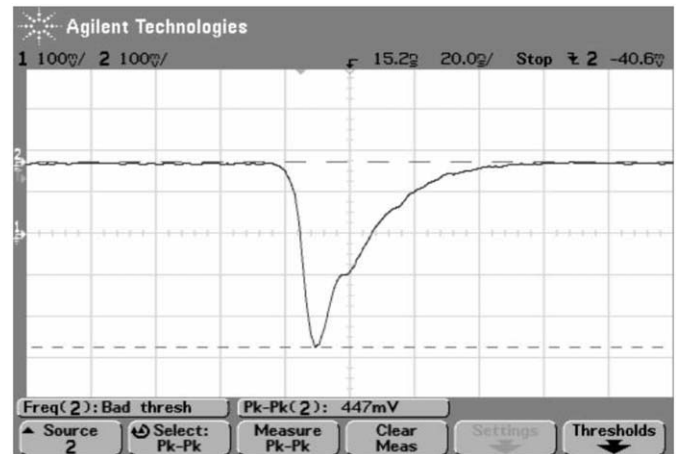

Fig. 3. Average induced pulse on a pick-up strip at 8 kV (100 mV/Div, 20 ns/Div, 50 Ω load) of a silicone coated P-120 grade bakelite RPC.
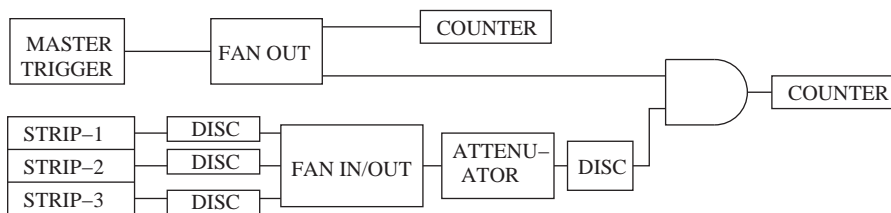

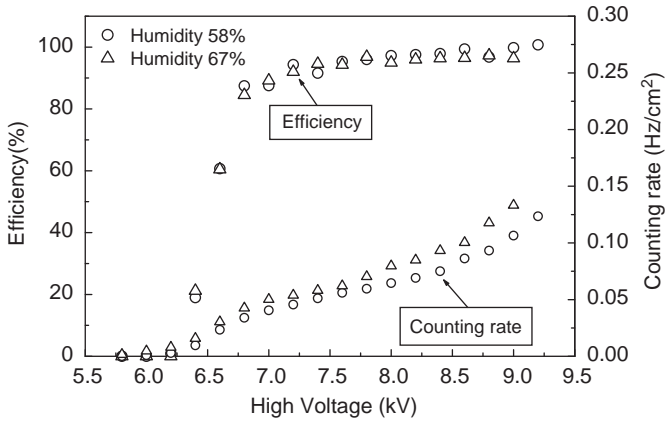**Fig. 1.** Schematic representation of the crosstalk measurement set-up.

Fig. 4. The efficiency and the counting rate versus high voltage for different humidities for a silicone coated P-120 grade bakelite RPC.
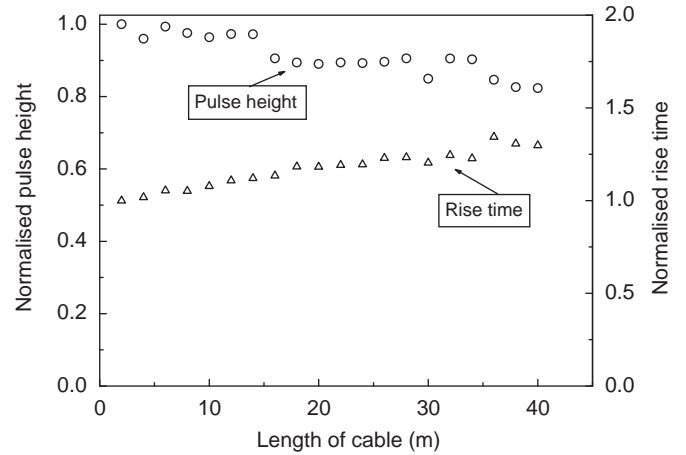

Fig. 5. Current versus voltage for different humidities for a silicone coated P-120 grade bakelite RPC.

Fig. 6. Variation of the normalised pulse height and rise time with the cable length for a silicone coated P-120 grade bakelite RPC.
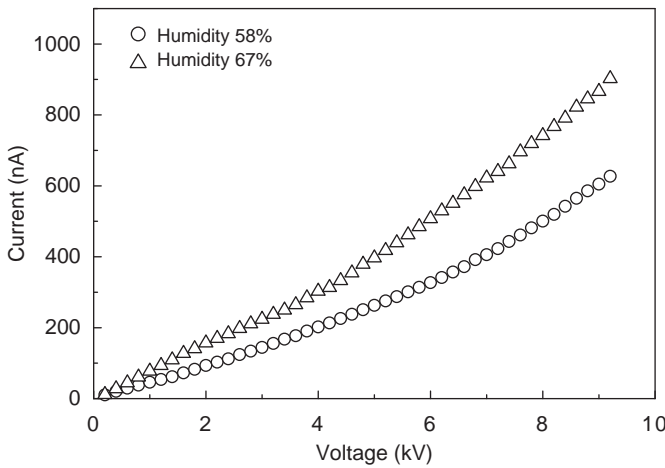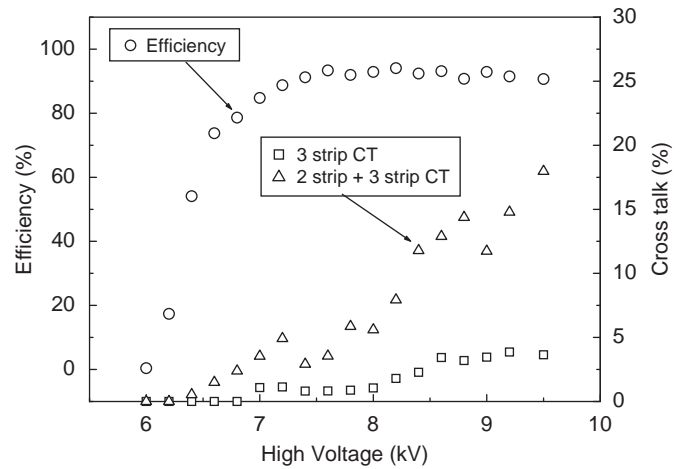

Fig. 7. Variation of the crosstalk with the high voltage in comparison with the efficiency for a silicone coated P-120 grade bakelite RPC.

Fig. 8. The time resolution as a function of HV for a silicone coated P-120 grade bakelite RPC.

counting rate (shown in Fig. 4) and the leakage currents, measured simultaneously and plotted in Fig. 5, are larger at higher humidity. These observations indicate that charge leakage through the exterior surfaces may be contributing more at higher humidity.

The long cable drive of RPC streamer pulse has been tested using RG-174/U coaxial cables. A maximum of 40 m RG-174/U coaxial cable has been used. The average pulse height of RPC in streamer mode was $\sim 300-500$ mV as shown in Fig. 3. The signal amplitude was attenuated to $\sim 80\%$ after 40 m cable drive. The rise time increases slightly at that length of cable. The variation of normalised pulse height and rise time are shown in Fig. 6.

The measurement of the crosstalk for a silicone coated RPC was carried out rigorously. When a single particle induces signal on two or more strips then the term crosstalk comes into the picture. The CT between the two and three RPC strips, defined in Section 3, had been measured by varying the applied HV and is shown in Fig 7. When the discrimination threshold after attenuation was set at 280 mV as stated in Section 3, the signals coming from the two adjacent strips as well as three adjacent strips simultaneously contributed to the crosstalk and it was found to be $<20\%$ (Fig. 7). The crosstalk between the three adjacent strips was found to be $<5\%$. These values of the crosstalk have been taken into account while estimating the final efficiency.

The time resolution of a silicone coated RPC was measured and it was found to be ~ 2 ns (FWHM of the time spectra) at 8 kV. The variation of time resolution with HV of that particular detector is shown in Fig. 8.
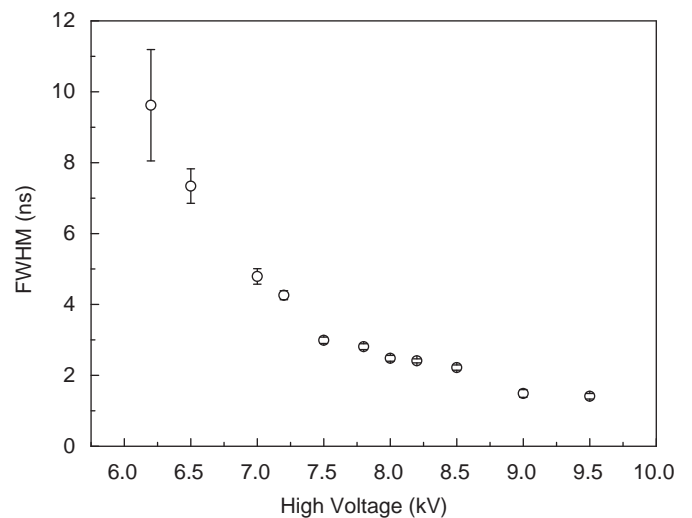
Finally, one module was made with 1.6 mm thick P-120 grade bakelite sheets with better surface finish. No coating was applied to that RPC. The efficiency curve and the variation of the counting
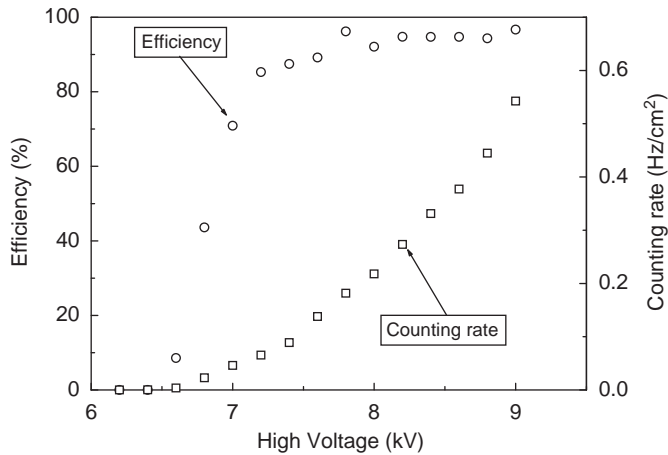
Fig. 9. The efficiency and the counting rate as a function of HV for uncoated P-120 grade bakelite RPC.

rate with HV is plotted in Fig. 9. The current for this particular RPC was found to be higher than that of the silicone coated one. It was about 2 μA at 8 kV.

5. Conclusions and outlook

In conclusion, a rigorous study of RPCs made from a particular grade of bakelite commercially available in India has been performed. An efficiency of >90% is obtained for silicone coated P-120 grade bakelite RPC. The effect of threshold and external humidity on the performance of the RPCs are presented in this paper. The current as well as the counting rate increases with the increase of environmental humidity.

The RPC streamer signals can be driven for a long distance without any significant attenuation. The crosstalk between two neighboring strips (which may be due to some real event) is found to be about 15% and that between three neighboring strips is about 5%. The measured time resolution of a particular silicone

coated RPC is found to be ∼2 ns which is comparable to any single gap glass or linseed oil coated bakelite RPC. Lastly the preliminary data of a uncoated RPC is reported which show encouraging results, as one can plan for large RPC (1 m × 1 m) with this particular grade of bakelite with better surface finish and without any coating.

Further studies in this direction are being carried out which include timing measurements of silicone coated RPCs and performance of oil-less RPCs. These will be reported at a later stage.

Acknowledgements

References

[1] R. Santonico, R. Cardarelli, Nucl. Instr. and Meth. 187 (1981) 377.
[2] INO Project Report, INO/2006/01, June 2006 ⟨http://www.imsc.res.in/~ino/⟩.
[3] V.M. Datar, et al., Nucl. Instr. and Meth. A (2009), doi:10.1016/j.nima.2008.12.129.
[4] J. Va'vra, Nucl. Instr. and Meth. A 515 (2003) 354.
[5] F. Anulli, et al., Nucl. Instr. and Meth. A 508 (2003) 128.
[6] F. Anulli, et al., Nucl. Instr. and Meth. A 515 (2003) 322.
[7] J. Zhang, et al., Nucl. Instr. and Meth. A 540 (2005) 102.
[8] S. Biswas, Talk given at IX International Workshop on Resistive Plate Chambers and Related Detectors, Mumbai, February 2008.
[9] S. Biswas, et al., arXiv:0802.2766.
[10] S. Biswas, et al., Nucl. Instr. and Meth. A (2009), doi:10.1016/j.nima.2008.12.131.
[11] S. Bose, et al., Nucl. Instr. and Meth. A (2009), doi:10.1016/j.nima.2008.12.151.

Study of timing properties of single gap high-resistive bakelite RPC

S. Biswas [a,*], S. Bhattacharya [b], S. Bose [b], S. Chattopadhyay [a], S. Saha [b], Y.P. Viyogi [c]

[a] *Variable Energy Cyclotron Centre, 1/AF Bidhan Nagar, Kolkata 700 064, India*
[b] *Saha Institute of Nuclear Physics, 1/AF Bidhan Nagar, Kolkata 700 064, India*
[c] *Institute of Physics, Sachivalaya Marg, Bhubaneswar, Orissa 751 005, India*

ARTICLE INFO

ABSTRACT

The time resolution for several single gap (2 mm) prototype Resistive Plate Chambers (RPC) made of high resistive ($\rho \sim 10^{10} - 10^{12}\,\Omega\,cm$), 2 mm thick matt finished bakelite paper laminates with silicone coating on the inner surfaces, has been measured. The time resolution for all the modules has been found to be ~2 ns at the plateau region.

© 2009 Elsevier B.V. All rights reserved.

1. Introduction

Performances of several single gap (2 mm) prototype Resistive Plate Chambers (RPC) [1] made of high resistive ($\rho \sim 10^{10} - 10^{12}\,\Omega\,cm$) bakelite paper laminates produced and commercially available in India has been carried out in recent times [2]. A thin silicone coating has been applied to the inner electrode faces of the detectors to make the surfaces smooth. Such high resistive electrodes are being explored since the detectors are one of the candidates of the proposed neutrino oscillation experiment in the India-based Neutrino Observatory (INO) [3]. One of the requirements for the INO RPC is to have a time resolution ~ 2 ns or better.

The silicone coated chambers, operated in the streamer mode using argon, tetrafluoroethane (R-134a) and isobutane in 34:59:7 mixing ratio, prepared by a gas mixing and flow control unit [4] have been tested with cosmic rays. The results of the long term test (with efficiency $>90\%$, counting rate of ~ 0.1 Hz/cm^2) and some other aspects such as crosstalk, dependence on threshold value, the effect of external humidity etc. of these silicone coated RPCs have been reported earlier [2,5]. In this article, we would like to present the timing characteristics of such single gap (2 mm) silicone coated RPCs.

2. Test setup and method of calculation

The time resolution of the RPC was measured in the same cosmic ray test bench described in Ref. [2]. The cosmic ray telescope was constructed using three scintillators, two placed above the RPC and one below. The individual time resolution of each RPC was estimated as follows. The triple coincidence of the signals obtained from the three scintillators was taken as the START signal (master trigger) for the TDC. The STOP signal was taken from a single RPC strip. Fig. 1 shows the schematic of the time resolution measurement setup.

The distribution of the time difference between the master trigger and the signal from one RPC strip is shown in Fig. 2. Time calibration was measured as 0.1 ns/channel. From the time difference spectrum, the full width at half maximum (FWHM) and the corresponding standard deviation (σ_{ij}), where i and j refer to scintillators and the RPC, were obtained by fitting a Gaussian function. The same σ_{ij} were obtained similarly for the three different pairs of the scintillators I, II and III. The intrinsic time resolutions of the RPC and the scintillators were obtained from the individual standard deviations σ_i, σ_j, which were extracted by solving the equations: $\sigma_{ij}^2 = \sigma_i^2 + \sigma_j^2$ [6]. Time resolution (FWHM) of the individual scintillators were obtained as: 3.20 ± 0.07 ns (scintillator I), 3.39 ± 0.08 ns (scintillator II) and 1.98 ± 0.02 ns (scintillator III), where the quoted uncertainties include statistical and fitting errors. The extracted time resolution (FWHM) of the RPC at 8 kV operating voltage for a typical run was: 2.48 ± 0.08 ns.

3. Results

The average signal arrival time (T), taken as the mean position of the fitted Gaussian peak in the time difference spectrum (such as in Fig. 2) and the time resolution (FWHM) τ of the RPC as function of the applied high voltage (HV) for the two 30 cm × 30 cm RPCs are shown in Fig. 3. The measured values of T include the delays introduced in both the START and STOP channels by the

* Corresponding author. Tel.: +9133 2337 1230; fax: +9133 2334 6871.
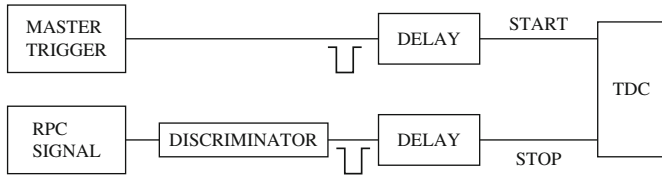*E-mail address:* saikatb@veccal.ernet.in (S. Biswas).

Fig. 1. Schematic representation of the time resolution measurement setup. A common start Phillips Scientific 7186 Time to Digital Converter (TDC) was used.
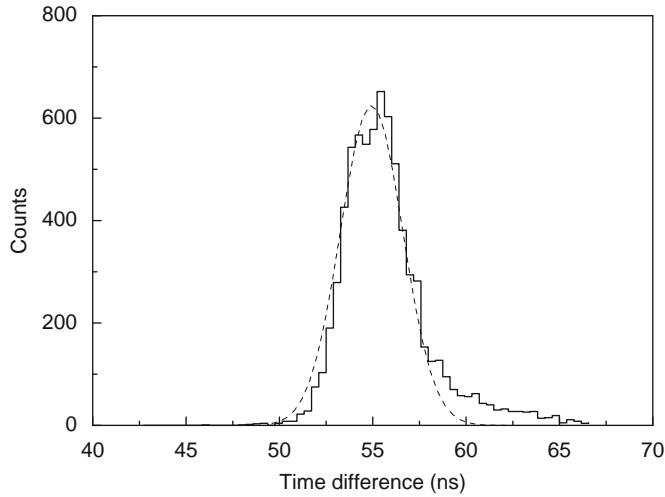

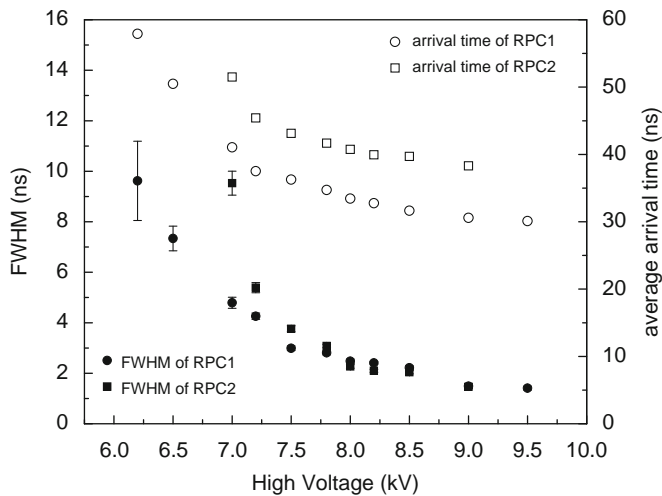**Fig. 2.** The distribution of the time difference between the RPC and the master trigger.

Fig. 3. The time resolution (FWHM) and the average signal arrival time with respect to the master trigger as a function of HV for two silicone coated RPC.

Fig. 4. The time resolution (FWHM) and the average signal arrival time as a function of period of operation.

Fig. 5. The time resolution (FWHM) and the average signal arrival time of one RPC with respect to another RPC as a function of HV.

Finally the time resolution between two RPCs was measured by taking the START signal from one RPC operated at constant voltage (8 kV), while the voltage of the other RPC was varied. The results are shown in Fig. 5. In this case, the average time resolution is found to be ~3 ns in the plateau region.

4. Conclusions and outlook

In conclusion, a systematic study on the timing properties of silicone coated RPCs made of bakelite paper laminates, commercially available in India has been performed. The measured time resolution of those RPCs have been found to be ~2 ns which is comparable to any single gap glass or linseed oil coated bakelite RPC. The study of the effect of continuous HV on the time resolution has also been performed. In the long term operation of the detector, 2–3 ns time resolution is obtained.

electronics shown in Fig. 1. The time resolution for both the modules improves and the average signal arrival time decreases with the increase of HV which is common to any gas filled detector. At the plateau region, the time resolution has been found to be ~2 ns.

One of the modules was tested for a long period (more than 130 days) at a constant high voltage of 8 kV and showed nearly constant values of the time resolution (~2–3 ns) and the average signal arrival time (~55 ns) as shown in Fig. 4.

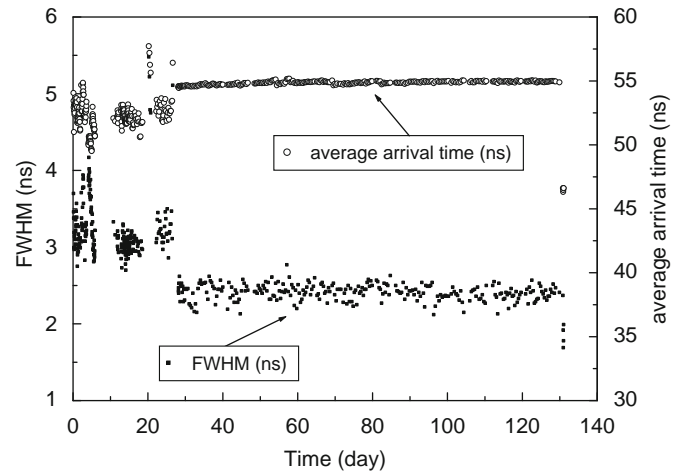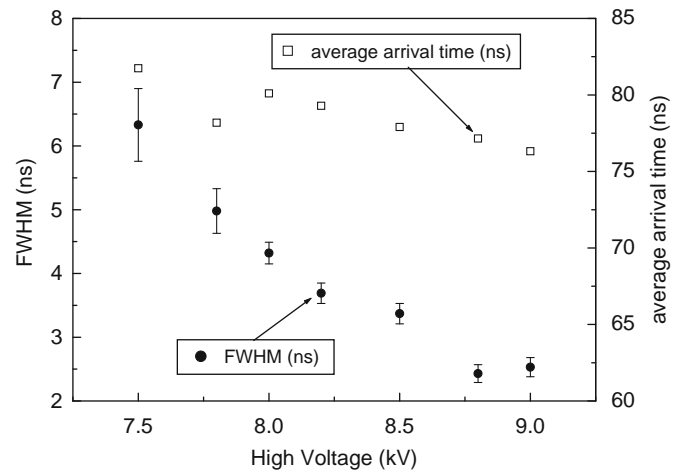## References

[1] R. Santonico, R. Cardarelli, Nucl. Instr. and Meth. 187 (1981) 377.
[2] S. Biswas, et al., Nucl. Instr. and Meth. A 602 (2009) 749.
[3] INO Project Report, INO/2006/01, June 2006, ⟨http://www.imsc.res.in/~ino/⟩.
[4] S. Bose, et al., Nucl. Instr. and Meth. A 602 (2009) 839.
[5] S. Biswas, et al., Nucl. Instr. and Meth. A 604 (2009) 310.
[6] P. Fonte, et al., Nucl. Instr. and Meth. A 449 (2000) 295.